Title

Development of Mass Spectrometry-based Workflows to Study Metal Interactions and Dynamics in the Extracellular Space

Author

Janisse, Samuel Elijah

Publication Date

2023

Peer reviewed|Thesis/dissertation

Development of Mass Spectrometry-based Workflows to Study Metal Interactions and Dynamics in the Extracellular Space

By

SAMUEL ELIJAH JANISSE
DISSERTATION

Submitted in partial satisfaction of the requirements for the degree of

DOCTOR OF PHILOSOPHY

in

Chemistry

in the

OFFICE OF GRADUATE STUDIES

of the

UNIVERSITY OF CALIFORNIA

DAVIS

Approved:

Marie C. Heffern, Chair

Sheila S. David

Carlito B. Lebrilla

Committee in Charge

2023

Table of Contents

Abstract of the Dissertation

Development of Mass Spectrometry-based Workflows to Study Metal Interactions and Dynamics in the Extracellular Space

The works included in this dissertation focus on the application of analytical and biochemical methodologies to study metal-binding and metal-regulating biomolecules. Additionally, aspects of molecular biology, programming, and spectroscopy are found in these works. This thesis describes the implementation of mass spectrometry-based techniques to understand metal dynamics in the extracellular space.

Chapter One describes the current state of mass-spectrometry-based applications toward the discovery of metal-binding species and methods to determine metal-interaction sites. This chapter highlights techniques for understanding metal dynamics of metal-binding biomolecules as well as monitoring the distribution of metal micronutrient speciation in the extracellular space. Topics include sample preparation, native and non-native mass spectrometry (NMS), size exclusion chromatography coupled with inductively coupled plasma mass spectrometry (SEC-ICP-MS), and immobilized metal affinity chromatography (IMAC). This chapter will provide the framework for the following chapters in this thesis.

Chapter Two describes efforts to elucidate the zinc and copper binding propensity and binding site of the peptide hormone C-peptide. Methods used include mass spectrometry (MS), nuclear magnetic resonance (NMR), ultraviolet–visible light spectroscopy, and isothermal calorimetry (ITC). These studies determined that Cu^{2+} binding occurs primarily at the N-terminus;

however, other interaction sites beyond what could be confidently detected may occur at the C-terminal region.

Chapter Three focuses on identifying copper-binding peptides by IMAC. This chapter includes work towards the development and the utilization of IMAC to enrich synthetic metal binding peptides as well as the peptide hormone hepcidin – showing possible structural dependence of Hepcidin for Cu^{2+} mediated ternary complex formation. IMAC work was further extended to identify Cu^{2+} binding peptides from enzymatically digested rice bran. Specific peptides were selected based on common sequence motifs and hydrophobicity. Selected peptides were investigated for their Cu^{2+} binding and anti-oxidative properties through chelator, copper reduction, and copper reactivity assays. Lastly, we demonstrate through *in vitro* studies followed by western blot increased AMP-activated protein kinase (AMPK) activation for each peptide, indicating a link between altered copper bioavailability and decreased diabetic complications.

Chapter Four includes developing and optimizing an IMAC procedure for enriching copper-interacting proteins from serum and plasma. This work describes buffer optimization, rational chelator selection, serum loading considerations, and applications for probing biological states. Specifically, this chapter describes the use of IMAC to investigate the strength of copper-mediated ternary complex formation of serum protein, revealing differences concerning the amount of serum applied to a fixed amount of resin. Further, work involving the analysis of plasma collected from patients with Wilson disease and without using a traditional proteomics workflow and the developed IMAC-proteomics workflow is described. Preliminary data from applying IMAC coupled with proteomics to enrich metal binding species from serum collected from obese and post-bariatric surgery mice. This work chapter showcases the use of IMAC beyond the

identification of metal interacting species and provides evidence of changes in metal-binding propensities in disease states.

Chapter Five describes collaborative work towards understanding monosaccharides' influence in the copper-containing ferroxidase ceruloplasmin. Previous work has demonstrated that ceruloplasmin concentration is decoupled to its bioactivity in the presence of monosaccharides such as glucose. Moreover, in the presence of ceruloplasmin degrades at a higher rate through an unknown mechanism. This chapter described our efforts to both substantiate these observations and elucidate the mechanism of glucose-dependent bioactivity.

Acknowledgements

Hard to imagine six years ago that I would be writing, let alone completing, my Ph.D dissertation. I would not have been able to last this long without the support, guidance, and patience of family and friends. All who have lent a hand, listened to my worries/doubts/frustrations, provided me with constructive feedback – I thank you from the bottom of my heart.

Mom and dad, thank you for your constant support both in and out of graduate school. From teaching me the value of hard work but to not take things too seriously. Thank you for encouraging me to explore new things from joining the swim team to pursue my curiosity about science like going out and collecting stream water samples so I could test it for chemicals in middle school. Thank you for teaching me to pursue my curiosities and passions. Your constant encouragement to not give up and press on was and is invaluable. The lessons I learned from you are invaluable and I am grateful for your continued support.

Matthew! Bro. Thanks for being one chill dude and putting up with my never-ceasing antics, which I think you have had to deal with the most over the years. Thank you for being an inspiration with your work ethic and precision like focus.

Mark and Holly, thank you for your support during grad school. I thank you for patience as I always seemed to be stressed out during the holidays – I promise it wasn't you! Devon, thank you for being a cool person and willing to bike the Cali coast with me during grad school – even though I was most definitely not prepared to do an extended bike trip. Also, thanks for keeping me from having to fish the bike rental from the bottom of the San Diego pier…

Dr. William Jewell, thank you for your help in figuring out how to maximize the utility of the Orbitrap. Your contributions shaped the research I was able to do in grad school.

Prof. Elizabeth Neumann, thank you for being an awesome mentor to me the last several months! I appreciate your willingness to chat about academia and mass spec. Thank you for letting me hang around whenever you and your lab were doing cool mass spec things. UC Davis Chemistry is lucky to have you in the department.

I would also like to thank all the members of the Heffern Lab. I would not be the scientist that I am today without each one of you. From the amazing post-docs to awesome grad students to the brilliant undergrads.

Prof. Michael Stevenson, thank you for being a great mentor when I first joined the lab. I will always appreciate the time you took to help me navigate those early years in the lab. Dr. Rebeca Fernandez, thank you for challenging me to think of things in a different light and providing invaluable scientific perspectives. Moreover, thank you for always being willing to read and provide constructive feedback on my writing – I am a much better writer thanks to you.

Vanessa, JJ, and Nate… you all have been such a tremendous source of joy during grad school. From the beginning, I have always felt supported and encouraged by you all. It has truly been an honor and privilege to work alongside of you all for the last five years – through all of the great laughs and crazy events. You all are truly remarkable people and scientists. I look forward to staying in touch and seeing all the things you will do and how you will continue to be awesome.

Jess, Chantel, Estely, and Amanda! It was a pleasure to work with you and learn from you. Jess, your attention to detail and figure making abilities still make me jealous. Chantel, thank you for putting up with my incessant questions about that one enzyme reaction and your cheerful attitude help make a great lab environment. Estely, thank you for always being willing to chat and letting me ramble on and on about mass spec stuff. It really is the best. Amanda, your excitement

about science really made working on the IMAC project more fun when you joined and learning how to do animal work alongside you was so much fun. Thank you all for being great lab mates!

Richard, thanks for always being willing to have a great argument/debate. I think after all of this time I would agree with your stance on cars – maybe. In all seriousness, thank you for being a great lab mate and sharing your passion for science policy. You are going to do great.

Samantha and Jacob, even though you both joined right at the end of my time in the Heffern Lab, I can already tell that you two are going to do great. You both are great, and the lab is lucky to have you two in it!

Manesh! Thank you for being an awesome undergrad in the lab. It was a blast to work with you during the first two years of grad school. We had a lot of laughs. Thank you for being patient with me as I was trying to figure out my projects and how to be a mentor.

Vibha! It was so much fun working in the lab with you. When the projects were and were not working you were a constant source of inspiration and motivation. Thank you for your patience and support. You are a brilliant scientist and are going to make an amazing doctor.

Prof. Marie Heffern. I will always appreciate the lessons you taught me about science. Thank you for allowing me to go after what I found interesting and encouraging me to follow my passions. Thank you for always being willing to meet with me, listen to my concerns, and provide valuable insights. You've led by example and showed me that success does not need to come at the expense of living life. I'll be forever grateful for being in your lab and the lessons I learned here at UC Davis.

Lastly, I would like to thank my partner in life, Sierra. There are no words that I can write to accurately convey how much your support, encouragement, and wisdom means to me. Your strength over the years is an inspiration and something I hope one day to emulate. From giving

your time to listen to me go over my talks repeatedly to telling me “YOU are going to be okay” when I needed to hear it – you have been the greatest support. I could not have done this without you. Sierra, looking forward to the next chapter!

Chapter 1

Mass Spectrometry based Methods for Investigating Metal Interacting Species in the Extracellular Space

Parts of this chapter are in a manuscript currently under review and may be published after dissertation submission.

1.1 Introduction

Metal ions are associated with 30-50% of protein function, serving diverse functions like structural cofactors, catalytic centers, and metabolite transporters.[1–4] To maintain a state of equilibrium, a network of proteins and molecules has evolved that regulate metal micronutrients via chaperones, transporters, storage proteins, and metal-binding small molecules like chelators.[5–8] Early identification of metal-binding molecules stemmed from isolated discoveries of tightly bound ions. As the field has progressed, increasing work has not only diversified the known subset of metalloproteins and peptides but has also introduced the concept that the biological metal population is subdivided into two distinct pools: the static pool, i.e. tightly-bound metal ions, and the more loosely bound or "labile" pool.[9]

Intracellular metal-based studies primarily focus on the static pool and can be separated into two categories. The first is that of metalloproteins and metalloenzymology in which the relationship between the structure and function of a protein is investigated. In these cases, it is typical for a metal to coordinate to a protein via amino acid residues, forming the first coordination sphere. In a metalloenzyme, the first and second coordination spheres around the metal ion establish the active site which control the reactivity of the enzyme.[10] The second category of metal micronutrient investigations is typically focused on metal toxicity. As mentioned above, tight regulation of all metals is essential to function, as such scientists have sought to define the intracellular pool of “free” and labile transition metals.

Less focus has been directed towards understanding metal interactions with extracellular biomolecules. The extracellular milieu is highly complex, consisting of a plethora of biomolecules like proteins, peptides, hormones, carbohydrates, lipids, amino acids, and metals. While existing analytical and protein isolation tools are frequently able to preserve the metal-biomolecule

interaction of the static pool, the labile pool may evade detection by traditional methods due to their weaker affinity and exchangeable nature. Therefore, the development of methods and techniques that enable the study of metal interactions of species that can readily exchange metal micronutrients with their environment is essential. In this chapter, we will discuss existing and emerging technologies used in studying metal-species interaction with a focus on metal binding species identification, metal speciation, and metal distribution via mass-spectrometry based techniques.

1.1.1 Structure from Sequence: Identifying Metalloproteins from Common Motifs

Almost twenty years ago it was estimated that approximately one-third of all purified proteins and enzymes necessitated a metal cofactor for their biological function,[11] but only a subset of metalloproteins had been isolated and validated. One classical approach for identifying proteins by their function is in alignment of consensus sequences. The sequencing of the human genome and subsequent purification and structural characterization of newly identified proteins provided scientists a wealth of information relating sequence to structure. As many of these proteins lacked known functions, bioinformatic analyses became common to identify relationships between structure and function in a high-throughput manner. In this way, predictive tools can be employed to the metalloproteome using known metal-binding motifs as search parameters in protein, family, and domain databases to yield predictions of proteins that bind metals with follow-up experimental structure/function characterization. While this approach has been powerful in identifying motifs within the same region in a protein, several metalloproteins that have been discovered would have evaded these bioinformatic-driven predictions. Although canonical motifs exist, such as the

copper-binding ATCUN motif[12] and the iron-binding 2-histidine-1-carboxylate motif, [13] additional factors that influence the specific role of amino acid residues on metal interactions are not strongly accounted for in sequence-based analysis. First, the same metal-binding motif that composes the primary coordination sphere of a metalloenzyme likely has a unique second coordination sphere that supports the enzyme function; a single motif can have divergent functions. In the case of a protein sequence with no structure, it is difficult to extrapolate amino acid positions from a sequence; residues which are sequentially distant may come together in a folded protein to form a metal coordination site. Finally, it is likely that non-canonical metal-binding motifs exist which have yet to be investigated. The many challenges that arise with the use of bioinformatic prediction highlights the importance of using a multi-faceted approach that discover and elucidate the function and dynamics of metal binding species in tandem. Bioinorganic chemists leverage a host of spectroscopic techniques such as UV-vis, NMR and EPR spectroscopy to gain crucial information regarding metal binding environment. While powerful, many of these techniques require high sample concentrations and/or present challenges in complex mixtures, limiting studies in many biological samples. Mass spectrometry offers promise for filling this gap. The remaining sections of this article will focus on recent advances on mass spectrometry in addressing studying metal-binding species.

1.1.2 Mass Spectrometry Approaches to Characterizing Spectroscopically Challenging Metal/Biomolecule Interactions

Mass spectrometry (MS) based techniques are appealing to study metal complexation to biomolecules due to their sensitivity, low sample volume requirement, and potential for high-throughput formats. A consideration in adapting applying mass spectrometry-based techniques with metal-binding interactions is the weaker nature of coordination bonds relative to covalent interactions. Electrospray ionization (ESI) based MS techniques is attractive to study interactions like metal coordination, as it preserves structure, post-translational modifications, and non-covalent interactions during ionization. Rapid assessment of metal adducts may be screened and assessed by coincubation of solutions with metal salts with biomolecules. ESI-MS based profiling can be further coupled with a multitude of fragmentation techniques such as collisionally induced dissociation (CID), rapid multi photon induced dissociation (RMPID), and electron capture/transfer dissociation (ECD/ETD) to identify the regions of metal binding within a larger peptide or protein.

The application MS based techniques fills an important gap in studying metal interactions with peptides and small proteins that lack both chromophoric residues or higher order structure, rendering study by traditional spectroscopic method difficult.[14–16] One such example is C-peptide, a hormone-like peptide co-secreted with insulin and zinc by pancreatic beta cells. Initially regarded to be inert, a host of studies have shown it to be linked to a multitude of improved biological outcomes independent of insulin.[17] The exact mechanism of C-peptide's bioactivity is unclear and inconsistencies with experimental results suggested an additional layer of regulation. Investigations into the inconsistencies led to the finding that metal interactions with C-peptide has notable impacts on its activity.[18] Direct coordination was initially thought to be unlikely due to the

lack of canonical metal binding sequence motifs in C-peptide, but a series of MS experiments by the Spence group revealed the formation of metal adducts with a number of divalent metal ions. In particular, the zinc adduct ion was visible at high abundance relative to the unmetallated species.[19] Tandem mass spectrometry studies of the C-peptide-Zn^{2+} species sought to isolate the Zn^{2+} interacting region by comparing the fragmentation spectra of the adduct against apo C-peptide. Although the fragmentation patterns were inconclusive regarding any definitive identification of the binding site, the data suggested the binding location was localized near the N-terminus.[19] Substitution of the hypothesized binding residues with alanine (E1A, E3A, D4A, E11A, and E27A) led to an obliteration of Zn^{2+} binding indicating the substituted residues are required for the interaction. Discussed in greater detail in Chapter 2, later work by our group further extended these findings, showing that C-peptide also forms an adduct with Cu^{2+}. Co-incubation of Cu^{2+} and Zn^{2+} showed the presence of only the Cu^{2+} adduct by high-resolution mass spectrometry, suggesting competitive binding to Cu^{2+} over Zn^{2+} when both species are present.[20] The data from the MS experiments were corroborated by additional spectroscopic studies (EPR, FTIR, and NMR), validating the use of the technique for assessing solution-phase dynamics. The MS-based studies with C-peptide showcases the power of MS-based experiments for systems that are otherwise challenging with existing biophysical techniques.

While ESI-MS techniques paired with fragmentation may reveal metal-binding regions, little structural information is acquired by these methods. Thus, complementing the fragmentation-based ESI-MS techniques, ion mobility mass spectrometry (IMMS) is emerging as a powerful approach for investigating metal-induced conformational changes. IMMS techniques used in tandem with computational based methods can aid in the elucidation structural conformers induced by metal coordination. This can be seen in the study of oxytocin, a neurohormone most commonly

associated with reproduction and childbirth.[21] The presence of divalent metal ions like Ca^{2+} and Zn^{2+} have been shown to affect hormonal activity, but whether these effects result from direct binding interactions remains unclear. The Bowers group coupled IMMS with molecular dynamics and density functional theory analysis to demonstrate and characterize metal binding to oxytocin. [22,23]. MS studies indicate binding of oxytocin to metals is dependent on pH with Zn^{2+}, Mg^{2+}, Ni^{2+}, Ca^{2+}, Mn^{2+}, Co^{2+}, and Cu^{2+} being coordinated at pH ~ 3. At higher pH only the Cu^{2+} and Ni^{2+} metal complex can be observed by MS. Metal adducts for both Ni and Cu showed several deprotonation states with the most abundant being the $[OT-3H+M]^-$ followed by a less intense $[OT-4H+M]^{2-}$ species. In contrast, no deprotonation was seen at lower pH, indicating metal facilitated deprotonation of three to four amide hydrogens at higher pH. CID, ion mobility, and computational experiments pointed to the most probable site of metal binding by four nitrogen atoms at residues 1, 6, 8, and 9 making a $4N_{1689}$ complex. Conversely, experiments conducted at lower pH suggested an octahedral 6O coordination by the carbonyl group or a trigonal bipyramidal 4O-1N coordination with the amine group of the N-terminus. The results illustrate how MS techniques can be aided with molecular modeling to reveal dynamics, such as the pH dependent interactions with the oxytocin backbone, information that would be overlooked by sequence-focused predictions.

1.1.3 Native Mass Spectometry of Metalloproteins: Metal Binding and Dynamics under Biologically-relevant Conditions

Metal-biomolecule interactions are sensitive to pH, redox environment, and 3-dimensional structures of the protein given the nature and intermediate strength of metal-ligand coordination bonds. These properties can pose challenges to conventional sample preparation methods for MS analysis, which often use low or high pH solvents that which influence metal interactions. Native

mass spectrometry (NMS) is a rapidly developing MS technique used to study intact biomolecules in their native state. The term "native" refers to the analyte state prior to ionization wherein the analyte most closely resembles its biological state. NMS has been developed to tackle an impressive size range of analytes from small molecules to large protein complexes in the hundreds of kDa size. [24,25] Importantly for metalloproteins and peptides, the approach can leave non-covalent interactions, including metal coordination bonds intact. NMS can be used in conjunction with ion mobility and fragmentation analysis to learn and retain biologically relevant structural information, including metal-induced conformational dynamics. A distinction with NMS from non-native MS techniques is the inclusion of a buffer to maintain pH in the biologically relevant range. Buffer choice can strongly influence quality of the of the data and the sensitivity of the experiment. The buffer needs be volatile and have a buffering range that encompasses the pH range of the endogenous environment. Ammonium acetate at concentrations ranging from 20-100 mM is commonly used as well as triethyl ammonium bicarbonate which produces lower charge states than ammonium acetate.[26] When studying large complexes, the mass range of the instrument can be a limiting factor, however, many modern instruments are being outfitted with extended mass range options allowing for large (kDa) complexes to be studied.

In the context of traditional structural biology methods which frequently require structural rigidity and homogeneity, NMS fills an important need in studying conformational dynamics of intrinsically disordered proteins and peptides. In the event where multiple conformers are present, such in the case where the metal can bind at multiple locations in a semi-disordered system, NMS data can provide conformational differentiation while simultaneously reporting on metal stoichiometry. This ability was recently showcased in assessing the metal binding of the antiangiogenic plasmin derived "histidine rich glycoprotein" peptide (HRP) fragment NMS.[27]

Studies have suggested that Zn^{2+} binds to the histidine-rich region (HRR) of HRP influencing its antiangiogenic properties. Martin et al. used NMS to quantify the binding of five to six Zn^{2+} ions to a peptide mimetic of the HRP proteolytic fragment consisting of the amino acids HRP330-364 (HRP330). IMMS experiments showed a decrease in arrival time when HRP330 was complexed to zinc, indicative of a more compact cross section. Increasing Zn^{2+} concentration leads to arrival time peak broadening suggesting the presence of multiple structural conformers.[28] Fragmentation by ETD and CID had reduced fragmentation in select regions of the peptide providing additional evidence of multiple locations of zinc binding.[28]

The preservation of biological conditions widens the bioinorganic applications of mass spectrometry beyond classical cytosolic proteins, including recent applications with membrane metalloproteins via incorporation into nanodisks and characterizing aggregation propensities.[29–31] For example, the copper centers of particulate methane monooxygenase (pMMO) have been probed using the nanodisk NMS platform. Authors were able localize the copper sites in pMMO and established a definitive correlation between copper loading at the PmoC site and methane oxidation.[32] Moreover, an emerging NMS technique called native ambient mass spectrometry (NiMS) is expanding the potential of NMS applications to studying metalloproteins directly in tissues. NiMS integrates NMS techniques with ambient mass spectrometry in which samples are analyzed with little to no pretreatment. Recent work by Hale and coworkers showed that NiMS could be used to look at metalated forms of GTPase Ran, paralbumin-alpha, and carbonic anhydrase localized in specific regions of rat brain.[33] While the method is currently limited in its sensitivity and size capabilities, further development of these technologies should provide exciting opportunities to observe tissue-specific differences metalloprotein states.

1.1.4 Consideration for Mass Spectrometry Analysis of Intact Biomolecules

While MS based techniques have promise in probing metal interactions, the information to be gleaned from ESI-MS should be interpreted with caution and paired with other solution-based validation methods. For instance, due to the nature of the electrospray process and ion generation, Cu^{2+} adduct formation may occur more readily during the desolvation of the charged droplets generated by ESI. Moreover, when analyzing transition metal complexes such as Cu and Fe via ESI-MS, oxidation state may change in the gas phase depending on source conditions, therein reducing, or increasing the metal-complex formation. However, changes in oxidation state of the bound metal can be determined by careful examination of the isotopic distribution of the metal complex with a mass spectrometer with high-resolution capability. A thorough study conducted by Bal et al. further substantiated these concerns by illustrating key differences between solution-phase metal binding equilibrium and gas-phase equilibrium.[34] Secondly, there is often uncertainty associated in using fragmentation-based studies for metal binding site localization. The difficultly arises from potential “metal hopping" which is akin to the “mobile proton theory” where the proton in transferred and facilitates the fragmentation process.[35] Therefore, care should be taken be when suggesting metal binding locations based on fragmentation spectra alone. Nevertheless, these studies highlight the power of mass spectrometry to quickly gain insight into metal binding, and MS remains an attractive means to elucidate the complex nature of metal binding dynamics.

1.1.5 Profiling Metal Populations based on Size

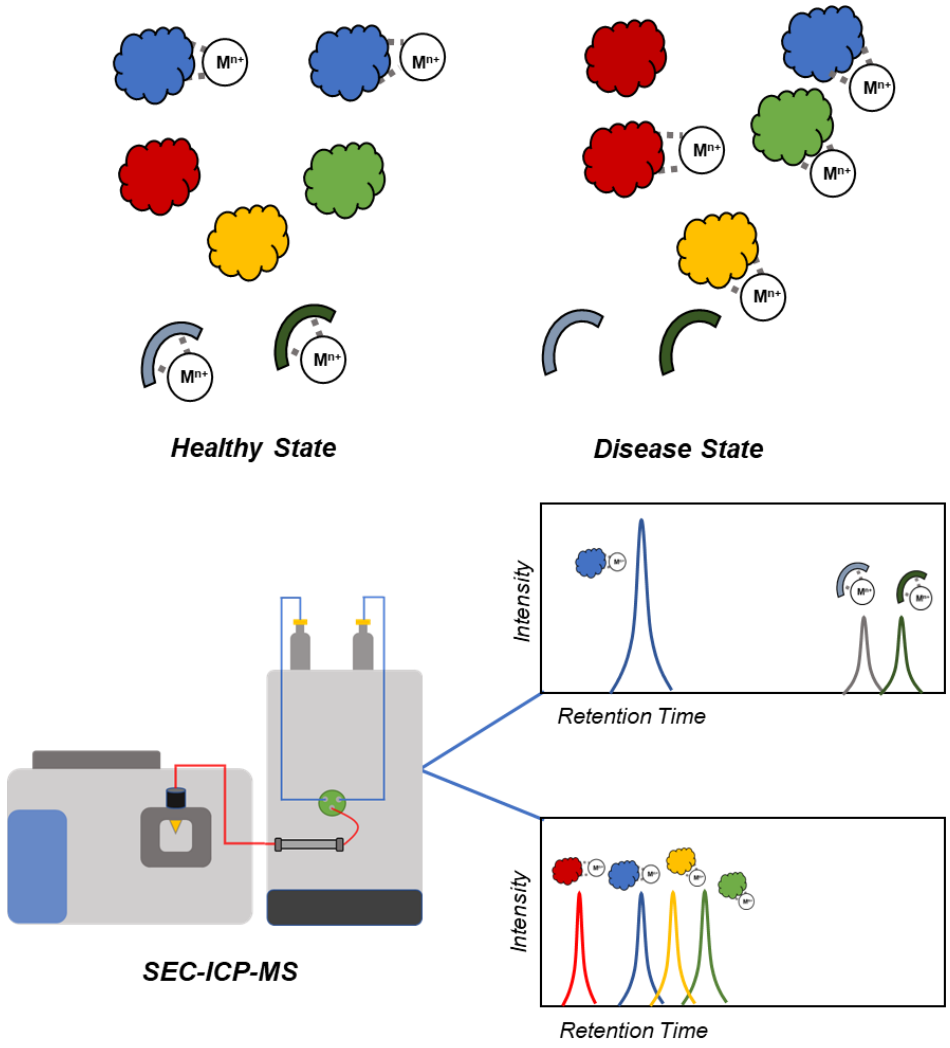

Figure 1.1. Profiling Metal Distribution by SEC-ICP-MS. The diversity of metal binding species is monitored by SEC-ICP-MS. Changes in metal distribution is used to assess disease states and progression.

While a few abundant metalloproteins have been established in the literature, a large majority of the metal-containing populations of biomolecules remain uncharacterized. The uncharacterized population is a mixture of large and small proteins and peptides as well as small molecule metabolites like citrate. Separating metal binding species via molecular weight cutoff (MWCO) filters is appealing due to experimental ease, efficiency, and range of cutoff sizes.[36]

Indeed this approach is the standard method for assessing copper status in the clinic. Copper populations are classified in terms of whether it is bound to the major carrier ceruloplasmin (CP). MWCO filtration is applied alongside total metal and/or immunoassay quantification of CP. Wilson disease, a genetic copper trafficking disorder, is typically monitored via comparison of the CP and non-CP bound copper (NCC) levels. MWCO filtration methods were recently leveraged in mice missing the copper importer Ctr1 to identify a novel copper carrier of < 2 kDa, termed small copper carrier (SCC), SCC was proposed to be responsible for increased urinary copper excretion in the mutant mice, indicating that low molecular weight metal binding species in the blood may influence and represent organism's metal status, warranting further investigation into their identities.[37]

Understanding not only total metal levels but also how the distribution shifts in disease states holds promise in diagnostics. The limitation with using strict MWCO approaches for this purpose is that it bins the copper pool into simply high- or low-molecular weight rather than a spectrum of sizes. Indirect methods like chelator/ultrafiltration methods also suffer from the inability to directly analyze speciated metal and rely on approximations and assumptions of metal binding. Other methods involving the use of NMS can be used to probe how speciation occurs in metalloproteins but currently lacks the ability to profile metal distribution in biofluids in a high-throughput manner. To this end, recent research has incorporated a combination of size exclusion chromatography (SEC) coupled to inductively coupled plasma mass spectrometry (ICP-MS). SEC separates analytes based on molecular weight while ICP-MS enables accurate metal quantitation. When combined, changes in metal speciation and distribution among molecular weight classes can be accurately measured and contrasted across conditions (Figure 1.1). SEC-ICP-MS has found utility is classifying Wilson disease based on copper distribution; monitoring zinc redistribution in

serum under high lipid content; as well as metalloprotein determination in human breast milk, serum, and cerebral spinal fluid.[38–44] One instance is the application of SEC-ICP-MS to monitor the redistribution of iron post intravenous injection of iron containing compounds used to treat iron deficiency. Using a custom SEC-ICP-MS, Neu et al. monitored the increase of iron binding species at different molecular weights after in injection of Ferrlecit (sodium ferric gluconate). Clear differences were observed for both protein bound (higher MW) and non-protein bound (lower molecular weight) species three hours post injection.[45] While still in the early stages of development SEC-ICP-MS used in conjunction with proteomics-based mass spectrometry techniques will provide a deeper picture into the complexities of metal dynamics and speciation.

1.1.6 Enriching Metal-Binding Species from Biological Mixtures

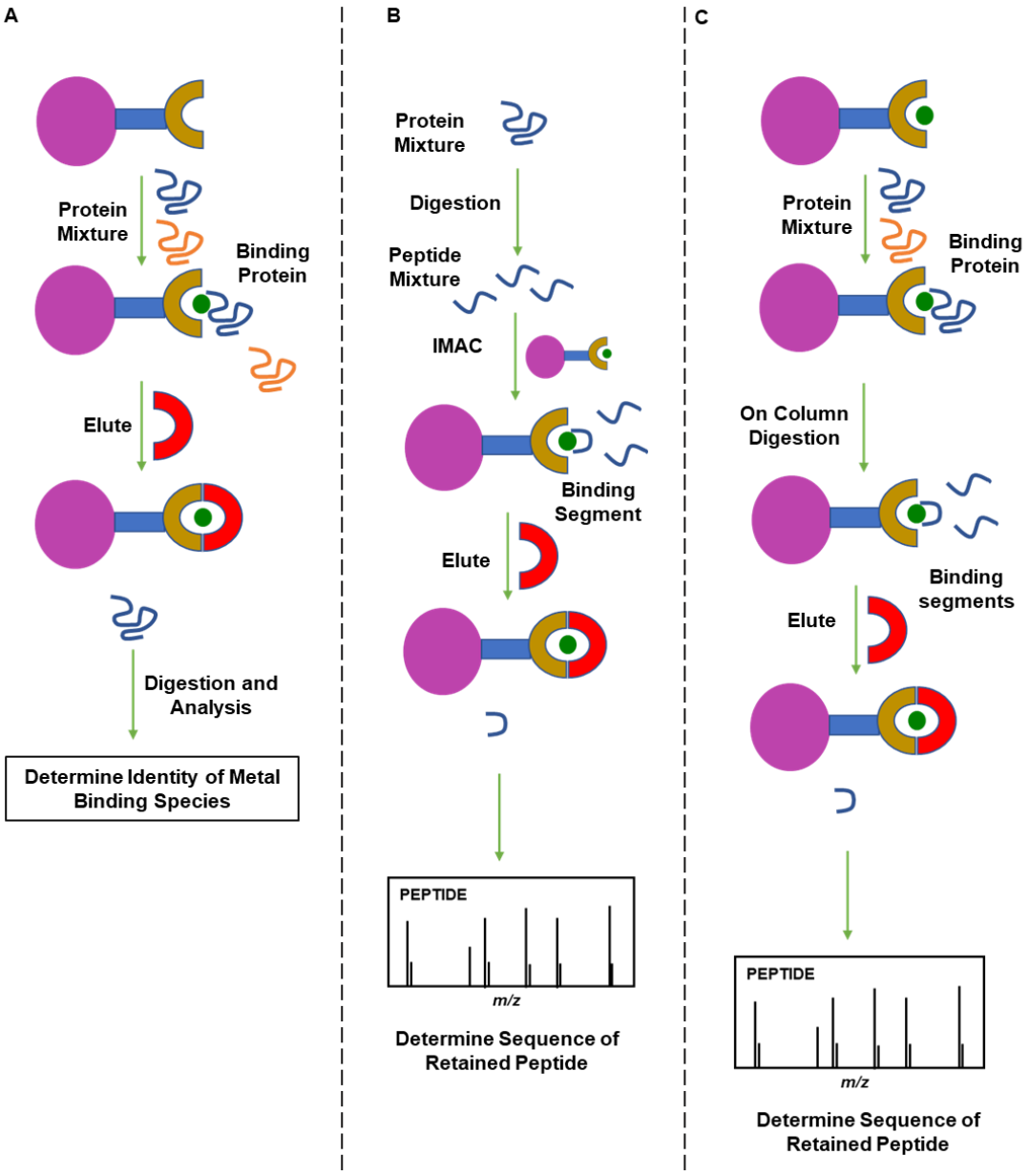

Figure 1.2. Varying Metal-binding Species Enrichment Methods via Immobilized Metal Affinity Chromatography. A) Traditional enrichment of proteins by IMAC. B) Identification of metal interaction sites of enzymatically digested proteins. C) On-resin protein digestion to identify putative metal interaction sites.

Complementary to developments in chromatography-paired ICP-MS, chromatographic enrichment of protein populations based on metal-binding propensities has the potential to identify new metal-binding populations. Bottom-up proteomics enables both the identification of proteins and a snapshot of the landscape of protein abundance in a biological mixture. Despite its utility, sample preparation involves harsh denaturing conditions and enzymatic digestion leading to a loss of metal coordination. This limitation may be circumvented by preserving metal-interaction information prior to the application of bottom-up proteomics. Immobilized metal affinity chromatography (IMAC) has the potential to fill this gap. IMAC was first introduced in the literature as a method for fractionating histidine and cysteine containing proteins.[46] While its most widespread use in current research is for the purification of histidine-tagged proteins, researchers have demonstrated its potential for identifying putative metal binding species that are difficult to predict based on sequence information alone.[47,48] IMAC comprises of three main components: an immobilizing resin, extending linker, and a metal chelating group. Biomolecules with metal binding propensities will interact with the immobilized metal creating a ternary complex whereas non-metal binding species will not interact with the resin, allowing their removal (Figure 1.2). In the early 2000s, several studies focusing on using IMAC to understand the metalloproteome illustrated the potential application of IMAC to gain biological insights. She *et al*. described cell line dependent differences between proteins enriched on a Cu^{2+} and Zn^{2+}-IMAC resin. Among those enriched on the Cu^{2+} loaded IMAC was protein disulfide isomerase (PDI) which had only been recently reported to bind Cu^{2+}. Smith *et al*. followed by separating microsomal and cytosolic components and applying each to a Cu^{2+}-IMAC resin. A total of 67 proteins were enriched with several not previously reported to associate with copper.[49,50]

IMAC has since found applications in understanding heavy metal toxicity. Through a combination of mercury loaded IMAC resin, 1D gel electrophoresis, and MALDI-TOF-MS, 31 mercury binding proteins from neuroblastoma cell (SK-N-SH) lysate were identified. Remarkably, many of the identified proteins function in a catalytic or structural role within the cell, pointing to a common mode of mercury toxicity involving the displacement of native metals from catalytic sites. For instance, the validity of the proposed mercury binding ability of protein disulfide isomerase and transketolase was substantiated by UV-Vis titration of Hg^{2+}.[51]

Although there is a dearth of knowledge regarding metal binding species and metal dynamics in the intracellular space, even less known regarding metal regulation in the extracellular space. IMAC has been uniquely applied to understand metal binding and regulation in blood proteins. Wang et al. applied serum to IMAC resins loaded with Zn^{2+}, Cd^{2+}, Ca^{2+}, Ni^{2+}, and Pb^{2+} resulting in over 700 protein identifications with several proteins showing metal specific enrichment levels. For example, transthyretin was moderately enriched in Ni^{2+} and Cu^{2+} whereas Zn^{2+} IMAC enriched transthyretin to lesser extent.[52] Extending IMAC's application to study metal binding dynamics, we explored the utilization of IMAC to study relative strength of Cu^{2+} - IDA interaction by incubating a fixed amount of resin with increasing percentages of serum. Both 1D-PAGE and mass spectrometry-based proteomics revealed key differences protein population with respect to increasing serum. The workflow was further extended to study differences in copper interacting proteins in Wilson disease and healthy controls. In additional to producing additional differentially abundant proteins, the IMAC workflow acted as a pseudo-clean up step while preserving key proteins abundance information in the non-traditional proteomics workflow.[53]

IMAC is also useful in studying dietary derived bioactive species that influence metal micronutrient metabolism. Peptides derived from enzymatic digestion of dietary foods and their

ability to act as an ionophores or chelators to facilitate transport of metal micronutrients is growing in interest.[54] The application of tilapia skin protein hydrolysates to Zn^{2+} loaded IMAC, several Zn^{2+} binding peptides were found at various molecular weights. Chelation capacity of the different molecular weight peptides increased as the molecular weight decreased. Several lower molecular weight peptides, including GFLGSP which was further analyzed, resisted further enzymatic degradation. Using monolayer of Caco-2 cells to model gastrointestinal transport, the authors discovered that GFLGSP transverses from the apical to the basolateral side of the cell via paracellular transport through tight junctions. The exact biological role GFLGSP and peptides with similar zinc binding properties are unclear, however, the possibility of proteolytic fragments of proteins acquired through the diet influencing the bioavailability of metal micronutrients by bypass metal transport systems warrants further investigation.[55]

IMAC enrichment generally infers the ability of a protein to bind to a metal ion with the interaction location being ambiguous. Pairing IMAC with protein digests can help circumvent this challenge. For instance, an initial IMAC enrichment followed by trypsin digestion and re-application of digested proteins to IMAC can point the specific sequences that interact with the resin (Figure 1.2). Smith et al. demonstrated this approach with *Streptococcus pneomiaie* lysates applied to Co^{2+} and Ni^{2+} IMAC resulting in over 200 putative metal binding proteins. Reapplication of tryptic peptides revealed the sequence motifs H(X)nH, M(X)nH, and H(X)nM. Comparing against background sequences the motifs showed significant enrichment, suggesting putative interaction sites.[56] To streamline this approach, She and coworkers showed that digestion-paired IMAC can be performed with a single enrichment step via “on-resin protein digestion” (Figure 1.2).[49] In on-resin digestion, the sample is first enriched on-column, but prior to elution of the bound species, the enzyme is applied directly to the resin. In theory, the remaining peptides

will be the sections of proteins interacting with the immobilized metal can be eluted and analyzed. The approach was used to find Bi^{3+} interacting sites of proteins from *H. pylori* to provide insight into the anti-bacterial mode of Bi-containing gastrointestinal drugs.[57 58]

1.2 Conclusions and Outlook

Developing analytical methods and tools that aid in the discovery of biologically relevant metal-interacting species and advance the understanding of metal dynamics is essential in improving human health. The increasing library of mass spectrometry-based tools is attractive and emerging technology will enable cutting edge breakthroughs in the field of metallomics. Combining the power of computational chemistry and mass spectrometry allows the exploration of metal binding site dynamics with respect to changes in post-translation modification, mutations, and ternary complex formation. While currently in its early stages, the implementation of native mass spectrometry-based imaging technologies with top-down proteomics will provide rich information on the temporal-spatial distribution of metal micronutrients and their metal-binding partners.

1.3 References

(1) Baradaran, R.; Berrisford, J. M.; Minhas, G. S.; Sazanov, L. A. Crystal Structure of the Entire Respiratory Complex i. *Nature* **2013**, *494* (7438), 443–448. https://doi.org/10.1038/nature11871.

(2) Putignano, V.; Rosato, A.; Banci, L.; Andreini, C. MetalPDB in 2018: A Database of Metal Sites in Biological Macromolecular Structures. *Nucleic Acids Res* **2018**, *46* (D1), D459–D464. https://doi.org/10.1093/nar/gkx989.

(3) Jiang, B.; Liu, G.; Zheng, J.; Chen, M.; Maimaitiming, Z.; Chen, M.; Liu, S.; Jiang, R.; Fuqua, B. K.; Dunaief, J. L.; Vulpe, C. D.; Anderson, G. J.; Wang, H.; Chen, H. Hephaestin and Ceruloplasmin Facilitate Iron Metabolism in the Mouse Kidney. *Sci Rep* **2016**, *6* (1), 39470. https://doi.org/10.1038/srep39470.

(4) Cassandri, M.; Smirnov, A.; Novelli, F.; Pitolli, C.; Agostini, M.; Malewicz, M.; Melino, G.; Raschellà, G. Zinc-Finger Proteins in Health and Disease. *Cell Death Discov* **2017**, *3* (1). https://doi.org/10.1038/cddiscovery.2017.71.

(5) Xiao, Z.; Brose, J.; Schimo, S.; Ackland, S. M.; la Fontaine, S.; Wedd, A. G. Unification of the Copper(I) Binding Affinities of the Metallo-Chaperones Atx1, Atox1, and Related Proteins: Detection Probes and Affinity Standards. *Journal of Biological Chemistry* **2011**, *286* (13), 11047–11055. https://doi.org/10.1074/jbc.M110.213074.

(6) Lee, V. J.; Heffern, M. C. Structure-Activity Assessment of Flavonoids as Modulators of Copper Transport. *Front Chem* **2022**, *10*. https://doi.org/10.3389/fchem.2022.972198.

(7) Massai, L.; Ciambellotti, S.; Cosottini, L.; Messori, L.; Turano, P.; Pratesi, A. Direct Detection of Iron Clusters in L Ferritins through ESI-MS Experiments. *Dalton Transactions* **2021**, *50* (45), 16464–16467. https://doi.org/10.1039/d1dt03106f.

(8) Yanatori, I.; Kishi, F. DMT1 and Iron Transport. *Free Radical Biology and Medicine*. Elsevier Inc. March 1, 2019, pp 55–63. https://doi.org/10.1016/j.freeradbiomed.2018.07.020.

(9) Ackerman, C. M.; Chang, C. J. Copper Signaling in the Brain and Beyond. *J Biol Chem* **2018**, *293* (13), 4628–4635. https://doi.org/10.1074/jbc.R117.000176.

(10) Fernandez, R. L.; Elmendorf, L. D.; Smith, R. W.; Bingman, C. A.; Fox, B. G.; Brunold, T. C. The Crystal Structure of Cysteamine Dioxygenase Reveals the Origin of the Large Substrate Scope of This Vital Mammalian Enzyme. *Biochemistry* **2021**, *60* (48), 3728–3737. https://doi.org/10.1021/acs.biochem.1c00463.

(11) Holm, R. H.; Kennepohl, P.; Solomon, E. I. Structural and Functional Aspects of Metal Sites in Biology. *Chem Rev* **1996**, *96* (7), 2239–2314. https://doi.org/10.1021/cr9500390.

(12) Gonzalez, P.; Bossak, K.; Stefaniak, E.; Hureau, C.; Raibaut, L.; Bal, W.; Faller, P. N-Terminal Cu-Binding Motifs (Xxx-Zzz-His, Xxx-His) and Their Derivatives: Chemistry, Biology and Medicinal Applications. *Chemistry - A European Journal* **2018**, *24* (32), 8029–8041. https://doi.org/10.1002/chem.201705398.

(13) Bruijnincx, P. C. A.; Lutz, M.; Spek, A. L.; Hagen, W. R.; Weckhuysen, B. M.; van Koten, G.; Gebbink, R. J. M. K. Modeling the 2-His-1-Carboxylate Facial Triad: Iron-Catecholato Complexes as Structural and Functional Models of the Extradiol Cleaving Dioxygenases. *J Am Chem Soc* **2007**, *129* (8), 2275–2286. https://doi.org/10.1021/ja064816x.

(14) Stevenson, M. J.; Uyeda, K. S.; Harder, N. H. O.; Heffern, M. C. Metal-Dependent Hormone Function: The Emerging Interdisciplinary Field of Metalloendocrinology. *Metallomics* **2019**, *11* (1), 85–110. https://doi.org/10.1039/c8mt00221e.

(15) Stevenson, M. J.; Farran, I. C.; Uyeda, K. S.; San Juan, J. A.; Heffern, M. C. Analysis of Metal Effects on C-Peptide Structure and Internalization. *ChemBioChem* **2019**, *20* (19), 2447–2453. https://doi.org/https://doi.org/10.1002/cbic.201900172.

(16) Kulprachakarn, K.; Chen, Y. L.; Kong, X.; Arno, M. C.; Hider, R. C.; Srichairatanakool, S.; Bansal, S. S. Copper(II) Binding Properties of Hepcidin. *Journal of Biological Inorganic Chemistry* **2016**, *21* (3), 329–338. https://doi.org/10.1007/s00775-016-1342-2.

(17) Wahren, J.; Ekberg, K.; Jörnvall, H. C-Peptide Is a Bioactive Peptide. *Diabetologia* **2007**, *50* (3), 503–509. https://doi.org/10.1007/s00125-006-0559-y.

(18) Meyer, J. A.; Froelich, J. M.; Reid, G. E.; Karunarathne, W. K. A.; Spence, D. M. Metal-Activated C-Peptide Facilitates Glucose Clearance and the Release of a Nitric Oxide Stimulus via the GLUT1 Transporter. *Diabetologia* **2008**, *51* (1), 175–182. https://doi.org/10.1007/s00125-007-0853-3.

(19) Keltner, Z.; Meyer, J. A.; Johnson, E. M.; Palumbo, A. M.; Spence, D. M.; Reid, G. E. Mass Spectrometric Characterization and Activity of Zinc-Activated Proinsulin C-Peptide and C-Peptide Mutants. *Analyst* **2010**, *135* (2), 278–288. https://doi.org/10.1039/b917600d.

(20) Stevenson, M. J.; Janisse, S. E.; Tao, L.; Neil, R. L.; Pham, Q. D.; Britt, R. D.; Heffern, M. C. Elucidation of a Copper Binding Site in Proinsulin C-Peptide and Its Implications for Metal-Modulated Activity. *Inorg Chem* **2020**, *59* (13), 9339–9349. https://doi.org/10.1021/acs.inorgchem.0c01212.

(21) Walter, M. H.; Abele, H.; Plappert, C. F. The Role of Oxytocin and the Effect of Stress During Childbirth: Neurobiological Basics and Implications for Mother and Child.

Frontiers in Endocrinology. Frontiers Media S.A. October 27, 2021. https://doi.org/10.3389/fendo.2021.742236.

(22) Wyttenbach, T.; Liu, D.; Bowers, M. T. Interactions of the Hormone Oxytocin with Divalent Metal Ions. *J Am Chem Soc* **2008**, *130* (18), 5993–6000. https://doi.org/10.1021/ja8002342.

(23) Liu, D.; Seuthe, A. B.; Ehrler, O. T.; Zhang, X.; Wyttenbach, T.; Hsu, J. F.; Bowers, M. T. Oxytocin-Receptor Binding: Why Divalent Metals Are Essential. *J Am Chem Soc* **2005**, *127* (7), 2024–2025. https://doi.org/10.1021/ja046042v.

(24) Leney, A. C.; Heck, A. J. R. Native Mass Spectrometry: What Is in the Name? *J Am Soc Mass Spectrom* **2017**, *28* (1), 5–13. https://doi.org/10.1007/s13361-016-1545-3.

(25) Zhou, M.; Lantz, C.; Brown, K. A.; Ge, Y.; Paša-Tolić, L.; Loo, J. A.; Lermyte, F. Higher-Order Structural Characterisation of Native Proteins and Complexes by Top-down Mass Spectrometry. *Chem Sci* **2020**, *11* (48), 12918–12936. https://doi.org/10.1039/d0sc04392c.

(26) Lemaire, D.; Marie, G.; Serani, L.; Laprévote, O. Stabilization of Gas-Phase Noncovalent Macromolecular Complexes in Electrospray Mass Spectrometry Using Aqueous Triethylammonium Bicarbonate Buffer. *Anal Chem* **2001**, *73* (8), 1699–1706. https://doi.org/10.1021/ac001276s.

(27) Magrì, A.; Grasso, G.; Corti, F.; Finetti, F.; Greco, V.; Santoro, A. M.; Sciuto, S.; la Mendola, D.; Morbidelli, L.; Rizzarelli, E. Peptides Derived from the Histidine-Proline Rich Glycoprotein Bind Copper Ions and Exhibit Anti-Angiogenic Properties. *Dalton Transactions* **2018**, *47* (28), 9492–9503. https://doi.org/10.1039/c8dt01560k.

(28) Martin, E. M.; Kondrat, F. D. L.; Stewart, A. J.; Scrivens, J. H.; Sadler, P. J.; Blindauer, C. A. Native Electrospray Mass Spectrometry Approaches to Probe the Interaction between

Zinc and an Anti-Angiogenic Peptide from Histidine-Rich Glycoprotein. *Sci Rep* **2018**, *8* (1), 1–13. https://doi.org/10.1038/s41598-018-26924-1.

(29) Wongkongkathep, P.; Han, J. Y.; Choi, T. S.; Yin, S.; Kim, H. I.; Loo, J. A. Native Top-Down Mass Spectrometry and Ion Mobility MS for Characterizing the Cobalt and Manganese Metal Binding of α-Synuclein Protein. *J Am Soc Mass Spectrom* **2018**, *29* (9), 1870–1880. https://doi.org/10.1007/s13361-018-2002-2.

(30) Fields, C. R.; Bengoa-Vergniory, N.; Wade-Martins, R. Targeting Alpha-Synuclein as a Therapy for Parkinson's Disease. *Front Mol Neurosci* **2019**, *12* (December), 1–14. https://doi.org/10.3389/fnmol.2019.00299.

(31) Moons, R.; Konijnenberg, A.; Mensch, C.; van Elzen, R.; Johannessen, C.; Maudsley, S.; Lambeir, A. M.; Sobott, F. Metal Ions Shape α-Synuclein. *Sci Rep* **2020**, *10* (1), 1–13. https://doi.org/10.1038/s41598-020-73207-9.

(32) Ro, S. Y.; Schachner, L. F.; Koo, C. W.; Purohit, R.; Remis, J. P.; Kenney, G. E.; Liauw, B. W.; Thomas, P. M.; Patrie, S. M.; Kelleher, N. L.; Rosenzweig, A. C. Native Top-down Mass Spectrometry Provides Insights into the Copper Centers of Membrane-Bound Methane Monooxygenase. *Nat Commun* **2019**, *10* (1), 1–12. https://doi.org/10.1038/s41467-019-10590-6.

(33) Sisley, E. K.; Hale, O. J.; Styles, I. B.; Cooper, H. J. Native Ambient Mass Spectrometry Imaging of Ligand-Bound and Metal-Bound Proteins in Rat Brain. *J Am Chem Soc* **2022**, *144* (5), 2120–2128. https://doi.org/10.1021/jacs.1c10032.

(34) Płonka, D.; Kotuniak, R.; Dąbrowska, K.; Bal, W. Electrospray-Induced Mass Spectrometry Is Not Suitable for Determination of Peptidic Cu(II) Complexes. *J Am Soc Mass Spectrom* **2021**, *32* (12), 2766–2776. https://doi.org/10.1021/jasms.1c00206.

(35) Wysocki, V. H.; Tsaprailis, G.; Smith, L. L.; Breci, L. A. Mobile and Localized Protons: A Framework for Understanding Peptide Dissociation. *Journal of Mass Spectrometry* **2000**, *35* (12), 1399–1406. https://doi.org/10.1002/1096-9888(200012)35:12<1399::AID-JMS86>3.0.CO;2-R.

(36) de Swart, L.; Hendriks, J. C. M.; van der Vorm, L. N.; Cabantchik, Z. I.; Evans, P. J.; Hod, E. A.; Brittenham, G. M.; Furman, Y.; Wojczyk, B.; Janssen, M. C. H.; Porter, J. B.; Mattijssen, V. E. J. M.; Biemond, B. J.; Mackenzie, M. A.; Origa, R.; Galanello, R.; Hider, R. C.; Swinkels, D. W. Second International Round Robin for the Quantification of Serum Non-Transferrin-Bound Iron and Labile Plasma Iron in Patients with Iron-Overload Disorders. *Haematologica* **2016**, *101* (1), 38–45. https://doi.org/10.3324/haematol.2015.133983.

(37) Gioilli, B. D.; Kidane, T. Z.; Fieten, H.; Tellez, M.; Dalphin, M.; Nguyen, A.; Nguyen, K.; Linder, M. C. Secretion and Uptake of Copper via a Small Copper Carrier in Blood Fluid. *Metallomics* **2022**, *14* (3). https://doi.org/10.1093/mtomcs/mfac006.

(38) Acosta, M.; Torres, S.; Mariño-Repizo, L.; Martinez, L. D.; Gil, R. A. Novel Method for Metalloproteins Determination in Human Breast Milk by Size Exclusion Chromatography Coupled to Inductively Coupled Plasma Mass Spectrometry. *J Pharm Biomed Anal* **2018**, *158*, 209–213. https://doi.org/10.1016/j.jpba.2018.06.003.

(39) Michalke, B.; Berthele, A.; Venkataramani, V. Simultaneous Quantification and Speciation of Trace Metals in Paired Serum and CSF Samples by Size Exclusion Chromatography–Inductively Coupled Plasma–Dynamic Reaction Cell–Mass Spectrometry (SEC-DRC-ICP-MS). *Int J Mol Sci* **2021**, *22* (16). https://doi.org/10.3390/ijms22168892.

(40) Latorre, M.; Herbello-Hermelo, P.; Peña-Farfal, C.; Neira, Y.; Bermejo-Barrera, P.; Moreda-Piñeiro, A. Size Exclusion Chromatography – Inductively Coupled Plasma – Mass Spectrometry for Determining Metal-Low Molecular Weight Compound Complexes in Natural Wines. *Talanta* **2019**, *195* (September 2018), 558–565. https://doi.org/10.1016/j.talanta.2018.11.055.

(41) Kirsipuu, T.; Zadorožnaja, A.; Smirnova, J.; Friedemann, M.; Plitz, T.; Tõugu, V.; Palumaa, P. Copper(II)-Binding Equilibria in Human Blood. *Sci Rep* **2020**, *10* (1), 5686. https://doi.org/10.1038/s41598-020-62560-4.

(42) Coverdale, J. P. C.; Barnett, J. P.; Adamu, A. H.; Griffiths, E. J.; Stewart, A. J.; Blindauer, C. A. A Metalloproteomic Analysis of Interactions between Plasma Proteins and Zinc: Elevated Fatty Acid Levels Affect Zinc Distribution. *Metallomics* **2019**, *11* (11), 1805–1819. https://doi.org/10.1039/c9mt00177h.

(43) Quarles, C. D.; MacKe, M.; Michalke, B.; Zischka, H.; Karst, U.; Sullivan, P.; Field, M. P. LC-ICP-MS Method for the Determination of "Extractable Copper" in Serum. *Metallomics* **2020**, *12* (9), 1348–1355. https://doi.org/10.1039/d0mt00132e.

(44) del Castillo Busto, M. E.; Cuello-Nunez, S.; Ward-Deitrich, C.; Morley, T.; Goenaga-Infante, H. A Fit-for-Purpose Copper Speciation Method for the Determination of Exchangeable Copper Relevant to Wilson's Disease. *Anal Bioanal Chem* **2022**, *414* (1), 561–573. https://doi.org/10.1007/s00216-021-03517-y.

(45) Neu, H. M.; Alexishin, S. A.; Brandis, J. E. P.; Williams, A. M. C.; Li, W.; Sun, D.; Zheng, N.; Jiang, W.; Zimrin, A.; Fink, J. C.; Polli, J. E.; Kane, M. A.; Michel, S. L. J. Snapshots of Iron Speciation: Tracking the Fate of Iron Nanoparticle Drugs via a Liquid

Chromatography-Inductively Coupled Plasma-Mass Spectrometric Approach. *Mol Pharm* **2019**, *16* (3), 1272–1281. https://doi.org/10.1021/acs.molpharmaceut.8b01215.

(46) PORATH, J.; CARLSSON, J. A. N.; OLSSON, I.; BELFRAGE, G. Metal Chelate Affinity Chromatography, a New Approach to Protein Fractionation. *Nature* **1975**, *258* (5536), 598–599. https://doi.org/10.1038/258598a0.

(47) Gaberc-Porekar, V.; Menart, V. Perspectives of Immobilized-Metal Affinity Chromatography. *J Biochem Biophys Methods* **2001**, *49* (1), 335–360. https://doi.org/https://doi.org/10.1016/S0165-022X(01)00207-X.

(48) Chang, Y. Y.; Li, H.; Sun, H. Immobilized Metal Affinity Chromatography (IMAC) for Metalloproteomics and Phosphoproteomics. *Inorganic and Organometallic Transition Metal Complexes with Biological Molecules and Living Cells* **2017**, 329–353. https://doi.org/10.1016/B978-0-12-803814-7.00009-5.

(49) She, Y. M.; Narindrasorasak, S.; Yang, S.; Spitale, N.; Roberts, E. A.; Sarkar, B. Identification of Metal-Binding Proteins in Human Hepatoma Lines by Immobilized Metal Affinity Chromatography and Mass Spectrometry. *Mol Cell Proteomics* **2003**, *2* (12), 1306–1318. https://doi.org/10.1074/mcp.M300080-MCP200.

(50) Smith, S. D.; She, Y. M.; Roberts, E. A.; Sarkar, B. Using Immobilized Metal Affinity Chromatography, Two-Dimensional Electrophoresis and Mass Spectrometry to Identify Hepatocellular Proteins with Copper-Binding Ability. *J Proteome Res* **2004**, *3* (4), 834–840. https://doi.org/10.1021/pr049941r.

(51) Li, Y.; He, B.; Hu, L.; Huang, X.; Yun, Z.; Liu, R.; Zhou, Q.; Jiang, G. Characterization of Mercury-Binding Proteins in Human Neuroblastoma SK-N-SH Cells with Immobilized

Metal Affinity Chromatography. *Talanta* **2018**, *178*, 811–817. https://doi.org/10.1016/j.talanta.2017.10.028.

(52) Wang, F.; Chmil, C.; Pierce, F.; Ganapathy, K.; Gump, B. B.; MacKenzie, J. A.; Mechref, Y.; Bendinskas, K. Immobilized Metal Affinity Chromatography and Human Serum Proteomics. *Journal of Chromatography B* **2013**, *934*, 26–33. https://doi.org/https://doi.org/10.1016/j.jchromb.2013.06.032.

(53) Janisse, S. E.; Sharma, V. A.; Caceres, A.; Medici, V.; Heffern, M. C. Systematic Evaluation of Copper(II)-Loaded Immobilized Metal Affinity Chromatography For Selective Enrichment of Copper-Binding Species in Human Serum and Plasma. *Metallomics* **2022**, mfac059. https://doi.org/10.1093/mtomcs/mfac059.

(54) Wang, T.; Lin, S.; Cui, P.; Bao, Z.; Liu, K.; Jiang, P.; Zhu, B.; Sun, N. Antarctic Krill Derived Peptide as a Nanocarrier of Iron through the Gastrointestinal Tract. *Food Biosci* **2020**, *36* (1), 100657. https://doi.org/10.1016/j.fbio.2020.100657.

(55) Ke, X.; Hu, X.; Li, L.; Yang, X.; Chen, S.; Wu, Y.; Xue, C. A Novel Zinc-Binding Peptide Identified from Tilapia (Oreochromis Niloticus) Skin Collagen and Transport Pathway across Caco-2 Monolayers. *Food Biosci* **2021**, *42* (May), 101127. https://doi.org/10.1016/j.fbio.2021.101127.

(56) Sun, X.; Yu, G.; Xu, Q.; Li, N.; Xiao, C.; Yin, X.; Cao, K.; Han, J.; He, Q. Y. Putative Cobalt- and Nickel-Binding Proteins and Motifs in Streptococcus Pneumoniae. *Metallomics* **2013**, *5* (7), 928–935. https://doi.org/10.1039/c3mt00126a.

(57) Wang, Y.; Tsang, C.-N.; Xu, F.; Kong, P.-W.; Hu, L.; Wang, J.; Chu, I. K.; Li, H.; Sun, H. Bio-Coordination of Bismuth in Helicobacter Pylori Revealed by Immobilized Metal

Affinity Chromatography. *Chem Commun (Camb)* **2015**, *51* (92), 16479–16482. https://doi.org/10.1039/c5cc04958j.

(58) Fang, X.; Yao, J.; Hu, X.; Li, Y.; Yan, G.; Wu, H.; Deng, C. Magnetic Mesoporous Silica of Loading Copper Metal Ions for Enrichment and LC-MS/MS Analysis of Salivary Endogenous Peptides. *Talanta* **2020**, *207* (July 2019), 120313. https://doi.org/10.1016/j.talanta.2019.120313.

Chapter 2

Analytical Investigation into Copper and Zinc Interaction Site of C-peptide

*Reprinted with permission from Stevenson, M. J.; Janisse, S. E.; Tao, L.; Neil, R. L.; Pham, Q. D.; Britt, R. D.; Heffern, M. C. Elucidation of a Copper Binding Site in Proinsulin C-Peptide and Its Implications for Metal-Modulated Activity. *Inorg Chem* **2020**, *59* (13), 9339–9349. https://doi.org/10.1021/acs.inorgchem.0c01212. Copyright 2023 American Chemical Society.

MS studies were conducted by SEJ; NMR, ITC, FTIR, UV-Vis was conducted primarily by MJS, RLN, and QDP; EPR was performed by LT. Section 2.3.2 is unpublished work that fit into the scope of the Chapter.

2.1 Abstract

The connecting peptide (C-peptide) is a hormone with promising health benefits in ameliorating diabetes-related complications, yet mechanisms remain elusive. Emerging studies point to a possible dependence of peptide activity on bioavailable metals, particularly Cu^{2+} and Zn^{2+}. However, little is known about the chemical nature of the interactions, hindering advances in its therapeutic applications. This work uncovers the Cu^{2+} - binding site in C-peptide that may be key to understanding its metal-dependent function. A combination of spectroscopic studies reveal that Cu^{2+} and Zn^{2+} bind to C-peptide at specific residues in the N-terminal region of the peptide and that Cu^{2+} is able to displace Zn^{2+} for C-peptide binding. The data point to a Cu^{2+}-binding site consisting of 1N3O square-planar coordination that is entropically driven. Furthermore, the entire random coil peptide sequence is needed for specific metal binding as mutations and truncations reshuffle the coordinating residues. These results expand our understanding of how metals influence hormone activity and facilitate the discovery and validation of both new and established paradigms in peptide biology.

2.2 Introduction

Endogenous peptides play a wide array of roles in biology from catalysts[1,2] to host defense[3,4] to extracellular signaling.[5–7] The proper function of these biomolecules is integral to healthy physiology as indicated by the number of diseases associated with their misregulation. Several reports have implicated metal ions in inducing aberrant functions in these peptides, such as promoting the pathological aggregation of the amyloid-β or αsynuclein peptides in association with Alzheimer's and Parkinson's diseases, respectively.[8–11] However, instances have also reported the necessity of these metals in other peptides; for instance, Zn^{2+} stabilizes the hexameric form of insulin for efficient storage in pancreatic vesicles.[12,13] This intricate balance in the bioinorganic chemistry of these peptides warrants further investigation to elucidate their native function and promote their therapeutic applications. While a number of bioactive peptides hold promise for clinical use such as in hormone therapies, progress has been hampered by a lack of understanding of the secondary factors, including metal ions, that may influence their activity. One such example is the connecting peptide (C-peptide) for which metals have a putative role in its activation. C-peptide is coreleased from β-cells in equimolar amounts with respect to insulin in response to elevated glucose in the blood.[14–18] While initially considered inert, C-peptide has emerged as a potential candidate for peptide-based therapy in diabetes for its diverse beneficial functions, most notably ameliorating vasculopathies and kidney dysfunction.[19–22] However, progress has been slowed by the lack of mechanistic clarity of its activity. Early work showed that C-peptide increases blood flow in several tissue types,[23–26] and later work by Spence and co-workers attributed these effects to the ability of the peptide to induce ATP release from red blood cells.[27–29] Interestingly, ATP release is enhanced by the presence of divalent metal ions including Zn^{2+}.[29] Further work from their laboratory showed that albumin is required for the transport of

both Zn^{2+} and C-peptide from pancreatic β-cells to red blood cells.[30] Another study reported a protective effect of C-peptide in preventing islet amyloid polypeptide (IAPP) aggregation in the pancreas but only in the presence of Zn^{2+}.[31] Recently, we uncovered a possible role for metals in mediating the internalization of the peptide; specifically, copper could inhibit the internalization of the peptide into HEK293 cells. Additionally, we determined that, in solution, Cu^{2+} directly interacts with C-peptide.[32]

Cu^{2+} binding was an intriguing discovery given that the peptide sequence does not contain classical copper binding residues, potentially pointing to the anchoring of Cu^{2+} through the terminal amine as seen with other peptides. Precisely defining this binding site poses challenges that are inherent to the structural aspects of the peptide. First, the short 31-mer peptide is primarily a random coil,[33,34] complicating the use of standard biophysical approaches for structural elucidation. In addition, our earlier work did not show any metal-specific alterations in the overall structure that could otherwise be used to probe the interaction.[32] Second, the peptide sequence (EAEDLQVGQVELGGGPGAGSLQPLALEGSLQ) is low in complexity, bearing only nine different residues, with glycine appearing seven times. Elucidating the metal binding site thus requires the question to be approached via multiple techniques to dissect the various pieces that contribute to the interaction. In this study, we sought to determine how and where Cu^{2+} binds to C-peptide and, given the reports on Zn^{2+}-dependent effects, whether the binding site is shared with Zn^{2+}. We found that Cu^{2+} binds to carboxylate groups at the N-terminus of C-peptide along with the terminal amine comprising a 1N3O square-planar geometry that is entropically driven. Moreover, this specific interaction requires the presence of the intact peptide, as both truncated and mutated analogues exhibit a reshuffling of the binding site. Consistent with our previous findings, Cu^{2+} exhibits higher-affinity binding to C-peptide than Zn^{2+} and consequently

outcompetes as well as precludes Zn^{2+} binding. The data suggest a model whereby Cu^{2+} binds preferentially at the N-terminal amine of the peptide and the E3 and D4 residues yet requires the remaining regions for site specificity. The elucidated Cu^{2+} binding site within C-peptide represents a unique ligand set in peptide biology and further expands the possibilities for metal/peptide hormone interactions.

2.3 Results and Discussion

2.3.1 C-peptide and Metal Binding by High Resolution Mass Spectrometry

Spence and colleagues demonstrated a metal-dependent physiological role of C-peptide: the incubation of erythrocytes with C-peptide induces ATP release but only if supplemented with Zn^{2+}.[27,29] Analysis via ESI-MS showed that Zn^{2+} directly interacts with C-peptide and that this interaction is most likely at one of the acidic residues.[27] Given our previous observations that both Zn^{2+} and Cu^{2+} could directly interact with C-peptide in solution and alter the cellular behavior of the peptide,[32] we sought to characterize the Cu^{2+}/C-peptide interactions, compare these observations to the previously studied Zn^{2+}/C-peptide adduct, and determine if the two metals could compete for C-peptide binding.

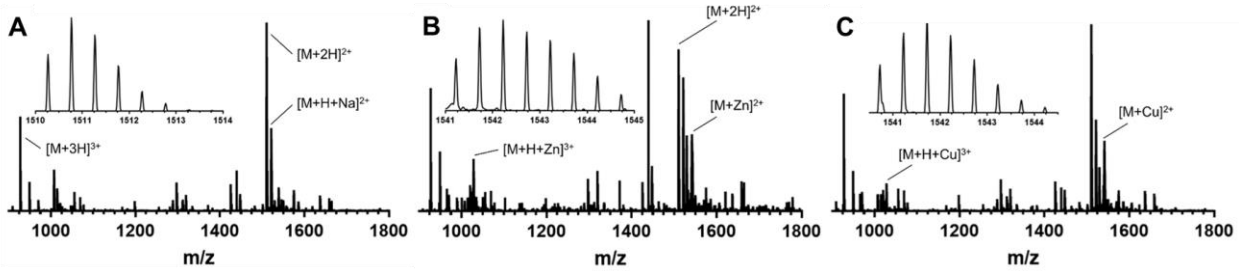

Figure 2.1. ESI-MS of (A) apo C-peptide, (B) Zn^{2+}/C-peptide, and (C) Cu^{2+}/C-peptide. The spectra demonstrate direct interactions between the metal ions and the peptide with a 1:1 metal-to-peptide ratio. All solutions were prepared in nanopure water at 50 μM C-peptide in the absence or presence of 1 equiv of the metal salt ($CuSO_4$ or $ZnClO_4$)

The mass spectra of apo C-peptide exhibit doubly and triply charged molecular ions corresponding to m/z values of 1510.27 ($[M + 2H]^{2+}$) and 1007.18 ([M + 3H]3+), respectively (Figure 2.1A). Additional peaks corresponding to C-peptide with sodium bound such as in $[M + H + Na]^{2+}$ were also observed (m/z = 1521.26) (Figure 2.1A). The addition of 1 equiv of Zn^{2+} results in shifts in the m/z values and indicates the presence of a Zn^{2+}/C-peptide adduct at a 1:1 metal to peptide ratio (m/z = 1541.22 $[M + Zn]^{2+}$ and 1027.81 $[M + H + Zn]^{3+}$) (Figure 2.1B). Spectra obtained via high-resolution ESI-MS confirmed the presence of the adduct by the expected isotopic distribution pattern for zinc as described by Tsednee et al.[35] These m/z values agree well with the previously reported masses obtained by the Spence group.[29] Similarly to Zn^{2+}, the addition of 1 equiv of Cu^{2+} to C-peptide results in the appearances of the doubly and triply charged 1:1 metal to-peptide adducts at m/z values of 1540.72 ($[M + Cu]^{2+}$) and 1027.49 ($[M + H + Cu]^{3+}$), respectively (Figure 2.1C). The experimental isotopic pattern is in good agreement with the theoretical isotopic distribution for Cu^{2+}.[35] These observations suggest that both Zn^{2+} and Cu^{2+} bind C-peptide in a 1:1 metal-to-peptide stoichiometry in the gas phase. To determine whether Cu^{2+} could outcompete Zn^{2+} for C-peptide binding, an equimolar amount of Cu^{2+} was added to a solution of the Zn^{2+}/C-peptide adduct, and the mass spectra of the resulting species were analyzed. The Cu^{2+} /C-peptide adduct clearly emerged, as indicated by the distinct Cu^{2+} isotopic distribution and the monoisotopic mass of 1540.72 m/z ($[M + Cu]^{2+}$), whereas no remaining peaks from the

Zn^{2+}:C-peptide adduct were observed (Figure 2.2). These data indicate that Cu^{2+} binds to C-peptide with a greater affinity than Zn^{2+}, and either the two metals compete for the same site or Cu^{2+} binding induces conformational changes that preclude Zn^{2+} binding.

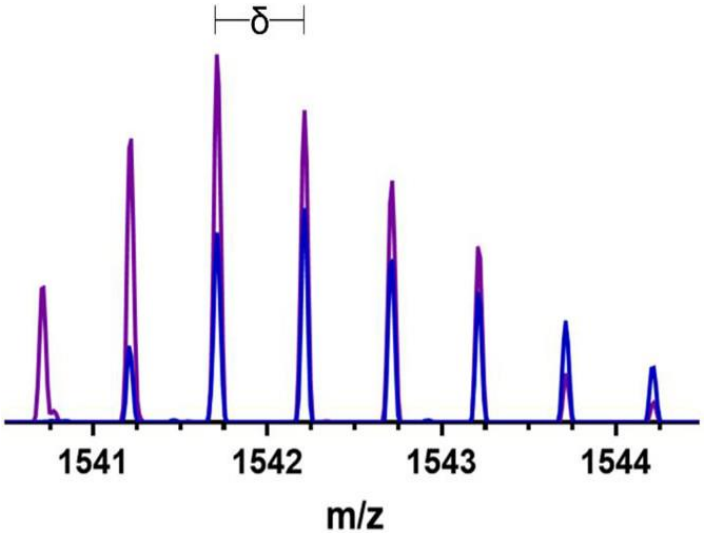

Figure 2.2. ESI-MS of C-peptide incubated with 1 equiv of Zn^{2+} (blue) and the resulting spectrum when 1 equiv of Cu^{2+} (purple) is added to the same solution. δ signifies the isotopic mass shift of the most intense peak present for C-peptide. Comparison of the spectra demonstrate the ability of Cu^{2+} to outcompete Zn^{2+} for C-peptide binding. Solutions were prepared in nanopure water at 50 μM C-peptide.

2.3.2 Isolating Metal Interaction Site via Tandem Mass Spectrometry

Having established metal/C-peptide binding, we sought identify the specific interaction site through tandem mass spectrometry. Tandem MS techniques have been used to identify regions of metal interaction in peptides by observing peptide fragments bound to the metal,[36] or by assessing differences in fragmentation between apo and metal-bound species.[37] Fragmenting doubly $[M+2H]^{2+}$ and triply $[M+3H]^{3+}$ charged apo C-peptide produced similar fragmentation patterns

(Figure 2.3A and Figure 2.4B) but incomplete sequence coverage. Most notable was a lack of fragmentation at the N- and C-termini.

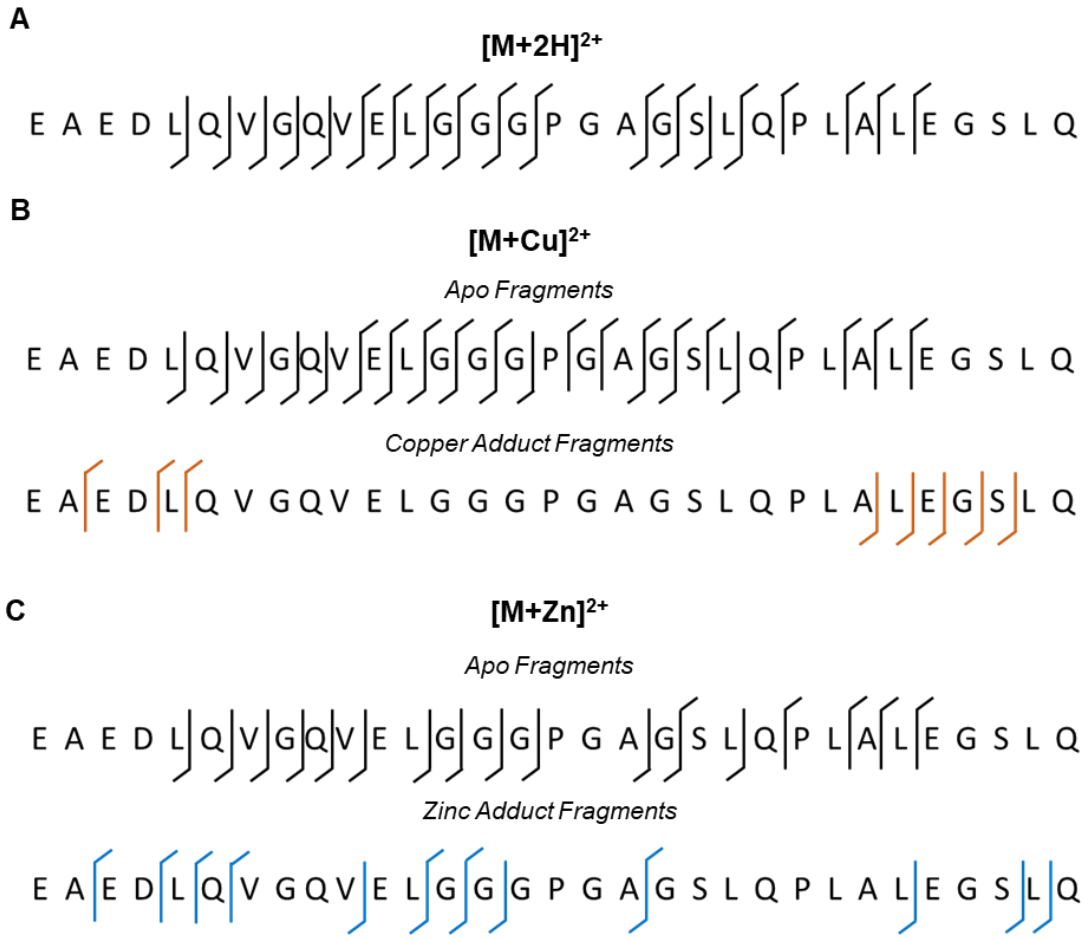

Figure 2.3. CID of doubly charged C-peptide and C-peptide metal adduct ions. A) b/y ions resulting from fragmentation of doubly charged $[M+2H]^{2+}$ C-peptide. B) apo and copper adduct b/y ions from fragmentation of $[M+Cu]^{2+\cdot}$ C) apo and zinc adduct b/y ions from fragmentation of $[M+Zn]^{2+\cdot}$

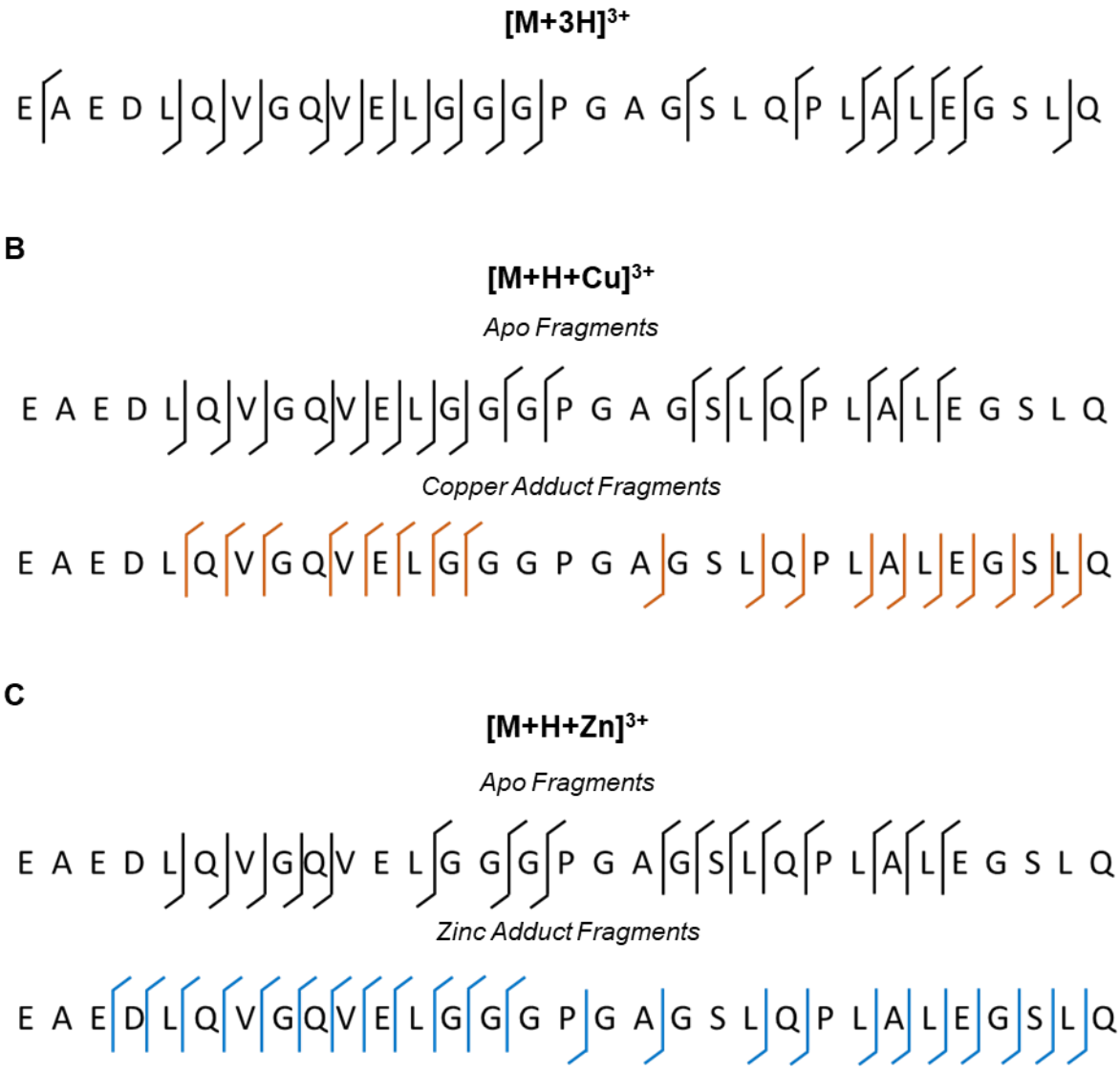

Figure 2.4. CID of triply charged C-peptide and C-peptide metal adduct ions. A) b/y ions resulting from fragmentation of triply charged $[M+3H]^{3+}$ C-peptide. B) apo and copper adduct b/y ions from fragmentation of $[M+H+Cu]^{3+}$. C) apo and zinc adduct b/y ions from fragmentation of $[M+H+Zn]^{3+}$.

Fragmentation of the doubly and triply charged copper and zinc C-peptide adducts produced significant number of fragment ions containing the metal ion. Spectra were inspected for both apo- and metal- bound product ions (Figure 2.3 and 2.4). Theoretical fragment assignments were based on Roepstoff and Fohlman nomenclature and are as follows: b ions represent the N-terminal fragment ions from cleavage across the amide bond whereas y ions are the C-terminal fragments.[38,39] Conformation of metal-fragment ions was performed by comparing the ion m/z to the theoretical mass of the metal bound b- and y-ion as well as and through inspection of their isotopic distribution (data not shown).

CID of each metal ion adduct led to a mixture of apo and metal bound product ions. For $[M+Cu]^{2+}$ and $[M+Zn]^{2+}$, there was sequence coverage similarity between the apo fragments and those of $[M+2H]^{2+}$. For both zinc and copper bound b- and y-ions, fragmentation near the N- and C-termini occurred producing b- and y-metal bound ions with significant length. CID of $[M+Cu]^{2+}$ produced minimal copper bound fragment ions and consisted primarily long of y- ions near the N-terminal and b- ions near the C-terminal regions. $[M+Zn]^{2+}$ fragmentation produced an increased amount of zinc bound b- and y-ion than $[M+Cu]^{2+}$ with fragmentation occurring throughout the sequence. Product ions of the triple charged $[M+H+Cu]^{3+}$ and $[M+H+Zn]^{3+}$ also did not produce complete sequence coverage or metal site localization. However, an increased number of metal bound b- and y- product ions occurred for both copper and zinc C-peptide adducts.

CID experiments were unable to directly isolate the copper and zinc interaction site of C-peptide. These data suggest the possibility of a sequence length dependence as MS/MS spectra did not contain metal bound b- or y-ions longer than 13 residues. It has been reported that changes in fragmentation propensity can be used to identify putative binding locations.[40] However, these data do not indicate a specific site of altered fragmentation when considering both apo and metal bound

product ion. As postulated by Spence and colleagues, the presence of long metal bound fragments with both the C- and N-terminal region may indicate multiple zinc and copper binding regions that are dependent on sequence length.[27]

While no definitive zinc or copper binding site of C-peptide was deduced from CID experiments, the ubiquitous presence of metal bound fragments containing the N- and C-terminal region suggest multiple sites of binding. It is possible that isobaric ions corresponding to C-peptide bound to zinc or copper at different locations were simultaneously fragmented. In this instance, a mixture of product ions would be observed in MS/MS spectra and inhibit accurate metal localization.

2.3.3 Isolating Metal Interaction Site via Nuclear Magnetic Resonance (NMR)

We sought to further probe the competition and binding location(s) of the metals via 1 H NMR spectroscopy, and we assessed for any characteristic shifts in resonances induced by the metals. In comparison to the spectra of apo C-peptide at pH 7.4 (Figure 2.5A and Figure 2.6A), the addition of Zn^{2+} results in subtle shifts of proton resonances throughout the spectrum, most visibly at 2.7, 3.7, 8.45, and 8.7 ppm (Figure 2.5B and Figure 2.6B), which could be attributed to CHβ protons on D4, glycine protons, and the backbone amide protons from D4 and E3, respectively. On the other hand, the addition of Cu^{2+} to C-peptide obliterates or weakens some signals (Figure 2.5C and Figure 2.6C). Because Cu^{2+} is paramagnetic, this loss of signal is most likely due to the paramagnetic broadening of protons in close proximity to the metal ion. Signal loss is specifically observed where peaks are expected for a set of aliphatic protons (1.4 ppm), the CHβ protons on D4 (2.7 ppm), glycine protons (3.7 ppm), and backbone amide protons from D4

(8.45 ppm) and E3 (8.7 ppm), and this obliteration of signal requires the saturation of the peptide with Cu^{2+} (Figure 2.7). Using these resonances as markers, we probed the competition between Cu^{2+} and Zn^{2+} by 1 H NMR. A stoichiometric amount of Cu^{2+} was added to the preformed Zn^{2+}/C-peptide complex or the reverse (Zn^{2+} added to the preformed Cu^{2+}/C-peptide complex) to determine if either metal could displace the other. In both scenarios, the resulting spectra are identical to that of Cu^{2+}/C-peptide with negligible resonances that correspond to Zn^{2+}/C-peptide and indicate that only the Cu^{2+}-bound form persists (Figure 2.5D,E and Figure 2.6D,E). Similarly, the simultaneous addition of stoichiometric equivalents of Cu^{2+} and Zn^{2+} to C-peptide results in a spectrum that is identical to the spectrum of Cu^{2+} /C-peptide (Figure 2.5F and Figure 2.5F). These NMR competition experiments show that Cu^{2+} can preferentially bind to and displace Zn^{2+} from C-peptide. Moreover, the lack of any observed bimetallic C-peptide complexes in the solutions containing both Cu^{2+} and Zn^{2+} suggest that both Cu^{2+} and Zn^{2+} bind to the same region of C-peptide, offering the possibility of the metal-mediated modulation of peptide activity.

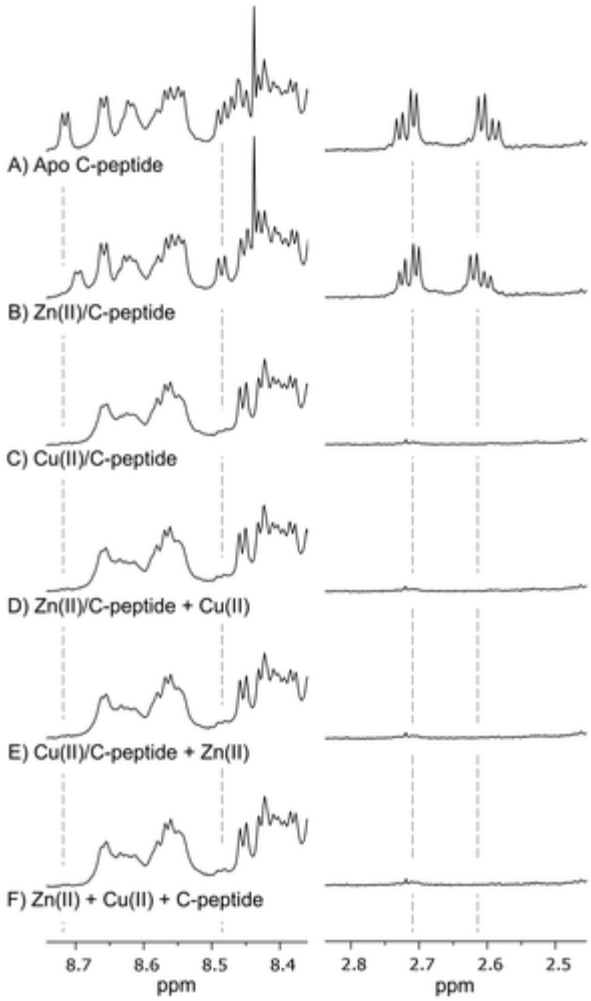

Figure 2.5. Highlighted regions of the ^{1}H NMR spectra of (A) apo C-peptide, (B) Zn^{2+}/C-peptide, (C) Cu^{2+} /C-peptide, (D) equimolar Cu^{2+} added to Zn^{2+}/C-peptide, (E) equimolar Zn^{2+} added to Cu^{2+}/C-peptide, and (F) Cu^{2+} and Zn^{2+} added to apo C-peptide simultaneously. Full spectra are shown in (Figure 2.6). The addition of Zn^{2+} induces shifts in proton resonances for CHβ protons on D4 (2.6 ppm) and backbone amide protons from D4 (8.45 ppm) and E3 (8.7 ppm), while Cu^{2+} obliterates proton resonances within these regions. The spectra of Cu^{2+} competition with Zn^{2+} (D–F) result in spectra that resemble Cu^{2+} /C-peptide and not Zn^{2+}/C-peptide, indicating that Cu^{2+} displaces Zn^{2+} for binding C-peptide. Solutions were prepared at 1.5 mM peptide in 95:5 (v/v) H_2O/D_2O with 10 mM Tris-d_{11} at pH 7.4, and spectra were collected at 800 MHz and 10 °C.

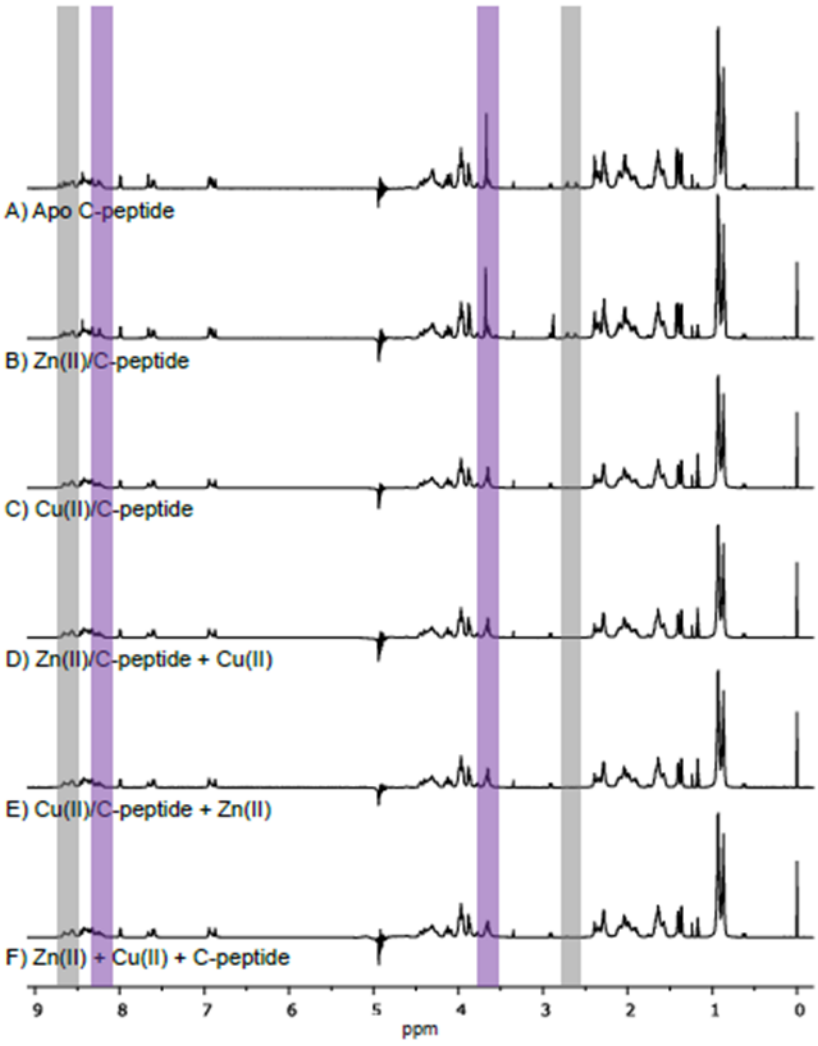

Figure 2.6. 1H NMR spectra of A) apo C-peptide, B) Zn^{2+}/C-peptide, C) Cu^{2+}/C-peptide, D) equimolar Cu^{2+} added to Zn^{2+}/C-peptide, E) equimolar Zn^{2+} added to Cu^{2+}/C-peptide, and F) Cu^{2+} and Zn^{2+} added to apo C-peptide simultaneously. Grey highlighted regions of spectra are enlarged and shown in Figure 2.5 and are due to CHβ protons on D4 (2.7 ppm) and backbone amide protons from E3 (8.7 ppm). Purple highlighted regions of the spectra are due to glycine protons (3.7 ppm) and the backbone amide proton from L5 (8.2 ppm). All spectra were collected at 800 MHz in 95:5 H2O:D2O and 10 mM Tris-d11, pH 7.4 at 10 °C. Addition of Zn^{2+} induces shifts in proton resonances while Cu^{2+} obliterates proton resonances within these regions. The spectra of Cu^{2+}

competition with Zn^{2+} (D, E, and F) result in spectra that resemble Cu^{2+}/C-peptide and not Zn^{2+}/C-peptide indicating that Cu^{2+} displaces Zn^{2+} for binding C-peptide.

To locate the metal binding region, the proton resonances of metal-bound and apo C-peptide were assigned through a combination of 2D NMR experiments (Tables 2.1−2.5). 1 H−1 H TOCSY NMR allows for the classification of resonances into spin systems, which can then be correlated to specific amino acids (Figure 2.8). However, given that the 31-mer C-peptide sequence consists of only nine different amino acids (7 G, 6 L, 4 E, 4 Q, 3 A, 2 P, 2 S, 2 V, and 1 D), the sequence-specific assignment required the implementation of 1 H−1 H NOESY spectroscopy via backbone NHi −CHαi and CHαi −NHi+1 correlations (Figure 2.8). Having assigned the 1 H chemical shifts, regional variations in the resonances were assessed by plotting the difference between the chemical shifts of metal-bound C-peptide and apo C-peptide, $\Delta\delta$ = δ(metalbound C-peptide) − δ(apo C-peptide) (Figures 2.9 and 2.10, results summarized in Figure 2.11).

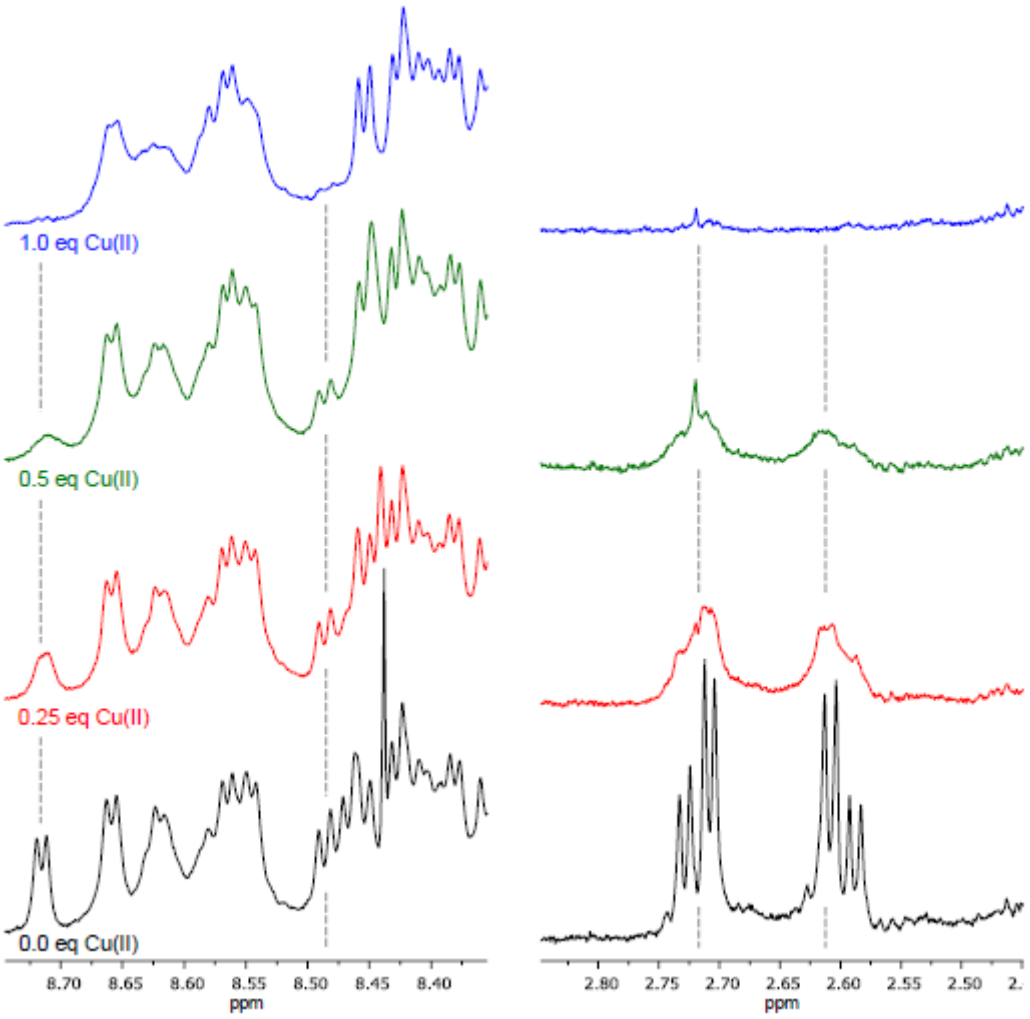

Figure 2.7. NMR spectra of 250 μM apo C-peptide (black) and 250 μM C-peptide with 62.5 μM (red), 125 μM (green), and 250 μM (blue) Cu^{2+}. Cu^{2+} obliterates the proton resonances of CHβ protons on D4 (2.6 ppm) and backbone amide protons from D4 (8.45 ppm) and E3 (8.7 ppm) (dashed lines). Solutions were prepared in 95:5 (v/v) H2O:D2O with 10 mM Tris-d11 at pH 7.4 and spectra were collected at 800 MHz and 10 °C.

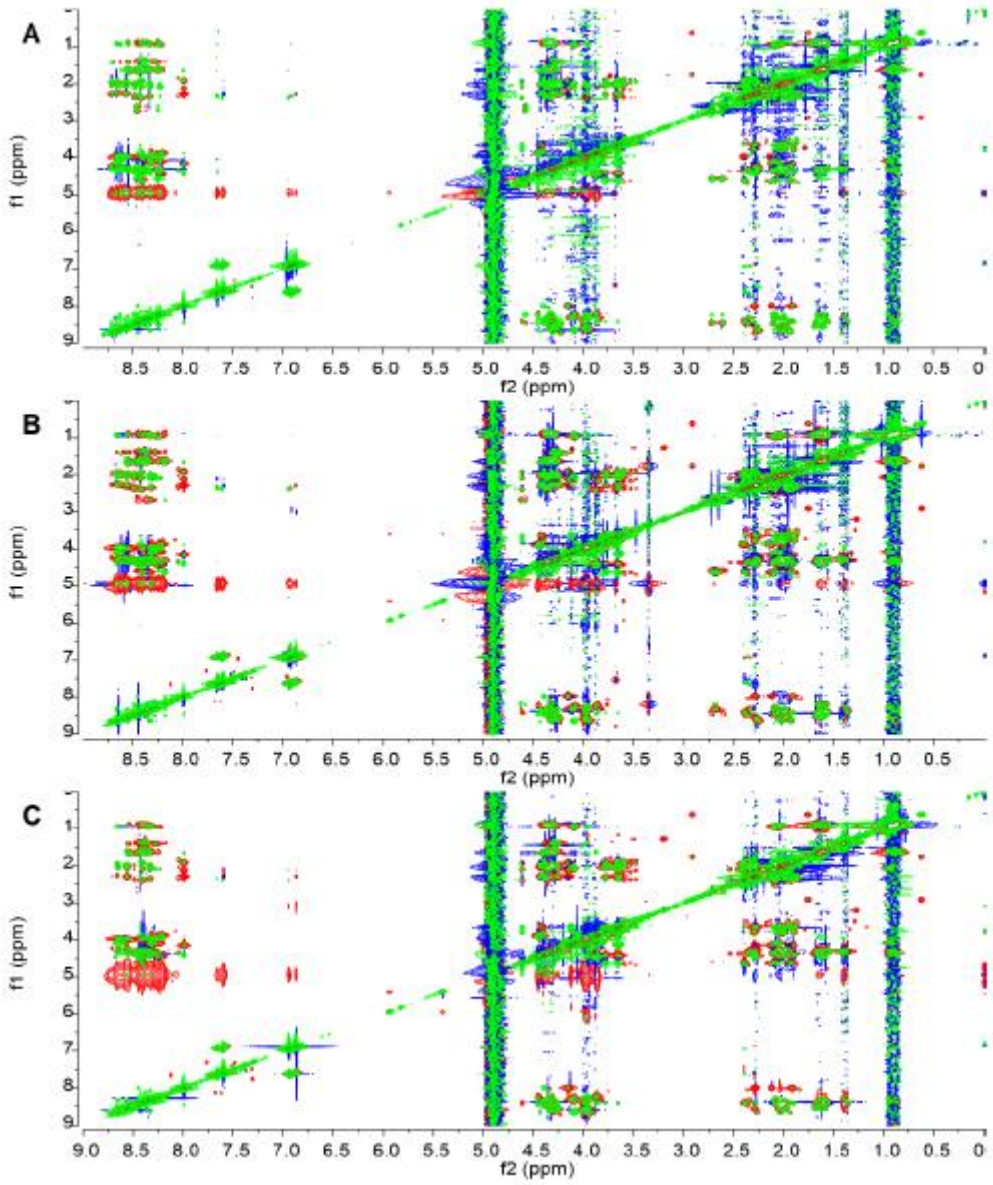

Figure 2.8. Overlay of full 1H-1H TOCSY (red-blue) and 1H-1H NOESY (green-blue) spectra for 1.5 mM A) apo C-peptide, B) Zn^{2+}/C-peptide, and C) Cu^{2+}/C-peptide. All spectra were collected at 800 MHz in 95:5 H2O:D2O and 10 mM Tris-d11, pH 7.4 at 10 °C.

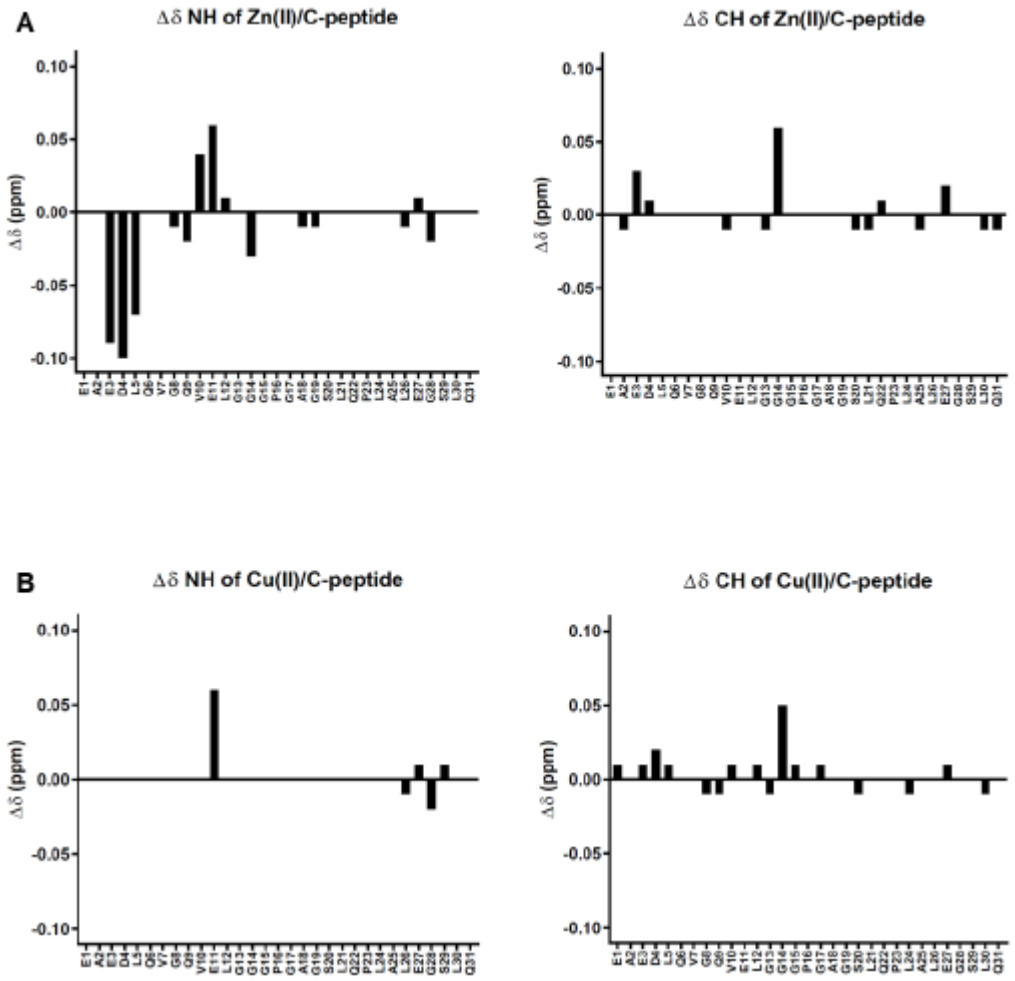

Figure 2.9. The Δδ (δ(M^{2+} /C-peptide) − δ(apo C-peptide)) of 1H chemical shifts (ppm) of the backbone amide (NH) and CHα protons plotted against C-peptide sequence for A) Zn^{2+}/C-peptide and B) Cu^{2+}/C-peptide. Δδ plots for the backbone side chain protons are shown in Figure 2.10. Solutions were prepared at 1.5 mM peptide in 95:5 (v/v) H2O:D2O with 10 mM Tris-d11 at pH 7.4 and spectra were collected at 800 MHz and 10 °C. The Δδ of NH for E3, D4, L5, V10, and E11 show significant effects on the 1H resonances compared with other NH protons and indicate a possible location of metal binding. 1H chemical shift assignments are tabulated in Table 2.1-2.5.

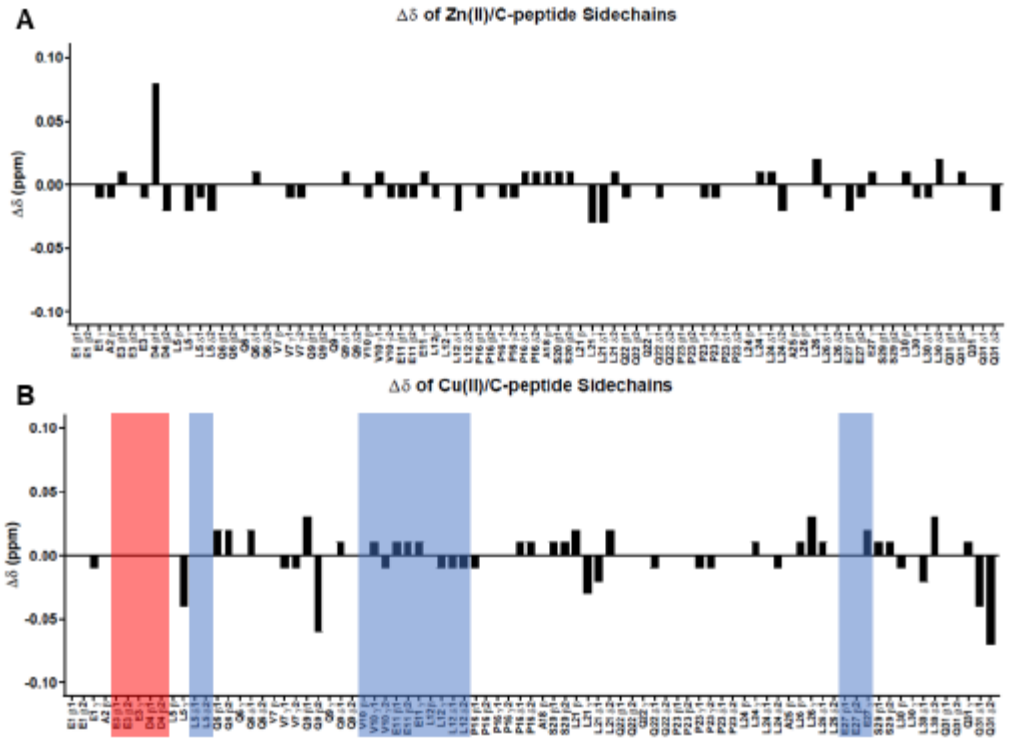

Figure 2.10. The Δδ (δ(M^{2+} /C-peptide) − δ(apo WT C-peptide)) of 1H chemical shifts (ppm) of amino acid side chains plotted against WT C-peptide sequence for A) Zn^{2+}/C-peptide and B) Cu^{2+} /C-peptide. Δδ plots for the backbone amide and CHα protons are shown in Figure 2.9. Solutions were prepared at 1.5 mM peptide in 95:5 (v/v) H2O:D2O with 10 mM Tris-d11 at pH 7.4 and spectra were collected at 800 MHz and 10 °C. The proton resonances with shading indicate reduced (blue) or obliterated (red) intensities. Coordination by Zn^{2+} on D4 and by Cu^{2+} on E3 and D4 show significant effects on the 1H resonances compared with other amino acid protons and indicate location of metal binding. 1H chemical shift assignments are tabulated in Tables 2.1-2.5.

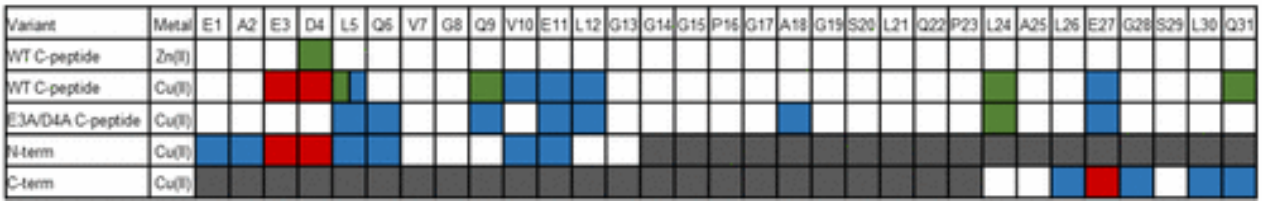

Figure 2.11. Visual depiction of the changes in proton resonances of C-peptide and its variants as a result of metal binding. Colored blocks indicate changes as follows: $\Delta\delta \geq 0.03$ (green), broadened signal (blue), obliterated signal (red), and truncated residues (gray). The corresponding spectra are (Figures 2.8, 2.26, and 2.27) and $\Delta\delta$ tables (Tables 2.1−2.5 and 2.9−2.11) are provided below. The changes in proton resonances indicate that the metals bind to C-peptide at E3 and D4; mutations (double mutant E3A/D4A) or truncations (N-term and C-term) lead to promiscuous metal binding.

Table 2.1. Chemical shifts of assigned proton NMR resonances of apo WT C-peptide. Solutions were prepared at 1.5 mM peptide in 95:5 (v/v) H2O:D2O with 10 mM Tris-d11 at pH 7.4 and spectra were collected at 800 MHz and 10 °C.

Chemical Shifts of Assigned ^{1}H NMR Resonances of Apo C-peptide at pH 7.4						
	Chemical Shifts at 10 °C (ppm)					
Residue	NH	CHα	CHβ	CHγ	CHδ	NHγ
E1	8.04	4.34	1.84, 2.04	2.33	-	-
A2	8.38	4.32	1.37	-	-	-
E3	8.71	4.22	1.94, 2.03	2.28	-	-
D4	8.46	4.57	2.60, 2.72	-	-	-
L5	8.25	4.31	1.64	1.62	0.86, 0.93	-
Q6	8.56	4.25	1.98, 2.04	2.28	-	6.86, 7.59
V7	8.32	4.11	2.03	0.93	-	-
G8	8.62	3.97	-	-	-	-
Q9	8.33	4.36	2.00, 2.09	2.34	-	6.91, 7.66
V10	8.23	4.09	2.09	0.94, 0.96	-	-
E11	8.60	4.30	1.93, 2.02	2.25	-	-
L12	8.54	4.34	1.68	1.63	0.88, 0.91	-
G13	8.40	3.99	-	-	-	-
G14	8.39	3.83	-	-	-	-
G15	8.58	3.97	-	-	-	-
P16	-	4.40	1.90, 2.29	2.02	3.77	-
G17	8.32	3.81	-	-	-	-
A18	8.45	3.98	1.35	-	-	-
G19	8.48	3.98	-	-	-	-
S20	8.24	4.46	3.87			
L21	8.40	4.37	1.63	1.63	0.90, 0.90	-
Q22	8.41	4.60	1.93, 2.09	2.39	-	6.95, 7.61
P23	-	4.41	1.90, 2.28	2.03	3.66	-
L24	8.35	4.33	1.64	1.59	0.89, 0.93	-
A25	8.28	4.31	1.40	-	-	-
L26	8.43	4.28	1.64	1.58	0.90, 0.93	-
E27	8.48	4.33	2.00, 2.12	2.35	-	-
G28	8.67	3.95	-	-	-	-
S29	8.20	4.44	3.86	-	-	-
L30	8.45	4.40	1.66	1.65	0.90, 0.90	-
Q31	7.99	4.16	1.92, 2.12	2.28	-	6.92, 7.66

Table 2.2. Chemical shifts of assigned proton NMR resonances of Zn^{2+}-bound WT C-peptide. Solutions were prepared at 1.5 mM peptide in 95:5 (v/v) H2O:D2O with 10 mM Tris-d11 at pH 7.4 and spectra were collected at 800 MHz and 10 °C. Values in parentheses are a minor feature.

Chemical Shifts of Assigned ^{1}H NMR Resonances of Zn(II)/C-peptide at pH 7.4						
	Chemical Shifts at 10 °C (ppm)					
Residue	NH	CHα	CHβ	CHγ	CHδ	NHγ
E1	8.04	4.34	1.84, 2.04	2.32	-	-
A2	8.38	4.31	1.36	-	-	-
E3	8.62	4.25	1.95, 2.03	2.27	-	-
D4	8.36 (8.32)	4.58 (4.62)	2.63, 2.70 (2.68)	-	-	-
L5	8.18	4.31	1.64	1.60	0.85, 0.91	
Q6	8.56	4.25	1.98, 2.04	2.28	-	6.87, 7.59
V7	8.32	4.11	2.03	0.92	-	-
G8	8.61	3.97	-	-	-	-
Q9	8.31	4.36	2.00, 2.09	2.34	-	6.92, 7.66
V10	8.27	4.08	2.08	0.95	-	-
E11	8.66	4.30	1.92, 2.01	2.26	-	-
L12	8.55	4.34	1.67	1.63	0.86, 0.91	-
G13	8.40	3.98	-	-	-	-
G14	8.36	3.89	-	-	-	-
G15	8.58	3.97	-	-	-	-
P16	-	4.40	1.89, 2.29	2.01	3.78	-
G17	8.32	3.81	-	-	-	-
A18	8.44	3.98	1.36	-	-	-
G19	8.47	3.98	-	-	-	-
S20	8.24	4.45	3.88	-	-	-
L21	8.40	4.36	1.63	1.60	0.87, 0.91	-
Q22	8.41	4.61	1.92, 2.09	2.39	-	6.94, 7.61
P23	-	4.41	1.90, 2.28	2.02	3.66	-
L24	8.35	4.33	1.64	1.60	0.90, 0.91	-
A25	8.28	4.30	1.40	-	-	-
L26	8.42	4.28	1.64	1.60	0.89, 0.93	-
E27	8.49	4.35	1.98, 2.11	2.36	-	-
G28	8.65	3.95	-	-	-	-
S29	8.20	4.44	3.86	-	-	-
L30	8.45	4.39	1.67	1.64	0.89, 0.92	-
Q31	7.99	4.15	1.92, 2.11	2.28	-	6.92, 7.64

Table 2.3. Chemical shifts of assigned proton NMR resonances of Cu^{2+} -bound WT C-peptide. Solutions were prepared at 1.5 mM peptide in 95:5 (v/v) H2O:D2O with 10 mM Tris-d11 at pH 7.4 and spectra were collected at 800 MHz and 10 °C. obl = obliterated signal; sm = reduced signal.

Chemical Shifts of Assigned ^{1}H NMR Resonances of Cu(II)/C-peptide at pH 7.4						
	Chemical Shifts at 10 °C (ppm)					
Residue	NH	CHα	CHβ	CHγ	CHδ	NHγ
E1	8.04	4.35	1.84, 2.04	2.32	-	-
A2	8.38	4.32	1.37 (1.25, 1.47 sm)	-	-	-
E3	8.71	4.23	obl	obl	-	-
D4	8.46	4.59	obl	-	-	-
L5	8.25	4.32	1.64 sm	1.60 sm	obl	-
Q6	8.56	4.25	2.00, 2.06	2.28	-	6.88, 7.59
V7	8.32	4.11	2.03	0.92	-	-
G8	8.62	3.96	-	-	-	-
Q9	8.33	4.35	2.03, 2.03	2.34	-	6.92, 7.66
V10	8.23	4.10	2.09	0.95	-	-
E11	8.66	4.30	1.94, 2.03 sm	2.26 sm	-	-
L12	8.54	4.35	1.68	1.62	0.87, 0.92	-
G13	8.40	3.98	-	-	-	-
G14	8.39	3.88	-	-	-	-
G15	8.58	3.98	-	-	-	-
P16	-	4.40	1.89, 2.29	2.02	3.78	-
G17	8.32	3.82	-	-	-	-
A18	8.45	3.98	1.35	-	-	-
G19	8.48	3.98	-	-	-	-
S20	8.24	4.45	3.88	-	-	-
L21	8.40	4.37	1.65	1.60	0.88, 0.92	-
Q22	8.41	4.60	1.93, 2.09	2.39	-	6.94, 7.61
P23	-	4.41	1.90, 2.28	2.02	3.66	-
L24	8.35	4.32	1.64	1.60	0.89, 0.92	-
A25	8.28	4.31	1.40	-	-	-
L26	8.42	4.28	1.65	1.61	0.91, 0.93	-
E27	8.49	4.34	2.00 sm, 2.00 sm	2.37	-	-
G28	8.65	3.95	-	-	-	-
S29	8.21	4.44	3.87	-	-	-
L30	8.45	4.39	1.65	1.65	0.88, 0.93	-
Q31	7.99	4.16	1.92, 2.12	2.29	-	6.88, 7.59

Table 2.4. Δδ of assigned proton NMR resonances of Zn^{2+}-bound WT C-peptide and apo WT C-peptide. Solutions were prepared at 1.5 mM peptide in 95:5 (v/v) H2O:D2O with 10 mM Tris-d11

at pH 7.4 and spectra were collected at 800 MHz and 10 °C. Visual representations shown in Figures 2.9 and 2.10. Values in parentheses are a minor feature.

Δδ of the Assigned ^{1}H NMR Resonances of Zn(II)/C-peptide at pH 7.4						
	Δδ = δ(Zn(II)/C-peptide) - δ(apo C-peptide) at 10 °C (ppm)					
Residue	NH	CHα	CHβ	CHγ	CHδ	NHγ
E1	0.00	0.00	0.00, 0.00	-0.01		
A2	0.00	-0.01	-0.01			
E3	-0.09	0.03	0.01, 0.00	-0.01		
D4	-0.10 (-0.14)	0.01 (0.05)	0.03, -0.02 (0.08, -0.02)			
L5	-0.07	0.00	0.00	-0.02	-0.01, -0.02	
Q6	0.00	0.00	0.00, 0.00	0.00		0.01, 0.00
V7	0.00	0.00	0.00	-0.01, -0.01		
G8	-0.01	0.00				
Q9	-0.02	0.00	0.00, 0.00	0.00		0.01, 0.00
V10	0.04	-0.01	-0.01	0.01, -0.01		
E11	0.06	0.00	-0.01, -0.01	0.01		
L12	0.01	0.00	-0.01	0.00	-0.02, 0.00	
G13	0.00	-0.01				
G14*	-0.03	0.06				
G15*	0.00	0.00				
P16		0.00	-0.01, 0.00	-0.01	0.01	
G17	0.00	0.00				
A18	-0.01	0.00	0.01			
G19	-0.01	0.00				
S20	0.00	-0.01	0.01			
L21	0.00	-0.01	0.00	-0.03	-0.03, 0.01	
Q22	0.00	0.01	-0.01, 0.00	0.00		-0.01, 0.00
P23		0.00	0.00, 0.00	-0.01	0.00	
L24	0.00	0.00	0.00	0.01	0.01, -0.02	
A25	0.00	-0.01	0.00			
L26	-0.01	0.00	0.00	0.02	-0.01, 0.00	
E27	0.01	0.02	-0.02, -0.01	0.01		
G28	-0.02	0.00				
S29	0.00	0.00	0.00			
L30	0.00	-0.01	0.01	-0.01	-0.01, 0.02	
Q31	0.00	-0.01	0.00, 0.01	0.00		0.00, -0.02

Table 2.5. Δδ of assigned proton NMR resonances of Cu^{2+} -bound WT C-peptide and apo WT C-peptide. Solutions were prepared at 1.5 mM peptide in 95:5 (v/v) H2O:D2O with 10 mM Tris-d11 at pH 7.4 and spectra were collected at 800 MHz and 10 °C. Visual representations shown in Figures 2.9 and 2.10. obl = obliterated signal; sm = reduced signal.

Δδ of the Assigned ^{1}H NMR Resonances of Cu(II)/C-peptide at pH 7.4						
	Δδ = δ(Cu(II)/C-peptide) - δ(apo C-peptide) at 10 °C (ppm)					
Residue	NH	CHα	CHβ	CHγ	CHδ	NHγ
E1	0.00	0.01	0.00, 0.00	-0.01		
A2	0.00	0.00	0.00 (-0.12 sm, 0.10 sm)			
E3	0.00	0.01	obl	obl		
D4	0.00	0.02	obl			
L5	0.00	0.01	0.00 sm	-0.04 sm	obl	
Q6	0.00	0.00	0.02, 0.02	0.00		0.02, 0.00
V7	0.00	0.00	0.00	-0.01, -0.01		
G8	0.00	-0.01				
Q9	0.00	-0.01	0.03, -0.06	0.00		0.01, 0.00
V10	0.00	0.01	0.00	0.01, -0.01		
E11	0.06	0.00	0.01, 0.01 sm	0.01 sm		
L12	0.00	0.01	0.00	-0.01	-0.01, -0.01	
G13	0.00	-0.01				
G14*	0.00	0.05				
G15*	0.00	0.01				
P16		0.00	-0.01, 0.00	0.00	0.01	
G17	0.00	0.01				
A18	0.00	0.00	0.00			
G19	0.00	0.00				
S20	0.00	-0.01	0.01			
L21	0.00	0.00	0.02	-0.03	-0.02, 0.02	
Q22	0.00	0.00	0.00, 0.00	0.00		-0.01, 0.00
P23		0.00	0.00, 0.00	-0.01	0.00	
L24	0.00	-0.01	0.00	0.01	0.00, -0.01	
A25	0.00	0.00	0.00			
L26	-0.01	0.00	0.01	0.03	0.01, 0.00	
E27	0.01	0.01	0.00 sm, 0.00 sm	0.02		
G28	-0.02	0.00				
S29	0.01	0.00	0.01			
L30	0.00	-0.01	-0.01	0.00	-0.02, 0.03	
Q31	0.00	0.00	0.00, 0.00	0.01		-0.04, -0.07

In the Δδ plots for Zn^{2+}/C-peptide, the most notable changes are observed with the NH protons, specifically at residues E3, D4, L5, V10, and E11 (Figure 2.9A and Table 2.4), potentially indicating a structural change occurring in the N-terminus of C-peptide upon Zn^{2+} binding. No significant changes are observed in the chemical shifts of the side-chain protons except for the

CHβ protons on D4, indicating this residue to be a possible binding locale (Figure 2.10A and Table 2.4). In contrast, the Δδ plots of Cu^{2+}/C-peptide show minimal changes in the NH and CHα resonances (Figure 2.9B and Table 2.5). However, consistent with the 1D 1 H NMR spectrum, the 2D 1 H−1 H homonuclear NMR experiments confirm the loss of a portion of the side-chain resonances. As indicated in the Δδ plots and chemical shift assignments, all side-chain proton resonances of E3 and D4 were obliterated with several signal reductions and shifts in proton resonances (Figure 2.11, Figure 2.10B, and Table 2.5). The lack of signals suggest a binding locale of Cu^{2+} to the N-terminal region, specifically at E3 and D4, that imposes only modest, if any, structural changes to C-peptide. Furthermore, the CHδ protons of L5 and the side-chain proton resonances of V10, E11, L12, and E27 were reduced in signal intensity coupled with shifts in proton resonances of L5, Q9, L24, and Q31 (Figure 2.11 and Figure 2.10B) and indicate possible transient Cu^{2+} binding interactions or sufficient proximity to the Cu^{2+} center to experience altered proton relaxation rates. From the NMR spectra, the main Cu^{2+} and Zn^{2+} binding locales are at E3 and D4.

2.3.4 Charactering the Coordination Environment of the Copper Center

C-peptide does not contain classical Cu^{2+} - binding residue histidine. While the carboxylate side chains of the available aspartate and glutamate residues could serve as ligands, Cu^{2+} binding modes containing only oxygen donors are uncommon in native peptides and proteins. On the basis of electronic absorption spectroscopy studies, we previously hypothesized that Cu^{2+} could be binding to a combination of the backbone amide nitrogens and the carboxylate side chains for a mixed NxOy ligand set.[32] To assess this hypothesis, we turned to electron paramagnetic resonance (EPR) spectroscopy, which probes the ligand environment around the paramagnetic Cu^{2+} (3d9 , S

= 1/2) center. For instance, if a nitrogen is directly bound to Cu^{2+}, then the 14N-hyperfine coupling is strong enough (~45 MHz) to yield characteristic hyperfine splittings in the X-band EPR spectrum, although the absence of hyperfine splitting does not preclude direct nitrogen coordination as evidenced by previous studies performed with Cu^{2+}/amyloid-β complexes.[41] The continuous wave (CW) X-band EPR spectrum of Cu^{2+}/C-peptide was acquired at 20 K in the presence of excess C-peptide and shows one axial Cu^{2+} component with g|| = 2.229 and A|| = 536 MHz, suggesting that all Cu^{2+} was bound by the peptide in a square-planar geometry. Using these parameters with the Peisach and Blumberg truth tables,[42] the data indicates either 4O with −2 charge, 1N3O with nearly neutral charge, or 2N2O with nearly neutral charge for the coordination environment. The possible binding modes may be further differentiated by determining whether any nitrogen hyperfine splittings are observed. Interestingly, no obvious 14N-hyperfine splitting at g⊥ (Figure 2.12A) suggests that the Cu^{2+} center is most likely in a 4O environment, although sometimes the 14N-hyperfine splitting pattern is difficult to resolve due to line-shape broadening.[43] Furthermore, the high-resolution two-dimensional method consisting of hyperfine sublevel correlation spectroscopy (HYSCORE) detects only weak hyperfine coupling from remote backbone nitrogens (Figure 2.12B).[44] If Cu^{2+} is coordinated to the side chains of E3 and D4, then the backbone amide nitrogens for each residue would be six and five bond lengths away, respectively, matching the experimental observations. However, it must be noted that nitrogen coordination is still possible because the lack of data does not preclude nitrogen coordination.[41] Combined with the NMR data, the EPR data support a model for Cu^{2+} binding to C-peptide through the side-chain carboxylate oxygens of E3 and D4 in a square-planar geometry. To provide further insight into the coordinating ligands, we turned to vibrational spectroscopy.

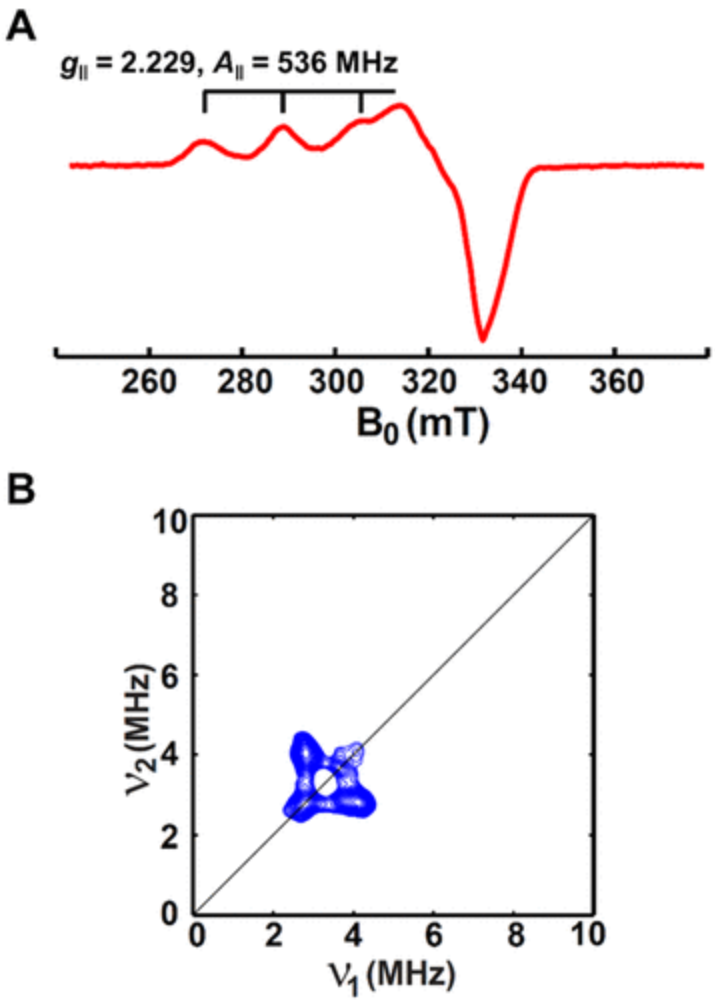

Figure 2.12. (A) CW X-band and (B) HYSCORE EPR spectra of Cu^{2+} bound to C-peptide obtained at 20 K. Samples were prepared with 0.5 mM Cu^{2+} and 1.0 mM C-peptide in 15 mM MOPS, pH 7.4, with 20% ethylene glycol as a glassing agent. The CW X-band and HYSCORE spectra indicate that Cu^{2+} is coordinated to two to four oxygens of C-peptide in a square-planar geometry but does not preclude coordination to nitrogen.

To identify the chemical nature of the oxygen-containing ligands, we implemented Fourier-transform infrared (FTIR) spectroscopy. In peptides and proteins, the position of the amide bands provides structural information. When bound to metals, the asymmetric (as) and symmetric (s)

stretching frequencies of oxygen-containing ligands provide insight into how the metal ion is coordinated: larger Δ(vas − vs) (∼200− 300 cm−1) typically corresponds to unidentate metal coordination whereas smaller Δ(vas − vs) of less than 150 cm−1 corresponds to bidentate coordination.[45–48] The FTIR spectrum of apo C-peptide shows amide I′ and amide II′ bands centered at 1645 and 1539 cm−1 , respectively (Figure 2.13, Table 2.6).

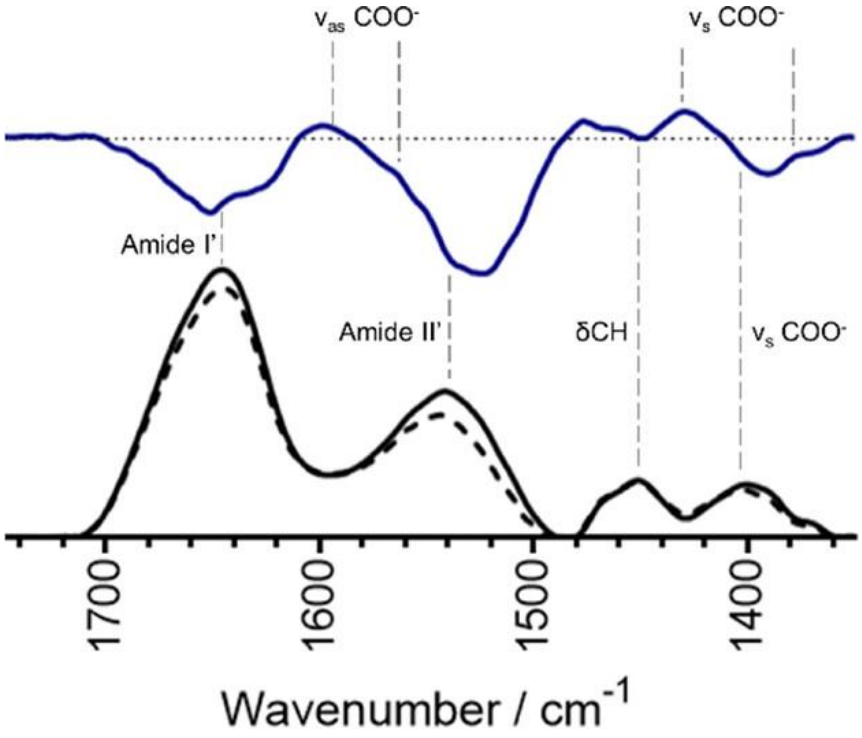

Figure 2.13. FTIR absorbance spectra of 1.2 mM apo C-peptide (solid black line) and 1.2 mM Cu^{2+}/peptide (dashed black line) at pH 7.4, with the difference spectrum (solid blue line). The dashed horizontal line for the difference spectra is set to zero. Vertical dashed lines indicate the bands associated with the given stretch or vibration. Spectra are buffer subtracted and normalized to the internal standard of the δCH centered at 1451 cm^{-1}. Frequencies for antisymmetric and symmetric bending and stretching of carboxylate groups are visible and indicate a combination of bidentate and unidentate coordination to Cu^{2+}.

Table 2.6. Frequencies of Key Vibrations (cm^{-1})

	amide I′	amide II′	δCH	ν_{as} COO^-	ν_s COO^-
apo	1645	1539	1451	n.d.	1401
$+Cu^{2+}$	1645	1539	1451	1597/1542	1428/1374

The position of the amide I′ band is indicative of a random coil peptide and in good agreement with previously published CD spectra.[49] Also seen in apo C-peptide is the presence of a νs COO− band at 1401 cm−1. However, since the νas COO− band is buried under the amide I′ and amide II′ bands and cannot be observed, a difference spectrum of Cu^{2+}/C-peptide minus apo C-peptide was calculated to locate the asymmetric stretching band. Both spectra were normalized to δCH at 1451 cm−1.[47] From the difference spectrum, the νas COO− bands are readily seen at 1597 and 1542 cm−1 along with the νs COO− bands at 1428 and 1379 cm−1, causing Δ(νas − νs) to range from 218 to 114 cm−1 . From these Δ(νas − νs) values, the Cu^{2+} coordination may be a combination of unidentate and bidentate to the carboxylate side chains. The second derivative of FTIR spectra was employed to further observe subtle changes in the bands and features of the peptide (Figure 2.14). Of note in this transformation are the stretching frequencies below 1300 cm−1, indicative of C−H and Ser(OH) stretching and bending.[50] In this region, the second derivatives of apo and Cu^{2+}-bound C-peptide are nearly identical, indicating that Cu^{2+} is not influencing the stretching and bending of CH and Ser(OH) bonds. The FTIR data thus further confirms that Cu^{2+} is binding to carboxylate ligands, likely the side chains of E3 and D4, in a combined unidentate and bidentate mode which would provide three of the four oxygens needed

for axial coordination to Cu^{2+}. Confirmation of the fourth ligand as the terminal amine proved challenging by FTIR due to its bending and stretching frequencies overshadowed by solvent and amide bands.[50]

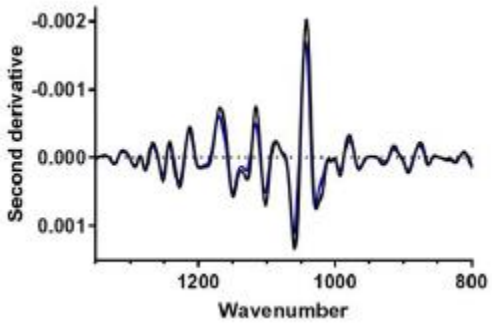

Figure 2.14. Second derivative FTIR spectra of WT C-peptide (black) and Cu^{2+}/C-peptide (blue) at low wavenumbers. The second derivative patterns between apo and Cu^{2+} -bound peptides are similar in this region indicating that the stretching and bending frequencies of serine are not affected by Cu^{2+}.

To further validate that the identity of the fourth ligand is nitrogen, we turned to electronic absorption spectroscopy which directly probes the Cu^{2+} center. The addition of 1 equiv of Cu^{2+} to C-peptide in 15 mM MOPS at pH 7.4 was similar to the previously published spectrum where a large band centered at 220 nm is attributed to the peptide backbone and a small absorption band centered at 638 nm is attributed to the d−d transition on the metal center of Cu^{2+}/C-peptide (Figure 2.15).[32] The high concentration of C-peptide (300 μM) was required to observe the weak d−d band, but at this concentration, no precipitation or aggregation was observed. The λmax of the d−d band at 638 nm is consistent with an amine coordinated to Cu^{2+}.[51] The only amine in C-peptide is the

N-terminal amine and is a common ligand for anchoring Cu^{2+} to peptides and proteins. The data from NMR, FTIR, EPR, and electron absorption spectroscopies can now be interpreted together. NMR shows that Cu^{2+} binds C-peptide through E3 and D4, with FTIR indicating bidentate and unidentate coordination and electronic absorption indicating the presence of a coordinated amine. With this ligand set, the charge at the metal center would be zero and the EPR data is now interpreted to have 1N3O square-planar coordination. This ligand set would have a low affinity, and Cu^{2+} would be relatively labile, thus providing leverage for other ligands to chelate Cu^{2+} away from C-peptide and making the Cu^{2+}/C-peptide complex kinetically favored. Considering our earlier finding that Cu^{2+} inhibits C-peptide internalization, the chelation of Cu^{2+} from C-peptide could serve as a means to restore the C-peptide internalization activity.

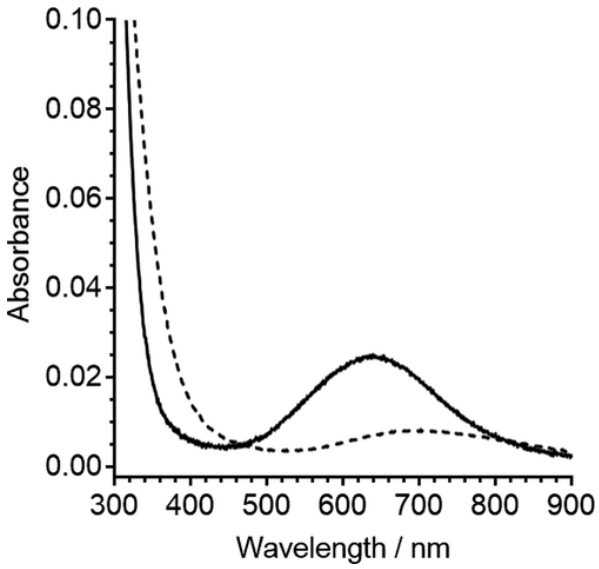

Figure 2.15. Spectra depicting the d–d band from 300 μM Cu^{2+}/C-peptide (solid line) and 300 μM Cu^{2+} in 15 mM MOPS at pH 7.4 shown as a reference (dashed line). The wavelengths of maximum absorption for the d–d band as determined by the first derivative of Cu^{2+} /C-peptide and Cu^{2+} in

buffer are 638 and 696 nm, respectively (Figure 2.21). The energy of the d–d band for Cu^{2+} /C-peptide suggests that Cu^{2+} is bound to at least one nitrogen ligand.

2.3.5 Binding Thermodynamics of the Copper/C-peptide Interaction

Through the structural studies, we show that C-peptide binds Cu^{2+} with a 1N3O ligand set. To determine the driving force of complexation, we turned to isothermal titration calorimetry (ITC) to measure the binding thermodynamics, namely, the enthalpy, binding affinity, and stoichiometry. From these parameters, the free energy and entropy of Cu^{2+} binding to C-peptide can be determined. Dissecting the binding free energy into enthalpic and entropic contributions provides valuable information regarding the driving force of the reaction. In our previous work, we calculated an apparent binding constant of Cu^{2+} to C-peptide in the 15−40 nM range via competition with the chromophoric ligand, phenanthroline.[32] Using this range as a starting point, Cu^{2+} was titrated into C-peptide in MOPS and MOPSO buffers, which were chosen for their small $K_{Cu2+\text{-buffer}}$ (Figure 2.16 and Figure 2.17),[52] in triplicate, and the experimental fit parameters are listed in Table 2.14. (There is a dearth of buffers with small $K_{Cu2+\text{-buffer}}$ that will allow for the study of low-affinity peptides and proteins.) Additionally, since the two buffers have different protonation enthalpies,[53] the number of protons that dissociate from C-peptide upon Cu^{2+} binding can be estimated from the slope of the protonation plot of $\Delta H_{ITC} + \Delta H_{Cu2+}$ -buffer vs $\Delta H_{\text{buffer-H}}$ (Figure 2.29).[54] The resulting thermograms are fit to the one-site binding model to provide the experimental binding thermodynamics summarized in Table 2.7. Moreover, these experiments revealed that approximately zero (0 ± 1) protons dissociate from C-peptide upon Cu^{2+} binding (Figure 2.18). This value, although it has a large error, is consistent with carboxylate ligands from the side chains of E3 and D4 and the partial protonation (~0.8 H+) of the terminal amine at pH

7.4. Taking into account the displacement of a negligible number of protons from C-peptide upon Cu^{2+} binding, the buffer independent thermodynamics at pH 7.4 are summarized in Table 2.8.

Table 2.7. Experimental fit parameters from at least three titrations in each buffer.

Buffer	n_{ITC}	K_{ITC}	ΔH_{ITC} (kcal mol^{-1})
MOPS	0.8 ± 0.2	2 (± 1) × 10^5	-1.3 ± 0.2
MOPSO	1.0 ± 0.1	5 (± 2) × 10^5	-1.31 ± 0.03

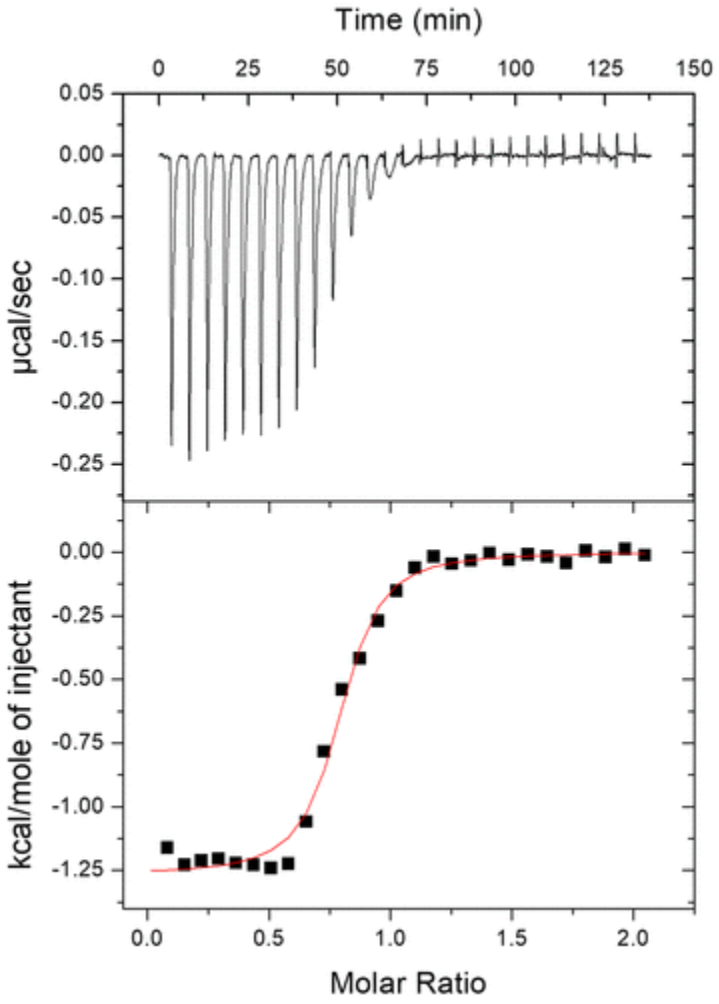

Figure 2.16. Representative thermogram of 1.0 mM Cu^{2+} titrated into 100 µM C-peptide in 15 mM MOPS at pH 7.4 with a red fit line: n = 0.769 ± 0.008, K_{ITC} = 1.1 (±0.2) × 10^6, and ΔH_{ITC} =

−1.27 ± 0.02 kcal mol^{-1}. Buffer-independent thermodynamics are summarized in Table 2.8 and indicate a predominantly entropic driving force.

Table 2.8. Buffer-Independent Thermodynamics of Cu(II) Binding to C-peptide at pH 7.4

buffer	$K_{Cu(II)/C\text{-}peptide}$	$\Delta G°_{Cu(II)/C\text{-}peptide}$ (kcal mol^{-1})	$\Delta H_{Cu(II)/C\text{-}peptide}$ (kcal mol^{-1})	$-T\Delta S_{Cu(II)/C\text{-}peptide}$ (kcal mol^{-1})	$\Delta S_{Cu(II)/C\text{-}peptide}$ (cal mol^{-1} K^{-1})
MOPS	$2 (\pm 1) \times 10^{8}$	–11.2 ± 0.4	–2 ± 1	–9 ± 1	30 ± 3
MOPSO	$6 (\pm 3) \times 10^{7}$	–10.5 ± 0.3	–2 ± 1	–9 ± 1	28 ± 3

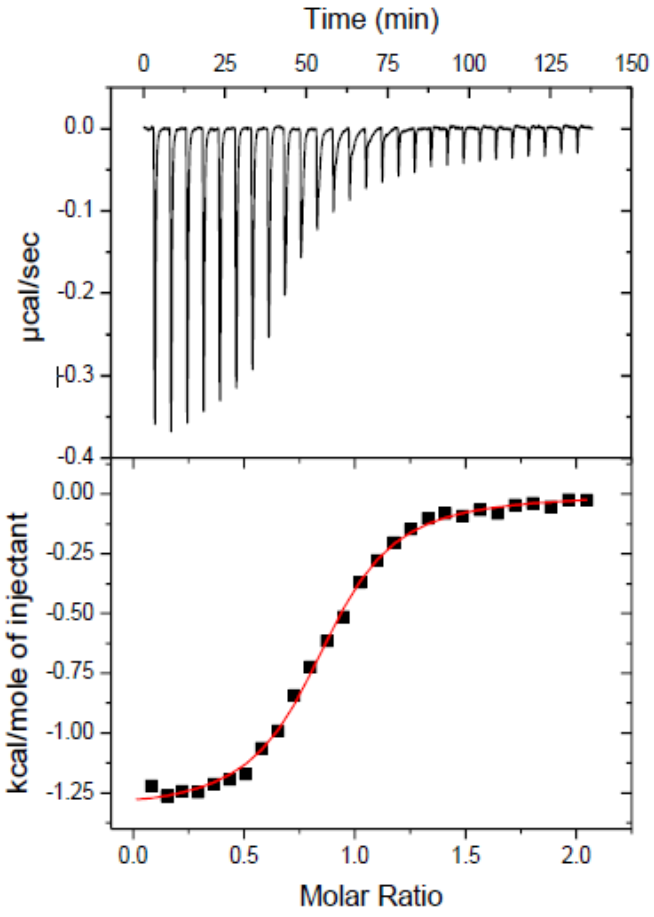

Figure 2.17. Representative thermogram of 1.0 mM Cu^{2+} titrated into 100 µM C-peptide in 15 mM MOPSO, pH 7.4 with red fit line: n = 0.852 ± 0.006; K_{ITC} = 3.0 (± 0.2) x 105; ΔH_{ITC} = −1.33 ± 0.01 kcal mol-1. Buffer-independent thermodynamics are summarized in Table 2.8 and indicate a predominantly entropic driving force.

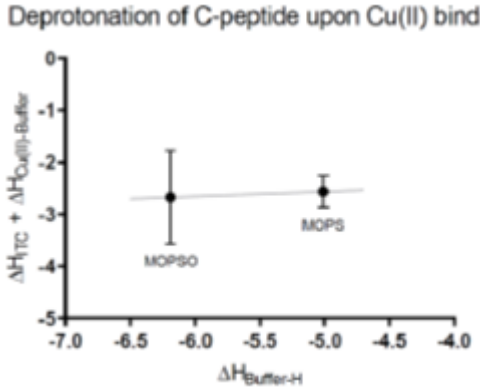

Figure 2.18. Analysis to determine the number of protons that are displaced from C-peptide upon Cu^{2+} binding. Protonation plot of $\Delta H_{ITC} + \Delta H_{Cu2+\ -Buffer}$ *vs.* $\Delta H_{Buffer-H}$ has a slope equal to the number of protons as detailed by Grossoehme *et al.* that are binding to the buffer and is equal to 0.1 ± 0.2. The error of the slope is estimated from subtraction of the minimum slope from the maximum slope between the error bars divided by two.

The formation constant determined here for C-peptide is consistent with what we previously reported.[32] The use of ITC allows for the decomposition of the free energy into its enthalpic and entropic contributions, and from this inspection, we see that Cu^{2+} binding is predominantly entropically driven. This favorable entropy may be the result of the desolvation of both C-peptide at the metal-binding site and the Cu^{2+} ion (the latter of which can have up to 10 water molecules surrounding it),[55] as well as the chelate effect. Given the NMR data and our previously reported CD spectra,[32] there is negligible structural rearrangement when Cu^{2+} binds, indicating a minimal entropic penalty from the peptide structure. The small enthalpic contribution may be from Cu^{2+} binding to carboxylate ligands ($\Delta H_{Cu2+\ -COO} \approx 1.2$ kcal mol−1) coupled with binding to the amine and small, favorable intrapeptide interactions.[53,56]

The parameters elucidated in our studies may point to the Cu^{2+}/C-peptide complex being a relevant species in the body. First, the local environment surrounding tissues is believed to have fluctuating metal content. After transport through blood to target tissues, C-peptide may bind to Cu^{2+}, thus inhibiting its internalization until either Cu^{2+} is chelated away by another higher-affinity ligand or displaced by another metal ion that does not inhibit internalization. This would be an example of a metal-mediate negative feedback mechanism. Second, there are numerous proteins within the blood, some of which have high Cu^{2+} affinities such as albumin. Work by Spence and

colleagues have shown that albumin is needed for C-peptide transport to cells, but the characteristics of such a ternary complex remain elusive. Understanding the Cu^{2+}/C-peptide complex is the first step in further probing the ternary complex, which we are actively studying.

Previously, we showed via competition with the chromophoric ligand, Zincon, that Zn^{2+} binds to C-peptide with an apparent binding constant of 10−100 μM.[32] However, titrations of Zn^{2+} into C-peptide by ITC showed no detectable binding in five buffered solutions: Tris, bis-Tris, PIPES, MOPS, and MOPSO (Figure 2.19). Of these buffers, the Zn^{2+} binding affinities to Tris and bis-Tris are reported to be log K = 2.27 and 2.38, respectively.[53] The lack of an observed binding isotherm indicates a low Zn^{2+}/C-peptide affinity that cannot compete with the Zn^{2+}-buffer complexes under the ITC experimental conditions studied here and does not preclude Zn^{2+} from binding to C-peptide. The estimation of an upper limit of the Zn^{2+}/C-peptide affinity is log K ≈ 5 and is consistent with the low affinity of the Zn^{2+}/C-peptide complex that we previously reported.[32]

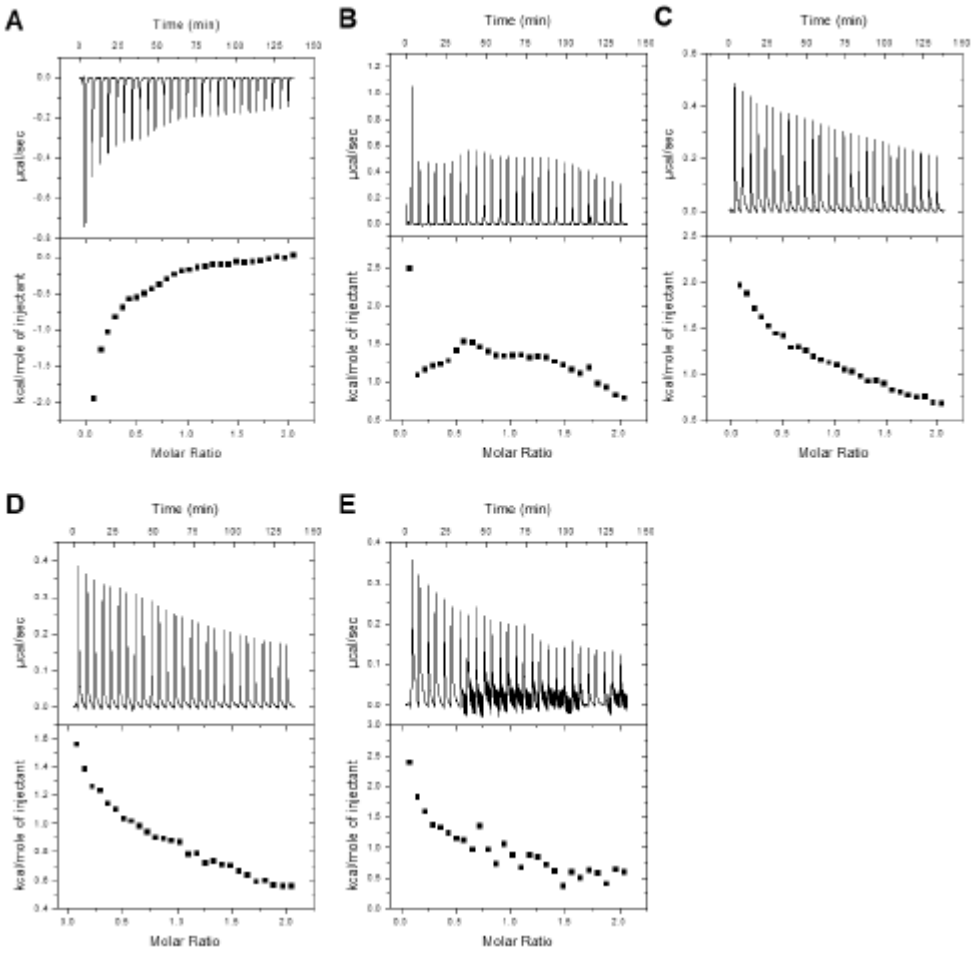

Figure 2.19. Representative thermograms of 1.0 mM Zn^{2+} titrated into 100 µM C-peptide in A) 15 mM Tris, pH 7.4, B) 15 mM bis-Tris, pH 7.4, C) 15 mM MOPS, pH 7.4, D) 15 mM MOPSO, pH 7.4, and E) 15 mM PIPES, pH 7.4. The titrations were inconsistent, do not indicate specific Zn^{2+}-binding, and are most likely from heat of dilution from the Zn^{2+} titration into the cell.

2.3.6 Metal Binding to C-peptides Variants and Truncations

The combination of spectroscopic and calorimetric data points to a 1N3O Cu^{2+} binding site within the native, or wild-type (WT), C-peptide. In order to confirm the identity of the binding ligands as the side chains of E3 and D4, we synthesized three variants of C-peptide with these

residues replaced with alanine: (1) a single-residue replacement at E3 (E3A), (2) a single-residue replacement at D4 (D4A), and (3) a double mutant with both E3 and D4 replaced (E3A/D4A). These C-peptide variants were then analyzed by electronic absorption spectroscopy and compared to WT C-peptide to screen for Cu^{2+} binding. As described above, Cu^{2+} bound to WT C-peptide featured a large band centered at 220 nm attributed to the peptide backbone and a small absorption band centered at 638 nm attributed to the d−d transition on the metal center of Cu^{2+}/C-peptide (Figure 2.20).[32] Surprisingly, the addition of 1 equiv of Cu^{2+} to each C-peptide variant was similar to that of WT C-peptide (Figure 2.20) with λ_{max} values for WT, E3A, D4A, and E3A/D4A C-peptide at 638, 637, 620, and 658 nm, respectively. The similar λ_{max} values for each variant indicate similar environments and energy splitting at the Cu^{2+} site and can be inferred to have similar 1N3O coordinating atoms and metal geometries. While E3 and D4 are replaced with alanine in the mutants, the carboxylate groups of E1, E11, E27, and the C-terminus remain available, potentially serving as alternate ligands. This may illustrate that Cu^{2+} can promiscuously bind to several other locales on C-peptide. Of the variants tested, the largest $\Delta\lambda_{max}$ from WT C-peptide is from E3A/D4A C-peptide and was thus further investigated and compared to that of the native peptide.

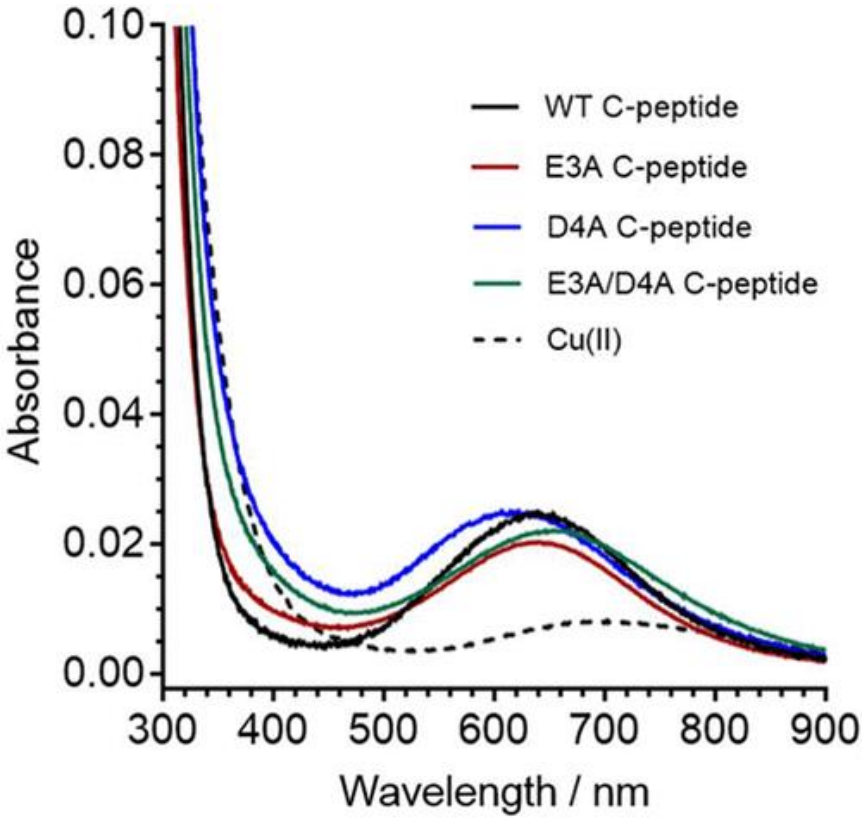

Figure 2.20. Spectra of C-peptide mutants depicting the d–d band from Cu^{2+}/peptide of 300 μM WT C-peptide (black), E3A C-peptide (red), D4A C-peptide (blue), E3A/D4A C-peptide (green), and 300 μM Cu^{2+} in 15 mM MOPS at pH 7.4 shown as reference (black dashed line). The wavelengths of maximum absorption for the d–d band as determined by the first derivative of WT, E3A, D4A, and E3A/D4A C-peptide and Cu in buffer are 638, 637, 620, 658, and 696 nm, respectively (Figure 2.21). The similar energy of the d–d band from Cu^{2+} suggests that the copper is bound to similar ligands in all peptides but that E3A/D4A C-peptide is red-shifted, most similar to buffer alone, and has the largest change in maximum absorption.

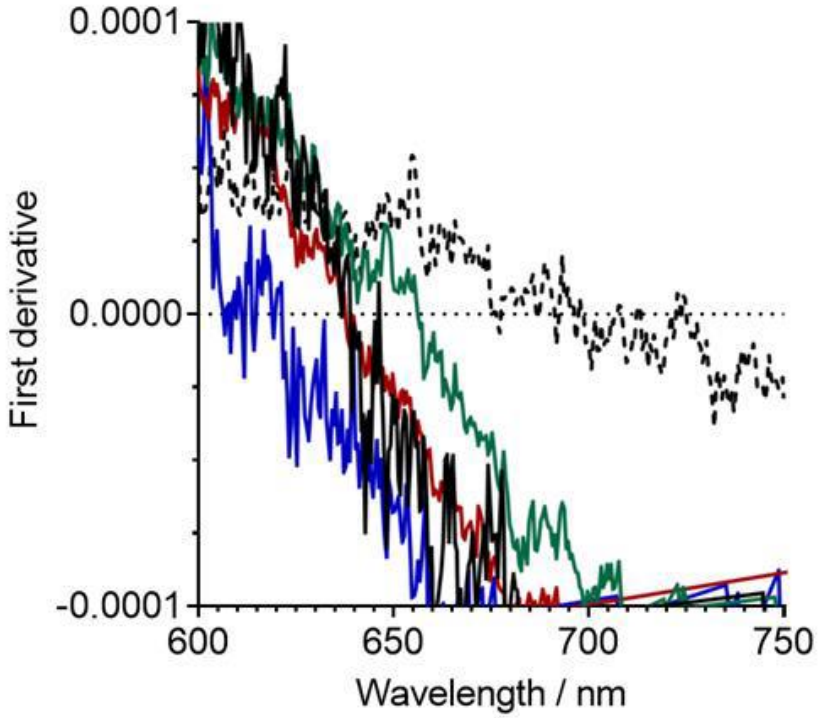

Figure 2.21. First derivatives of the spectra shown in Figure 2.15 corresponding to WT C-peptide (black), E3A C-peptide (red), D4A C-peptide (blue), E3A D4A C-peptide (green), and Cu^{2+} in 15 mM MOPS, pH 7.4 (black, dashed). λ_{max} for the d-d band as determined by the first derivative of WT, E3A, D4A, E3A D4A C-peptide, and Cu^{2+} in buffer are 638, 637, 620, 658, and 696 nm, respectively. Derivatives of spectra were processed by a 20-point smoothing. The similar energy of the d-d band from Cu^{2+} suggests that the Cu^{2+} is bound to similar ligands in all peptides. The λ_{max} of E3A D4A C-peptide is red-shifted, is most similar to buffer alone, and exhibits the largest change in λ_{max} among the mutants relative to WT C-peptide.

We next sought to determine the Cu^{2+} binding location on E3A/D4A C-peptide via 2D 1 H−1 H NOESY and TOCSY NMR spectroscopy, and we assessed the paramagnetic broadening of the proton resonances from Cu^{2+} interactions. Unlike WT C-peptide, no resonances were completely obliterated upon Cu^{2+} addition, but several residue side chains had reduced intensities

(Figure 2.11, Figures 2.22 and 2.23, and Tables 2.9−2.11). Since the resulting NMR spectra reflect the summation of all species in solution, this observation may suggest that Cu^{2+} is binding to different regions of C-peptide, resulting in different populations. Furthermore, the differences in the signal reduction pattern between E3A/D4A and WT C-peptide substantiate the claim that Cu^{2+} binds to E3 and D4 in WT C-peptide, and this binding gets reshuffled when those residues are replaced. Interestingly, in the E3A/D4A variant the proton resonances of the NH and CHα protons do not change substantially (Table 2.19) as compared to those of WT C-peptide (Table 2.5) and indicate little structural rearrangement of the peptide upon Cu^{2+} binding. Furthermore, ITC was performed to understand the thermodynamic differences between WT and E3A/D4A C-peptide (Figure 2.24). Interestingly, statistical analysis show that the thermodynamic data are similar (Table 2.12); however, the stoichiometry for E3A/D4A C-peptide is 0.5, indicating that one Cu^{2+} binds per two peptides. This substantiates a reshuffling of the Cu^{2+} binding site on E3A/D4A C-peptide different than that of WT C-peptide.

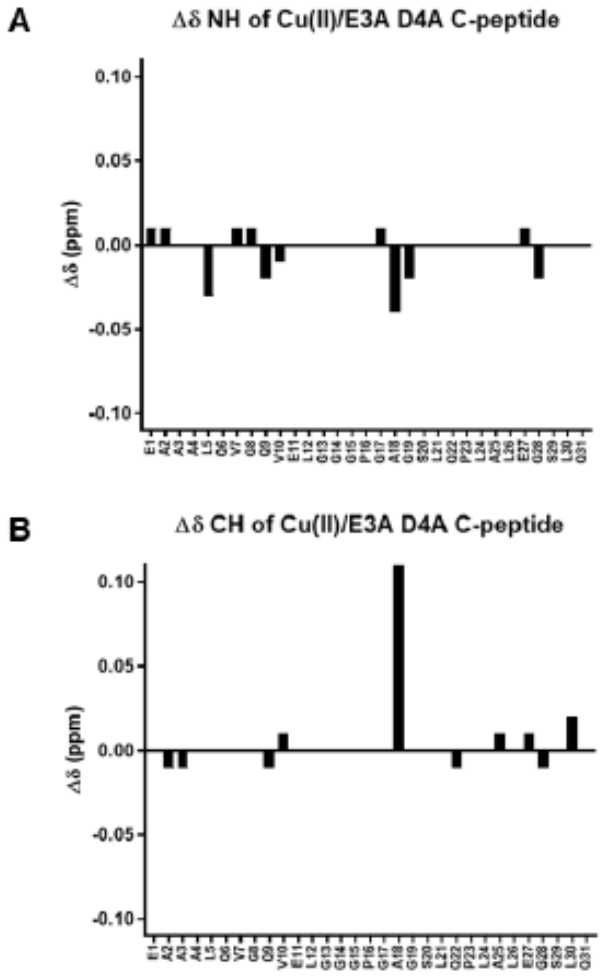

Figure 2.22. The Δδ (δ(Cu^{2+} /E3A D4A C-peptide) − δ(apo E3A D4A C-peptide)) of 1H chemical shifts (ppm) of the A) backbone amide (NH) and B) CHα protons plotted against peptide sequence. Solutions were prepared at 1.5 mM peptide in 95:5 (v/v) H2O:D2O with 10 mM Tris-d11 at pH 7.4 and spectra were collected at 800 MHz and 10 °C. Δδ plots for the backbone side chain protons are shown in Figure 2.23. The small Δδ indicate minimal changes in peptide structure upon Cu^{2+} binding. 1H chemical shift assignments are tabulated in Tables 2.9-2.11.

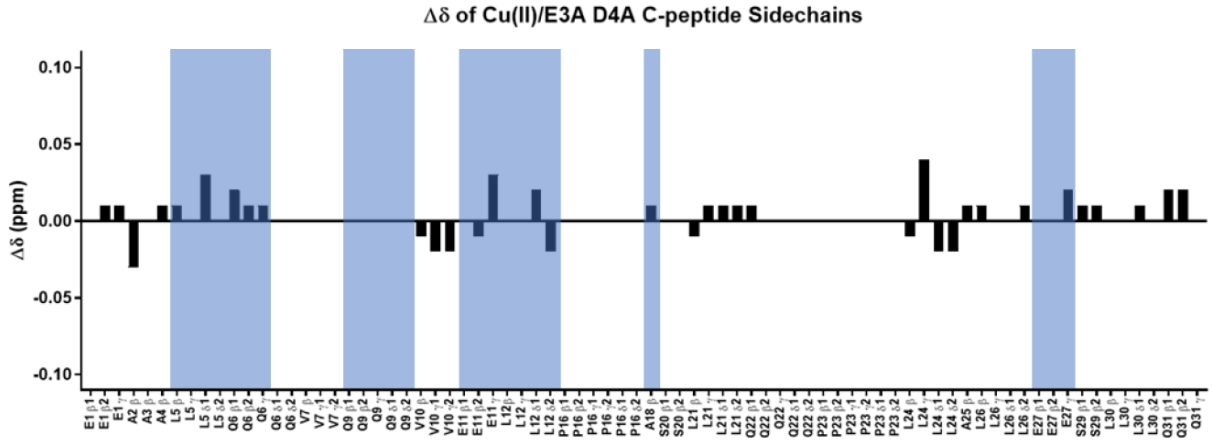

Figure 2.23. The Δδ (δ(Cu^{2+} /E3A D4A C-peptide) − δ(apo E3A D4A C-peptide)) of 1H chemical shifts (ppm) of amino acid side chains plotted against peptide sequence. Solutions were prepared at 1.5 mM peptide in 95:5 (v/v) H2O:D2O with 10 mM Tris-d11 at pH 7.4 and spectra were collected at 800 MHz and 10 °C. Δδ plots for the backbone amide and CHα protons are in the Figure 2.22. The proton resonances with shading indicate reduced (blue) intensities. Mutation of the Cu^{2+} binding site (E3 and D4) to alanines shifts Cu^{2+}-binding to other residues (Q6, E11, and E27) that also had reduced intensities in WT and indicate multiple modes of Cu^{2+} binding where the preferential is E3 and D4. 1H chemical shift assignments are tabulated in Tables 2.9-2.11.

Table 2.9. Chemical shifts of assigned proton NMR resonances of apo E3A D4A C-peptide. Solutions were prepared at 1.5 mM peptide in 95:5 (v/v) H2O:D2O with 10 mM Tris-d11 at pH 7.4 and spectra were collected at 800 MHz and 10 °C.

Chemical Shifts of Assigned ^{1}H NMR Resonances of Apo E3A D4A C-peptide at pH 7.4						
	Chemical Shifts at 10 °C (ppm)					
Residue	NH	CHα	CHβ	CHγ	CHδ	NHγ
E1	8.04	4.34	1.84, 2.03	2.31	-	-
A2	8.44	4.31	1.38	-	-	-
A3	8.40	4.28	1.37	-	-	-
A4	8.37	4.31	1.36	-	-	-
L5	8.30	4.31	1.62	1.56	0.89, 0.92	-
Q6	8.56	4.25	1.98, 2.04	2.28	-	6.87, 7.59
V7	8.31	4.12	2.05	0.92	-	-
G8	8.66	3.96	-	-	-	-
Q9	8.32	4.36	2.00, 2.09	2.34	-	6.92, 7.67
V10	8.35	4.09	2.06	0.94, 0.94	-	-
E11	8.66	4.30	1.94, 2.04	2.25	-	-
L12	8.54	4.34	1.67	1.61	0.88, 0.92	-
G13	n.d.	n.d.	-	-	-	-
G14	n.d.	n.d.	-	-	-	-
G15	n.d.	n.d.	-	-	-	-
P16	-	n.d.	n.d.	n.d.	n.d.	-
G17	8.39	3.98	-	-	-	-
A18	8.54	4.25	1.37	-	-	-
G19	8.58	3.97	-	-	-	-
S20	8.24	4.45	3.87	-	-	-
L21	8.40	4.37	1.63	1.61	0.88, 0.93	-
Q22	8.41	4.61	1.93, 2.09	2.39	-	6.94, 7.61
P23	-	4.61	1.92, 2.39	2.09	3.65, 3.77	-
L24	8.35	4.32	1.63	1.58	0.95, 0.95	-
A25	8.27	4.30	1.40	-	-	-
L26	8.42	4.28	1.63	1.58	0.91, 0.93	-
E27	8.47	4.37	1.97, 2.09	2.35	-	-
G28	8.61	3.98	-	-	-	-
S29	8.20	4.44	3.86	-	-	-
L30	8.45	4.38	1.66	1.66	0.88, 0.93	-
Q31	7.99	4.15	1.9, 2.11	2.28	-	6.87, 7.59

Table 2.10. Chemical shifts of assigned proton NMR resonances of Cu^{2+}-bound E3A D4A C-peptide. Solutions were prepared at 1.5 mM peptide in 95:5 (v/v) H2O:D2O with 10 mM Tris-d11 at pH 7.4 and spectra were collected at 800 MHz and 10 °C.

Chemical Shifts of Assigned ^{1}H NMR Resonances of Cu(II)/E3A D4A C-peptide at pH 7.4						
	Chemical Shifts at 10 °C (ppm)					
Residue	NH	CHα	CHβ	CHγ	CHδ	NHγ
E1	8.05	4.34	1.84, 2.04	2.32	-	-
A2	8.45	4.30	1.35	-	-	-
A3	8.40	4.27	1.37	-	-	-
A4	8.37	4.31	1.37	-	-	-
L5	8.27	4.31	1.63	1.56	0.92, 0.92	-
Q6	8.56	4.25	2.00, 2.05	2.29	-	n.d.
V7	8.32	4.12	2.05	0.92	-	-
G8	8.67	3.96	-	-	-	-
Q9	8.30 and 8.32	4.35	2.00, 2.09	2.34	-	n.d.
V10	8.34	4.10	2.05	0.92	-	-
E11	8.66	4.30	1.94, 2.03	2.28	-	-
L12	8.54	4.34	1.67	1.61	0.90, 0.90	-
G13	n.d.	n.d.	-	-	-	-
G14	n.d.	n.d.	-	-	-	-
G15	n.d.	n.d.	-	-	-	-
P16	-	n.d.	n.d.	n.d.	n.d.	-
G17	8.40	3.98	-	-	-	-
A18	8.50	4.37	1.38	-	-	-
G19	8.56	3.97	-	-	-	-
S20	8.24	4.45	3.87	-	-	-
L21	8.40	4.37	1.62	1.62	0.89, 0.94	-
Q22	8.41	4.60	1.94, 2.09	2.39	-	6.94, 7.61
P23	-	n.d.	n.d.	n.d.	n.d.	-
L24	8.35	4.32	1.62	1.62	0.93, 0.93	-
A25	8.27	4.31	1.41	-	-	-
L26	8.42	4.28	1.64	1.58	0.91. 0.94	-
E27	8.48	4.38	1.97, 2.09	2.37	-	-
G28	8.59	3.97	-	-	-	-
S29	8.20	4.44	3.87	-	-	-
L30	8.45	4.40	1.66	1.66	0.89, 0.93	-
Q31	7.99	4.15	1.92, 2.13	2.28	-	n.d.

Table 2.11. Δδ of assigned proton NMR resonances of Cu^{2+} -bound E3A D4A C-peptide and apo E3A D4A C-peptide. Solutions were prepared at 1.5 mM peptide in 95:5 (v/v) H2O:D2O with 10

mM Tris-d11 at pH 7.4 and spectra were collected at 800 MHz and 10 °C. Visual representations shown in Figures 2.22 and 2.23

Δδ of the Assigned ^{1}H NMR Resonances of Cu(II)/E3A D4A C-peptide at pH 7.4						
	Δδ = δ(Cu(II)/C-peptide) - δ(apo C-peptide) at 10 °C (ppm)					
Residue	NH	CHα	CHβ	CHγ	CHδ	NHγ
E1	0.01	0.00	0.00, 0.01	0.01	-	-
A2	0.01	-0.01	-0.03	-	-	-
A3	0.00	-0.01	0.00	-	-	-
A4	0.00	0.00	0.01	-	-	-
L5	-0.03	0.00	0.01	0.00	0.03, 0.00	-
Q6	0.00	0.00	0.02, 0.01	0.01	-	n.d.
V7	0.01	0.00	0.00	0.00	-	-
G8	0.01	0.00	-	-	-	-
Q9	-0.02 and 0.00	-0.01	0.00, 0.00	0.00	-	n.d.
V10	-0.01	0.01	-0.01	-0.02, -0.02	-	-
E11	0.00	0.00	0.00, -0.01	0.03	-	-
L12	0.00	0.00	0.00	0.00	0.02, -0.02	-
G13	n.d.	n.d.	-	-	-	-
G14	n.d.	n.d.	-	-	-	-
G15	n.d.	n.d.	-	-	-	-
P16	-	n.d.	n.d.	n.d.	n.d.	-
G17	0.01	0.00	-	-	-	-
A18	-0.04	0.12	0.01	-	-	-
G19	-0.02	0.00	-	-	-	-
S20	0.00	0.00	0.00	-	-	-
L21	0.00	0.00	-0.01	0.01	0.01, 0.01	-
Q22	0.00	-0.01	0.01, 0.00	0.00	-	0.00, 0.00
P23	-	n.d.	n.d.	n.d.	n.d.	-
L24	0.00	0.00	-0.01	0.04	-0.02, -0.02	-
A25	0.00	0.01	0.01	-	-	-
L26	0.00	0.00	0.01	0.00	0.00, 0.01	-
E27	0.01	0.01	0.00, 0.00	0.02	-	-
G28	-0.02	-0.01	-	-	-	-
S29	0.00	0.00	0.01	-	-	-
L30	0.00	0.02	0.00	0.00	0.01, 0.00	-
Q31	0.00	0.00	0.02, 0.02	0.00	-	n.d.

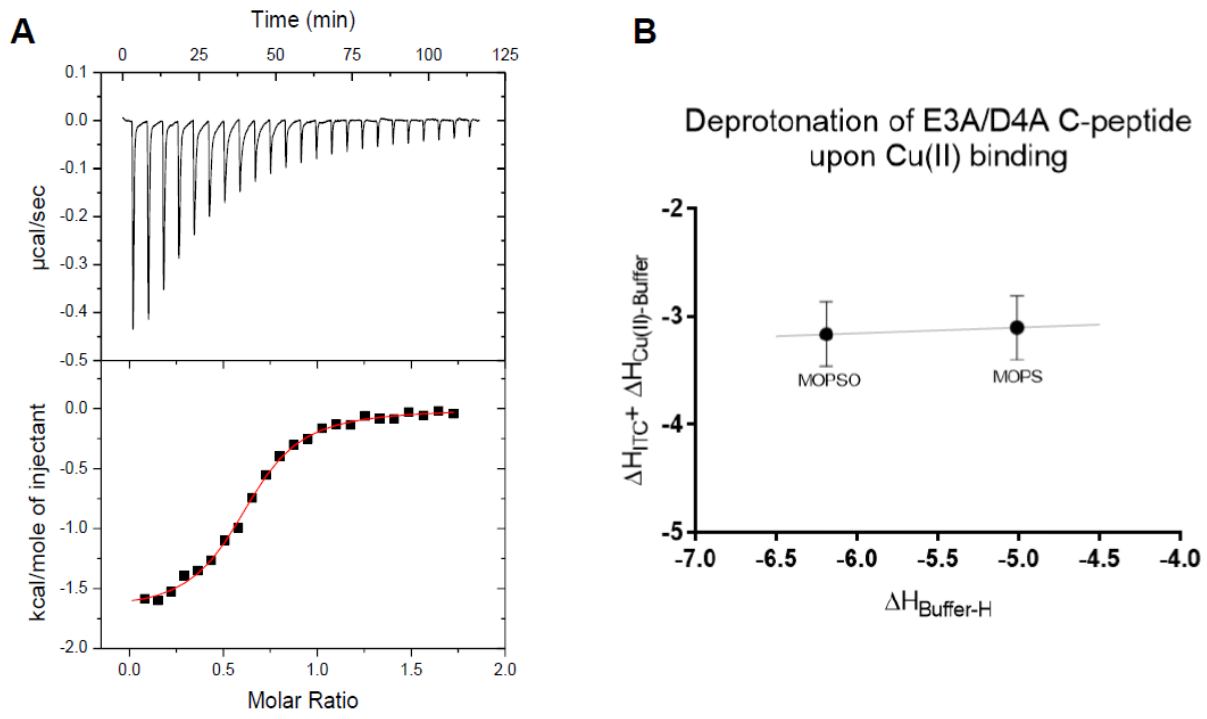

Figure 2.24. A) Representative thermogram of 1.0 mM Cu^{2+} titrated into 100 µM E3A/D4A C-peptide in 15 mM MOPSO, pH 7.4 with red fit line: n = 0.621 ± 0.006; K_{ITC} = 2.6 (± 0.2) x 105; ΔH_{ITC} = −1.70 ± 0.02 kcal mol-1. B) Protonation plot of $\Delta H_{ITC} + \Delta H_{Cu2+ -Buffer}$ *vs.* $\Delta H_{Buffer-H}$ has a slope equal to the number of protons as detailed by Grossoehme *et al.*1 that are binding to the buffer and is equal to 0.1 ± 0.6. The large error of the slope is estimated from subtraction of the minimum slope from the maximum slope between the error bars divided by two. Buffer-independent thermodynamics are summarized in Table 2.12 and indicate a predominantly entropic driving force.

We next investigated the role of each segment of C-peptide to learn if a portion of the peptide would be suitable for Cu^{2+} binding or if the full-length peptide is needed.[33] C-peptide is believed to be tripartite in function, where the N-terminal, flexible middle, and C-terminal portions differ in structure and bioactivity.[33,57] Peptides were synthesized to contain either the N-terminal

segment (N-term) comprising residues E1 to G13 or the C-terminal (C-term) segment comprising residues L24 to Q31. These two truncations leave out the glycine- and proline-rich middle segment, which does not contain carboxylate-bearing residues. We anticipated the N-term peptide to preserve the E3/D4 binding interaction as in WT C-peptide, whereas the C-term peptide would resemble the rearranged binding observed for the E3A/D4A C-peptide.

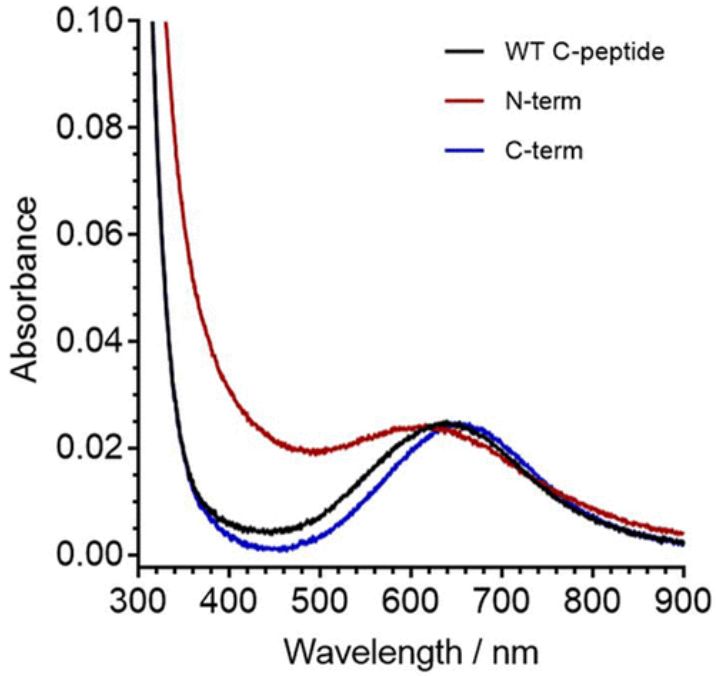

Figure 2.30. Spectra of C-peptide mutants depicting the d–d band from Cu^{2+}-peptide of 300 μM WT C-peptide (black), N-term (red), and C-term (blue) in 15 mM MOPS at pH 7.4. The wavelengths of maximum absorption for the d–d band of WT, N-term, and C-term C-peptide are 640, 623, and 658 nm, respectively. The similar energy of the d–d band from Cu^{2+} suggests that the copper is bound to similar ligands.

Upon Cu^{2+} addition to these truncated peptides, the electronic absorption spectra of N-term and C-term show distinct d−d bands at 623 and 658 nm, respectively, similar to the full-length peptides (Figure 2.30). The similarity in energies and intensities to WT C-peptide suggests that

Cu^{2+} is bound to similar ligands with a similar geometry in both truncations. This is confirmed by the EPR experiments wherein the CW and HYSCORE spectra of the truncations closely resemble those of the WT C-peptide and have similar fitting parameters (Figures 2.25 and 2.26). This indicates that all three peptides coordinate Cu^{2+} in a 1N3O square-planar geometry. It is worth noting in the CW EPR spectrum of C-term that there is an extra set of features centered at ~290 mT that may point to another, albeit minor, population of Cu^{2+}. Signal reduction analysis of the NMR resonances of N-term shows the obliteration of the proton resonance signals for E3 and D4 with broadened signal intensities from E1, A2, L5, Q6, V10, and E11 (Figure 2.11 and Figure 2.27). In the case of C-term, E27 proton resonances were obliterated and L26, G28, L30, and Q31 were reduced with Cu^{2+} present (Figure 2.11 and Figure 2.28). While the Cu^{2+} coordination sphere may thus be similar between the WT peptide and the truncated peptides, the NMR data may indicate that Cu^{2+} is binding to or interacting with more residues or that there are multiple populations of Cu^{2+} -containing adducts present in the truncated peptides as compared to in WT C-peptide. The resonance broadening in the C-term truncation also suggests that while Cu^{2+} may bind to the C-terminal portion of the peptide in a truncated form, it is not the predominant species in WT C-peptide. Interestingly, Cu^{2+} binding to the truncations seen by ITC is nearly identical to that of WT C-peptide and indicates similar binding thermodynamics (Figure 2.29 and Table 2.12).

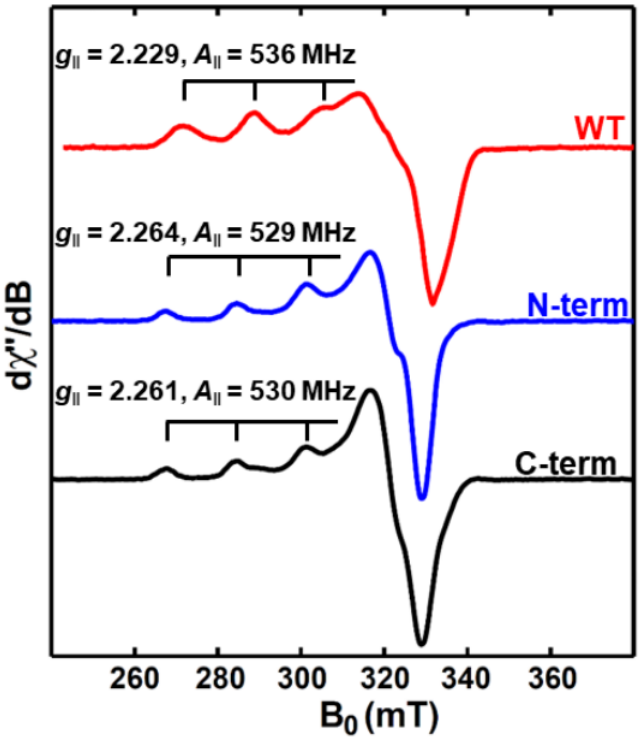

Figure 2.25. X-band EPR of Cu^{2+} bound to WT C-peptide (red), N-term (blue), and C-term (black) and collected at 20 K. WT C-peptide from Figure 2.12 is shown here for clarity of comparisons to truncations. Samples were prepared with 0.5 mM Cu^{2+} and 1.0 mM C-peptide in 15 mM MOPS, pH 7.4 with 20% ethylene glycol as a glassing agent. These spectra indicate that Cu^{2+} is bound in a square planar geometry to either 4O or 3O1N coordination.

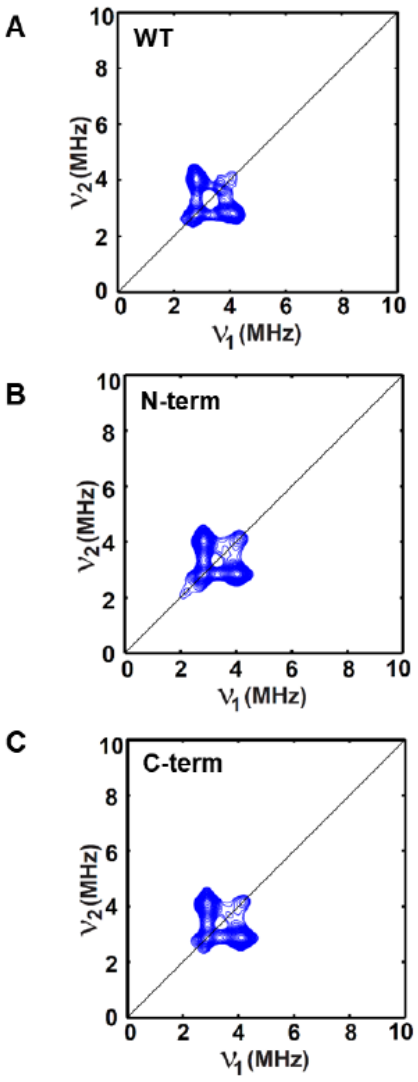

Figure 2.26. HYSCORE spectra of Cu^{2+} bound to A) WT C-peptide, B) N-term, and C) C-term and collected at 20 K. WT C-peptide from Figure 2.12 is shown here for clarity of comparisons to truncations.

Table 2.12. ITC experimental fit parameters from 1.0 mM Cu^{2+} titrated into 100 μM peptide in 15 mM buffer, pH 7.4 at 25 °C. Titrations were in triplicate for all WT C-peptide, N-term, and C-

term, and in duplicate for E3A/D4A C-peptide. The data show that E3A/D4A C-peptide has a smaller nITC indicating 1:2 Cu^{2+}:peptide stoichiometry and that C-term has a smaller KITC than the other peptides.

Variant	Buffer	nITC	KITC	ΔH_{ITC} (kcal mol^{-1})	$K_{Cu(II)/C\text{-}peptide}$	$\Delta H_{Cu(II)/C\text{-}peptide}$ (kcal mol^{-1})
WT	MOPS	0.8 ± 0.2	2 (± 1) × 10^6	-1.3 ± 0.2	2 (± 1) × 10^8	-2 ± 1
	MOPSO	1.0 ± 0.1	5 (± 2) × 10^5	-1.31 ± 0.03	6 (± 3) × 10^7	-2 ± 1
E3A/D4A	MOPS	0.5 ± 0.2	1 (± 0.6) × 10^6	-1.8 ± 0.2	9 (± 6) × 10^7	-3 ± 1
	MOPSO	0.55 ± 0.07	4 (± 1) × 10^5	-1.80 ± 0.09	4 (± 1) × 10^7	-2.8 ± 0.8
N-term	MOPS	0.6 ± 0.2	2.0 (± 0.7) × 10^6	-1.1 ± 0.4	n.d.	n.d.
C-term	MOPS	0.7 ± 0.1	3 (± 1) × 10^5	-1.28 ± 0.06	n.d.	n.d.

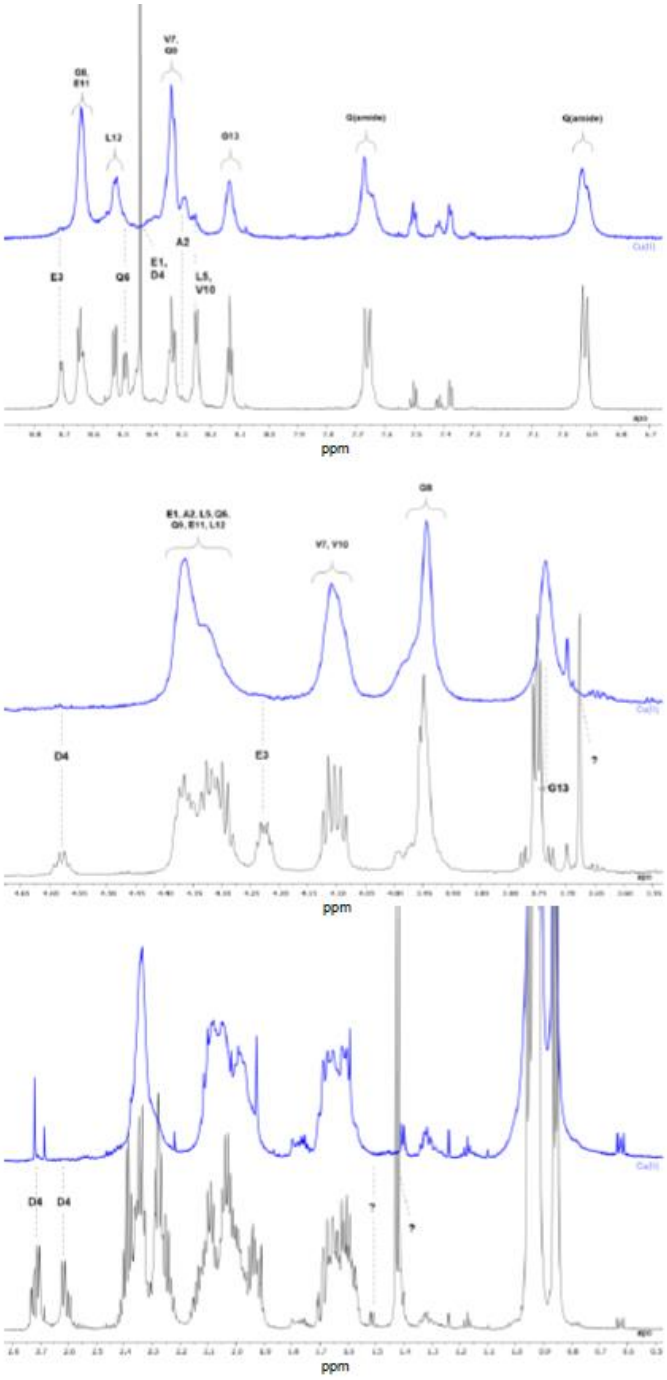

Figure 2.27. NMR spectra of apo and Cu^{2+} bound N-term C-peptide with assigned peaks and noted differences when Cu^{2+} is bound. Solutions were prepared at 1.5 mM peptide in 95:5 (v/v) H2O:D2O with 10 mM Tris-d11 at pH 7.4 and spectra were collected at 800 MHz and 10 °C.

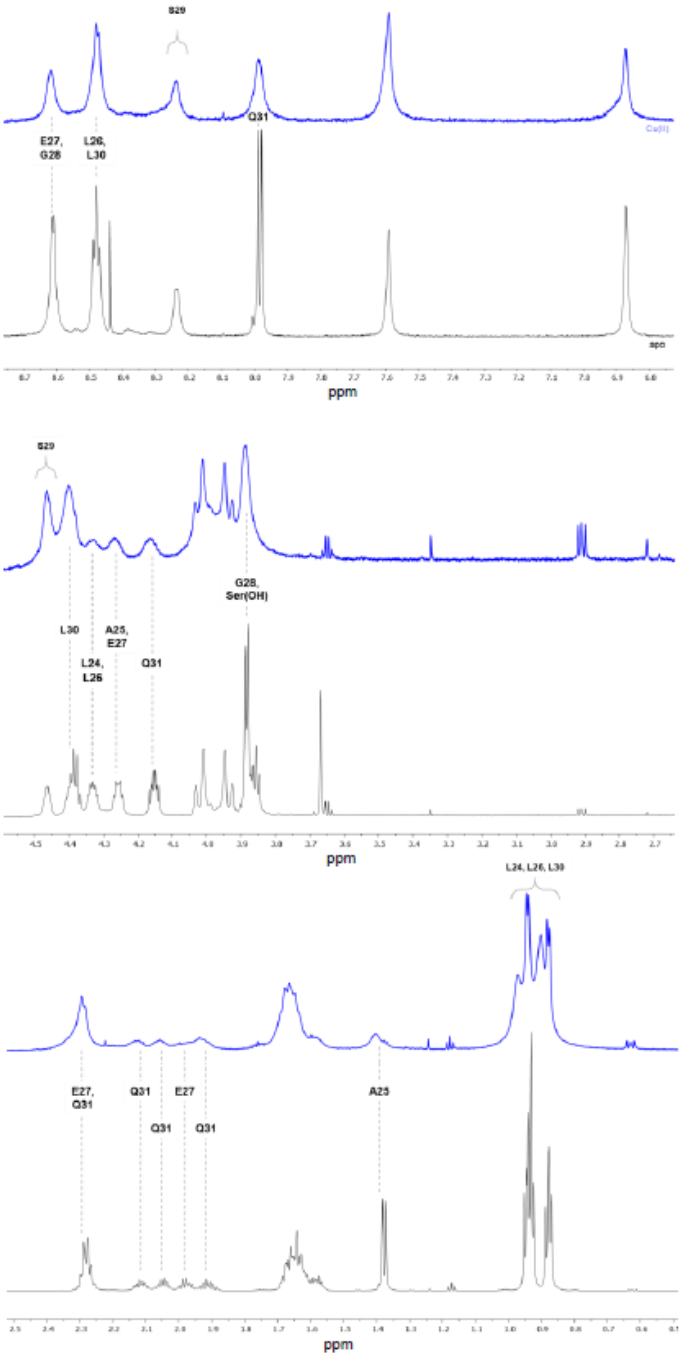

Figure 2.28. Representative thermogram of 1.0 mM Cu^{2+} titrated into A) 100 μM N-term and B) 100 μM C-term in 15 mM MOPSO, pH 7.4. Red fit line for A) n = 0.64 ± 0.01; K_{ITC} = 2.2 (± 0.5) x 106; ΔH_{ITC} = −1.34 ± 0.02 kcal mol-1, and B) n = 0.860 ± 0.009; K_{ITC} = 4.0 (± 0.4) x 105; ΔH_{ITC} = −1.30 ± 0.02 kcal mol-1. The average best fit data are summarized in Table 2.12.

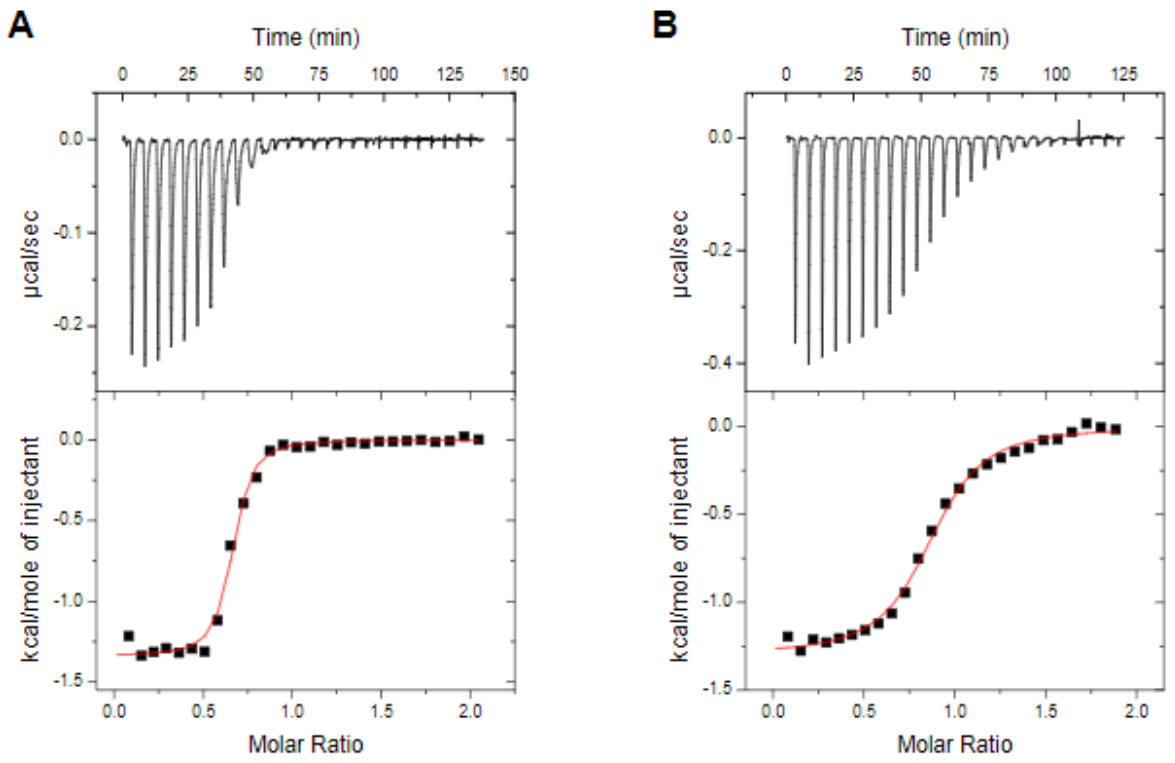

Figure 2.29. Representative thermogram of 1.0 mM Cu^{2+} titrated into A) 100 µM N-term and B) 100 µM C-term in 15 mM MOPSO, pH 7.4. Red fit line for A) n = 0.64 ± 0.01; KITC= 2.2 (± 0.5) x 106; ΔHITC = −1.34 ± 0.02 kcal mol-1, and B) n = 0.860 ± 0.009; KITC= 4.0 (± 0.4) x 105; ΔHITC= −1.30 ± 0.02 kcal mol-1. The average best fit data are summarized in Table 2.12.

The differences in binding modes between the truncations and WT C-peptide may indicate that despite the full-length peptide being a random coil, all three segments are required for precise Cu^{2+} binding to the N-terminal region of the peptide. Cu^{2+} coordination to the terminal amine may serve as an anchor, as seen in other peptides, directing Cu^{2+} binding to the N-terminus in the WT C-peptide. Then, given the promiscuous binding to the N-term peptide, the middle glycine- and proline-rich segments of the full-length peptide may perhaps orient the two termini in such a way

that occludes Cu^{2+} binding promiscuously to the other acidic residues, thus facilitating precise Cu^{2+} binding to E3 and D4 residues

2.4 Conclusion

Previous work has shown that WT C-peptide interacts with a variety of transition metals, but it was Cu^{2+} that showed a decrease in internalization into HEK293 cells. In this study, we sought to determine the binding locale of Cu^{2+} to WT C-peptide along with the binding thermodynamics. Cu^{2+} binds at the terminal amine and carboxylates of E3 and D4 of WT C-peptide in a 1N3O square-planar geometry and is able to outcompete Zn^{2+} for binding. Cu^{2+} has a higher affinity for C-peptide and is entropically driven, most likely from desolvation of the peptide and metal ion coupled with the chelate effect. However, given the relatively low affinity for Cu^{2+}, Cu^{2+}/ C-peptide may be a kinetic product existing transiently in the body. Interestingly, the precision of Cu^{2+} binding to WT C-peptide is seen through the truncation experiments; both truncations bind Cu^{2+} differently, even given that one, N-term, contains the Cu^{2+} binding ligands in WT C-peptide. Even though WT C-peptide is a random coil and Cu^{2+} has no noticeable effect on secondary structure, the discrepancy in Cu^{2+} binding between the WT and truncated peptides may point to the importance of the middle segment of C-peptide in conformational behavior. The glycine- and proline-rich middle segment may orient the two termini, providing steric hindrance to inhibit Cu^{2+} binding to the C-terminus and facilitating only one species on the N-terminus, without which there is promiscuity in the Cu^{2+} binding. This study provides insight into the role that Cu^{2+} plays in C-peptide regulation and shows that the fold of C-peptide is important along with its metal cofactor. The metal-mediated negative feedback mechanism of random coil peptide hormones presents a different paradigm for hormone regulation.

Because the exact function and mechanism of action of C-peptide remain open questions, the relevance of the presence of the metal that we and others have observed may be a key missing piece that would help unravel such biological pathways. Elucidating the binding site and the consequences of mutating it offers powerful chemical information with immediate utility for future biological investigations. While this work has expanded our understanding of this particular peptide, we posit that several other bioactive peptides may indeed require metal cofactors for the function beyond the classical modes. Expanding our understanding of how metals may influence such activity will facilitate the discovery and validation of both new and established paradigms in peptide biology.

2.5 Methods

2.5.1 Peptide Synthesis

Peptide Synthesis. Wild-type human C-peptide, E3A, D4A, E3A/D4A C-peptide, and N-terminus (N-term, E1-G13) and Cterminus (C-term, L24-Q31) truncations were synthesized by means of a heated Fmoc-based solid-phase synthesis (SPPS). Peptides were synthesized on the 0.2 mmol scale. For the N-term truncation, Wang resin preloaded with Fmoc-Gly-OH was swelled overnight in five times the resin volume of DMF. For wild-type, E3A, D4A, E3A/D4A, and the C-terminus truncation, Wang resin preloaded with Fmoc-GlnFigure 10. Spectra of C-peptide mutants depicting the d−d band from Cu^{2+} /peptide of 300 μM WT C-peptide (black), N-term (red), and C-term (blue) in 15 mM MOPS at pH 7.4. The wavelengths of maximum absorption for the d−d band of WT, Nterm, and C-term C-peptide are 640, 623, and 658 nm, respectively. The similar energy of the d−d band from Cu^{2+} suggests that the copper is bound to similar ligands. Inorganic

Chemistry pubs.acs.org/IC Article https://dx.doi.org/10.1021/acs.inorgchem.0c01212 Inorg. Chem. 2020, 59, 9339−9349 9346 (Trt)-OH was swelled overnight in 5 times the resin volume of DMF. The following procedures were repeated in the synthesis of the target peptides. After swelling overnight, the resin was washed 10 times with DMF. Each residue was then deprotected with 3 times the resin volume of 25% 4-methylpiperidine in DMF. The first rinse was shaken by hand for 1 min, and the second rinse was placed on an orbital shaker for an additional 10 min. The resin was then washed 10 times with 2 times the resin volume of DMF. Amino acids (4 equiv) and HBTU (3.9 equiv) were both dissolved in minimal amounts of DMF, and 10 equiv of DIEA was added. The amino acid, HBTU, and DIEA solution was then added to the resin and incubated at 95 °C for 5 min, shaken, and incubated again at 95 °C for an additional 5 min. The solution was cooled for 2 min on an orbital shaker and then washed 10 times with 2 times the resin volume of DMF. The procedure was repeated starting from the Fmoc deprotection step for each additional amino acid. Following the final amino acid coupling, the resin was washed 10 times with DMF followed by an additional 10 times with DCM, after which the resin was dried out overnight. Cleavage of both the peptide and protecting groups from the resin consisted of dissolving the dried resin in a minimal amount of 95:5 TFA/water solution and shaking for 1−4 h. This solution was poured drop by drop into 40 mL of chilled diethyl ether to form a precipitate, followed by centrifugation at 3900 rpm for 10 min. The supernatant was decanted, and 40 mL of chilled diethyl was poured over the crude peptide, followed by centrifugation as described above. This process was repeated two additional times, and the resulting crude peptide was dried with a slow stream of air overnight.

2.5.2 Mass Spectrometry

C-peptide solutions were prepared at 50 μM for each sample, with CuSO4 and ZnClO4 added at 1 equiv in nanopure water. For Zn^{2+} and Cu competition experiments, an equimolar amount of ZnClO4 was added to a 50 μM C-peptide solution and divided into aliquots. Immediately, to 1 aliquot an equimolar amount of CuSO4 was added, which was then added to the Zn(II)/C-peptide solution. A Thermofisher LTQ XL Orbitrap was used for all experiments and operated in positive ion mode at a resolution set at 60,000 for MS scans. Source conditions were as follows: flow rate of 5 μL/min, spray voltage of 3.5 kV, capillary temperature of 275 °C, capillary voltage of 44 V, and tube lens offset voltage of 185 V. Acquired spectra were averaged over 50 scans before peak assignments. For collisional induced disassociated, ions were selected and fragmented in the linear ion trap with a normalized collisional energy of 25. Resulting fragments were analyzed in the Orbitrap mass analyzer with a resolution of 30,000. Spectra were sum over 50 scans prior to analysis.

2.5.3 NMR

NMR experiments were performed on a Bruker Avance III 800 MHz spectrometer equipped with a CPTCI cryoprobe. Peptide samples were prepared at a final concentration of 1.5 mM and dissolved in 95:5 (v/v) H2O/D2O solution buffered at pH 7.4 with 10 mM deuterated Tris-d11. For metal-peptide spectra, the samples were prepared differently in order to minimize metal coordination by Tris buffer. Peptide samples were first dissolved in Milli-Q water and the pH was adjusted to 7.4, followed by the addition of a 1 mol equiv of metal chloride salt and then 10 mM Tris-d11 at pH 7.4. All NMR spectra were collected at 10 °C in 5 mm NMR tubes. The chemical shifts were measured downfield compared to the internal standard (sodium trimethylsilylpropanesulfonate (DSS)). Solvent suppression for 1D, TOCSY, and NOESY spectra

was achieved by using excitation sculpting using 180 water-selective pulses with gradients. One dimensional spectra were collected using 16K data points with 64 scans. Gradient-based phase-selective 1 H−1 H 2D spectra were collected with mixing times of 20 or 80 ms for TOCSY experiments and 100 or 200 ms for NOESY experiments. Two-dimensional spectra were collected using 4096 data points in t2 for 512 t1 values and averaged over 16 scans. NMR spectra were processed with MestreNova.

Combinations of 1D, TOCSY, and NOESY spectra were used to assign the proton resonances of peptides with and without the treatment of metals. 1 H−1 H TOCSY spectra were first used to assign the spin systems of individual amino acids. Subsequently, the sequence-specific assignments were determined by backbone NHi − CHai and CHai −NH + 1 correlations from the 1 H−1 H NOESY spectra.

2.5.4 EPR

The X-band spectra presented in this work are pseudomodulated spectra using a modulation amplitude of 3.0 mT. X-band twopulse electron spin−echo (ESE)-detected field-swept EPR spectra (π/ 2-τ-π-τ-echo) were collected at 20 K on the Bruker Biospin EleXsys 580 spectrometer by employing a split-ring (MS5) resonator. Experiment parameters were as follows: $\pi/2$ = 12 ns and τ = 300 ns. EPR samples were prepared by dissolving peptides of known mass in Milli-Q water and adjusting the pH to 7.4 so that the final concentration was 1.0 mM peptide. CuCl2 was subsequently added to the peptide solution for a final concentration of 0.5 mM, and MOPS at pH 7.4 was added for a final concentration of 15 mM. To this solution, 20% ethylene glycol was added to act as a glassing agent.

Hyperfine sublevel correlation spectroscopy (HYSCORE) is a two dimensional pulse EPR technique which correlates nuclear spin-flip transition frequencies in a one-electron-spin manifold

to those in another electron-spin manifold. HYSCORE spectra were recorded at 20 K on the Bruker Biospin EleXsys 580 spectrometer by employing a split-ring (MS5) resonator for the X-band. Pulse sequence π/2-τ-π/2- t1-π-t2-π/2-τ-echo was programmed with the PulseSPEL programmer via the XEPR interface. The pulse length for the inversion pulse (tπ) and the π/2 pulse (tπ/2) was 24 ns. Eight-step phase cycling was used. Time-domain spectra were baseline-corrected (third-order polynomial), apodized with a hamming window, zero-filled to 8-fold points, and fast Fourier transformed to yield the frequency-domain spectra. Particular spectrometer settings are given in the corresponding figure captions.

2.5.5 ITC

Samples were prepared immediately prior to use. Peptides of known masses were dissolved in buffer that was treated with Chelex 100 and subsequently filtered. Metal chloride salts were dissolved in water and diluted to working concentrations in buffer. The buffer and pH of both samples were carefully matched prior to each experiment.

All ITC measurements were carried out in triplicate on a MicroCal VP-ITC. Titrations were conducted at 25.0 ± 0.1 °C with 25−30 injections of 10 μL of titrant and stirring at 307 rpm. For each figure containing ITC data, the raw, baseline-corrected ITC data is presented in the top panel as heat flow versus time. The integrated and concentration-normalized heat for each injection is presented in the bottom panel after subtraction of the heat of dilution from the final injections. The data in the bottom panel are fit to one site using a nonlinear least-squares analysis. The thermodynamics reported are the average of at least three experiments, and the error is the standard deviation. A post hoc analysis to determine the independent thermodynamics follows Grossoehme et al. [54]

2.5.6 FTIR

Peptides of known masses were dissolved in 15 mM MOPS in D2O with corrected pH 7.4. CuCl2 was dissolved in Milli-Q water. Apo samples were prepared by diluting metal-free peptide to 1.2 mM, while Cu^{2+} /peptide samples were prepared by diluting peptide to 1.2 mM and adding CuCl2 to a final concentration of 1.2 mM. Two microliters of sample was deposited onto the diamond crystal and dried under a stream of argon. Spectra were collected on a Bruker Alpha FTIR spectrophotometer from 4000 to 600 cm−1 at a 2 cm−1 resolution and averaged for 128 scans. Spectra were subsequently processed with OPUS software to remove atmospheric humidity and CO2, baseline-adjusted, and smoothed at 21 points. The spectra from MOPS buffer were then subtracted from all spectra and intensities at the normalized CH vibration (1451 cm−1).

2.5.7 UV-Vis

All measurements were recorded on a UV-1900 (Shimadzu) at room temperature using quartz cuvettes (Starna Cells) with a path length of 1 cm. For metal titrations into apo Cpeptide and both its respective N- and C-terminus truncations, each peptide was dissolved in 15 mM MOPS at pH 7.4 to a final concentration of 100 μM. The CuCl2 solution was dissolved in MilliQ water, and 50−500 μM CuCl2 was added to each peptide. After equilibration for 3 min at room temperature, each measurement was recorded, with water being the spectral reference. After data collection, the spectrum of MOPS buffer alone was subtracted, and the data were normalized in order to account for dilution.

2.6 References

(1) Hamley, I. W. Small Bioactive Peptides for Biomaterials Design and Therapeutics. *Chem. Rev.* **2017**, *117*, 14015.

(2) Zozulia, O.; Dolan, M. A.; Korendovych, I. v. Catalytic Peptide Assemblies. *Chem. Soc. Rev.* **2018**, *47* (10), 3621.

(3) Zasloff, M. Antimicrobial Peptides of Multicellular Organisms. *Nature* **2002**, *415* (6870), 389.

(4) Jeżowska-Bojczuk, M.; Stokowa-Sołtys, K. Peptides Having Antimicrobial Activity and Their Complexes with Transition Metal Ions. *Eur. J. Med. Chem.* **2018**, *143*, 997.

(5) Stevenson, M. J.; Uyeda, K. S.; Harder, N. H. O.; Heffern, M. C. Metal-Dependent Hormone Function: The Emerging Interdisciplinary Field of Metalloendocrinology. *Metallomics* **2019**, *11* (1), 85.

(6) Nyberg, F.; Hallberg, M. Growth Hormone and Cognitive Function. *Nat. Rev. Endocrinol.* **2013**, *9* (6), 357.

(7) Sangkhae, V.; Nemeth, E. Regulation of the Iron Homeostatic Hormone Hepcidin. *Adv. Nutr.* **2017**, *8* (1), 126.

(8) Travaglia, A.; Pietropaolo, A.; la Mendola, D.; Nicoletti, V. G.; Rizzarelli, E. The Inorganic Perspectives of Neurotrophins and Alzheimer's Disease. *J. Inorg. Biochem.* **2012**, *111*, 130.

(9) Tõugu, V.; Karafin, A.; Palumaa, P. Binding of Zinc(II) and Copper(II) to the Full-Length Alzheimer's Amyloid-β Peptide. *J. Neurochem.* **2008**, *104* (5), 1249.

(10) Sharp, P. *Metallobiology*; 2014.

(11) Viles, J. H. Metal Ions and Amyloid Fiber Formation in Neurodegenerative Diseases. Copper, Zinc and Iron in Alzheimer's, Parkinson's and Prion Diseases. *Coord. Chem. Rev.* **2012**, *256* (19–20), 2271.

(12) Norouzi, S.; Adulcikas, J.; Sohal, S. S.; Myers, S. Zinc Stimulates Glucose Oxidation and Glycemic Control by Modulating the Insulin Signaling Pathway in Human and Mouse Skeletal Muscle Cell Lines. *PLoS One* **2018**, *13*, 1.

(13) Meyer, J. A.; Spence, D. M. A Perspective on the Role of Metals in Diabetes: Past Findings and Possible Future Directions. *Metallomics* **2009**, *1* (1), 32.

(14) Davidson, H. W.; Rhodes, C. J.; Hutton, J. C. Intraorganellar Calcium and PH Control Proinsulin Cleavage in the Pancreatic Beta Cell via Two Distinct Site-Specific Endopeptidases. *Nature* **1988**, *333* (6168), 93.

(15) Steiner, D. F. On the Role of the Proinsulin C-Peptide. *Diabetes* **1978**, *27* (Supplement_1), 145.

(16) Wilcox, G. Insulin and Insulin Resistance. *Clin. Biochem. Rev.* **2005**, *26* (2), 19.

(17) Izumi, T.; Kasai, K.; Gomi, H. Secretory Vesicle Docking to the Plasma Membrane: Molecular Mechanism and Functional Significance. *Diabetes, Obes. Metab.* **2007**, *9* (SUPPL. 2), 109.

(18) Castle, J. D.; Cameron, R. S.; Arvan, P.; von Zastrow, M.; Rudnick, G. Similarities and Differences among Neuroendocrine, Exocrine, and Endocytic Vesicles. *Ann. N. Y. Acad. Sci.* **1987**, *493*, 448.

(19) Johansson, B. L.; Sjöberg, S.; Wahren, J. The Influence of Human C-Peptide on Renal Function and Glucose Utilization in Type 1 (Insulin-Dependent) Diabetic Patients. *Diabetologia* **1992**, *35* (2), 121.

(20) Johansson, J.; Ekberg, K.; Shafqat, J.; Henriksson, M.; Chibalin, A.; Wahren, J.; Jörnvall, H. Molecular Effects of Proinsulin C-Peptide. *Biochem. Biophys. Res. Commun.* **2002**, *295* (5), 1035.

(21) Ekberg, K.; Brismar, T.; Johansson, B. L.; Jonsson, B.; Lindström, P.; Wahren, J. Amelioration of Sensory Nerve Dysfunction by C-Peptide in Patients with Type 1 Diabetes. *Diabetes* **2003**, *52* (2), 536.

(22) Bhatt, M. P.; Lim, Y. C.; Ha, K. S. C-Peptide Replacement Therapy as an Emerging Strategy for Preventing Diabetic Vasculopathy. *Cardiovasc. Res.* **2014**, *104* (2), 234.

(23) Forst, T.; Kunt, T. Effects of C-Peptide on Microvascular Blood Flow and Blood Hemorheology. *Exp. Diabesity Res.* **2004**, *5* (1), 51.

(24) Zierath, J.; Handberg, A.; Tally, M.; Wallberg-Henriksson, H. C-Peptide Stimulates Glucose Transport in Isolated Human Skeletal Muscle Independent of Insulin Receptor and Tyrosine Kinase Activation. *Diabetologia* **1996**, *39* (3), 306.

(25) Stevens, M. J.; Zhang, W.; Li, F.; Sima, A. A. F. C-Peptide Corrects Endoneurial Blood Flow but Not Oxidative Stress in Type 1 BB/W or Rats. *Am. J. Physiol. - Endocrinol. Metab.* **2004**, *287*, E497.

(26) Jensen, M. E.; Messina, E. J. C-Peptide Induces a Concentration-Dependent Dilation of Skeletal Muscle Arterioles Only in Presence of Insulin. *Am. J. Physiol. - Hear. Circ. Physiol.* **1999**, *276*, H1223.

(27) Keltner, Z.; Meyer, J. A.; Johnson, E. M.; Palumbo, A. M.; Spence, D. M.; Reid, G. E. Mass Spectrometric Characterization and Activity of Zinc-Activated Proinsulin C-Peptide and C-Peptide Mutants. *Analyst* **2010**, *135* (2), 278.

(28) Meyer, J. A.; Froelich, J. M.; Reid, G. E.; Karunarathne, W. K. A.; Spence, D. M. Metal-Activated C-Peptide Facilitates Glucose Clearance and the Release of a Nitric Oxide Stimulus via the GLUT1 Transporter. *Diabetologia* **2007**, *51* (1), 175.

(29) Meyer, J. A.; Subasinghe, W.; Sima, A. A. F.; Keltner, Z.; Reid, G. E.; Daleke, D.; Spence, D. M. Zinc-Activated C-Peptide Resistance to the Type 2 Diabetic Erythrocyte Is Associated with Hyperglycemia-Induced Phosphatidylserine Externalization and Reversed by Metformin. *Mol. BioSyst.* **2009**, *5* (10), 1157.

(30) Liu, Y.; Chen, C.; Summers, S.; Medawala, W.; Spence, D. M. C-Peptide and Zinc Delivery to Erythrocytes Requires the Presence of Albumin: Implications in Diabetes Explored with a 3D-Printed Fluidic Device. *Integr. Biol. (United Kingdom)* **2015**, *7* (5), 534.

(31) Ge, X.; Kakinen, A.; Gurzov, E. N.; Yang, W.; Pang, L.; Pilkington, E. H.; Govindan-Nedumpully, P.; Chen, P.; Separovic, F.; Davis, T. P.; Ke, P. C.; Ding, F. Zinc-Coordination and C-Peptide Complexation: A Potential Mechanism for the Endogenous Inhibition of IAPP Aggregation. *Chem. Commun.* **2017**, *53* (68), 9394.

(32) Stevenson, M. J.; Farran, I. C.; Uyeda, K. S.; San Juan, J. A.; Heffern, M. C. Analysis of Metal Effects on C-Peptide Structure and Internalization. *ChemBioChem* **2019**, *20* (19), 2447.

(33) Landreh, M.; Johansson, J.; Wahren, J.; Jörnvall, H. The Structure, Molecular Interactions and Bioactivities of Proinsulin C-Peptide Correlate with a Tripartite Molecule. *Biomol. Concepts* **2014**, *5* (2), 109.

(34) Mares-Guia, T. R.; Maigret, B.; Martins, N. F.; Maia, A. L. T.; Vilela, L.; Ramos, C. H. I.; Neto, L. J.; Juliano, M. A.; dos Mares-Guia, M. L.; Santoro, M. M. Molecular Dynamics

and Circular Dichroism Studies of Human and Rat C-Peptides. *J. Mol. Graphics Modell.* **2006**, *25* (4), 532.

(35) Tsednee, M.; Huang, Y.-C.; Chen, Y.-R.; Yeh, K.-C. Identification of Metal Species by ESI-MS/MS through Release of Free Metals from the Corresponding Metal-Ligand Complexes. *Sci. Rep.* **2016**, *6* (1), 26785.

(36) Abbas, I. M.; Vranic, M.; Hoffmann, H.; El-Khatib, A. H.; Montes-Bayón, M.; Möller, H. M.; Weller, M. G. Investigations of the Copper Peptide Hepcidin-25 by LC-MS/MS and NMR+. *Int J Mol Sci* **2018**, *19* (8).

(37) Martin, E. M.; Kondrat, F. D. L.; Stewart, A. J.; Scrivens, J. H.; Sadler, P. J.; Blindauer, C. A. Native Electrospray Mass Spectrometry Approaches to Probe the Interaction between Zinc and an Anti-Angiogenic Peptide from Histidine-Rich Glycoprotein. *Sci Rep* **2018**, *8* (1), 1–13.

(38) Roepstorff, P.; Fohlman, J. Letter to the Editors. *Biomed Mass Spectrom* **1984**, *11* (11), 601.

(39) Chu, I. K.; Siu, C. K.; Lau, J. K. C.; Tang, W. K.; Mu, X.; Lai, C. K.; Guo, X.; Wang, X.; Li, N.; Xia, Y.; Kong, X.; Oh, H. bin; Ryzhov, V.; Tureček, F.; Hopkinson, A. C.; Siu, K. W. M. Proposed Nomenclature for Peptide Ion Fragmentation. *Int J Mass Spectrom* **2015**, *390*, 24–27.

(40) Pu, D.; Vincent, J. B.; Cassady, C. J. The Effects of Chromium(III) Coordination on the Dissociation of Acidic Peptides. *Journal of Mass Spectrometry* **2008**, *43* (6), 773–781.

(41) Dorlet, P.; Gambarelli, S.; Faller, P.; Hureau, C. Pulse EPR Spectroscopy Reveals the Coordination Sphere of Copper(II) Ions in the 1–16 Amyloid-β Peptide: A Key Role of the First Two N-Terminus Residues. *Angew. Chem., Int. Ed.* **2009**, *48* (49), 9273.

(42) Peisach, J.; Blumberg, W. E. Structural Implications Derived from the Analysis of Electron Paramagnetic Resonance Spectra of Natural and Artificial Copper Proteins. *Arch. Biochem. Biophys.* **1974**, *165* (2), 691.

(43) Rao, G.; Bansal, S.; Law, W. X.; O'Dowd, B.; Dikanov, S. A.; Oldfield, E. Pulsed Electron Paramagnetic Resonance Insights into the Ligand Environment of Copper in Drosophila Lysyl Oxidase. *Biochemistry* **2017**, *56* (29), 3770.

(44) Murphy, D. M.; Caretti, I.; Carter, E.; Fallis, I. A.; Göbel, M. C.; Landon, J.; Doorslaer, S. v; Willock, D. J. Visualizing Diastereomeric Interactions of Chiral Amine–Chiral Copper Salen Adducts by EPR Spectroscopy and DFT. *Inorg. Chem.* **2011**, *50* (15), 6944.

(45) Nara, M.; Tanokura, M. Infrared Spectroscopic Study of the Metal-Coordination Structures of Calcium-Binding Proteins. *Biochem. Biophys. Res. Commun.* **2008**, *369* (1), 225.

(46) Deacon, G. B. Relationships between the Carbon-Oxygen Stretching Frequencies of Carboxylato Complexes and the Type of Carboxylate Coordination. *Coord. Chem. Rev.* **1980**, *33* (3), 227.

(47) Gerbino, E.; Mobili, P.; Tymczyszyn, E.; Fausto, R.; Gómez-Zavaglia, A. FTIR Spectroscopy Structural Analysis of the Interaction between Lactobacillus Kefir S-Layers and Metal Ions. *J. Mol. Struct.* **2011**, *987* (1–3), 186.

(48) Tackett, J. E. FT-IR Characterization of Metal Acetates in Aqueous Solution. *Appl. Spectrosc.* **1989**, *43* (3), 483.

(49) Walker, J. M.; Kleinschmidt, J. H. *Methods in Molecular Biology: Lipid–Protein Interactions*; 2013.

(50) Barth, A. Infrared Spectroscopy of Proteins. *Biochim. Biophys. Acta, Bioenerg.* **2007**, *1767* (9), 1073.

(51) Sigel, H.; Martin, R. B. Coordinating Properties of the Amide Bond. Stability and Structure of Metal Ion Complexes of Peptides and Related Ligands. *Chem. Rev.* **1982**, *82* (4), 385.

(52) Magyar, J. S.; Godwin, H. A. Spectropotentiometric Analysis of Metal Binding to Structural Zinc-Binding Sites: Accounting Quantitatively for PH and Metal Ion Buffering Effects. *Anal. Biochem.* **2003**, *320*, 39.

(53) Martell, A.; Smith, R.; Motekaitis, R. NIST Critically Selected Stability Constants of Metal Complexes Database, Version 8.0. *US Dept. of Commerce, NIST Standard Reference Data Program, Gaithersburg, MD* **2004**.

(54) Grossoehme, N. E.; Spuches, A. M.; Wilcox, D. E. Application of Isothermal Titration Calorimetry in Bioinorganic Chemistry. *J. Biol. Inorg. Chem.* **2010**, *15* (8), 1183.

(55) Marcus, Y. A Simple Empirical Model Describing the Thermodynamics of Hydration of Ions of Widely Varying Charges, Sizes, and Shapes. *Biophys. Chem.* **1994**, *51* (2–3), 111.

(56) Daniele, P. G.; Zerbinati, O.; Aruga, R.; Ostacoli, G. Thermodynamic and Spectrophotometric Study of Copper(II) and Cadmium(II) Homo- and Hetero-Nuclear Complexes with L-Histidylglycine in an Aqueous Medium. *J. Chem. Soc., Dalton Trans.* **1988**, *3* (5), 1115.

(57) Henriksson, M.; Nordling, E.; Melles, E.; Shafqat, J.; Ståhlberg, M.; Ekberg, K.; Persson, B.; Bergman, T.; Wahren, J.; Johansson, J.; Jörnvall, H. Separate Functional Features of Proinsulin C-Peptide. *Cell. Mol. Life Sci.* **2005**, *62* (15), 1772.

Chapter 3

Application of IMAC to Enrich Copper-binding Peptides

This work was done in collaboration with Vanessa J. Lee (VJL) and may appear in her thesis. Specifically, generating rice bran hydrolysates (RBH), enriching for Cu^{2+} binding peptides from RBH via IMAC, cell culture, Zincon assay, 3-CCS assay, pic-DTZ, and western blot were primarily conducted by VJL. SEJ conducted mass spectrometry, peptide identification, and mass spectrometry data analysis of rice bran hydrolysates. SEJ also preformed all work shown in sections 3.2.1 and 3.2.2 describing IMAC method development and enrichment of synthetic peptides and hepcidin.

3.1 Introduction

3.1.1. Metal Regulation via Peptide Based Compounds

Bioactive peptides have a wide variety of physiological functions spanning cellular regulation to altering metabolism. One of the most important classes of bioactive peptides are peptide hormones, which are long-range chemical messengers that are synthesized and excreted by endocrine organs, such as the pancreas or pituitary glands, to invoke responses to external stimuli in target tissues or maintain homeostasis. Metals have been shown to influence the function and bioavailability of peptide hormones. For instance, insulin, a hormone that regulates blood glucose levels, relies on zinc binding for efficient packaging in the secretory vesicles of the pancreas prior to release in the bloodstream. Dysfunction of insulin release in diabetes is coupled with zinc deficiency.[1] Beyond insulin, metals have been implicated in other peptide hormones including but not limited to oxytocin, gastrin, hepcidin, and bradykinin.[2–6] These reported metal peptide interactions and disease states associated with metal misregulation, such as Wilson's disease, Alzheimer's disease, and β-Thalassemia, indicate the importance of metal micronutrient regulation and possible metal-dependent pathways for peptide hormones.[7–9]

In addition to peptide hormones' role in influencing metal metabolism, peptide-based chelators and ionophores have shown to be another source of altered metal bioavailability. Ionophores comprise various compounds with the ability to bind non-covalently to metal ions and facilitate their transfer across cell membranes.[10] Metal transport can be broadly classified into two classes: the first being larger protein complexes imbedded in the membrane creating an ion channel across the cell membrane. Examples of protein ion transporters include the copper transporter CTR1, the divalent metal transporter DMT1, and the ZIP/ZnT zinc transporters.[11–13] The second

consist of smaller organic and peptide-based compounds that form metal complexes that enable their movement across the membrane bilayer leading to cellular metal acquisition. Conversely, chelators are compounds that bind metal ions resulting in the reduction of bioavailable metal ions (Figure 1). Like ionophores, chelators are derived from several classes. For example, bacteria have evolved to secrete peptide-like compounds called siderophores that coordinate metal ions, such as iron and copper with high affinity. Additionally, small organic molecules both naturally and synthetically produced are used to reduce the number of available micronutrients for a variety of purposes including disease treatment. Peptide based ionophores and chelators are of increasing interest as they can have a range of chemical properties based on their primary sequence allowing the tuning of binding affinities as well as hydrophobicity enabling selective chelation of metal ions. Specifically, emerging research points to a link between nutritional derived peptides and improved physiological outcomes.[14–16]

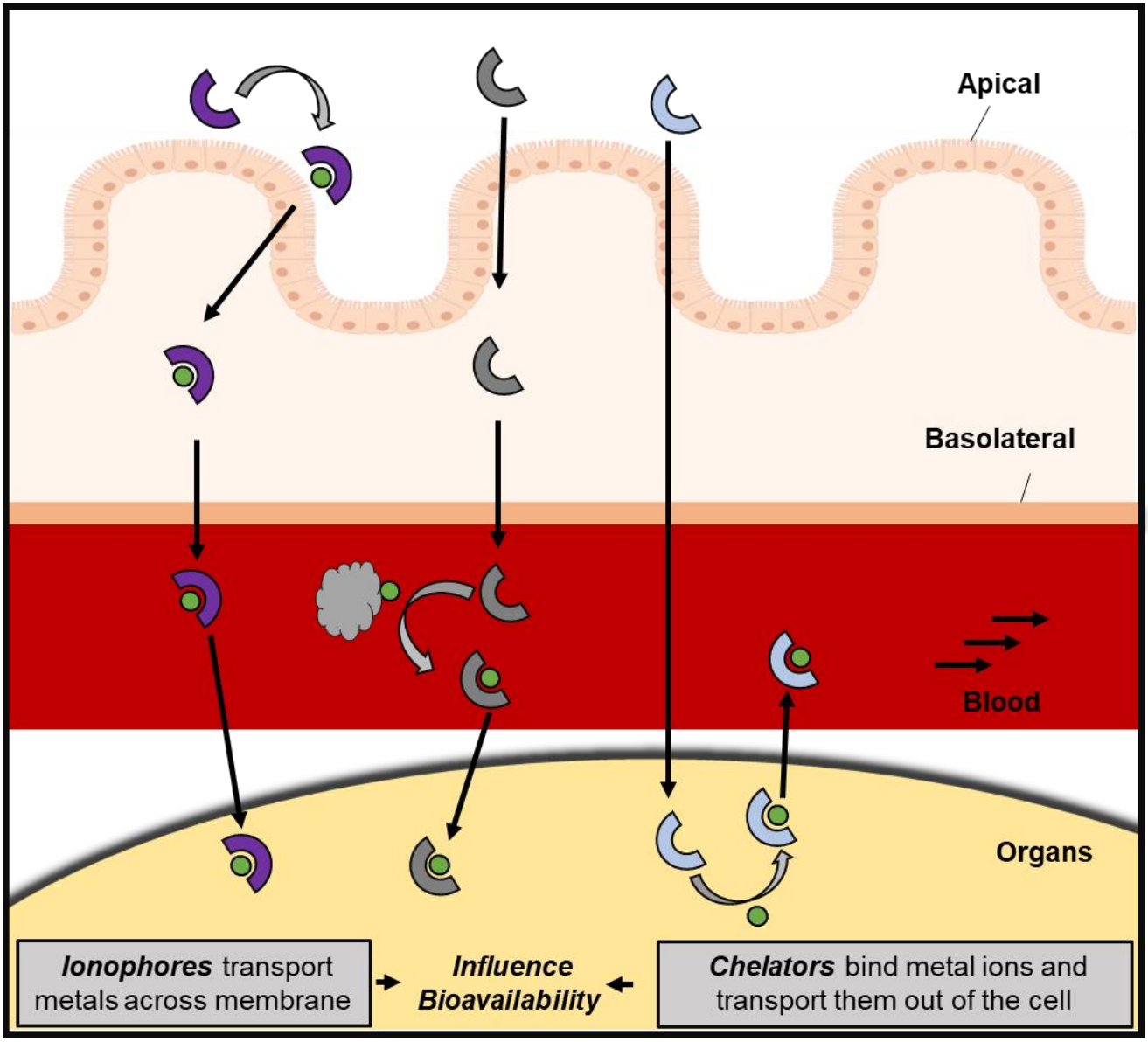

Figure 3.1. Diagram illustrating metal transport via non-membrane bound ionophores and chelators. Ionophores transport metal ions across the cell membrane into the blood and organs. Chelators deprive metal micronutrients from organs through direct binding to withhold metal utilization or removal .

In this chapter we describe the application of the chromatographic technique, IMAC, to study peptide/metal interactions. IMAC utilizes an analyte's affinity towards a metal ion such as

Cu^{2+}, Zn^{2+}, Fe^{3+}, and Ni^{2+} by immobilizing loaded metal chelates to a stationary phase.[17–19] One of the most prominent and earliest applications of IMAC is the purification of affinity-tagged recombinant proteins, in which the unnatural affinity tag, typically consisting of multiple histidines, imparts metal binding ability to peptides and proteins that would otherwise be unlikely to bind, allowing for their purification via IMAC. IMAC has also been applied to the study of the phosphopeptidome by taking advantage of the natural affinity of phosphate groups towards metals ions such as Fe^{3+} and Ga^{3+}.[20] Additionally, IMAC has been implemented in the enrichment of metalloproteins with specific metal affinity. *Barnett et al.* used a Zn^{2+} immobilized iminodiacetate (IDA) IMAC to enrich zinc binding proteins from cyanobacteria which led to the discovery of proteins believed to have a role in zinc metabolism.[21] Other applications of IMAC include probing for proteins that interact with toxic metals such as Pb^{4+}.[22] identifying bismuth binding proteins in *H. pylori* as potential therapeutic targets,[23] proteomics of copper binding proteins in rice,[24,25] discovery Fe^{2+} chelating peptides in soybeans,[26] and enrichment of peptides and proteins from urine for bladder cancer biomarker discovery.[27]

We hypothesize that a population of metal-binding peptides both endogenous and nutritionally derived have evaded discovery due to the labile nature of the metal-peptide interaction. This lability could disrupt the complex during sample preparation making it challenging to uncover and predict metal-binding properties of the peptidome in a high-throughput way. This chapter describes work towards developing and applying IMAC based methods for the enrichment and identification of Cu^{2+} interacting peptides. This work also describes the influence of isolated Cu^{2+} interacting peptides derived from rice bran proteins on AMPK activation through a combination of chelation and *in vitro* studies.

3.2 Results and Discussion

3.2.1 Immobilized Metal Affinity Chromatography of Synthetic Peptides

To determine the viability of IMAC for metal peptide enrichment, Cu^{2+} was chosen due to its association with peptide hormones such as hepcidin[28] and oxytocin,[29] as well as its involvement in disease states including Non-Alcoholic Fatty Liver disease (NAFLD)[30]. To this end, a series of unstructured peptides based on the well-studied amino terminal Cu^{2+}- and Ni^{2+}-binding (ATCUN) motif with the general sequence NH_2-Xxx-Zzz-His-peptide,[31] and the previously synthesized peptide Amide-KRAFFVLHTR-NH_2 (RK10)[32] as well as NH_2-HHK(Dys)H-COOH to serve as model peptides were synthesized. Among these was a peptide with the sequence Amide-RTHLVFFARK-NH_2 (RTH), anticipated to have high affinity for Cu^{2+}, and two others with a single amino acid substitution, Amide-ATHLVFFARK-NH_2 (ATH) and Amide-RTALVFFARK-NH_2 (RTA). Additionally, a peptide with the sequence FAVAG, was synthesized with no polar, acidic, or basic groups to use as a negative (weak to no metal binding) control.

Table 3.1. Sequences for synthetic peptides and their rounded m/z values.

Model Peptide Sequence	Abbreviation	Mass (g/mol)	$[M+2H]^{2+}$	$[M+3H]^{3+}$	$[M+4H]^{4+}$
Amide-RTHLVFFARK-NH_2	RTH	1273	637	425	319
Amide-RTALVFFARK-NH_2	RTA	1208	605	403	303
Amide-ATHLVFFARK-NH_2	ATH	1188	595	397	298
NH_2-HHK(Dys)H-COOH	DP4	792	397	265	199
NH_2-FAVAG-COOH	FAVAG	464	--	--	--

In the initial experiments, peptides were spiked into loading buffer (50 mM phosphate and 300 sodium chloride at pH 7.4) and the solution was incubated for 120 min in a syringe containing the Cu^{2+}-IMAC resin. After incubation and subsequent washing, unbound peptide was removed via washing with loading buffer competed off the resin with a solution containing imidazole (300 mM). ESI-MS revealed showed that RTH was absent in the last wash fraction but present in the first elution fraction, supporting the notion that the peptide was retained by interactions with Cu^{2+}-IMAC while FAVAG was solely present in the flow through fraction (Figure 3.1). This observation suggests a selective retention of RTH on the Cu^{2+}-IMAC resin on account of amino acid composition rather than nonspecific interactions between the peptides and resin.

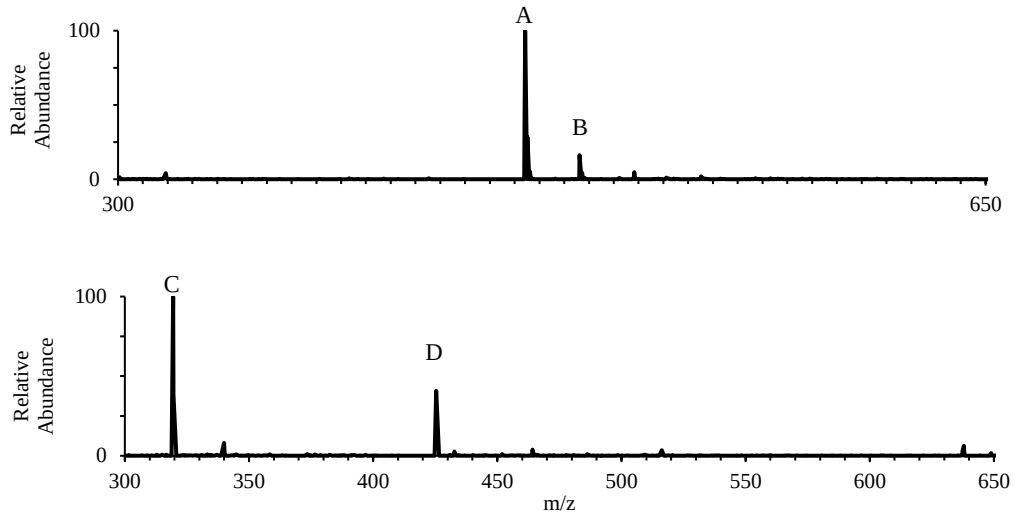

Figure 3.2. Cu^{2+}-IMAC enrichment of RTH from RTH and FAVAG spiked phosphate buffer. Top: flow-through containing FAVAG (A: 464.2 m/z $[M+H]^+$, B: 486.2 m/z $[M+Na]^+$). Bottom: first elution fraction containing RTH (C: 319.4 m/z $[M+4H]^{4+}$; D: 425.45 $[M+3H]^{3+}$)

Having shown selective retention of Cu^{2+}-binding peptides to Cu(II)-IMAC in buffer, we next sought to determine the viability of the approach in cell culture media. RTH was spiked into Dulbecco's Modified Eagle Media (DMEM) with and without fetal bovine serum (FBS) and the

solutions were subjected to chromatographic workflows with and without the IMAC enrichment step.

With IMAC enrichment, RTH was observed in the first elution fraction for both media types indicating either that the media's components were successfully removed, the components did not interfere RTH retention, or a combination of the two (Figure 3.2 and 3.2). In contrast to the IMAC-enriched fractions, when the IMAC step was skipped, significant peaks were observed between 320 m/z to 400 m/z that were not present by IMAC enrichment, further validating a key selection role in the IMAC enrichment step. (Figure 3.3). Due to the detection of BSA during analysis, the G10 size exclusion column was substituted with a high molecular weight cut-off spin column (MWCO <30 kDa). This minor adjustment showed complete removal of BSA during subsequent experiments.

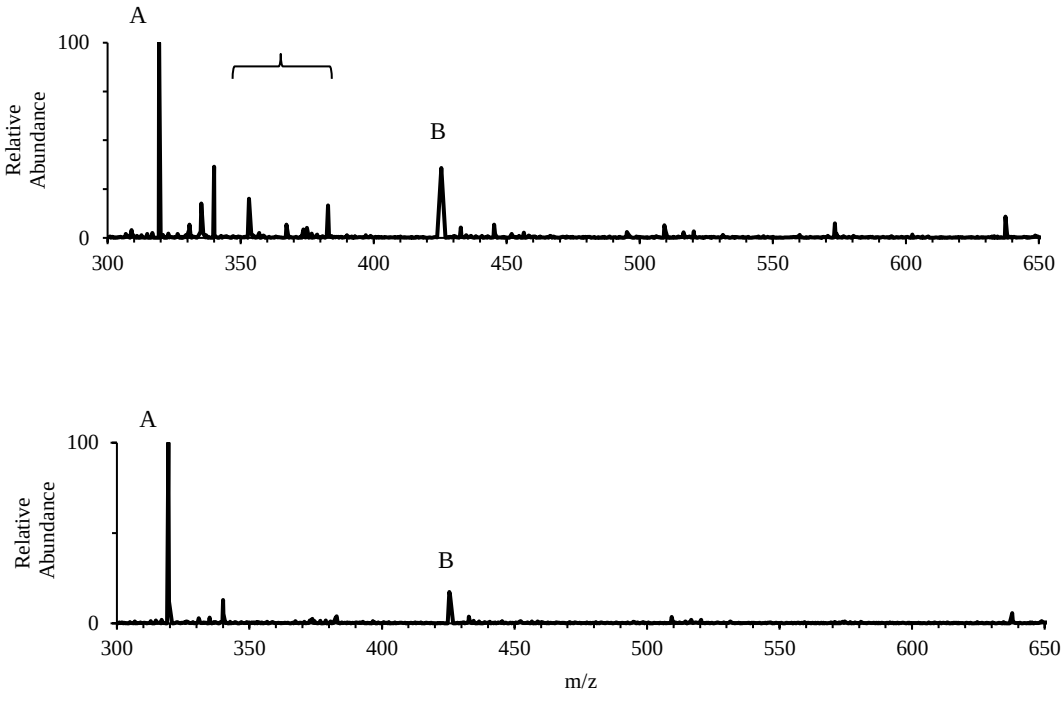

Figure 3.3. Cu^{2+}-IMAC enrichment of RTH (A: 319.4 m/z $[M+4H]^{4+}$; B: 425.4 $[M+3H]^{3+}$) from spiked DMEM (FBS). Top: without IMAC enrichment. Bracket: 320 to 400 m/z. Bottom: with IMAC enrichment.

With selective enrichment of the copper binding peptide RTH from both buffer and cell culture media containing fetal bovine serum, we next assessed IMAC's ability to simultaneously enrich several putative copper binding peptides. A mixture containing synthetic peptides described above (table 3.1) were spiked into cell media (with FBS) and applying the peptide IMAC workflow followed by MS analysis of the flow through and elution fractions. ESI-MS of the elution fraction revealed ions corresponding to the doubly, triply, and quadruply charged RTH peptide; as well as the doubly and triply charged ATH peptides. No ions corresponding to RTA were seen in the MS spectra from elution fraction but the triply charged ion was present in the flow through. Interestingly, the single charged FAVAG peptide was detected, however, the presence was likely due to insufficient washing post sample incubation rather than peptide binding as prior experiments showed FAVAG unable to bind the copper loaded IMAC resin.

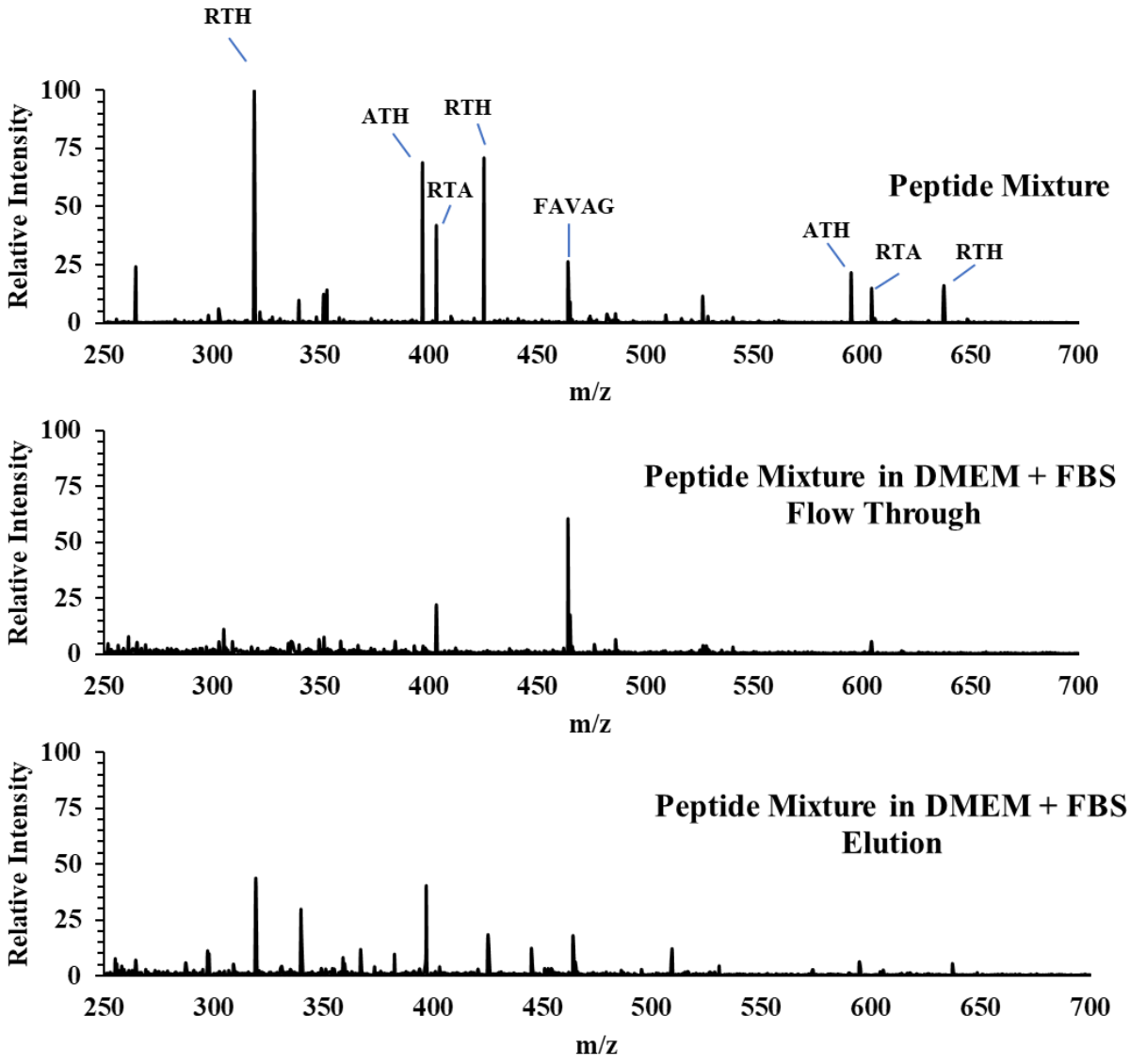

Figure 3.4. Cu^{2+}-IDA-IMAC Enrichment of Synthetic Peptides. Top: ESI-MS of synthetic mixture without IMAC enrichment. Middle: ESI-MS of collected flow through from IMAC enrichment. Bottom: elution fraction of

3.2.2 Immobilized Metal Affinity Chromatography of Hepcidin-25

Having established the Cu^{2+}-IMAC workflow with model peptides, we next sought to apply our system to the enrichment of the biologically relevant peptide hormone hepcidin-25. Hepcidin is an iron-regulatory hormone that, interestingly, contains an ATCUN motif; the Cu^{2+}-binding of

this peptide may carry relevance in regulating iron-copper crosstalk. The peptide contains eight cysteine residues, and it is unclear whether the reduced free-thiol form, the oxidized form with intramolecular disulfides, or both are biologically active. Initially, we attempted enrichment on reduced hepcidin spiked into IMAC loading buffer. However, no signal was observed in any of the fractions analyzed. The lack of signal may have been due to uncontrolled intermolecular disulfide bond formation between multiple hepcidin monomers, causing aggregation during the two-hour incubation. To circumvent this potential challenge, the oxidized form of hepcidin was generated with a controlled protocol using DMSO and water and low peptide concentrations to favor the formation of intramolecular disulfide bonds. With this modification, successful retention of hepcidin on the resin was achieved (Figure 3.5).

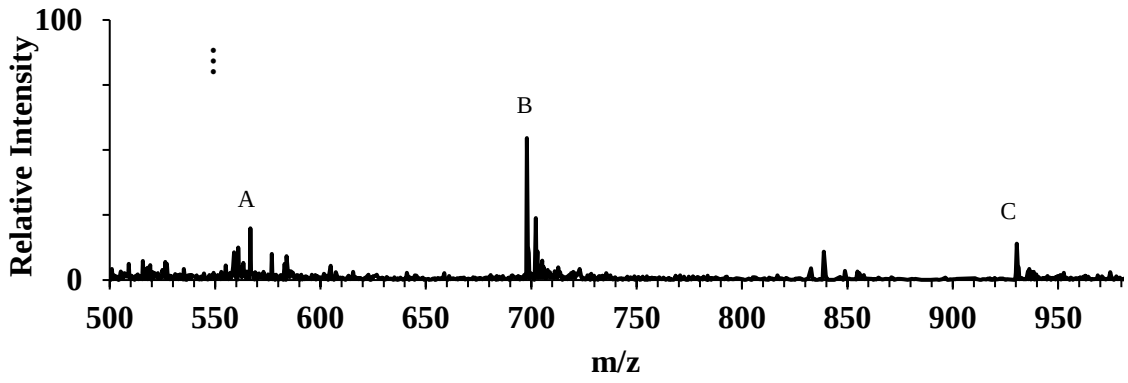

Figure 3.5. Cu^{2+}-IMAC enrichment of oxidized hepcidin. First elution step containing oxidized hepcidin-25 (A: 559.0 m/z $[M+5H]^{5+}$, B: 698.3 m/z $[M+4H]^{4+}$; C: 930.4 m/z $[M+3H]^{3+}$).

The ability to enrich multiple copper interacting peptides from a complex mixture, such as cell media containing serum, has broad implications for discovering endogenous metal interacting peptides. These data indicate IMAC's utility for discovery-based studies directed towards investigating peptide hormones and peptide chelators that have biological functions.

3.2.3 Enrichment of Rice Bran Peptides via Cu^{2+} Loaded IDA-IMAC Resin

Through unknown mechanisms, rice bran hydrolysates have been linked to decreased oxidative stress and amelioration of metabolic syndrome complications, such as insulin resistance and dyslipidemia.[33,34] Changes in copper regulation have also been linked to metabolic disorders[35,36] and peptides derived from dietary sources have been implicated in modulating bioavailability of metal micronutrients,[37] suggesting an interplay between diet and micronutrient bioavailability. To this end, we next sought to apply IMAC to enrich Cu^{2+} binding peptides from enzymatically digested rice bran proteins. The rational for using two enzymatic digestion schemes for generating rice bran peptides was to increase the diversity of peptides generated. The increase in diversity can be leveraged to identify putative motifs that bind copper *in vivo.* The first digestion scheme was papain, an enzyme found in papaya that cleaves C-terminal of basic amino acids, leucine, and glycine. The second enzymatic digestion condition mimicked human physiological digestion by first digesting RBP with pepsin in acidic conditions followed by trypsin digestion in slightly basic conditions. Pepsin is found in the stomach and has promiscuous cleavage but largely cleaves at aromatic and hydrophobic residues. Conversely, trypsin is specific to cleaving C-terminal to arginine and lysine.[38]

Fractions from Cu^{2+}-IDA-IMAC enrichment of peptides derived from both papain and pepsin/trypsin showed significant differences in copper binding ability. Using the Zinon competition assay, which relies on monitoring intensity changes of the Zincon-Cu^{2+} complex's absorbance, the elution fractions from both enzymatic schemes produced a higher amount of total chelated copper when compared to the flow through fractions (Figure 3.6). These data are consistent with our previous work (see Chapter 4) which suggested that IMAC can select for stronger metal binders.

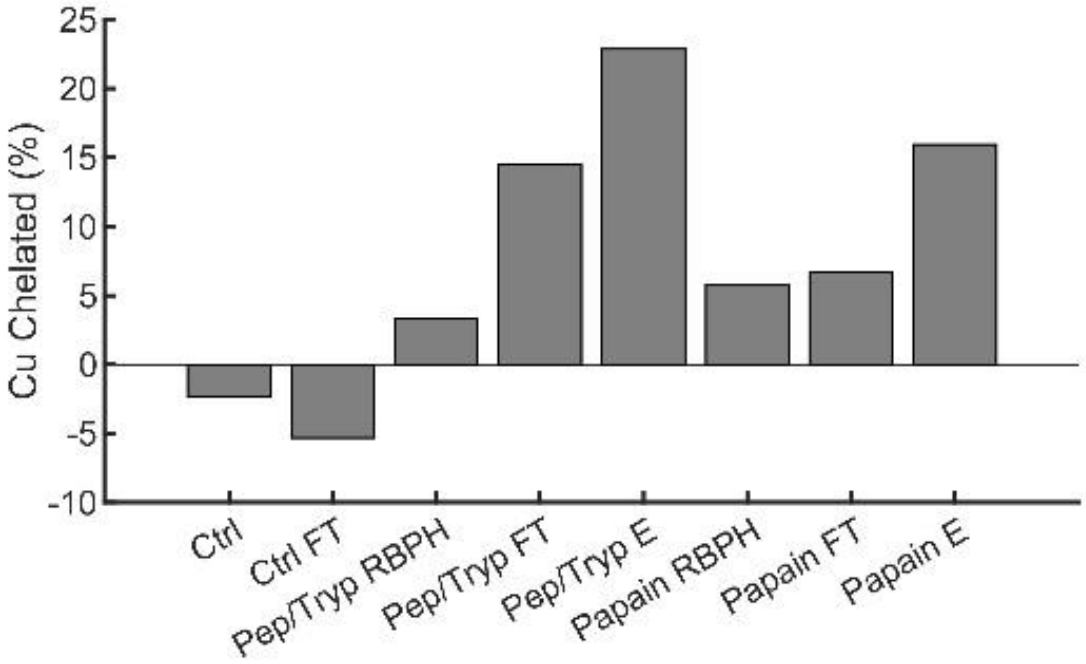

Figure 3.6. Percentage of copper chelated determined by ligand competition woth the chromophoric chelator, Zincon. Flow through fractions (FT) exhibit less percentage of copper chelated when compared to elution fractions (E) indicating greater copper binding affinity for E.

To identify the peptides with the strongest metal binding ability the elution fractions were desalted and separated in the microflow regime (50 μL/min) on a C18 column connected online to an Orbitrap-HF mass spectrometer. MS2 spectra were acquired over the course of the LC run in data-dependent mode and searched against the UP000059680 (*oryza sativa*) FASTA database. Only considering peptides identified with a probability greater than 0.99, enrichment of rice bran peptide hydrolysates via Cu loaded IDA IMAC resin revealed 112 peptide identifications for rice bran peptides (RBP) generated from papain and over 200 peptides with the pepsin/trypsin scheme.

The peptide identifications were analyzed for common sequence motifs using a custom python script. In brief, a sequence motif of length N was specified and for each peptide ID a section

of length N starting at N-terminus was recorded and appended into a list. If the length of the peptide was longer than the sequence motif length N then an additional section of length N would be recorded starting at the next amino acid from the N-terminus. This repeats until the C-terminal amino acid is included. The process then repeats for every peptide ID.

Peptides at varying lengths with motifs detected in both the trypsin/pepsin and papain experiments were chosen and synthesized (Table 3.2) based on their hydrophobicity and analyzed for their copper binding ability. The hydrophobicity of the peptides were analyzed via the method of Kyte and Doolittle to calculate the grand average of hydropathy index (GRAVY).[39] A negative GRAVY value indicates a peptides hydrophobicity while a positive value indicates a more hydrophilic peptide. The magnitude of the GRAVY score represents the extent of a peptide's hydrophobicity or hydrophilicity.

Table 3.2. Selected Cu^{2+} binding peptides enriched from bulk rice bran hydrolysates generated via papain and trypsin/pepsin digestion.

Peptide Identifier	Peptide Sequence	GRAVY Score
1A	RHASEGG	-1.57
1B	ASEGGHG	-0.99
1C	RHASEGGHG	-1.62
2A	HWPLPPF	-0.33
2B	PHWPLPPF	-0.49
2C	GPHWPLPPF	-0.48
3A	VPSGHPI	0.16
3B	VVPSGHPI	0.66
3C	FVVPSGHPI	0.90

3.2.4 Assessment of Copper binding Properties of Synthesized Rice Bran Peptides

The capacity of copper binding of each synthesized peptide was determined by the Zincon competition assay (Figure 2.7A). Peptides with the highest binding capacity are 1A, 1C, and 1B. General copper binding affinities determined by the Zincon assay were also corroborated by use of the pic-DTZ assay, which uses Cu^{2+}-responsive bioluminescence system to detect reactive Cu^{2+}. (Figure 2.7B) that is dependent on correlatively accessible copper for detection.[40] These data are unsurprising as peptides 1A, 1B, and 1C contain a histidine at the second residue on the N-terminal region. This represents the XH motif, which is a known Cu^{2+} binding motif with high binding affinities.[41]

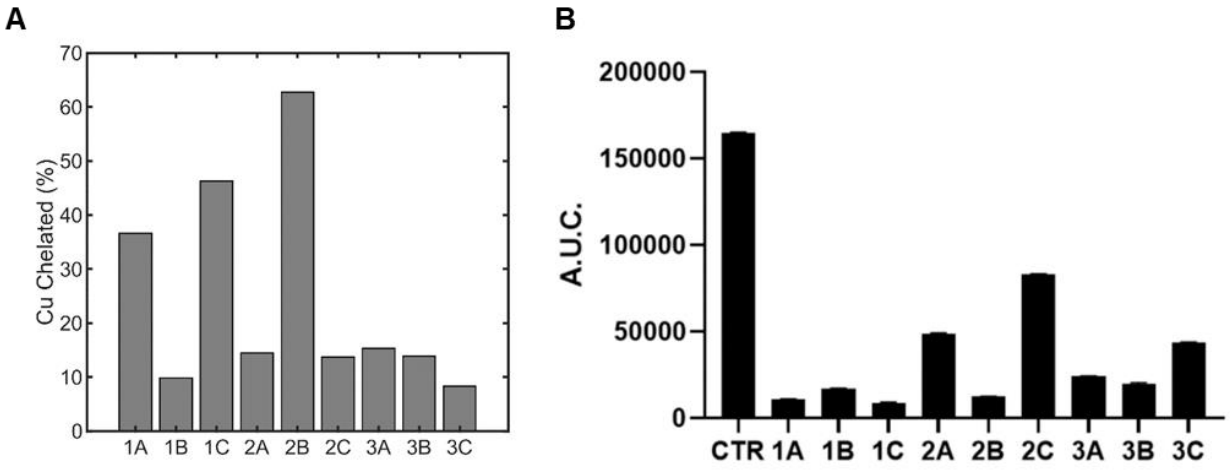

Figure 3.7. Copper binding assessment. A) Zincon competition assay expressed as percent copper chelated. Higher percentage corresponds to decreased Cu^{2+}-Zincon complex. B) pic-DTZ assay of coordinatively accessible copper. Higher light output corresponds to more coordinatively accessible copper.

We hypothesized that the reduction in the signal from the pic-DTZ assay stems from the ability of the peptides to reduce redox-active copper. We assessed this hypothesis using a fluorescent assay with coumarin 3-carboxylic acid.[43] 3-CCA reacts with hydroxide radicals formed from reduction of Cu^{2+} by ascorbic acid, producing the fluorescent product 7-OH-CCA. This allows monitoring of copper-derived redox activity associated with oxidative stressed. The least amount of hydroxide radicle formation occurs in the presence of peptides 1A, 1B, and 1C (Figure 3.8). The data observed correlates with both Zincon and pic-DTZ assays, indicating a correlation between chelation strength and coordinatively accessible copper. Contrasting the peptides series, both the 1- and 2-series reduced radical formation to a greater degree than the 3-series.

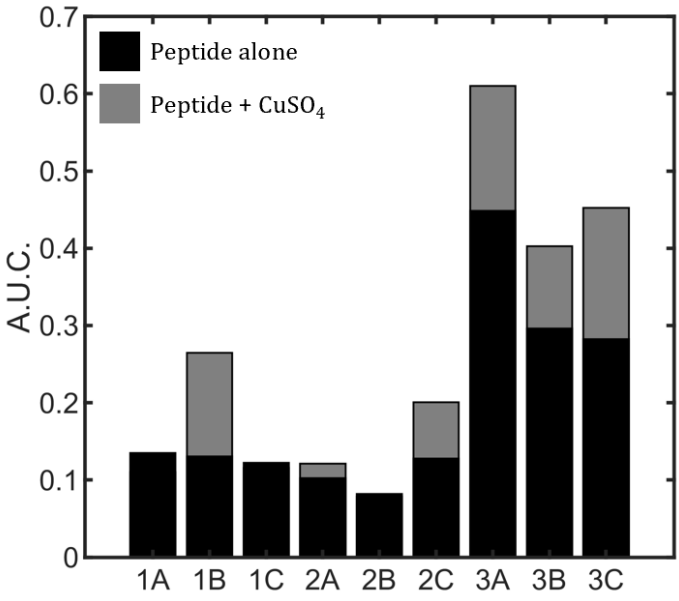

Figure 2.8. 3-CCA assay measuring the production of hydroxide radicals in solution. Hydroxide radicles are formed Fluorescence indicates the presence of hydroxide radicals.

3.2.5 AMPK Activation by Cu^{2+} binding Rice Bran Peptides

Impaired AMPK activation is repressed in hyperglycemic conditions and observed in metabolic disorders making it an attractive target in treating type-2-diabetes.[44,45] *In vitro* studies show addition of rice bran hydrolysates to hepatocytes under a hyperglycemic condition ameliorates glucose induced AMPK suppression and induced insulin resistance.[46] There also exists a link between copper bioavailability and AMPK.[47] Therefore, we hypothesized that the increased phosphorylated AMPK (pAMPK) observed in rice bran hydrolysate application was due to a changes in copper bioavailability. To this end, we applied the synthesized Cu^{2+} binding peptides to hepatocytes under differing levels of glucose. Western blot of HepG2 cell lysates from 24 h stimulation with low (1 g/L) glucose, high glucose (10 g/L) glucose, and high glucose with copper or rice bran peptides (1A-C, 2A-C, and 3A-C) reveal differences in pAMPK (Figure 3.9).

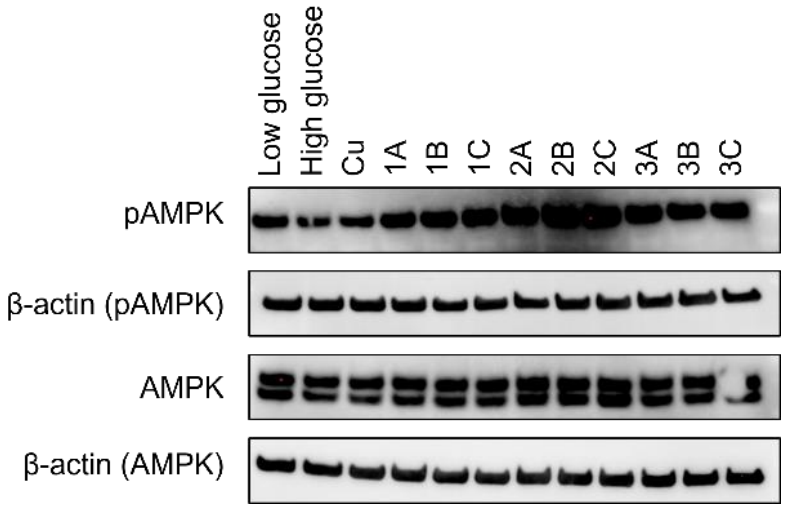

Figure 3.9. Western blot for pAMPK and AMPK with beta actin as loading control. Samples collected from HepG2 cell lysates treated with low glucose (1 g/L), high glucose (10 g/L), and high glucose (10 g/L) with copper or synthesized peptides (1A-C, 2A-C, 3A-C).

Under high glucose conditions, pAMPK is lower than that of HepG2 cells with low levels of glucose while little difference occurs in HepG2 cells treated with copper under high glucose conditions. Cell treatment with synthesized peptides lead to increases in pAMPK for each peptide with the most significant being the 2-series (2A - HWPLPPF; 2B - PHWPLPPF; 2C – GPHWPLPPF). Contrasting the GRAVY score each series of peptides, the 2-series peptides are more hydrophilic than the 3-series and but less than the 1-series. These data suggest that the level of pAMPK activation is dependent on the degree of hydrophobicity – with peptides being only slightly hydrophilic producing the greatest increase of pAMPK. Nevertheless, the 1-, 2-, and 3-series peptides all elicited an increase in pAMPK, suggesting movement across the membrane provided that the mechanism is dependent on peptide internalization. Of particular interest is the peptide 2B (PHWPLPPF). Peptide 2B can chelate copper (Figure 3.7A) with high efficiency – reducing the amount of available coordinatively accessible copper (Figure 3.7B) as well as preventing formation of hydroxide radicals (Figure 3.8). Treatment of HepG2 cells under hyperglycemic conditions with peptide 2B led to the largest pAMPK increase (Figure 3.9). Taken together, these data suggest the level of AMPK activation is highly dependent on both the ability for the peptides to cross the cell membrane, bind copper, and prevent radical formation.

3.4 Conclusions and Outlook

The development of analytical tools and methods to isolate metal-interacting biomolecules is vital toward understanding the interplay between diet, metal micronutrients, and human health outcomes. We show that utilizing Cu^{2+} loaded IDA-IMAC resin allows the enrichment of both synthetic peptides and the endogenous peptide hormone, hepcidin, from buffered solution and cell media containing fetal bovine serum. This approach was further extended to isolating Cu^{2+} binding peptides derived from rice bran protein enzymatically digested with papain or trypsin/pepsin. The

peptides 1A-C, 2A-C, and 3A-C (Table 3.1) were identified by LC-MS/MS and selected based on sequence commonality and hydrophobicity. All peptides showed copper chelating ability with the most significant being those containing the N-XH- motif. Assessed by the 3-CCA assay, peptides 1A, 1C, and 2B reduced the production of hydroxide radicals in the presence of Cu^{2+} to the greatest degree – showing correlation between chelation efficiency and radical production. Lastly, *in vitro* experiments indicate that hydrophobicity is a factor in the activation of AMPK, which may be linked to cell membrane transversal.

While the exact mechanism of pAMPK activation is unknown, data discussed in this chapter point to a link between copper binding peptides derived from enzymatically digested rice bran proteins, copper bioavailability, and AMPK activation. Future studies should focus on elucidating the mechanism of AMPK activation by copper binding peptides through monitoring the level of copper present intra- and extracellularly before and after peptide addition.

3.5 Materials and Methods

3.5.1 Solid Phase Peptide Synthesis

Model peptides and C-peptides were synthesized via solid phase peptide synthesis. All peptides were synthesized via standard Fmoc-protected solid-phase methods on a Rink-amide resin. For synthetic model peptides 0.4413 g corresponding to 0.204 mmol of rink-amide resin was added to approximately 5x the volume of DMF and allowed to swell for 1 h under constant rotation. Once swollen, the resin was washed 5x with 2x resin volume of DMF then Fmoc protected with 3x resin volume of 25% piperidine in DMF for 10 min followed by washing with DMF.

For amino acid coupling, approximately 5 equiv the theoretical loading capacity of resin was dissolved in 5 equiv of HBTU and 20 equiv of DIEA. Once dissolved the amino acid mixture

was added to the deprotected rink-amide resin allowed to couple for 40 min. Following amino acid addition, the uncoupled amino acid were removed by washing 10x with DMF then Fmoc deprotected. The first amino acid of the sequence was loaded with a prolonged coupling step (20 h), and the remaining uncoupled Rink-amide resin was capped using a 3:2 acetic anhydride:pyridine solution for 30 min followed a 4x DMF wash. The initial loading percentage was determined by deprotecting the Fmoc group, measuring its absorbance, and applying Beer's Law to find the concentration.

After the last amino acid addition, the resin wash washed 10x with DMF followed by 10x with DCM and dried. To cleave the peptides off resin and remove side chain protecting groups, a solution of 95% trifluoroacetic acid (TFA) was added to the dried resin and allowed to shake for 2 h. The cleaved peptide was precipitated by adding the TFA solution to chilled ether (approximately 40 mL for 0.2 mmol synthesis).

3.5.2 IMAC Enrichment of Synthetic Peptides and Hepcidin-25

For enrichment of synthetic peptides from loading buffer, approximately 0.2 mg of crude peptide or purified Hepcidin, were dissolved in 1 mL of loading buffer (50 mM phosphate, 300 mM NaCl, pH 7.5). To a 3 mL syringe, 0.5 mL of Profinity IDA-IMAC resin (BioRad) was added and washed with nano pure water followed by 3 mL of metal equilibration buffer (50 mM acetic acid, 300 mM NaCl, pH 3.0). After equilibration 1 mL of a 300 mM copper sulfate solution was added and incubated for 10 min. Excess metal was removed by washing with metal equilibration buffer followed by 5 mL wash of loading buffer (50 mM phosphate, 300 mM NaCl, pH 7.5). Sample was added and incubated at room temperature under constant rotation for 2 h. After incubation, unbound peptides were removed by washing with 10 mL of loading buffer and retained peptides were eluted with three 0.5 mL additions of 500 mM imidazole in loading buffer.

Enrichment of synthetic peptides from cell media, approximately ~0.2 mg of crude peptide (ATH, RTH, ATH, DP4, and FAVAG) was added to 1 mL of DMEM with and without FBS. The solution was added to a 30 kDa Amicon molecular weight cutoff filter and centrifuge at 14,000 rpm for 10 min. The eluent was then added to the copper loaded IDA-IMAC resin, and the enrichment was performed as described previously.

The resulting fractions from each IMAC experiment was desalted via a solid phase extraction cartridge (C18 Discovery SPE, 100 mg). Cartridges were first washed 2 mL of ACN followed by 2 mL of 0.1% TFA. Sample was added and allow to flow through via gravity. After all of the sample was eluted, the cartridge was washed with 5 mL of 0.1% TFA and retained analytes were eluted with 80:20 ACN/H_2O with 0.1% TFA. Desalted peptides were dried *in vacuo* via a SpeedVac.

3.5.3 Rice Bran Protein Extraction

Rice bran was defatted using a 1:3 w/v ratio of rice bran to hexanes (3x for 30 min). After defatting, the mixture was centrifuged at 4000 g for 30 min at 25°C. The resulting supernatant was removed and the remaining solid was dried overnight. After drying, the solid was suspended in nanopure water with a final ratio of 1:4 w/v of rice bran protein to water. The pH of the mixture was adjusted to 9.5 with 1 M NaOH and stirred 500 rpm for 45 min at room temperature. The mixture was then centrifuged at 15,000 g for 30 minutes followed by removal and pH adjustment to 4.5 with 1 M HCl of the supernatant. The resulting precipitate was dried via lyophilization.

3.5.4 Generating of Rice Bran Peptides

8 mg/mL solution of extracted rice bran protein (RBPE) in water were prepared. Enzymatic digestion of RBPE with papain was conducted at an enzyme:protein ratio of 1:100 at 37C. Post

digestion the pH was adjusted to 9.5 with 1 M NaOH and allowed to incubate for 30 min. For enzymatic digestion using pepsin and trypsin, a 1:100 enzyme/protein solution was prepared using pepsin and adjusting the pH to 1.5. The pepsin/protein solution was allowed to incubate for 120 min at 37 °C under constant shaking. After pepsin digestion, the solution was neutralized with 1 M NaOH followed by addition of trypsin to reach a 1:100 trypsin/protein ratio. The solution was incubated at 37 °C for 120 min under constant shaking followed by heating to 95 °C for 10 min to stop digestion. The resulting solution was centrifuged at 3000 rpm for 10 min and the supernatant was removed and dried via lyophilization.

3.5.5 Cu^{2+}-IDA-IMAC of Copper Binding Rice Bran Peptides

Enrichment of copper binding rice bran peptides (RBP) was performed on a copper loaded IDA-IMAC resin. To a 5 mL fritted centrifuge tube, 1 mL of IDA-IMAC resin (BioRad) was added and washed with nanopure water followed by metal loading with 1 M $CuSO_4$. Excess metal was washed with nanopure water and resin was equilibrated with 3 mL of PBS and rice bran peptides dissolved in PBS (25 mg in 4 mL) was added and incubated for 1 h under constant rotation. Unbound peptides were removed with 30 mL of PBS and bound peptides eluted with three 1 mL additions of 0.5 M acetic acid or 50 mM EDTA. Peptides were then dried via lyophilization. Peptides were desalted via the procedure described in *2.5.3*.

3.5.6 LC-MS/MS of Copper Binding Rice Bran Hydrolysates

Dried peptides were reconstituted in nanopure water and quantified via a peptide fluorescent assay (Pierce). 5 µg of peptide were analyzed by microflow liquid chromatography connected online to the mass spectrometer (Ultimate 3000 and Orbitrap-HF). Peptides were loaded onto a 1 mm x 150 mm PepMap C18 column and separated at a flow rate of 50 µL/min with a

gradient ranging from 3% acetonitrile to 80% acetonitrile over 80 min, a ramp to 95% for 4 min, , a isocratic hold at 95% for 4 min, followed by a ramp down to 3% over 4 min, followed by a hold at 3% for 28 min. MS1 and MS2 data were acquired on Xcalibur (Thermo Fisher Scientific). MS spray voltage was set to 4 kV; capillary temperature set to 320 ºC; sheath, auxiliary, and spare gas maintained at 35, 5, and 0, respectively; and S-Lens set to 40. MS1 spectra were collected at a resolution of 60,000 with a AGC target of 3e6 and a max ion injection time of 50 ms. The mass range of MS1 was 250-2000 Da. MS2 spectra were collected in using data-dependent acquisition (DDA) with the top 12 ions from the MS1 scan being selected for fragmentation with dynamic exclusion set to 15 s. The normalized collision energy was set to 28%. For MS2 spectra, the AGC was set to 1e5 with a maximum ion injection time of 86 ms and spectra were acquired at a resolution of 15,000.

3.5.7 Peptide Identification of Rice Bran Peptide

Raw LC-MS/MS files were searched using MSFragger in FragPipe.[48,49] Spectra were searched against the Uniprot protein database UP000059680 (*oryza sativa*) concatenated with the reverse protein sequences (decoys) and common contaminates. A “closed” search was conducted with a precursor tolerance set to -1.2 and 1.2 Da and fragment mass tolerance set to 20 ppm. Digestion constrains were set to “non-specific” and maximum of two missed cleavages with cysteine methionine oxidation (+15.994900), pyro-glutamic acid or loss of ammonia at the peptide N-terminus (-17.0265), N-terminal acetylation (+42.0106), and loss of water on glutamate on peptide N-terminus (-18.0106) as variable modifications. The reverse-decoy method was used to estimate FDR. Peptide (PSM) and protein FDR was set to 0.01.

3.5.8 Identifying Putative Copper Binding Peptide Sequences

Peptide identifications from the pepsin/trypsin and papain digestion experiment were imported into python. Peptides with a probability less than 0.99 were removed and sequence motifs were generated via custom python script. For each peptide identified, a section of length N, where N was required to be equal to or less than the total length of the peptide, was added to a list. For peptides with lengths greater than N, sequences were recorded iteratively from the N-terminus till the C-terminus was contained in the sequence motif. The generated motif list was then filtered based on frequency and the most frequent motifs were compared across digestion conditions using the normalized Hamming distance. [50]

3.5.9 Zincon Assay and Copper Chelation Assessment

Copper chelating capacity was assessed using a colorimetric Cu^{2+} chelator, pyrocatechol violet. 10 μg of each sample, determined by the Pierce quantitative fluorometric peptide assay (ThermoFisher, Waltham, MA), was added to each well in a 96-well plate. Stock solutions 2 mM zincon, and 2 mM $CuSO_4$ were prepared. Final concentrations in each well were 200 μM pyrocatechol violet, 200 μM zincon, and 100 μM $CuSO_4$. Each sample in PBS, pH 7.4 was allowed to incubate with the $CuSO_4$ for 10 minutes at 37°C before addition of pyrocatechol violet. The pyrocatechol violet-copper complex absorbs at 600 nm at pH 7.4. The zincon-copper complex absorbs at 615 nm at pH 7.4. The copper chelating percent was calculated as follows:

Copper chelating % = $[(A_{control}-A_{sample})/A_{control}]\times100\%$; where A_{sample} is the absorbance of the sample and copper subtracted from the absorbance of the sample, copper, and chelator.

The pic-DTZ assay was conducted according to our established protocol.[40] Pic-DTZ was dissolved in ethanol followed by a dilution to 15 μM in DPBS (Gibco) at pH 7.4. The 100 nM rNluc was prepared by dissolving rNluc in DPBS. 25 μL of the rNluc solution was added to a 96-

well plate containing preformed peptide-Cu^{2+} complex. To each well 25 μL of the pic-DTZ solution was added and luminescence was recorded for 1 h. The area was then integrated and compared across peptides.

3.5.10 3-CCA Assay

A stock solution of 2.5 mM 3-coumarin carboxylic acid and 500 μM ascorbic acid was prepared in 10 mM phosphate buffer, pH 7.4. 50 μL of the CCA/ascorbic acid solution was added to 200 μL of pre-incubated peptide/$CuSO_4$ solutions at the described concentrations in 10 mM phosphate buffer, pH 7.4. Time-dependent fluorescence intensity measurements were recorded with excitation at 388 nm and emission at 450 nm over the course of 90 minutes using a Spectramax i3x microplate reader (Molecular Devices, San Jose, CA).

3.5.11 Cell Culture and Western blot

Hep G2 cells were maintained in 1 g/L DMEM media supplemented with 10% fetal bovine serum, 1% sodium pyruvate, 1% glutamine, 1% Penicllin-Strepomycin. Cells were incubated at 37°C with 5% CO_2 in complete media until 70% confluence. Cells were plated at 300,000 cells/well in 6-well plates and allowed to grow for 24 hours. To induce insulin resistance, complete media was replaced with high glucose (10 g/L) starvation media lacking fetal bovine serum for 18 hours. Cells were stimulated with low glucose (1 g/L glucose) complete DMEM or high glucose (10 g/L) complete DMEM and supplemented with the RBPH fractions for 24 hours.

After stimulation, cells were washed with DPBS and lysed with 60 μL RIPA buffer. Whole cell lysates were centrifuged at 15,000 g at 4°C for 1 hour. The supernatant was collected and stored at -20°C. Protein quantification was performed using the BCA assay. 10 μg of protein was loaded into SDS-PAGE gels and transferred to polyvinylidene difluoride (PVDF) membranes. The

membranes were incubated at 4°C overnight with primary antibodies (pAMPK, AMPK, β-actin). The membranes were washed three times with tris buffered saline with Tween (TBST) and incubated in secondary antibodies. Images were recorded using a BioRad ChemiDoc imaging system and processed in ImageLab.

3.6 References

(1) Li, Y. V. Zinc and Insulin in Pancreatic Beta-Cells. *Endocrine* **2014**, *45* (2), 178–189.

(2) Naletova, I.; Nicoletti, V. G.; Milardi, D.; Pietropaolo, A.; Grasso, G. Copper, Differently from Zinc, Affects the Conformation, Oligomerization State and Activity of Bradykinin. *Metallomics* **2016**, *8* (8), 750–761.

(3) Wyttenbach, T.; Liu, D.; Bowers, M. T. Interactions of the Hormone Oxytocin with Divalent Metal Ions. *J Am Chem Soc* **2008**, *130* (18), 5993–6000.

(4) Kovac, S.; Anderson, G. J.; Baldwin, G. S. Gastrins, Iron Homeostasis and Colorectal Cancer. *Biochim Biophys Acta* **2011**, *1813* (5), 889–895.

(5) Rossi, E. Hepcidin - the Iron Regulatory Hormone. *Clinical Biochemist Reviews* **2005**, *26* (3), 47–49.

(6) Liu, D.; Seuthe, A. B.; Ehrler, O. T.; Zhang, X.; Wyttenbach, T.; Hsu, J. F.; Bowers, M. T. Oxytocin-Receptor Binding: Why Divalent Metals Are Essential. *J Am Chem Soc* **2005**, *127* (7), 2024–2025.

(7) Bandmann, O.; Weiss, K. H.; Kaler, S. G. Wilson's Disease and Other Neurological Copper Disorders. *Lancet Neurol* **2015**, *14* (1), 103–113.

(8) Lee, H. J.; Korshavn, K. J.; Kochi, A.; Derrick, J. S.; Lim, M. H. Cholesterol and Metal Ions in Alzheimer's Disease. *Chem Soc Rev* **2014**, *43* (19), 6672–6682.

(9) Origa, R.; Galanello, R.; Ganz, T.; Giagu, N.; Maccioni, L.; Faa, G.; Nemeth, E. Liver Iron Concentrations and Urinary Hepcidin in β-Thalassemia. *Haematologica* **2007**, *92* (5), 583 LP – 588.

(10) Kaushik, V.; Yakisich, J. S.; Kumar, A.; Azad, N.; Iyer, A. K. V. Ionophores: Potential Use as Anticancer Drugs and Chemosensitizers. *Cancers*. MDPI AG October 1, 2018.

(11) Eisses, J. F.; Kaplan, J. H. The Mechanism of Copper Uptake Mediated by Human CTR1: A Mutational Analysis. *Journal of Biological Chemistry* **2005**, *280* (44), 37159–37168.

(12) Yanatori, I.; Kishi, F. DMT1 and Iron Transport. *Free Radical Biology and Medicine*. Elsevier Inc. March 1, 2019, pp 55–63.

(13) Hara, T.; Takeda, T. aki; Takagishi, T.; Fukue, K.; Kambe, T.; Fukada, T. Physiological Roles of Zinc Transporters: Molecular and Genetic Importance in Zinc Homeostasis. *Journal of Physiological Sciences*. Springer Tokyo March 1, 2017, pp 283–301.

(14) Fathi, P.; Moosavi-Nasab, M.; Mirzapour-Kouhdasht, A.; Khalesi, M. Generation of Hydrolysates from Rice Bran Proteins Using a Combined Ultrasonication-Alcalase Hydrolysis Treatment. *Food Biosci* **2021**, *42*.

(15) Hunsakul, K.; Laokuldilok, T.; Sakdatorn, V.; Klangpetch, W.; Brennan, C. S.; Utama-ang, N. Optimization of Enzymatic Hydrolysis by Alcalase and Flavourzyme to Enhance the Antioxidant Properties of Jasmine Rice Bran Protein Hydrolysate. *Sci Rep* **2022**, *12* (1).

(16) Phongthai, S.; D'Amico, S.; Schoenlechner, R.; Homthawornchoo, W.; Rawdkuen, S. Fractionation and Antioxidant Properties of Rice Bran Protein Hydrolysates Stimulated by in Vitro Gastrointestinal Digestion. *Food Chem* **2018**, *240*, 156–164.

(17) Cheung, R. C. F.; Wong, J. H.; Ng, T. B. Immobilized Metal Ion Affinity Chromatography: A Review on Its Applications. *Appl Microbiol Biotechnol* **2012**, *96* (6), 1411–1420.

(18) Block, H.; Maertens, B.; Spriestersbach, A.; Brinker, N.; Kubicek, J.; Fabis, R.; Labahn, J.; Schäfer, F. Chapter 27 Immobilized-Metal Affinity Chromatography (IMAC). A Review. *Methods Enzymol* **2009**, *463* (C), 439–473.

(19) Ueda, E. K. M.; Gout, P. W.; Morganti, L. Current and Prospective Applications of Metal Ion-Protein Binding. *J Chromatogr A* **2003**, *988* (1), 1–23.

(20) Honys, D.; Fı, J. Enrichment Techniques Employed in Phosphoproteomics. *Amino Acids* **2012**, *43* (3), 1025–1047.

(21) Barnett, J. P.; Scanlan, D. J.; Blindauer, C. A. Identification of Major Zinc-Binding Proteins from a Marine Cyanobacterium: Insight into Metal Uptake in Oligotrophic Environments. *Metallomics* **2014**, *6* (7), 1254–1268.

(22) Aryal, B. P.; Paunesku, T.; Woloschak, G. E.; He, C.; Jensen, M. P. A Proteomic Approach to Identification of Plutonium-Binding Proteins in Mammalian Cells. *J Proteomics* **2012**, *75* (5), 1505–1514.

(23) Wang, Y.; Tsang, C.-N.; Xu, F.; Kong, P.-W.; Hu, L.; Wang, J.; Chu, I. K.; Li, H.; Sun, H. Bio-Coordination of Bismuth in Helicobacter Pylori Revealed by Immobilized Metal Affinity Chromatography. *Chem Commun (Camb)* **2015**, *51* (92), 16479–16482.

(24) Chen, C.; Song, Y.; Zhuang, K.; Li, L.; Xia, Y.; Shen, Z. Proteomic Analysis of Copper-Binding Proteins in Excess Copper-Stressed Roots of Two Rice (Oryza Sativa L.) Varieties with Different Cu Tolerances. *PLoS One* **2015**, *10* (4), 1–19.

(25) Song, Y.; Zhang, H.; Chen, C.; Wang, G.; Zhuang, K.; Cui, J.; Shen, Z. Proteomic Analysis of Copper-Binding Proteins in Excess Copper-Stressed Rice Roots by Immobilized Metal Affinity Chromatography and Two-Dimensional Electrophoresis. *BioMetals* **2014**, *27* (2), 265–276.

(26) Lv, Y.; Liu, Q.; Bao, X.; Tang, W.; Yang, B.; Guo, S. Identification and Characteristics of Iron-Chelating Peptides from Soybean Protein Hydrolysates Using IMAC-Fe3+. *J Agric Food Chem* **2009**, *57* (11), 4593–4597.

(27) Frantzi, M.; Zoidakis, J.; Papadopoulos, T.; Zürbig, P.; Katafigiotis, I.; Stravodimos, K.; Lazaris, A.; Giannopoulou, I.; Ploumidis, A.; Mischak, H.; Mullen, W.; Vlahou, A. IMAC Fractionation in Combination with LC-MS Reveals H2B and NIF-1 Peptides as Potential Bladder Cancer Biomarkers. *J Proteome Res* **2013**, *12* (9), 3969–3979.

(28) Tselepis, C.; Ford, S. J.; Kie, A. T. M. C.; Vogel, W.; Zoller, H.; Simpson, R. J.; Castro, J. D.; Iqbal, T. H.; Ward, D. G. Characterization of the Transition-Metal-Binding Properties of Hepcidin. **2010**, *296*, 289–296.

(29) Bal, W.; Kozlowski, H.; Lammek, B.; Pettit, L. D. Potentiometric and Spectroscopic Studies of the CulI I) Complexes of Ala-Arg ' -Vasopressin and Oxytocin : Two Vasopressin-Like Peptides. **1992**, *202*, 193–202.

(30) Heffern, M. C.; Min, H.; Au-yeung, H. Y.; Bittner, G. C. Van De; Ackerman, C. M. In Vivo Bioluminescence Imaging Reveals Copper Deficiency in a Murine Model of Nonalcoholic Fatty Liver Disease. **2016**, *113* (50), 14219–14224.

(31) Gonzalez, P.; Bossak, K.; Stefaniak, E.; Hureau, C.; Raibaut, L.; Bal, W.; Faller, P. N-Terminal Cu-Binding Motifs (Xxx-Zzz-His, Xxx-His) and Their Derivatives: Chemistry, Biology and Medicinal Applications. *Chemistry - A European Journal* **2018**, *24* (32), 8029–8041.

(32) Meng, J.; Zhang, H.; Dong, X.; Liu, F.; Sun, Y. RTHLVFFARK-NH2: A Potent and Selective Modulator on Cu2+-Mediated Amyloid-β Protein Aggregation and Cytotoxicity. *J Inorg Biochem* **2018**, *181* (October 2017), 56–64.

(33) Senaphan, K.; Sangartit, W.; Pakdeechote, P.; Kukongviriyapan, V.; Pannangpetch, P.; Thawornchinsombut, S.; Greenwald, S. E.; Kukongviriyapan, U. Rice Bran Protein

Hydrolysates Reduce Arterial Stiffening, Vascular Remodeling and Oxidative Stress in Rats Fed a High-Carbohydrate and High-Fat Diet. *Eur J Nutr* **2018**, *57* (1), 219–230.

(34) Ren, L. kun; Fan, J.; Yang, Y.; Liu, X. fei; Wang, B.; Bian, X.; Wang, D. feng; Xu, Y.; Liu, B. xiang; Zhu, P. yu; Zhang, N. Identification, in Silico Selection, and Mechanism Study of Novel Antioxidant Peptides Derived from the Rice Bran Protein Hydrolysates. *Food Chem* **2023**, *408*.

(35) Weksler-Zangen, S.; Jörns, A.; Tarsi-Chen, L.; Vernea, F.; Aharon-Hananel, G.; Saada, A.; Lenzen, S.; Raz, I. Dietary Copper Supplementation Restores-Cell Function of Cohen Diabetic Rats: A Link between Mitochondrial Function and Glucose-Stimulated Insulin Secretion. *Am J Physiol Endocrinol Metab* **2013**, *304*, 1023–1034.

(36) Morrell, A.; Tallino, S.; Yu, L.; Burkhead, J. L. The Role of Insufficient Copper in Lipid Synthesis and Fatty-Liver Disease. *IUBMB Life*. Blackwell Publishing Ltd April 1, 2017, pp 263–270.

(37) Ke, X.; Hu, X.; Li, L.; Yang, X.; Chen, S.; Wu, Y.; Xue, C. A Novel Zinc-Binding Peptide Identified from Tilapia (Oreochromis Niloticus) Skin Collagen and Transport Pathway across Caco-2 Monolayers. *Food Biosci* **2021**, *42* (May), 101127.

(38) Vandermarliere, E. Getting Intimate with Trypsin, the Leading Protease in Proteomics. **2011**, No. i, 221–235.

(39) Kyte, J.; Doolittle, R. F. *A Simple Method for Displaying the Hydropathic Character of a Protein*; 1982; Vol. 157.

(40) O'Sullivan, J. J.; Medici, V.; Heffern, M. C. A Caged Imidazopyrazinone for Selective Bioluminescence Detection of Labile Extracellular Copper(Ii) . *Chem Sci* **2022**, *13* (15), 4352–4363.

(41) Gonzalez, P.; Bossak, K.; Stefaniak, E.; Hureau, C.; Raibaut, L.; Bal, W.; Faller, P. N-Terminal Cu-Binding Motifs (Xxx-Zzz-His, Xxx-His) and Their Derivatives: Chemistry, Biology and Medicinal Applications. *Chemistry - A European Journal*. Wiley-VCH Verlag June 7, 2018, pp 8029–8041.

(42) Rakshit, A.; Khatua, K.; Shanbhag, V.; Comba, P.; Datta, A. Cu2+ Selective Chelators Relieve Copper-Induced Oxidative Stress: In Vivo. *Chem Sci* **2018**, *9* (41), 7916–7930.

(43) Manevich, Y.; Held, K. D.; Biaglow, J. E. Coumarin-3-Carboxylic Acid as a Detector for Hydroxyl Radicals Generated Chemically and by Gamma Radiation. *Radiat Res* **1997**, *148* (6), 580–591.

(44) Coughlan, K. A.; Valentine, R. J.; Ruderman, N. B.; Saha, A. K. AMPK Activation: A Therapeutic Target for Type 2 Diabetes? *Diabetes, Metabolic Syndrome and Obesity: Targets and Therapy*. Dove Medical Press Ltd. June 24, 2014, pp 241–253.

(45) Entezari, M.; Hashemi, D.; Taheriazam, A.; Zabolian, A.; Mohammadi, S.; Fakhri, F.; Hashemi, M.; Hushmandi, K.; Ashrafizadeh, M.; Zarrabi, A.; Ertas, Y. N.; Mirzaei, S.; Samarghandian, S. AMPK Signaling in Diabetes Mellitus, Insulin Resistance and Diabetic Complications: A Pre-Clinical and Clinical Investigation. *Biomedicine and Pharmacotherapy*. Elsevier Masson s.r.l. February 1, 2022.

(46) Boonloh, K.; Kukongviriyapan, U.; Pannangpetch, P.; Kongyingyoes, B.; Senggunprai, L.; Prawan, A.; Thawornchinsombut, S.; Kukongviriyapan, V. Rice Bran Protein Hydrolysates Prevented Interleukin-6-and High Glucose-Induced Insulin Resistance in HepG2 Cells. *Food Funct* **2015**, *6* (2), 566–573.

(47) Xie, L.; Yuan, Y.; Xu, S.; Lu, S.; Gu, J.; Wang, Y.; Wang, Y.; Zhang, X.; Chen, S.; Li, J.; Lu, J.; Sun, H.; Hu, R.; Piao, H.; Wang, W.; Wang, C.; Wang, J.; Li, N.; White, M. F.; Han,

L.; Jia, W.; Miao, J.; Liu, J. Downregulation of Hepatic Ceruloplasmin Ameliorates NAFLD via SCO1-AMPK-LKB1 Complex. *Cell Rep* **2022**, *41* (3).

(48) Kong, A. T.; Leprevost, F. V; Avtonomov, D. M.; Mellacheruvu, D.; Nesvizhskii, A. I. MSFragger: Ultrafast and Comprehensive Peptide Identification in Mass Spectrometry-Based Proteomics. *Nat Methods* **2017**, *14* (5), 513–520.

(49) Yu, F.; Teo, G. C.; Kong, A. T.; Haynes, S. E.; Avtonomov, D. M.; Geiszler, D. J.; Nesvizhskii, A. I. Identification of Modified Peptides Using Localization-Aware Open Search. *Nat Commun* **2020**, *11* (1), 4065.

(50) Mohammadi-Kambs, M.; Hölz, K.; Somoza, M. M.; Ott, A. Hamming Distance as a Concept in DNA Molecular Recognition. *ACS Omega* **2017**, *2* (4), 1302–1308.

Chapter 4

Systematic Evaluation of Copper(II)-Loaded Immobilized Metal Affinity Chromatography For Selective Enrichment of Copper-Binding Species in Serum and Plasma

*This chapter is a modified version of following published article: Janisse, S. E.; Sharma, V. A.; Caceres, A.; Medici, V.; Heffern, M. C. Systematic Evaluation of Copper(II)-Loaded Immobilized Metal Affinity Chromatography For Selective Enrichment of Copper-Binding Species in Human Serum and Plasma. *Metallomics* **2022**, mfac059. https://doi.org/10.1093/mtomcs/mfac059. Experimental procedures and data pertaining to serum collected from mice post bariatric and sham surgery is unpublished and included in this chapter due to its relevance.

4.1 Abstract

Copper is essential in a host of biological processes, and disruption of its homeostasis is associated with diseases including neurodegeneration and metabolic disorders. Extracellular copper shifts in its speciation between healthy and disease states, and identifying molecular components involved in these perturbations could widen the panel of biomarkers for copper status. While there have been exciting advances in approaches for studying the extracellular proteome with mass-spectrometry-based methods, the typical workflows disrupt metal-protein interactions due to the lability of these bonds either during sample preparation or in gas-phase environments. We sought to develop and apply a workflow to enrich for and identify protein populations with copper-binding propensities in extracellular fluids using an immobilized metal affinity chromatography (IMAC) resin. The strategy was optimized using human serum to allow for maximum quantity and diversity of protein enrichment. Protein populations could be differentiated based on protein load on the resin, likely on account of differences in abundance and affinity. The enrichment workflow was applied to plasma samples from patients with Wilson disease (WD) and protein IDs and differential abundancies compared to healthy subjects were compared to those yielded from a traditional proteomic workflow. While the IMAC workflow preserved differential abundance and protein ID information from the traditional workflow, it identified several additional proteins being differentially abundant including those involved in lipid metabolism, immune system, and antioxidant pathways. Our results suggest the potential for this IMAC workflow to identify new proteins as potential biomarkers in copper-associated disease states. Lastly, the IMAC workflow was applied to serum collected from obese and post bariatric surgery mice resulting in several differentially enriched proteins.

4.2 Introduction

4.2.1 Copper Regulation

Copper is an essential metal in biology in processes that include growth, cellular respiration, redox homeostasis , and lipid metabolism.[1–5] While most well-studied as a redox-active cofactor tightly-bound in enzyme active sites, emerging tools for capturing copper dynamics have illuminated new roles for exchangeable copper pools at protein surfaces in cellular signaling and allosteric regulation, but the majority of the studies on these copper pools have focused on intracellular environments.[4] The extracellular copper pool has received less attention in large part due to a lack of tools for studying this milieu. Traditional, non-invasive methods for assessing extracellular copper parameters rely on quantitation of either total serum/plasma copper with methods like inductively-coupled plasma mass spectrometry (ICP-MS) or measuring the copper-carrying protein, ceruloplasmin (CP), with immunoassays like ELISA. However, the aberrant compartmentalization of extracellular copper pools has been implicated in various disease processes, such as in promoting the aggregation of amyloid-beta peptides in Alzheimer's disease and angiogenesis in cancer progression.[6] In Wilson disease (WD), which is caused by a mutation of the copper transporter ATP7B, an elevated amount of non-CP-bound copper is observed, but the composition of the ligands for this extracellular copper pool remains unclear.[7,8] Elucidating extracellular components associated with copper under both healthy and disease states may expand our mechanistic understanding of extracellular copper signaling as well as contribute to the pool of potential biomarkers that report on copper status.

4.2.2 Labile Copper is Lost During Conventional Analytical Workflows

Advances in mass-spectrometry (MS)-based protein identification have significantly expanded our understanding of the blood proteome.[9,10] However, information on exchangeable metal sites are typically lost in these strategies due to the labile nature of coordination bonds and the redox susceptibility of metals like copper in standard sample preparation workflows do not consider the labile nature of metal mediated ternary complexes that may have physiological relevance. Additionally, many metal-binding sites are present in low abundance and can frequently evade identification in post-acquisition analytics. In this work, we sought to establish an approach that could preserve and enrich for metal-binding information in plasma and serum samples with subsequent integration into MS-based proteomics workflows.

4.2.3 Immobilized Metal Affinity Chromatography Captures Metal Interactions

Immobilized metal affinity chromatography (IMAC) is a powerful chromatographic technique used to enrich analytes with a propensity for metal coordination. Designed in the 1970s, it was optimized for and is most commonly used as a fast and efficient chromatographic method to purify recombinant affinity-tagged (i.e His-tag) proteins.[11] IMAC includes three main components: a solid support bead usually composed of agarose, an extending linker, and a chelate loaded with the metal ion of interest (most commonly Ni^{2+} for His-tagged protein purification). Upon addition of a metal-coordinating species, ternary complex formation occurs between the immobilized metal chelate and the metal-binding species, resulting in retention of the species on the stationary phase, separating it from non-coordinating species in the mobile phase. Bound species can subsequently be eluted by weakening the coordination bond via ligand competition or

pH modulation. IMAC has been applied to study endogenous metal coordinating species in a variety of systems, such as rice roots, bacteria, hepatocytes, and serum.[12–15]

In this work, we optimized and applied the IMAC technology alongside gel electrophoresis and mass spectrometry analysis to enrich for and gain insight into Cu^{2+}-binding species as potential biomarkers for copper status. We employed the resin in the form of a solid-phase extraction set up rather than a column format to allow increased residence time of proteins with the resin for maximum protein enrichment. In establishing a workflow, we observed that the composition of the enriched protein population showed key differences between low and high protein loading, offering the possibility of differentiating protein populations based on their Cu^{2+} affinities. We extended our approach to assess retained protein populations in samples acquired from WD patients and compared the protein identifications to those from a traditional serum proteomic workflow. The IMAC-enriched samples both preserved the changes observed in the traditional workflow as well as identified differentially abundant proteins that did not appear in the traditional workflow. Our results illustrate the utility of Cu^{2+}-IMAC to enrich for copper-interacting protein markers that may otherwise evade identification by current serum and plasma proteomics approaches.

4.4 Results and Discussion

4.3.1 Influence of Buffer, Serum Loading, and Incubation Time on the Amount of Protein Retained in Cu^{2+}- IMAC Resin

The majority of existing protocols for using IMAC resins have been designed and optimized for the purification and isolation of histidine-tag-labeled proteins on Ni^{2+}-loaded columns. We sought to establish a protocol that would allow for us to adapt the method to capture a mixture of unlabeled native species based on their Cu^{2+}-binding affinities. Our initial goal was to select a system that could enrich for a high diversity of proteins with metal-binding capacity while maintaining the protein's native structure, as well as ensure adequate total protein recovery for subsequent analysis. The most common commercially-available IMAC resin employ tridentate iminodiacetic acid (IDA), tetradentate nitriloacetic acid (NTA), and pentadentate tris-carboxymethyl ethylene diamine (TED) chelates. We reasoned that lower coordinative Cu^{2+} saturation of IDA would allow for greater diversity in protein binding over the NTA and TED chelates, and thus opted to use the commercially-available Profinity IDA-IMAC resin (Biorad, Hercules, CA). Instead of using the resin within a continuous-flow column set up, we incorporated an incubation period with the IDA-IMAC to allow flexibility in the adsorption time of the sample to maximize protein capture. In our workflow, the IMAC resin is loaded with Cu^{2+}, washed with water to remove unbound Cu^{2+}, and equilibrated with binding buffer (PBS or BTS). The sample is then introduced to the equilibrated column and the suspension is incubated to allow for protein binding. After incubation the unbound proteins are washed off using binding buffer and retained proteins are eluted with 50 mM EDTA. We first assessed whether this described set up could exhibit a concentration-dependent capture of proteins from human serum. Commercially obtained pooled human serum was diluted in buffer at

a fixed volume of 0.5 mL but with varying percentages of serum (50, 75, 125, 200, and 300 µL, corresponding to 10%, 15%, 25%, 40%, and 60% v/v, respectively) and applied to a fixed amount of resin (0.25 mL). We compared two dilution buffers: Phosphate Buffered Saline (PBS) and Bis-Tris Buffered Saline, two common buffers used to maintain physiological pH. Protein was subsequently eluted from the resin with imidazole (0 mM, 1 mM, 5 mM, and 10 mM), and total protein levels in the eluents were quantified with a Bradford assay. For both PBS and BTS, a positive linear trend from 10% serum to 40% serum was observed with respect to protein concentration (Figure 4.1A). At greater than 40% serum, a break from linearity and a concentration plateau emerged, indicative of protein saturation of the resin above this serum content. The incubations in PBS resulted higher protein recovery than BTS at all volumes tested (Figure 4.1A). Since using PBS as the diluent resulted in a higher total protein binding to the resin, we used PBS in subsequent experiments. To assess the effect of incubation time on protein recovery, a 0.5 mL solution of 15% serum in PBS was incubated with 0.25 mL of Cu^{2+}-IDA-IMAC resin at various incubation times (Figure 4.1B). An increase in protein recovery was observed between 0 min and 5 min incubation, followed by plateau in protein concentration after 5 min, suggesting that while protein adsorption occurs rapidly, the solid-phase extraction set up allows higher protein recovery than a column chromatography set up, the latter being akin to the 0 min incubation period. Subsequent studies were performed at 60 min incubation times to ensure ample adsorption time onto the resin.

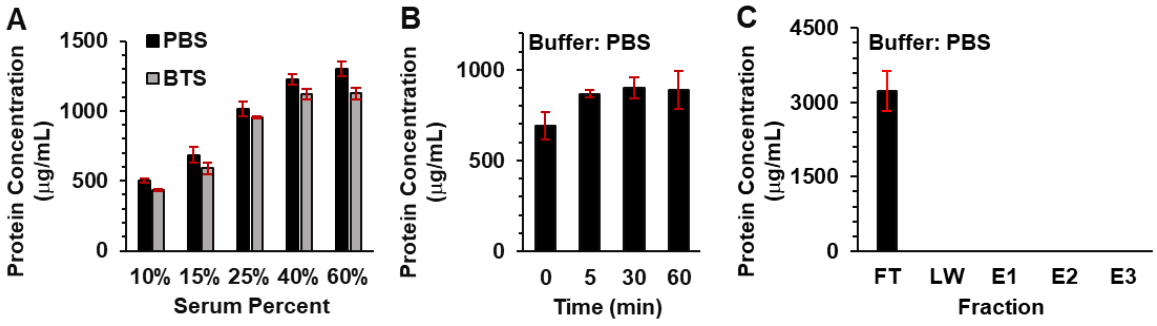

Figure 4.1. Protein concentrations of the elution fraction from Cu^{2+} -IDA-IMAC experiments determined by the Bradford assay as a factor of (A) increasing serum percentage (10% - 60%) and (B) varying incubation time (0-60 min). (C) Protein concentration of the fraction from unloaded IDA-IMAC incubated with 30% serum. Bar plots show mean values with error bars representing standard deviation (n = 3). Black bars representing experiments conducted in PBS and grey bars BTS.

4.3.2 Cu^{2+}-IDA-IMAC Protein Population Dependence

With a protocol established for protein enrichment, we assessed the composition of proteins retained on resin. Serum was applied to the resin at different serum percentages in PBS for 60 minutes, and proteins in the elution fractions were separated and stained via 1D gel electrophoresis. The band profiles were compared to assess relative protein populations. Interestingly, the band profile between 55-100 kDa show clear differences at the different serum percentages, indicating that the protein composition is dependent on the total amount of serum applied to the Cu^{2+}-IDA-IMAC resin. For instance, bands at >180 kDa, one at ~70 kDa, and one between ~40 kDa (indicated with green arrows in Figure 4.2) all increase with increasing serum percentage. However, this increase is not global as bands at ~100 kDa and ~60 kDa (indicated with blue arrows in Figure

4.2) decrease with increasing serum percentage. We reasoned that the differential enrichment with respect to serum volume is attributed to the presence of protein competition for the immobilized Cu^{2+}. At low serum volumes, there is an excess of available binding sites on the Cu^{2+}-IDA-IMAC resin. The excess in binding sites may allow for the retention of proteins with a range of binding affinities. Conversely, high serum volumes, corresponding to a higher amount of total protein may lead to a stoichiometric excess of protein with copper binding ability relative to available coordination sites. In this scenario, proteins with a greater affinity for the immobilized copper ion would outcompete lower-affinity proteins. This hypothesis was first postulated by Porath and Olin where they observed a disproportionate increase in adsorbed protein with increasing serum amount applied to a Ni^{2+} TED column.[16]

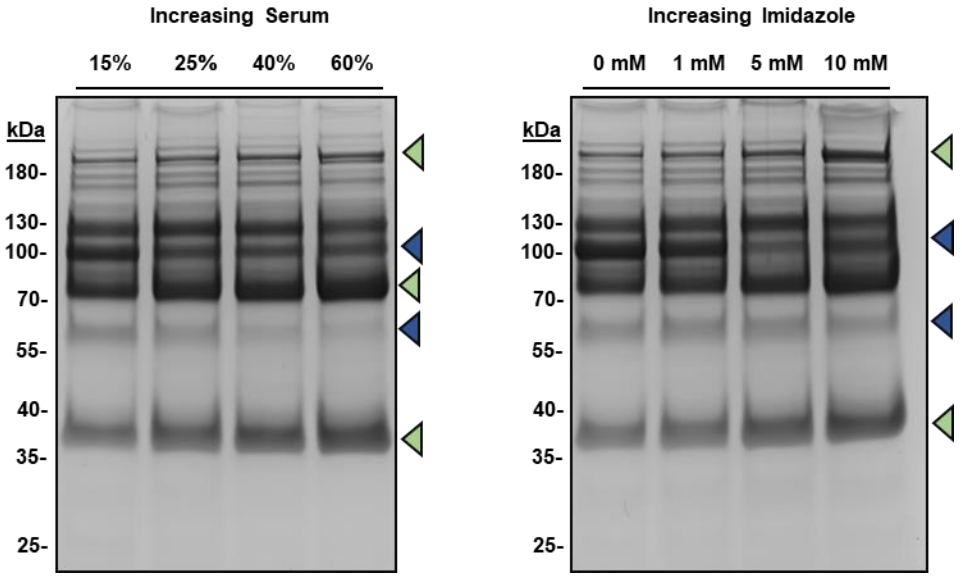

Figure 4.2. 1D gel electrophoresis of proteins retained and eluted from the Cu^{2+} -IDA-IMAC resin under (left) increasing percentages of pooled human serum (15 – 60%) and (right) increasing addition of imidazole to the sample prior to loading. Samples were incubated with the resin for 60 minutes with PBS as the diluent.

To further substantiate this hypothesis, we added increasing amounts of imidazole (final concentration of 0, 1, 5, 10, and 20 mM) to 0.5 mL of a serum solution containing 75 µL serum. Imidazole is able to coordinate to the copper center in Cu^{2+}-IDA with high affinity, thus serving as a model for a high-affinity protein binder.[17,18] Increasing the imidazole content yields a band pattern that resembles the changes observed by increasing serum volume, with similar bands increasing and decreasing accordingly. Thus, the changes accompanying increasing imidazole content suggest that on-column competition for the immobilized Cu^{2+} may indeed be what drives differential retention with protein loading. These data suggest serum loading may be potentially leveraged as a means of differentially enriching protein populations based on resin affinity.

Having observed population differences by gel electrophoresis, we aimed to identify the composition of the retained protein population under high and low serum percentages. 15% and 60% serum in a fixed volume of 0.5 mL in PBS were used as "low" and "high" serum amount, respectively. Each condition was run on the IMAC resin in quadruplicate and the eluents were analyzed by microflow liquid chromatography - tandem mass spectrometry (µLC-MS/MS) coupled with a protein identification via MSFragger. The workflow identified more than 200 (Table 4.1 and 4.2) proteins filtered at a 99% protein probability with a minimum of two peptides per ID. Differential binding between high and low serum percentages was assessed by filtering out proteins with any missing values, quantile normalizing the protein intensity values, applying LIMMA to generate a moderated t-statistic and subsequent p-value. The p-values were adjusted via the Benjamini-Hochberg method to adjust for multiple hypothesis testing. Proteins that showed +/- 0.75 $\log_2$ fold change ($\log_2$FC) and false discovery rate (FDR) adjusted p-value of less than 0.1 were considered differentially abundant indicating differential binding with respect to serum volume.

The differential binding analysis revealed serum proteins with elevated enrichment in the "high" serum samples with previous associations with copper. For instance, hemopexin (HP) showed elevated enrichment in the "high" serum samples. Hemopexin is an acute phase serum protein expressed by the liver that binds to heme with a strong affinity (K_d <1 pM).[19] The main role of hemopexin is to participate in heme recycling by binding and transporting to the LDL-receptor-related 1 (LRP1) protein for internalization.[20] Previous research indicates hemopexin's ability to bind divalent metals, such as Cu^{2+}.[21] The endocytosis of the heme-HPX complex increases cytosolic copper, while metal binding leads to a decrease in the heme-hemopexin complex stability.[22] Another example of a protein with elevated enrichment in the "high" serum samples is coagulation factor XII (F12); a previous study has shown that metal ions, including copper, may indeed activate F12-mediated coagulation.[23] Finally, peptide fragments of another identification, histidine-rich glycoprotein (HRG), have been shown to bind copper, and copper has been proposed to be associated with the antiangiogenic activity of the protein.[24,25]

Other proteins with elevated enrichment in the "high" serum samples include proteins associated with metabolic disorders in which copper misregulation has been implicated. Of note is alpha-2-HS-glycoprotein (AHSG), also referred to as fetuin-A (Fet-A), a glycoprotein synthesized in the liver involved in various processes including inhibition of ectopic calcification and fatty acid metabolism.[26] Moreover, elevated Fet-A has been associated with metabolic disorders including non-alcoholic fatty liver, type 2 diabetes, and metabolic syndrome, all of which present altered copper homeostasis.[27]

Table 4.1. Selected differentially abundant proteins from serum loading experiments. Magnitude of change between conditions are represented as absolute value of log_2 fold change over the contrasting condition.

Protein Name	*Absolute log_2 Fold Change*	*Adjusted p-value (FDR)*
Proteins More Abundant at Higher Serum Percentage		
Alpha-2-HS-glycoprotein (AHSG)	0.88	1.53E-07
Coagulation factor XII (F12)	1.08	5.15E-07
Coagulation factor V (F5)	0.91	9.37E-06
Coagulation factor XII (F12)	1.08	5.15E-07
Complement C1q subcomponent subunit A (C1QA)	0.85	3.41E-07
Complement C1q subcomponent subunit B (C1QB)	0.90	5.39E-06
Complement C1q subcomponent subunit C (C1QC)	0.80	1.69E-05
Complement component (C6)	0.90	2.37E-06
Complement factor H (FH)	0.94	1.55E-07
Hemopexin (HP)	0.84	2.03E-07
Histidine-rich glycoprotein (HRG)	0.91	1.24E-06
Proteins More Abundant at Lower Serum Percentage		
Albumin (HSA)	1.89	6.05E-06
Ceruloplasmin (CP)	1.26	2.35E-08
Complement component (C2)	0.89	1.47E-03
Complement component (C9)	2.47	1.24E-08
Complement factor B (CFB)	0.90	4.90E-07

The abundance of various members of the complement system is also dependent on the amount of serum applied. CFH, C1QA, C1QB, C1QC, and C6 were higher in abundance in the "high" serum experiment while CFB, C2, and C9 were higher in the "low" serum experiment. The association of complement factor H (FH) with copper has been observed within the context of inducing FH oligomerization.[28] These findings are interesting as the complement system is involved in immune system response to infections and an increase in copper levels has been observed at sites of infection.[29,30] The exact biological ramifications of copper accumulation at these sites are currently unknown. However, our experiments may offer the speculation towards dynamic differential copper binding directly to proteins of the complement system within these sites.

At higher serum volume, CP is inversely correlated with Factor V (F5) and Factor XII (F12), with CP being less enriched and the latter two showing increased enrichment. The opposite binding trend for CP and F5 is intriguing as both have been considered members of the same protein family and evolutionary linked.[31] While CP has been more extensively studied for its role in copper metabolism and transport, F5 has been suggested to bind copper in a 1:1 metal-protein ratio.[32] A study conducted with metals, including $Cu^{2+,}$ immobilized on a NTA-bound liposomes induced clotting at a higher rate than without the metals present.[23] This observation was attributed to an interaction between the immobilized metals and various contact pathway proteins. Along with the observed elevated enrichment of F12 in the "high" serum samples, our experiments may suggest possible metal/protein interactions in influencing contact pathway activation.

Unexpectedly, serum albumin showed a decrease in abundance with respect to increasing serum applied to the Cu^{2+}-IDA IMAC resin. Albumin is a highly abundant serum protein containing multiple metal binding sites including a Cys34, an N-terminal binding site (NBS), a multi-metal binding site (MBS), and an unknown fourth site. The NBS site (Asp-Ala-His) has an estimated dissociation constant of constant between log K_d = -11.18 to log K_d = -16.18 and transports copper in the bloodstream.[33] However, despite the high Cu^{2+} affinity of the NBS site, it is unknown if albumin is binding to the immobilized copper at the NBS site. If binding occurs at the NBS site, the formation of the tertiary complex between the Cu^{2+}-IDA IMAC resin and albumin may lead to significant reduction in binding strength due to the incomplete ATCUN-Cu^{2+} complex formation, preventing one or more coordinating sites from interacting with the immobilized Cu^{2+}. If the geometry of albumin binding is altered, then the actual binding strength may be lowered resulting in displacement by other proteins at higher serum volumes. This supports our hypothesis

that the application and comparison of varying serum percentages to the IMAC resin can be used to gauge the strength of ternary complex formation of serum proteins.

These studies illustrate important experimental considerations for implementing IMAC for metal binding protein/species discovery-based studies. To date no detailed and in-depth proteomic analysis of the protein population changes with respect to the total protein applied on an IMAC resin have been reported. While further focused studies are required to understand the dynamic nature of metal-protein binding and both the specifics and detailed thermodynamics of the protein identified, our studies demonstrate the potential for IMAC as a tool to gauge the relative strength of Cu^{2+} binding of species present in a complex biological matrix such as serum.

Table 4.2. Proteins $\log_2$ fold change, p-value, and adjusted p-value determined by LIMMA in the "high vs low" serum IMAC experiment.

Name	Gene	$\log_2$FC	p-value	Adjusted p-value
Alpha-1-acid glycoprotein 2	ORM2	-0.7815604	5.441E-05	9.664E-05
Alpha-1-antichymotrypsin	SERPINA3	-2.5221295	4.509E-09	5.366E-08
Alpha-1-antitrypsin	SERPINA1	-1.9132359	2.489E-10	4.936E-09
Alpha-1B-glycoprotein	A1BG	-0.7856805	1.332E-05	2.598E-05
Alpha-2-antiplasmin	SERPINF2	-0.7439557	0.0002398	0.0003944
Alpha-2-HS-glycoprotein	AHSG	0.8812936	2.18E-08	1.526E-07
Alpha-2-macroglobulin	A2M	0.1989208	0.0072627	0.0096029
Angiotensinogen	AGT	-0.606474	1.672E-05	3.159E-05
Antithrombin-III	SERPINC1	0.3874043	0.000242	0.0003944
Apolipoprotein A-I	APOA1	0.4608475	0.0002694	0.0004332
Apolipoprotein A-II	APOA2	-0.6853057	0.0067082	0.0089694
Apolipoprotein A-IV	APOA4	0.3365439	0.0002941	0.0004667
Apolipoprotein B-100	APOB	-1.0548668	2.132E-08	1.526E-07
Apolipoprotein C-I	APOC1	0.5783609	6.654E-05	0.0001165
Apolipoprotein C-III	APOC3	-0.904722	8.23E-06	1.689E-05
Apolipoprotein D	APOD	-0.5193244	8.475E-05	0.0001441
Apolipoprotein E	APOE	-0.2415409	0.0131902	0.0170612
Apolipoprotein L1	APOL1	-0.2764708	0.0629409	0.0720189
Apolipoprotein M	APOM	-0.3891482	0.0027534	0.0038548
Apolipoprotein(a)	LPA	0.3168261	0.1138526	0.1249934
Beta-2-glycoprotein 1	APOH	-1.4622977	1.038E-07	5.146E-07
Beta-Ala-His dipeptidase	CNDP1	-0.2184844	0.2663495	0.2855459
C4b-binding protein alpha chain	C4BPA	1.0964545	8.013E-09	7.335E-08

C4b-binding protein beta chain	C4BPB	1.0947488	1.298E-07	6.177E-07
Carboxypeptidase B2	CPB2	0.340328	0.0015414	0.002237
Carboxypeptidase N subunit 2	CPN2	-1.3258361	1.384E-07	6.221E-07
CD5 antigen-like	CD5L	-0.4219037	0.0004607	0.0007029
Ceruloplasmin	CP	-1.2644103	1.581E-09	2.352E-08
Clusterin	CLU	0.7321953	6.062E-07	2.004E-06
Coagulation factor V	F5	0.9097185	4.175E-06	9.374E-06
Coagulation factor XII	F12	1.0797074	9.964E-08	5.146E-07
Coagulation factor XIII B chain	F13B	1.0627102	4.454E-07	1.606E-06
Complement C1q subcomponent subunit A	C1QA	0.8475108	5.73E-08	3.409E-07
Complement C1q subcomponent subunit B	C1QB	0.9016046	1.903E-06	5.391E-06
Complement C1q subcomponent subunit C	C1QC	0.7946907	8.217E-06	1.689E-05
Complement C1r subcomponent	C1R	0.6853489	3.06E-06	7.003E-06
Complement C1s subcomponent	C1S	0.6356677	4.623E-07	1.618E-06
Complement C2	C2	-0.88607	0.0009889	0.001471
Complement C3	C3	-0.4000137	4.814E-05	8.68E-05
Complement C4-A	C4A	0.0605905	0.3220992	0.3422304
Complement C4-B	C4B	-0.5164368	1.761E-06	5.112E-06
Complement C5	C5	0.7283356	9.188E-08	4.97E-07
Complement component C6	C6	0.9020297	7.373E-07	2.371E-06
Complement component C7	C7	-0.2408932	0.0469103	0.0552705
Complement component C8 alpha chain	C8A	0.2005167	0.0427012	0.0508144
Complement component C8 beta chain	C8B	0.2981406	0.0001279	0.0002144
Complement component C8 gamma chain	C8G	0.1811221	0.0557994	0.0644673
Complement component C9	C9	-2.4702309	7.322E-10	1.245E-08
Complement factor B	CFB	-0.8990739	8.652E-08	4.903E-07
Complement factor H	CFH	0.936249	2.349E-08	1.553E-07
Complement factor H-related protein 2	CFHR2	0.8940878	1.036E-06	3.162E-06
Complement factor I	CFI	0.615663	1.099E-06	3.269E-06
Fibrinogen alpha chain	FGA	1.0212776	7.574E-07	2.372E-06
Fibronectin	FN1	0.857345	2.29E-06	6.057E-06
Fibulin-1	FBLN1	0.9217881	2.512E-06	6.229E-06
Ficolin-3	FCN3	0.7594743	3.372E-07	1.254E-06
Gelsolin	GSN	0.789087	1.809E-08	1.435E-07
Haptoglobin	HP	-3.2881159	2.235E-13	2.66E-11
Haptoglobin-related protein	HPR	-0.6533742	2.482E-07	1.019E-06
Hemoglobin subunit alpha	HBA1	-0.3645925	0.0010445	0.0015345
Hemoglobin subunit beta	HBB	-0.2356528	0.0104789	0.0137032
Hemopexin	HPX	0.8328513	3.245E-08	2.033E-07
Heparin cofactor 2	SERPIND1	-1.3357927	5.933E-09	5.884E-08
Histidine-rich glycoprotein	HRG	0.9064745	3.225E-07	1.238E-06
Hyaluronan-binding protein 2	HABP2	0.2103043	0.0303923	0.0369049
Immunoglobulin heavy constant alpha 1	IGHA1	-1.1622858	5.376E-09	5.816E-08
Immunoglobulin heavy constant alpha 2	IGHA2	-1.8249161	2.051E-10	4.88E-09
Immunoglobulin heavy constant delta	IGHD	-0.6139776	7.292E-06	1.549E-05
Immunoglobulin heavy constant gamma 1	IGHG1	0.6501783	1.796E-07	7.635E-07
Immunoglobulin heavy constant gamma 2	IGHG2	0.2090736	0.0785577	0.0890321
Immunoglobulin heavy constant gamma 3	IGHG3	0.8840913	9.737E-09	8.276E-08
Immunoglobulin heavy constant gamma 4	IGHG4	-0.0084904	0.8923819	0.8999445
Immunoglobulin heavy constant mu	IGHM	-0.624745	1.473E-05	2.827E-05

Immunoglobulin heavy variable 1-18	IGHV1-18	0.6280449	0.000413	0.0006466
Immunoglobulin heavy variable 2-26	IGHV2-26	0.3795384	0.0145945	0.0186746
Immunoglobulin heavy variable 3-11	IGHV3-11	0.2423238	0.0308243	0.0370514
Immunoglobulin heavy variable 3-64	IGHV3-64	0.1703752	0.0952093	0.1068859
Immunoglobulin heavy variable 3-66	IGHV3-66	0.1918919	0.36947	0.3856748
Immunoglobulin heavy variable 3-7	IGHV3-7	0.3023876	0.0152098	0.019255
Immunoglobulin heavy variable 5-51	IGHV5-51	0.3334193	0.0033453	0.0046289
Immunoglobulin J chain	JCHAIN	-0.6801785	5.483E-07	1.864E-06
Immunoglobulin kappa constant	IGKC	0.4633292	7.152E-06	1.547E-05
Immunoglobulin kappa variable 1-5	IGKV1-5	0.4378089	0.0034621	0.0047355
Immunoglobulin kappa variable 3-20	IGKV3-20	0.1871151	0.0169955	0.0212891
Immunoglobulin kappa variable 4-1	IGKV4-1	0.195071	0.0540739	0.0630863
Immunoglobulin lambda-like polypeptide 1	IGLL1	0.340224	0.0004489	0.0006938
Immunoglobulin lambda variable 1-51	IGLV1-51	0.4105235	0.0016516	0.0023679
Immunoglobulin lambda variable 3-19	IGLV3-19	0.5518321	1.166E-05	2.351E-05
Immunoglobulin lambda variable 3-21	IGLV3-21	0.3870641	0.0999163	0.1111219
Immunoglobulin lambda variable 4-69	IGLV4-69	0.4804008	0.0007329	0.001104
Immunoglobulin lambda variable 6-57	IGLV6-57	0.3630513	0.0211507	0.0262181
Insulin-like growth factor-binding protein complex acid labile subunit	IGFALS	0.7652923	2.495E-06	6.229E-06
Inter-alpha-trypsin inhibitor heavy chain H1	ITIH1	-1.9234379	8.752E-11	3.782E-09
Inter-alpha-trypsin inhibitor heavy chain H2	ITIH2	-2.1606379	1.172E-10	3.782E-09
Inter-alpha-trypsin inhibitor heavy chain H3	ITIH3	-1.660864	2.773E-09	3.667E-08
Inter-alpha-trypsin inhibitor heavy chain H4	ITIH4	-0.0420399	0.5747628	0.5896274
Kallistatin	SERPINA4	0.7400055	1.412E-07	6.221E-07
Keratin, type I cytoskeletal 10	KRT10	-0.1056798	0.6721256	0.6836149
Keratin, type I cytoskeletal 9	KRT9	-0.2954098	0.3694058	0.3856748
Keratin, type II cytoskeletal 1	KRT1	-0.2273773	0.4380461	0.4532825
Kininogen-1	KNG1	0.5305291	1.327E-05	2.598E-05
Lipopolysaccharide-binding protein	LBP	0.6850354	2.867E-06	6.763E-06
N-acetylmuramoyl-L-alanine amidase	PGLYRP2	-1.94339	1.271E-10	3.782E-09
Plasma kallikrein	KLKB1	0.5573041	2.021E-05	3.758E-05
Plasma protease C1 inhibitor	SERPING1	-1.1262555	2.053E-06	5.681E-06
Plasma serine protease inhibitor	SERPINA5	0.6007343	2.185E-05	4.001E-05
Plasminogen	PLG	-0.1338847	0.1892661	0.2047515
Properdin	CFP	1.3541013	2.662E-06	6.465E-06
Protein AMBP	AMBP	-0.4299844	0.0020359	0.0028842
Prothrombin	F2	0.2134237	0.0051165	0.0069189
Serotransferrin	TF	-0.7110688	2.456E-06	6.229E-06
Serum albumin	ALB	-1.8918274	2.285E-06	6.057E-06
Serum amyloid A-4 protein	SAA4	-0.003246	0.9730159	0.9730159
Serum amyloid P-component	APCS	-0.5826737	8.047E-05	0.0001388
Serum paraoxonase/arylesterase 1	PON1	-0.2454884	0.0226818	0.0278262
Transthyretin	TTR	-1.0758239	2.734E-07	1.084E-06
Vitamin D-binding protein	GC	0.3390712	0.1144898	0.1249934
Vitamin K-dependent protein S	PROS1	0.5881293	5.48E-06	1.208E-05
Vitronectin	VTN	0.6710731	2.898E-06	6.763E-06

4.3.3 Protein Population Is Different with IMAC Enrichment – Wilson Disease

In comparing abundancies between CTL and WD samples, the traditional workflow produced 8 differentially abundant proteins while the IMAC workflow produced 36 (Figure 4.3A-C), indicating that IMAC may allow for enrichment of a protein population that is otherwise missed in the absence of this step (Table 4.3 and 4.4). Several proteins, including alpha-2-macroglobin (a2M), ceruloplasmin (CP), complement component C7 (C7), apolipoprotein L1 (APOL1), and amyloid P-component (APCS) were found to be differentially abundant in WD plasma in both workflows. In addition to differential abundances in proteins between CTL and WD samples, in analyzing the collective identifications made across both CTL and WD samples, we identified that the IMAC procedure enriched for seven proteins that were otherwise below detection via the traditional workflow. Conversely, three proteins were identified with the traditional workflow that were excluded from detection in the IMAC-enriched samples (Table 4.5).

In both the traditional and IMAC workflow, various apolipoproteins (designated with the APO- prefix) were observed to be differentially abundant. Apolipoproteins are mainly synthesized in the liver and intestines and participate in triglyceride and cholesterol transport.[34] Apolipoproteins are potentially connected to WD in that aberrant cholesterol, Very-Low-Density-Lipoprotein (VLDL), and lipid metabolism have been observed in patients as well as in *Atp7b-/-* knockout mice, model of WD.[35,36] In the traditional workflow, APOL1 showed a decrease in abundance in WD plasma. In contrast, the IMAC workflow showed a decrease in both APOL1 and APOC1 alongside the decreased abundance of additional apolipoproteins, APOA1, APOA4, APOB, and APOH (beta-2-glycoprotein), compared to healthy controls. Furthermore, APOF was detected in CTL samples but not detected in WD plasma in both the traditional and IMAC

workflows. Apolipoproteins have been previously associated with hepatic injury. For instance, a previous proteomics found a decrease in APOE and APOL1 in the plasma of patients with different stages of liver fibrosis due to chronic hepatitis C.[37] Additionally, changes to apolipoproteins have been loosely associated with copper. For instance, an inverse correlation was observed between copper and apolipoproteins, with elevated APOA1, APOA2, and APOE identified in rats with copper deficiency.[38] Copper has also been shown to bind to and be reduced by APOB within the context of LDL oxidation.[39] Moreover, certain lipoproteins have been suggested to utilize copper for ferroxidase activity, such as the > 800 kDa protein "ferroxidase II".[40,41] While many questions remain regarding how apolipoprotein and lipoprotein, serum copper, and hepatic metabolism are interconnected, our studies alongside the previous studies may highlight their interplay as potential markers in diseases such as WD.

Several proteins were determined to be differentially abundant uniquely in the IMAC workflow, such as Transthyrien (TTR), haptoglobin, and paraoxonase/arylesterase 1 (PON1). Several studies have pointed to conformational changes to TTR in the presence of several metals, with metals mediating potential enzymatic function as well as even neuroprotective roles such as amyloid-beta binding.[42–45] Haptoglobin's primary role is to bind to free hemoglobin leading to the clearance and degradation of hemoglobin and a decrease in haptoglobin is often associated with hemolytic anemia which results from the lysing of red blood cells.[46,47] Hemolytic anemia is a common presentation of WD with approximately 10-15% of WD patients developing the complication. PON1 has been shown to potentiate CCl_4 liver damage in mice transfected with human PON1, suggesting a protective function against oxidative damage.[48] These data suggest retention of biologically relevant trends as there is precedence of the aforementioned proteins being differentially abundant in WD.[49]

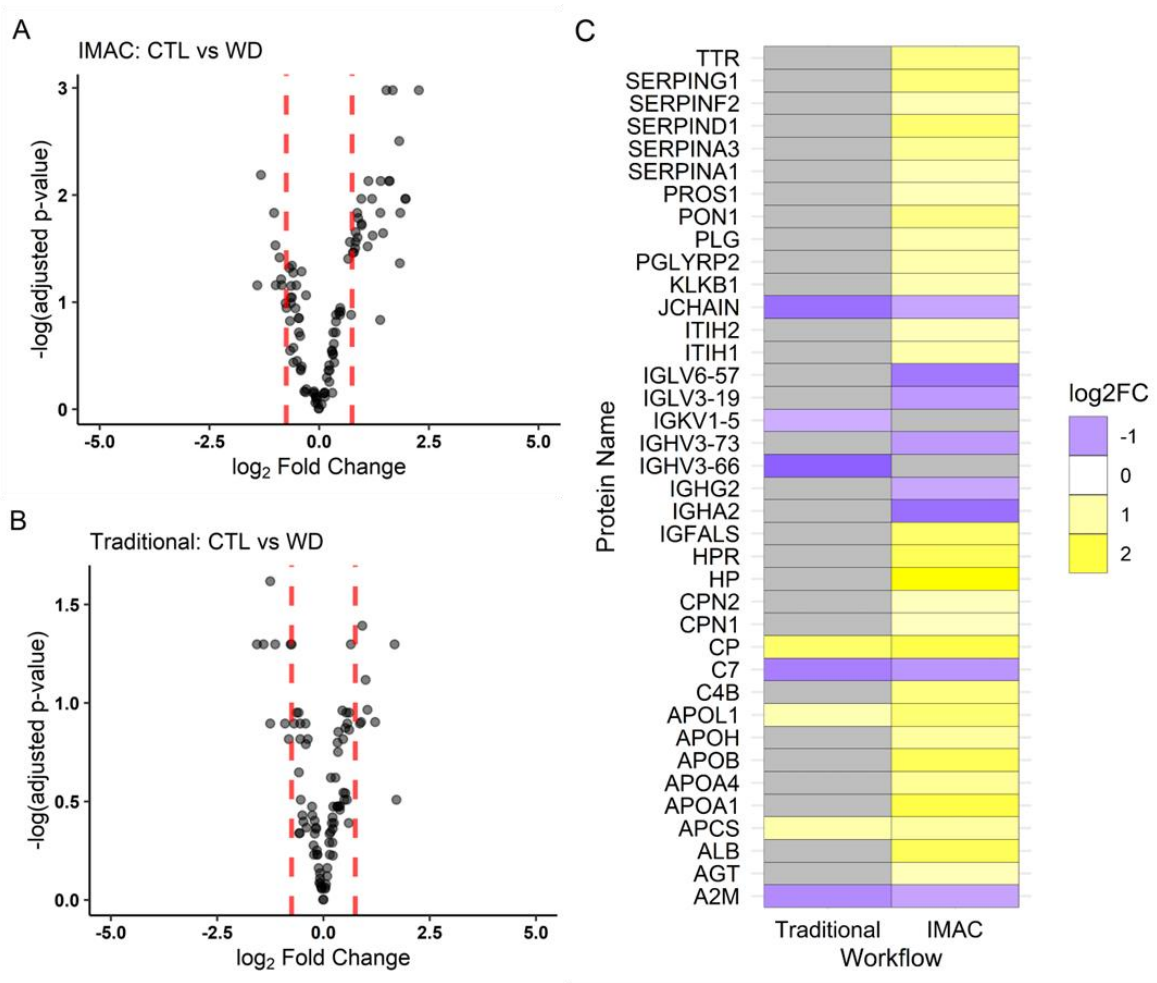

Figure 4.3. Volcano plots (-$\log_{10}$ of adjusted p-value[q-value] vs $\log_2$FC) of each contrast made. (A) IMAC: Healthy control (CTL) vs WD (B) traditional: Healthy controls (CTL) vs WD. Vertical dashed lines represent logFC change cutoffs at -0.75 and 0.75. Negative $\log_2$ fold changes in A and B indicate proteins were less abundant in healthy than WD plasma. (C) Heatmap of differentially abundant proteins found in the traditional and IMAC workflows. Blue indicates proteins found more abundant in the WD plasma. Yellow indicates proteins found less abundant in WD plasma. Grey indicates proteins not found differentially abundant.

One explanation for the difference observed in the IMAC flow compared to the traditional IMAC workflow when contrasting heathy vs Wilson disease plasma is that non-CP bound copper in WD is influencing protein-Cu^{2+}-IDA binding dynamics. While the exact concentration of

cheatable metal micronutrients in the blood is poorly understood, the amount of cheatable copper has been shown to be increased in WD. The increase in cheatable copper could lead to an increase in metalated serum proteins and influence the ability to bind to the Cu^{2+} loaded IMAC resin, resulting in "non-specific" copper interaction with a one or several residues on the surface.[50] For example, if the site of metal interaction is already occupied prior to addition to the Cu^{2+} loaded IMAC resin, ternary complex formation may be inhibited resulting in no IMAC retention or a shift towards a "non-specific" copper binding location. The change of interaction site may result in a decrease in Cu^{2+}-IDA interaction strength and therefore lower enrichment efficacy. Lastly, it should be noted that proteins enriched on the Cu^{2+}-IDA IMAC resin do not confirm biologically relevant copper binding and follow up spectroscopic studies are required to validate specific Cu^{2+} binding.

Table 4.3. Proteins log_2 fold change, p-value, and adjusted p-value determined by LIMMA in the "Healthy vs Wilson disease" plasma IMAC experiment.

Name	Gene	log2FC	p-value	Adjusted p-value
Alpha-1-antichymotrypsin	SERPINA3	1.2057737	0.0011215	0.0108284
Alpha-1-antitrypsin	SERPINA1	0.8665951	0.0023738	0.0146665
Alpha-1B-glycoprotein	A1BG	0.1729757	0.4061916	0.5040691
Alpha-2-antiplasmin	SERPINF2	0.8733716	0.0057907	0.0248516
Alpha-2-HS-glycoprotein	AHSG	0.1074643	0.6501399	0.7123873
Alpha-2-macroglobulin	A2M	-0.9024695	0.0118945	0.0382853
Angiotensinogen	AGT	0.8300886	0.0066401	0.0273241
Apolipoprotein A-I	APOA1	1.9601585	0.0013514	0.0108284

Apolipoprotein A-IV	APOA4	1.2189156	0.0053201	0.0238248
Apolipoprotein B-100	APOB	1.8367094	0.0142707	0.0432318
Apolipoprotein L1	APOL1	1.588574	0.000646	0.0073927
Beta-2-glycoprotein 1	APOH	1.1222144	0.0005245	0.0073927
C4b-binding protein alpha chain	C4BPA	0.6615565	0.0126295	0.0394193
C4b-binding protein beta chain	C4BPB	0.4897313	0.0626968	0.1218447
Carboxypeptidase N catalytic chain	CPN1	0.7660597	0.0103326	0.0343309
Carboxypeptidase N subunit 2	CPN2	0.7925008	0.0099558	0.0341817
CD5 antigen-like	CD5L	-0.7657245	0.0475232	0.1019768
Ceruloplasmin	CP	1.9711125	0.0013667	0.0108284
Clusterin	CLU	0.3808149	0.0703153	0.130968
Coagulation factor XII	F12	0.3444491	0.2659546	0.3650598
Coagulation factor XIII A chain	F13A1	-0.1400319	0.625325	0.7000921
Complement C1q subcomponent subunit A	C1QA	-0.4630288	0.0807036	0.1408893
Complement C1q subcomponent subunit B	C1QB	-0.4653018	0.0805838	0.1408893
Complement C1q subcomponent subunit C	C1QC	-0.6209449	0.0406016	0.0900079
Complement C1r subcomponent	C1R	0.2379697	0.3442389	0.4337943
Complement C1r subcomponent-like protein	C1RL	-0.4314137	0.1324989	0.2067787
Complement C1s subcomponent	C1S	0.310554	0.2182207	0.3079005
Complement C2	C2	-0.0701839	0.7231423	0.7678727
Complement C3	C3	0.2907263	0.1980122	0.2872571
Complement C4-A	C4A	-0.0084789	0.9824475	0.9824475
Complement C4-B	C4B	1.4563614	0.0048349	0.0226362
Complement C5	C5	0.211418	0.3401343	0.4337943
Complement component C6	C6	0.4504519	0.0648068	0.123613
Complement component C7	C7	-1.0292443	0.0021082	0.0146665
Complement component C8 alpha chain	C8A	0.319099	0.1208521	0.1915042
Complement component C8 beta chain	C8B	0.4785677	0.0561077	0.1133156
Complement component C8 gamma chain	C8G	0.2933023	0.1886058	0.281542
Complement factor B	CFB	0.2287124	0.2896246	0.3874199
Complement factor H	CFH	-0.1169658	0.5660379	0.677546
Complement factor I	CFI	0.1206057	0.622912	0.7000921
Fibrinogen alpha chain	FGA	-0.0735158	0.7187755	0.7678727
Fibrinogen beta chain	FGB	-0.0604189	0.7719328	0.8113172
Fibrinogen gamma chain	FGG	-0.0971242	0.6425699	0.7116634
Fibronectin	FN1	-0.6648724	0.19234	0.2830146
Fibulin-1	FBLN1	-0.6494368	0.0410716	0.0900079
Ficolin-3	FCN3	-0.3981406	0.3013794	0.3979754
Gelsolin	GSN	0.1237168	0.6007379	0.695236
Haptoglobin	HP	2.2698427	2.524E-05	0.0010509
Haptoglobin-related protein	HPR	1.8484812	0.0024207	0.0146665
Hemoglobin subunit alpha	HBA1	-0.3392009	0.5722962	0.677546
Hemoglobin subunit beta	HBB	-0.3090613	0.5910215	0.6917638
Hemopexin	HPX	-0.0379733	0.8589164	0.8846839
Heparin cofactor 2	SERPIND1	1.6055527	0.0005673	0.0073927
Histidine-rich glycoprotein	HRG	0.0540089	0.8834253	0.9009189
Immunoglobulin heavy constant alpha 1	IGHA1	-0.5870675	0.1757425	0.2661982
Immunoglobulin heavy constant alpha 2	IGHA2	-1.4102117	0.0286658	0.0695445
Immunoglobulin heavy constant gamma 1	IGHG1	-0.2978279	0.0376035	0.0860703
Immunoglobulin heavy constant gamma 2	IGHG2	-0.853902	0.02758	0.0692863

Immunoglobulin heavy constant gamma 3	IGHG3	0.7272422	0.0724775	0.130968
Immunoglobulin heavy constant gamma 4	IGHG4	0.3003482	0.6252975	0.7000921
Immunoglobulin heavy constant mu	IGHM	-0.0902832	0.831604	0.8652042
Immunoglobulin heavy variable 1-18	IGHV1-18	-0.6476708	0.0485211	0.1019933
Immunoglobulin heavy variable 2-5	IGHV2-5	-0.7440961	0.0560044	0.1133156
Immunoglobulin heavy variable 3-11	IGHV3-11	-0.4653766	0.120495	0.1915042
Immunoglobulin heavy variable 3-64	IGHV3-64	-0.58733	0.2693645	0.3650598
Immunoglobulin heavy variable 3-66	IGHV3-66	-0.6667278	0.0887759	0.1499003
Immunoglobulin heavy variable 3-73	IGHV3-73	-0.9883023	0.027126	0.0692863
Immunoglobulin heavy variable 5-51	IGHV5-51	-0.6206004	0.0154701	0.0455264
Immunoglobulin J chain	JCHAIN	-0.8673158	0.0230765	0.0609456
Immunoglobulin kappa constant	IGKC	-0.4029628	0.0185793	0.0517207
Immunoglobulin kappa variable 1-5	IGKV1-5	-0.6786975	0.0167039	0.0477918
Immunoglobulin kappa variable 1-6	IGKV1-6	-0.5381423	0.0575594	0.1140119
Immunoglobulin kappa variable 2-24	IGKV2-24	-0.2928308	0.5354362	0.6488227
Immunoglobulin kappa variable 3-20	IGKV3-20	-0.5918588	0.0195695	0.0530436
Immunoglobulin kappa variable 4-1	IGKV4-1	-0.5209185	0.0290331	0.0695445
Immunoglobulin lambda variable 3-19	IGLV3-19	-0.997569	0.0077141	0.0294277
Immunoglobulin lambda variable 6-57	IGLV6-57	-1.3267728	0.000315	0.0064895
Insulin-like growth factor-binding protein complex acid labile subunit	IGFALS	1.6771842	1.216E-05	0.0010509
Inter-alpha-trypsin inhibitor heavy chain H1	ITIH1	0.9633426	0.0034106	0.0184892
Inter-alpha-trypsin inhibitor heavy chain H2	ITIH2	0.8195276	0.0087955	0.0312391
Inter-alpha-trypsin inhibitor heavy chain H3	ITIH3	0.2322566	0.4524004	0.554729
Inter-alpha-trypsin inhibitor heavy chain H4	ITIH4	0.3753274	0.1189792	0.1915042
Kallistatin	SERPINA4	0.3156479	0.2102012	0.3007044
Keratin, type I cytoskeletal 10	KRT10	-0.5040133	0.2534984	0.3528424
Keratin, type I cytoskeletal 9	KRT9	-0.4206144	0.3453508	0.4337943
Keratin, type II cytoskeletal 1	KRT1	-0.4222254	0.3214696	0.4191312
Kininogen-1	KNG1	0.7005534	0.0068973	0.0273241
Lumican	LUM	0.1302567	0.7036925	0.7629508
N-acetylmuramoyl-L-alanine amidase	PGLYRP2	0.9683542	0.0037088	0.0191001
Plasma kallikrein	KLKB1	0.8871477	0.0028627	0.0163808
Plasma protease C1 inhibitor	SERPING1	1.5307302	3.061E-05	0.0010509
Plasminogen	PLG	0.9587818	0.0013658	0.0108284
Probable non-functional immunoglobulin heavy variable 3-35	IGHV3-35	-0.6378658	0.0301308	0.0705335
Protein AMBP	AMBP	0.3336286	0.1591689	0.2446924
Prothrombin	F2	1.3909114	0.0851238	0.1461292
Selenoprotein P	SELENOP	-0.0064273	0.9734758	0.9824475
Serotransferrin	TF	0.4727659	0.0715648	0.130968
Serum albumin	ALB	1.8232434	0.0001214	0.0031272
Serum amyloid P-component	APCS	1.105361	0.0082102	0.0302017
Serum paraoxonase/arylesterase 1	PON1	1.3934817	0.0022286	0.0146665
Transthyretin	TTR	1.4008766	0.0006324	0.0073927
Vitamin K-dependent protein S	PROS1	0.8287166	0.0045159	0.0221496
Vitronectin	VTN	0.3818835	0.0912257	0.1515524

Table 4.4. Proteins log_2 fold change, p-value, and adjusted p-value determined by LIMMA in the "Healthy vs Wilson disease" plasma traditional experiment.

Name	Gene	log2FC	p-value	Adjusted p-value
Afamin	AFM	-0.6901792	0.0342823	0.127081
Alpha-1-acid glycoprotein 1	ORM1	0.5613528	0.034062	0.127081
Alpha-1-acid glycoprotein 2	ORM2	0.4636132	0.0512155	0.1523566
Alpha-1-antichymotrypsin	SERPINA3	0.1364449	0.3861694	0.5108326
Alpha-1-antitrypsin	SERPINA1	-0.2684278	0.1786012	0.3351723
Alpha-1B-glycoprotein	A1BG	-0.1719699	0.2980538	0.4352532
Alpha-2-antiplasmin	SERPINF2	0.1440845	0.3401146	0.4605153
Alpha-2-HS-glycoprotein	AHSG	-0.0826842	0.6923575	0.7767914
Alpha-2-macroglobulin	A2M	-1.136372	0.003832	0.0503201
Angiotensinogen	AGT	0.0871127	0.6662656	0.7567461
Antithrombin-III	SERPINC1	0.3471306	0.0425905	0.1399402
Apolipoprotein A-I	APOA1	0.1487475	0.4685754	0.5887044
Apolipoprotein A-II	APOA2	-0.0046749	0.985114	0.9950434
Apolipoprotein A-IV	APOA4	-0.3955663	0.2810258	0.4287217
Apolipoprotein B-100	APOB	0.2192948	0.4976525	0.5945978
Apolipoprotein C-I	APOC1	0.6431551	0.0042846	0.0503201
Apolipoprotein C-III	APOC3	1.0343554	0.0129411	0.1082345
Apolipoprotein D	APOD	-0.0701838	0.7519449	0.8235587
Apolipoprotein E	APOE	-0.3697438	0.0529936	0.1523566
Apolipoprotein L1	APOL1	0.9143009	0.0008799	0.0404767
Apolipoprotein M	APOM	0.515357	0.0378329	0.1338704
Beta-2-glycoprotein 1	APOH	-0.0816063	0.635648	0.7309951
C4b-binding protein alpha chain	C4BPA	0.6055226	0.0193914	0.1118124
Carboxypeptidase N subunit 2	CPN2	0.5363808	0.017388	0.1118124
CD5 antigen-like	CD5L	-0.8143296	0.0516	0.1523566
Ceruloplasmin	CP	1.673051	0.0049226	0.0503201
Clusterin	CLU	0.2332114	0.1727557	0.3351723
Coagulation factor XII	F12	0.4902864	0.1395478	0.3098527
Complement C1q subcomponent subunit B	C1QB	-0.5462054	0.0322997	0.127081
Complement C1q subcomponent subunit C	C1QC	-0.5449149	0.0514696	0.1523566
Complement C1r subcomponent	C1R	-0.2036282	0.3403808	0.4605153
Complement C1s subcomponent	C1S	-0.1458351	0.4813932	0.5887044
Complement C2	C2	-0.207501	0.2366281	0.3958143
Complement C3	C3	0.0352927	0.8546536	0.8784707
Complement C4-A	C4A	-0.472006	0.2438779	0.4006565
Complement C4-B	C4B	0.8573585	0.0272769	0.127081
Complement C5	C5	0.0587738	0.7694249	0.8327893
Complement component C7	C7	-1.253036	0.0002617	0.0240766
Complement component C8 beta chain	C8B	0.4677304	0.1208835	0.285161
Complement component C9	C9	-0.2235766	0.4863211	0.5887044
Complement factor B	CFB	-0.0469822	0.8300888	0.8678201
Complement factor H	CFH	-0.1757336	0.2842611	0.4287217
Complement factor I	CFI	-0.113189	0.5919845	0.6893997
Corticosteroid-binding globulin	SERPINA6	-0.1564578	0.4381963	0.5599175

Fibrinogen alpha chain	FGA	0.3855429	0.192976	0.3481135
Fibrinogen beta chain	FGB	0.3663645	0.1797424	0.3351723
Fibrinogen gamma chain	FGG	0.3860971	0.1628834	0.3330061
Fibronectin	FN1	1.7151779	0.1442629	0.3098527
Gelsolin	GSN	-0.146429	0.4742103	0.5887044
Haptoglobin	HP	1.2133616	0.0244111	0.1247679
Hemoglobin subunit alpha	HBA1	-0.5703401	0.3234813	0.4578504
Hemoglobin subunit beta	HBB	-0.556006	0.3285677	0.4580034
Hemopexin	HPX	-0.2670332	0.2104763	0.3716624
Heparin cofactor 2	SERPIND1	0.3244594	0.1679599	0.3351723
Histidine-rich glycoprotein	HRG	-0.4148136	0.0597493	0.1616745
Immunoglobulin heavy constant alpha 1	IGHA1	-1.2536788	0.0340049	0.127081
Immunoglobulin heavy constant gamma 1	IGHG1	-0.4234856	0.0284276	0.127081
Immunoglobulin heavy constant gamma 2	IGHG2	-0.9048745	0.0345329	0.127081
Immunoglobulin heavy constant gamma 3	IGHG3	0.5514956	0.1480537	0.3098527
Immunoglobulin heavy constant gamma 4	IGHG4	0.5949662	0.2592508	0.4069588
Immunoglobulin heavy constant mu	IGHM	-0.49467	0.2141099	0.3716624
Immunoglobulin heavy variable 3-66	IGHV3-66	-1.5663792	0.00364	0.0503201
Immunoglobulin J chain	JCHAIN	-1.409213	0.0022638	0.0503201
Immunoglobulin kappa constant	IGKC	-0.5838446	0.0194456	0.1118124
Immunoglobulin kappa variable 1-5	IGKV1-5	-0.7742245	0.002387	0.0503201
Immunoglobulin kappa variable 3-20	IGKV3-20	-0.7473508	0.0045137	0.0503201
Immunoglobulin kappa variable 4-1	IGKV4-1	-0.6299586	0.0176195	0.1118124
Inter-alpha-trypsin inhibitor heavy chain H1	ITIH1	0.3418321	0.067403	0.1771737
Inter-alpha-trypsin inhibitor heavy chain H2	ITIH2	0.2130475	0.2233355	0.3804974
Inter-alpha-trypsin inhibitor heavy chain H4	ITIH4	0.2168006	0.2961029	0.4352532
Kallistatin	SERPINA4	0.3186034	0.1821588	0.3351723
Keratin, type I cytoskeletal 9	KRT9	-0.0962861	0.7394339	0.8196135
Keratin, type II cytoskeletal 1	KRT1	-0.2320254	0.4078928	0.5285372
Kininogen-1	KNG1	0.088334	0.5831348	0.6878
Leucine-rich alpha-2-glycoprotein	LRG1	-0.533895	0.1481904	0.3098527
N-acetylmuramoyl-L-alanine amidase	PGLYRP2	-0.0578408	0.797637	0.8532861
Pigment epithelium-derived factor	SERPINF1	-0.0014154	0.9950434	0.9950434
Plasma protease C1 inhibitor	SERPING1	0.2807875	0.0987763	0.2391427
Plasminogen	PLG	0.331272	0.0569095	0.1586569
Protein AMBP	AMBP	-0.0368367	0.8593735	0.8784707
Prothrombin	F2	0.4441166	0.0142307	0.1091019
Retinol-binding protein 4	RBP4	0.8842175	0.0230778	0.1247679
Serotransferrin	TF	0.0483636	0.8166154	0.8635473
Serum albumin	ALB	0.1763092	0.0977409	0.2391427
Serum amyloid A-4 protein	SAA4	0.211064	0.388677	0.5108326
Serum amyloid P-component	APCS	0.9921593	0.0082843	0.0762157
Serum paraoxonase/arylesterase 1	PON1	0.5147102	0.1249039	0.2872789
Thyroxine-binding globulin	SERPINA7	-0.5764833	0.0879957	0.2248779
Transthyretin	TTR	0.6051863	0.0401239	0.1367185
Vitamin D-binding protein	GC	0.1974474	0.2609844	0.4069588
Vitronectin	VTN	0.1707371	0.3143502	0.4518784
Zinc-alpha-2-glycoprotein	AZGP1	0.2465035	0.2578534	0.4069588

Interestingly, sulfhydryl oxidase 1 (QSOX1) was identified exclusively in the IMAC workflow. QSOX1 is involved in disulfide bond formation and positively correlated with pancreatic and breast tumor cell growth.[51] QSOX1 may act in a protective manner during periods of increased oxidative stress, as observed in in PC12 and overexpression studies with MCF-7 cells.[52] To date, no correlation between QSOX1 or Cu^{2+} binding has been observed, although an increase in both extracellular non-CP bound copper and oxidative stress has been documented in WD. The mechanism of QSOX1 in protecting against oxidative stress remains elusive and further investigation is necessary to support a relation between copper, QSOX1, and WD. However, it may be possible for QSOX1 to bind directly to non-CP bound copper in the extracellular space and reduce the ability for ROS generation. Additionally, the IMAC workflow revealed beta-Ala-His peptidase (CNDP1) to be present only in the healthy plasma samples. CNDP1 acts to degrade the dipeptide B-Ala-His (carnosine), which is has been associated with protection against reactive species generation and has been suggested to be directly involved in maintaining copper homeostasis.[53,54] CNDP1 knockout studies lead to an increase in carnosine levels and our data imply that CNDP1 levels are lower in WD which could be linked to a systemic reaction to increased oxidative stress by excess copper in the blood. Taken together, these two protein hits demonstrate the potential value of the IMAC workflow for enriching otherwise overlooked proteins with implications in both disease pathology as well as in biomarker discovery.

A common concern with enrichment techniques is the added variability they may impart. For each additive step in a workflow, artificial variability is added onto already complex biological variability that confound data and ultimately reduce significant conclusions. In our results, both the protein identifications as well as the patterns of differential abundance with Wilson's disease follow the same trends in both workflows. This indicates that the IMAC workflow does not occlude

information obtained in the traditional workflow. Importantly, while preserving biological trends in the traditional workflow, the addition of IMAC also brings to light proteins that are otherwise absent in the traditional workflow (QSOX1 and CNDP1) with potential disease relevance.

Table 4.5. Proteins found exclusively in either healthy or Wilson disease plasma in the IMAC and traditional (no IMAC) workflow.

Protein Name	***Condition***
Traditional Workflow	
Apolipoprotein F	CTL
Carboxypeptidase N catalytic chain	CTL
Insulin-like growth factor-binding protein complex acid labile subunit	CTL
IMAC Workflow	
Apolipoprotein F	CTL
Beta-Ala-His dipeptidase	CTL
Coagulation factor XI	CTL
IgGFc-binding protein	WD
Immunoglobulin heavy variable 3-20	WD
Phosphatidylcholine-sterol acyltransferase	WD
Probable non-functional immunoglobulin heavy variable 3-38	WD
Sulfhydryl oxidase 1	WD
High vs Low	
Attractin	LOW
Corticosteroid-binding globulin	LOW
Serum amyloid A-1 protein	HIGH
Immunoglobulin heavy variable 1-2	HIGH
Hepatocyte growth factor-like protein	HIGH
Proteoglycan 4	HIGH

4.3.4 Protein Population with IMAC Enrichment – Bariatric Surgery

Copper dysregulation has also been observed in bariatric surgery, also commonly referred to as gastric bypass, which is typically preformed on morbidly obese patients. There are multiple procedures involving removing a portion of the stomach (sleeve gastrectomy) or dividing the

intestines by creating a small pouch, redirecting the one part of the divided intestine to the created stomach pouch, therefore bypassing a large portion of the intestinal tract.[55] While primarily conducted to aid in weight loss, comorbidities including hypertension and type 2 diabetes are reduced post gastric bypass. Furthermore, current research suggests the application of gastric bypass towards treatment of diabetes post-surgery in alpha cell GLP-1 production leading to an increase in alpha cell insulin secretion.[56] However, despite the increasing application of gastric bypass, an imbalance in micronutrients, such as a decrease in copper, has been reported in patients' post-surgery suggesting an alteration in metal metabolism.

To this end, we sought to extend the application of the IMAC workflow to mouse serum collected post vertical sleeve gastronomy. LC-MS/MS results revealed over 160 proteins above a 99% protein probability and greater than two peptides per ID (Table 4.6). Out of the proteins identified 56 proteins were considered differentially abundant, with 27 and 29 proteins being more and less abundant post VSG surgery, respectively. Of particular interest are transthyretin, catalase, adiponectin, and superoxide dismutase [Cu-Zn] (SOD). Transthyretin is a ~55 kDa blood protein involved in the binding and transport of hormones produced by the thyroid.[60] Lower levels were observed in VSG surgery mice which has associated with insulin resistance in obese mice.[61,62] Catalase was also observed to be lower in VSG mice compared to obese mice, which has been observed in cardiac mitochondria of mice fed a high fat diet to compensate for the increase in levels of H_2O_2 generated by fatty-acid oxidation.[63] Moreover, an increase in SOD has been shown in obese mouse plasma,[64] which agrees well with our data with sham surgery mice showing higher SOD than post VSG.

Adiponectin was found to be in lower abundance in VSG mouse serum by the IMAC procedure. Adiponectin is a 29 kDa protein primary produced by adipose tissue and involved in

regulating glucose transport as well as increasing fatty acid oxidation.[65] Lower levels are observed in the obese and conversely adiponectin levels are increased with weight loss and improved fitness of obese individuals with type 2 diabetes.[66,67] Moreover, adiponectin levels increase gradually post gastric bypass to levels near lean adiponectin levels 12 months after surgery.[68] Adiponectin can exist in multiple forms low molecular weight (LMW) trimers and hexamers and a 16 mer high molecular weight (HMW) form which arranged as a hexamier of trimers.[69] The HMW form of adiponectin is more biologically active than the LMW forms, as suggested by the greater potency of HMW adiponectin on AMPK phosphorylation in C2C12 monocytes.[70] It is possible for that discrepancy between our IMAC workflow data and literature could be due to a difference in binding capacity of the LMW compared to HMW species. If there is a shift in the ratio between the LMW species to HMW adiponectin in mice post gastric bypass surgery and HMW forms lose or have reduced Cu^{2+} binding capacity this could result in the appearance of lower adiponectin levels in VSG mouse serum when there is more biologically active HMW adiponectin present.

Table 4.6. Proteins $\log_2$ fold change, p-value, and adjusted p-value determined by LIMMA in the "Obese vs VSG" serum IMAC experiment.

Name	logFC	p-value	Adjusted p-value
Haptoglobin	7.4050979	1.57E-07	2.58E-05
Ig gamma-1 chain C region secreted form	3.267218	0.0001351	0.008374338
Ig gamma-2B chain C region	3.0141278	0.0001854	0.008374338
Ig heavy chain V region 6.96	2.4079208	0.000238	0.008374338
Ig kappa chain V-II region 17S29.1	2.7378653	0.0002553	0.008374338
Ig kappa chain V-V region MOPC 173	2.351468	0.0005675	0.015510821
Ig heavy chain V region 1-62-3	2.1850157	0.0008807	0.020632445
Ig heavy chain V region 36-65	1.9656301	0.0018311	0.034837791
Ig kappa chain V-II region 26-10	2.0756769	0.0020366	0.034837791
Ig kappa chain V-V region MOPC 41	2.1047152	0.0023367	0.034837791
Ig heavy chain V region VH558 A1/A4	2.0164109	0.0023271	0.034837791
Ig kappa chain V-V region K2 (Fragment)	2.244043	0.0027926	0.035400841
Ig lambda-2 chain C region	2.3807028	0.0036444	0.035400841
Hemopexin	1.5549084	0.0038386	0.035400841

Ig kappa chain V19-17	2.3370782	0.003914	0.035400841
Ig kappa chain V-V region L6 (Fragment)	2.0787035	0.0041013	0.035400841
Antithrombin-III	-1.099373	0.0029961	0.035400841
Transthyretin	-2.1544724	0.0043463	0.035639969
Complement C1q subcomponent subunit A	1.6563894	0.0036431	0.035400841
Ig heavy chain V-III region J606	1.6105673	0.0048262	0.037690504
Serine protease inhibitor A3M	-1.1541126	0.0037637	0.035400841
Ig lambda-1 chain C region	1.5598848	0.0058007	0.042874923
Immunoglobulin kappa constant	1.712702	0.0065358	0.042874923
Serum paraoxonase/arylesterase 1	-1.5692169	0.0079169	0.047505268
Adiponectin	-1.2925522	0.0076737	0.047505268
Inter-alpha-trypsin inhibitor heavy chain H3	1.4683273	0.0093069	0.052632062
Betaine--homocysteine S-methyltransferase 1	-1.4798946	0.006481	0.042874923
Apolipoprotein C-I	-2.3173021	0.0101653	0.053777865
Catalase	-0.9789949	0.0064472	0.042874923
Leukemia inhibitory factor receptor	-1.5164424	0.0081107	0.047505268
Extracellular superoxide dismutase [Cu-Zn]	-1.5673811	0.0096859	0.05294977
Interleukin-1 receptor accessory protein	-1.6985221	0.0120004	0.059029091
Ig kappa chain V-V region L7 (Fragment)	1.6325963	0.0135093	0.059879173
Peroxiredoxin-2	-1.139866	0.0125977	0.059029091
Ig gamma-2A chain C region secreted form	2.0642089	0.0147667	0.062095852
Plasma kallikrein	-1.3070532	0.0133721	0.059879173
Hepatocyte growth factor activator	-1.1748882	0.0111437	0.057111491
Serine protease inhibitor A3K	-1.6781681	0.0154835	0.063482461
Insulin-like growth factor-binding protein complex acid labile subunit	-1.1341345	0.0125964	0.059029091
Gelsolin	-1.265023	0.0175149	0.066226083
Ig lambda-1 chain V region	1.2415104	0.0180275	0.066226083
Prothrombin	-1.2669794	0.0187043	0.066226083
Inhibitor of carbonic anhydrase	-1.0879933	0.0189808	0.066226083
Carboxypeptidase B2	0.8147835	0.0143889	0.062095852
Ig heavy chain V region AC38 205.12	1.6142692	0.0193832	0.066226083
Alpha-1-antitrypsin 1-4	-1.5636954	0.0192433	0.066226083
Coagulation factor XIII B chain	-0.8329402	0.0163611	0.065444211
Beta-2-glycoprotein 1	-1.1419812	0.0218084	0.072991458
Heparin cofactor 2	-0.9311606	0.0177022	0.066226083
Alpha-1-antitrypsin 1-1	-1.2898206	0.0263874	0.084853496
Beta-2-microglobulin	-1.2640104	0.031799	0.094818745
Hemoglobin subunit alpha	-1.0409598	0.0343183	0.099441331
Glutathione peroxidase 3	-0.9158487	0.0296374	0.093042566
Secreted phosphoprotein 24	-0.7125335	0.0249334	0.081781665
Mannan-binding lectin serine protease 2	-0.8103279	0.0308129	0.093580009

Apolipoprotein A-II	-1.6526484	0.0396825	0.110303773
Fibrinogen gamma chain	1.18417	0.0413862	0.113122257
Vitamin K-dependent protein Z	-0.7977482	0.0300686	0.093042566
Ig alpha chain C region	1.4035742	0.0449271	0.114546163
Fibrinogen beta chain	1.169551	0.0453041	0.114546163
Carboxypeptidase N subunit 2	-0.915503	0.0451011	0.114546163
Hemoglobin subunit beta-1	-0.9944538	0.0478795	0.115371961
Carboxypeptidase N catalytic chain	-0.868202	0.0453994	0.114546163
Ig lambda-3 chain C region	1.3330725	0.0448697	0.114546163
Fibrinogen alpha chain	1.1492687	0.0505582	0.115371961
Carbonic anhydrase 2	-0.962873	0.0486237	0.115371961
Apolipoprotein A-I	-1.0537759	0.0526452	0.116673247
Alpha-1-antitrypsin 1-2	-1.175484	0.0513546	0.115371961
Platelet-activating factor acetylhydrolase	0.6316112	0.0345619	0.099441331
Ig kappa chain V-V region MOPC 149	1.5614038	0.0495643	0.115371961
Phosphatidylinositol-glycan-specific phospholipase D	-0.8419516	0.0496575	0.115371961
Mannose-binding protein A	-0.7890314	0.0563936	0.123314045
Coagulation factor XII	-0.8302726	0.0662464	0.133461892
Ig kappa chain V-VI region NQ2-17.4.1	1.1572734	0.0671699	0.133461892
H-2 class I histocompatibility antigen, Q10 alpha chain	-1.0800469	0.06751	0.133461892
Apolipoprotein E	-0.9790454	0.0675447	0.133461892
Complement component C9	-0.7987049	0.0509928	0.115371961
Retinol-binding protein 4	-1.3017441	0.0610586	0.128389863
Coagulation factor XIII A chain	-0.6625359	0.0495253	0.115371961
Ig heavy chain V region 441	0.7656584	0.0666313	0.133461892
Purine nucleoside phosphorylase	-0.5249556	0.0361042	0.102087649
Flavin reductase (NADPH)	-0.8561174	0.0851388	0.162357765
Ig heavy chain V region 23	1.3362239	0.0870289	0.164054548
Complement component C8 beta chain	-0.7660713	0.0906289	0.168899388
Aldehyde dehydrogenase 1A1	-0.6400794	0.0573895	0.123840599
Complement component C8 gamma chain	-0.7981938	0.0941856	0.172678289
Ig heavy chain V region 3-6	0.6551072	0.0693377	0.135373544
Sorbitol dehydrogenase	-0.8031453	0.0610635	0.128389863
Complement component C8 alpha chain	-0.7235287	0.0958154	0.172678289
Alpha-1-antitrypsin 1-5	-0.7647677	0.1110268	0.193601655
Inter alpha-trypsin inhibitor, heavy chain 4	0.6514943	0.1072766	0.191232261
CD5 antigen-like	0.6681803	0.1089429	0.192114335
Phospholipid transfer protein	-0.5705564	0.0826507	0.159467284
Immunoglobulin J chain	0.7591795	0.126175	0.21369981
Apolipoprotein A-IV	-0.6815716	0.1320749	0.221023366
Phosphatidylcholine-sterol acyltransferase	-0.5514682	0.0950296	0.172678289

Murinoglobulin-1	-0.6109476	0.1582385	0.254422763
Apolipoprotein C-III	-0.9264893	0.1405149	0.23044449
Pregnancy zone protein	-0.775292	0.1646096	0.262096851
Pancreatic alpha-amylase	-0.685584	0.1569565	0.254422763
Selenoprotein P	-0.5727984	0.1740817	0.269333994
Carbonic anhydrase 3	-0.5914787	0.1263956	0.21369981
Mannan-binding lectin serine protease 1	-0.4349368	0.1121473	0.193601655
Ig gamma-3 chain C region	0.5023697	0.1936039	0.290244367
Inter-alpha-trypsin inhibitor heavy chain H2	-0.5313581	0.1946761	0.290244367
Carboxylesterase 1C	-0.7386439	0.1738623	0.269333994
Ig kappa chain V-III region PC 2880/PC 1229	0.8435565	0.2098466	0.31004368
Ficolin-1	-0.4366859	0.1360557	0.225385184
Ceruloplasmin	0.6013466	0.2242708	0.324234547
Protein AMBP	0.4618391	0.2289937	0.326564876
Apolipoprotein M	-0.6082065	0.2253826	0.324234547
Alpha-2-HS-glycoprotein	-0.4392741	0.2436251	0.344435533
Complement factor D	-0.7868844	0.2548525	0.357229153
Albumin	-0.7477476	0.2625077	0.361775268
Alpha-2-antiplasmin	-0.467642	0.2611323	0.361775268
Immunoglobulin heavy constant mu	0.5632228	0.2815237	0.384749085
Nucleoside diphosphate kinase B	-0.4689514	0.1720983	0.269333994
Complement factor I	-0.4476583	0.287388	0.389517652
Lumican	-0.5209387	0.2222003	0.324234547
Inter-alpha-trypsin inhibitor heavy chain H1	-0.3974859	0.3300188	0.440025123
Vitamin D-binding protein	0.4238623	0.2978984	0.400453576
Complement factor H	0.3389519	0.3567334	0.468034253
Complement C5	-0.3712046	0.3730127	0.485508598
Bisphosphoglycerate mutase	-0.5639997	0.1919835	0.290244367
Coagulation factor V	-0.3353389	0.1885462	0.288986729
Plasma protease C1 inhibitor	-0.3197178	0.4158616	0.532822677
Epidermal growth factor receptor	-0.6144225	0.3456812	0.457191246
Serum amyloid A-4 protein	-0.2825093	0.4566595	0.567364823
Clusterin	-0.2557891	0.4931366	0.599069668
Complement C1s-A subcomponent	-0.2821223	0.379954	0.4906492
Histidine-rich glycoprotein	-0.2419991	0.5167994	0.623199224
Kininogen-1	-0.2277798	0.5720482	0.674934533
N-acetylmuramoyl-L-alanine amidase	-0.2521084	0.4402107	0.55534279
Complement C4-B	0.1717687	0.6408363	0.734945115
Vitronectin	-0.1497076	0.7087996	0.784995126
Fibronectin	0.2051365	0.665407	0.752598309
Serotransferrin	0.1361783	0.7246378	0.792270715

Protein Z-dependent protease inhibitor	-0.238654	0.4861848	0.595032126
Complement C3	0.1413617	0.7076397	0.784995126
Apolipoprotein B-100	-0.1906012	0.637059	0.734945115
Ig kappa chain V-VI region NQ2-6.1	0.1070136	0.8776546	0.902666403
Fetuin-B	-0.0963981	0.8042656	0.850964841
C4b-binding protein	-0.054246	0.8930076	0.909647495
Complement factor B	0.0598194	0.8748938	0.902666403
Actin, cytoplasmic 1	0.0200307	0.9582558	0.958255771
Plasminogen	0.087337	0.8806501	0.902666403
C-reactive protein	-0.2247241	0.4321969	0.549459677
Glyceraldehyde-3-phosphate dehydrogenase	-0.2588412	0.4512618	0.564938492
Angiotensinogen	-0.1400211	0.7605121	0.819726687
Properdin	-0.1192479	0.7131968	0.784995126
Sulfhydryl oxidase 1	-0.0753128	0.8132614	0.852047942
Alcohol dehydrogenase 1	-0.2824716	0.5445652	0.651888264
L-lactate dehydrogenase A chain	-0.0981625	0.7347656	0.798023592
Glutathione S-transferase P 1	-0.2255659	0.6641943	0.752598309
Complement C1r-A subcomponent	-0.0811192	0.764745	0.819726687
Coagulation factor X	-0.3903687	0.6238895	0.725658712
Transcobalamin-2	-0.1555831	0.5497651	0.653344052
Extracellular matrix protein 1	0.0306667	0.9264538	0.932137592
Vitamin K-dependent protein S	-0.1913704	0.4858713	0.595032126
Complement C2	-0.0618098	0.7969577	0.84870825
Afamin	-0.3236691	0.81568	0.852047942
Glutathione S-transferase Mu 1	-0.0332862	0.9130187	0.924290557
Pyruvate kinase PKM	-0.1210917	0.6087031	0.713052167
Fumarylacetoacetase	-0.1064834	0.7042403	0.784995126

4.4 Conclusions and Outlook

Copper is essential for maintaining biological homeostasis and must be tightly regulated to preserve proper physiology or risk disease onset. Despite the importance of copper in biological processes, much remains to be understood with respect to the dynamics of copper regulation, particularly in extracellular environments, in part due to the dearth of techniques to study the proteins involved, many of which may have low abundance. To this end, we employed Cu^{2+}-IMAC

coupled with a proteomics workflow as a means of enriching for copper-associated parameters. We optimized the conditions for metal-binding protein enrichment on a Cu^{2+}-IDA-IMAC resin via a solid-phase extraction set up that is amenable to high-throughput workflows. We found that distinct protein changes occur with increasing serum volume applied and attributed these differences to protein competition for the immobilized Cu^{2+}, resulting in an increase of stronger Cu^{2+} binding proteins at higher volumes, pointing the possibility of using IMAC to differentially enrich for proteins based on their Cu^{2+} affinities. We also contrasted healthy plasma to plasma from patients diagnosed with WD using a proteomics workflow with and without the addition of Cu^{2+}-IMAC. The integration of the IMAC workflow both preserved expected protein differences as well as identified additional differentially abundant proteins when compared to the no-IMAC workflow. The differences in proteins found differentially abundant between both workflows suggest IMAC provides an additional layer of information regarding protein-copper binding or as pseudo-depletion step of highly abundant serum proteins. Analysis of Cu^{2+}-IDA-IMAC enriched serum proteins from obese and post-bariatric surgery mice reveal several differentially enriched proteins – extending the use of IMAC towards understanding Cu^{2+} dynamics in bariatric surgery patients. Differential enrichment of adiponectin, a serum protein that is dependent on oligomerization for bioactivity, may indicate IMAC's ability to enrich specific proteoforms based on their Cu^{2+} interaction ability. We note that the proteins identified in the IMAC workflow only suggest the propensity of Cu^{2+} binding *in vivo*, and further structural as well as biological studies are required to validate whether Cu^{2+} ions bind to the proteins and whether these proteins are valid markers for copper status. Nevertheless, Cu^{2+} IMAC technique enables a rapid and efficient means to assess differences in the global profile of the serum proteome based on their copper affinities and could provide insight into how these modulations influence copper regulation.

4.5 Materials and Methods

4.5.1 Cu^{2+} - IDA – IMAC Enrichment of Pooled Human Serum Proteins

0.25 mL of IDA-IMAC (BioRad) resin was placed in a fritted centrifuge tube, washed with 5 mL of nanopure water, loaded with 1 mL of 0.5 M $CuSO_4$, washed with 5 mL nanopure water to remove unbound Cu^{2+}, equilibrated with 3 mL of loading buffer (PBS or BTS), then incubated with various percentages of pooled human serum (Sigma Aldrich) diluted to 500 µL with loading buffer (50, 75, 125, 250, 300 µL of serum corresponding to 10, 15, 25, 50, and 60 percent serum, respectively) . The proteins were incubated with the Cu^{2+}-IDA-IMAC resin by slowly rotating for 0, 5, 30, and 60 min. Unbound species were washed out with 10 mL wash buffer (PBS or BTS); a final wash of 0.5 mL was collected separately. Retained proteins were then eluted with four 0.5 mL additions of 50 mM EDTA dissolved in water and pH adjusted to ~8 with HCl. The protein concentration of each fraction was determined by the Bradford method. For imidazole competition experiments, imidazole was added to 75 µL of pooled human serum diluted to 500 µL in PBS to reach a final concentration of 1, 5, 10, and 20 mM imidazole and incubated for 60 min before washing and eluting with EDTA as described previously. For the unloaded IDA-IMAC experiments, the same procedure was followed with 30% serum being used for protein loading.

4.5.2 Cu^{2+}-IDA-IMAC enrichment of plasma samples from healthy and WD subjects as well as serum collected from mice post bariatric and sham surgery

Human plasma samples from healthy individuals (biological replicates, n = 4) and individuals with Wilson's disease (biological replicates, n = 4) were obtained by Dr Valentina

Medici (UC Davis). All subjects provided written informed consent prior to participation following the Declaration of Helsinki. The protocol was approved by UCD Institutional Review Board (protocol # 818454). 75 µL of each sample was diluted to 500 µL in PBS and the IMAC enrichment procedure was carried out as described above with an incubation time of 60 min. Serum from obese (n = 3) and post-bariatric surgery was provided by Professor Bethany Cummings (UC Davis).

4.5.3 Gel Electrophoresis

12.5 ug of protein from the elution fractions was prepared with 2-mecaptoethanol (BME) and LDS sample buffer and heated at 70^0C for 15 min before loading into a 4-12% Bis-Tris SDS-PAGE gel and run at 100 V for 60 min. After separation, the gel was stained with Imperial protein stain (Pierce) and subsequent destaining with water.

4.5.4 S-trap protein digestion of serum and plasma samples

An aliquot of the elution fractions from the IMAC experiments corresponding to 300 µg protein (quantified by the Bradford assay) were concentrated on a 3 kDa MWCO filter (MilliporeSigma™ Amicon™ Ultra) and washed with PBS to remove EDTA. The concentrated proteins were then digested following the S-trap procedure (ProtiFi). In brief, equal volume of 100 mM triethyl ammonium bicarbonate (TEAB) with 10% SDS was added to the concentrated protein samples in equal volume, reduced with 5 mM dithiothreitol for 15 min at 55 ºC, alkylated with 20 mM iodoacetamide for 30 min at room temperature in the dark, then acidified with H_3PO_4 to 1.2%. To the resulting protein solution, six volumes of 90:10 MeOH/1 M TEAB (100 mM final TEAB concentration) was added and inverted immediately. Following colloidal formation, the samples were added to the S-trap, spun at 4000 rpm, and washed with 90:10 MeOH/TEAB solution. The trapped proteins were then digested with 125 µL of 50 mM TEAB containing 10 µg of trypsin

overnight at 37 ºC. After overnight digestion, 125 µL of 50 mM TEAB was added and incubated at 37 ºC for an additional hour. The tryptic peptides were then eluted with TEAB, 0.1% formic acid (FA), and 50% ACN/0.1% FA and dried via vacuum centrifugation. The traditional workflow followed the same procedure described above without the IMAC enrichment and MWCO step.

4.5.5 µLC-MS/MS Analysis

Dried peptides were reconstituted in 0.1% FA and quantified via a peptide fluorescent assay (Pierce). Peptide concentrations were normalized to the lowest sample concentration. 10 µg of peptide were analyzed by microflow liquid chromatography connected online to the mass spectrometer (Ultimate 3000 and Orbitrap-HF). Peptides were loaded onto a 1 mm x 150 mm PepMap C18 column and separated at a flow rate of 50 µL/min with a gradient ranging from 3% acetonitrile to 50% acetonitrile over 50 min, a ramp to 95% for 5 min, followed by a ramp down to 1% over 5 min, followed by a hold at 1% for 5 min. MS1 and MS2 data were acquired on Xcalibur (Thermo Fisher Scientific). MS spray voltage was set to 4 kV; capillary temperature set to 320 ºC; sheath, auxiliary, and spare gas maintained at 35, 5, and 0, respectively; and S-Lens set to 40. MS1 spectra were collected at a resolution of 60,000 with a AGC target of 3e6 and a max ion injection time of 50 ms. The mass range of MS1 was 360-1300 Da. MS2 spectra were collected in using data-dependent acquisition (DDA) with the top 12 ions from the MS1 scan being selected for fragmentation with dynamic exclusion set to 15 s. The normalized collision energy was set to 28%. For MS2 spectra, the AGC was set to 1e5 with a maximum ion injection time of 86 ms and spectra were acquired at a resolution of 15,000.

4.5.6 Peptide and Protein Identification and Quantification

Raw LC-MS/MS files were searched using MSFragger in FragPipe.[71,72] Spectra were searched against the Uniprot protein database (*homo sapiens*) concatenated with the reverse protein sequences (decoys) and common contaminates. A "closed" search was conducted with a precursor tolerance set to -50 and 50 ppm and fragment mass tolerance set to 20 ppm. The search was constrained to semi tryptic enzymatic cleavage with a maximum of two missed cleavages with cysteine alkylation (+57.021460) set as a fixed modification and methione oxidation (+15.994900), pyro-glutamic acid or loss of ammonia at the peptide N-terminus (-17.0265), and loss of water on glutamate on peptide N-terminus (-18.0106) as variable modifications. The reverse-decoy method was used to estimate FDR. Peptide (PSM) and protein FDR was set to 0.01. Label free quantification was conducted using the MaxLFQ algorithm employing "match between runs (MBR)"[58] and "normalization of ions" between experiment groups.[73] A minimum of two ions were required for protein quantification and a retention time tolerance of one minute was used for both feature detection and MBR.

4.5.7 Differential Protein Abundance Detection

Data analysis was conducted in R. The output table containing the protein abundance values ("Unique MaxLFQ Intensity") produced by MaxLFQ with MBR was used for differential protein abundance determination. Proteins that contained only one unique peptide and contained missing values in any condition were removed. The remaining proteins were median-normalized and the p-value was calculated using the "moderated t-statistic" in the LIMMA R package. The p-value was adjusted with Benjamini-Hochberg FDR method. Proteins showing a $\log_2$ fold change ($\log_2$FC) of +/- 0.75 and adjusted p-value less than 0.1 were considered differentially abundant.

4.6 References

(1) Heffern, M. C.; Park, H. M.; Au-Yeung, H. Y.; Van de Bittner, G. C.; Ackerman, C. M.; Stahl, A.; Chang, C. J. In Vivo Bioluminescence Imaging Reveals Copper Deficiency in a Murine Model of Nonalcoholic Fatty Liver Disease. *Proc Natl Acad Sci U S A* **2016**, *113* (50), 14219–14224. https://doi.org/10.1073/pnas.1613628113.

(2) Festa, R. A.; Thiele, D. J. Copper: An Essential Metal in Biology. *Current Biology* **2011**, *21* (21), R877–R883. https://doi.org/https://doi.org/10.1016/j.cub.2011.09.040.

(3) Tainer, J. A.; Getzoff, E. D.; Richardson, J. S.; Richardson, D. C. Structure and Mechanism of Copper, Zinc Superoxide Dismutase. *Nature* **1983**, *306* (5940), 284–287. https://doi.org/10.1038/306284a0.

(4) Krishnamoorthy, L.; Cotruvo, J. A.; Chan, J.; Kaluarachchi, H.; Muchenditsi, A.; Pendyala, V. S.; Jia, S.; Aron, A. T.; Ackerman, C. M.; Wal, M. N. V.; Guan, T.; Smaga, L. P.; Farhi, S. L.; New, E. J.; Lutsenko, S.; Chang, C. J. Copper Regulates Cyclic-AMP-Dependent Lipolysis. *Nat Chem Biol* **2016**, *12* (8), 586–592. https://doi.org/10.1038/nchembio.2098.

(5) Harder, N. H. O.; Lee, H. P.; Flood, V. J.; San Juan, J. A.; Gillette, S. K.; Heffern, M. C. Fatty Acid Uptake in Liver Hepatocytes Induces Relocalization and Sequestration of Intracellular Copper. *Front Mol Biosci* **2022**, *9* (April), 1–13. https://doi.org/10.3389/fmolb.2022.863296.

(6) Harris, E. D. A Requirement for Copper in Angiogenesis. *Nutr Rev* **2004**, *62* (2), 60–64. https://doi.org/10.1301/nr.2004.feb.60-64.

(7) Gerosa, C.; Fanni, D.; Congiu, T.; Piras, M.; Cau, F.; Moi, M.; Faa, G. Liver Pathology in Wilson's Disease: From Copper Overload to Cirrhosis. *J Inorg Biochem* **2019**, *193*, 106–111. https://doi.org/https://doi.org/10.1016/j.jinorgbio.2019.01.008.

(8) O'Sullivan, J. J.; Medici, V.; Heffern, M. C. A Caged Imidazopyrazinone for Selective Bioluminescence Detection of Labile Extracellular Copper(Ii) . *Chem Sci* **2022**, *13* (15), 4352–4363. https://doi.org/10.1039/d1sc07177g.

(9) Geyer, P. E.; Holdt, L. M.; Teupser, D.; Mann, M. Revisiting Biomarker Discovery by Plasma Proteomics. *Mol Syst Biol* **2017**, *13* (9), 942. https://doi.org/10.15252/msb.20156297.

(10) Ignjatovic, V.; Geyer, P. E.; Palaniappan, K. K.; Chaaban, J. E.; Omenn, G. S.; Baker, M. S.; Deutsch, E. W.; Schwenk, J. M. Mass Spectrometry-Based Plasma Proteomics: Considerations from Sample Collection to Achieving Translational Data. *J Proteome Res* **2019**, *18* (12), 4085–4097. https://doi.org/10.1021/acs.jproteome.9b00503.

(11) PORATH, J.; CARLSSON, J. A. N.; OLSSON, I.; BELFRAGE, G. Metal Chelate Affinity Chromatography, a New Approach to Protein Fractionation. *Nature* **1975**, *258* (5536), 598–599. https://doi.org/10.1038/258598a0.

(12) Song, Y.; Zhang, H.; Chen, C.; Wang, G.; Zhuang, K.; Cui, J.; Shen, Z. Proteomic Analysis of Copper-Binding Proteins in Excess Copper-Stressed Rice Roots by Immobilized Metal Affinity Chromatography and Two-Dimensional Electrophoresis. *BioMetals* **2014**, *27* (2), 265–276. https://doi.org/10.1007/s10534-014-9707-x.

(13) Wang, Y.; Tsang, C.-N.; Xu, F.; Kong, P.-W.; Hu, L.; Wang, J.; Chu, I. K.; Li, H.; Sun, H. Bio-Coordination of Bismuth in Helicobacter Pylori Revealed by Immobilized Metal Affinity Chromatography. *Chem Commun (Camb)* **2015**, *51* (92), 16479–16482. https://doi.org/10.1039/c5cc04958j.

(14) Smith, S. D.; She, Y. M.; Roberts, E. A.; Sarkar, B. Using Immobilized Metal Affinity Chromatography, Two-Dimensional Electrophoresis and Mass Spectrometry to Identify

Hepatocellular Proteins with Copper-Binding Ability. *J Proteome Res* **2004**, *3* (4), 834–840. https://doi.org/10.1021/pr049941r.

(15) Wang, F.; Chmil, C.; Pierce, F.; Ganapathy, K.; Gump, B. B.; MacKenzie, J. A.; Mechref, Y.; Bendinskas, K. Immobilized Metal Affinity Chromatography and Human Serum Proteomics. *Journal of Chromatography B* **2013**, *934*, 26–33. https://doi.org/https://doi.org/10.1016/j.jchromb.2013.06.032.

(16) Porath, J.; Olin, B. Immobilized Metal Affinity Adsorption and Immobilized Metal Affinity Chromatography of Biomaterials. Serum Protein Affinities for Gel-Immobilized Iron and Nickel Ions. *Biochemistry* **1983**, *22* (7), 1621–1630. https://doi.org/10.1021/bi00276a015.

(17) Porath, J. Immobilized Metal Ion Affinity Chromatography. *Protein Expr Purif* **1992**, *3* (4), 263–281. https://doi.org/https://doi.org/10.1016/1046-5928(92)90001-D.

(18) Bornhorst, J. A.; Falke, J. J. Purification of Proteins Using Polyhistidine Affinity Tags. *Methods Enzymol* **2000**, *326*, 245–254. https://doi.org/10.1016/s0076-6879(00)26058-8.

(19) Tolosano, E.; Altruda, F. Hemopexin: Structure, Function, and Regulation. *DNA Cell Biol* **2002**, *21* (4), 297–306. https://doi.org/10.1089/104454902753759717.

(20) Tolosano, E.; Fagoonee, S.; Morello, N.; Vinchi, F.; Fiorito, V. Heme Scavenging and the Other Facets of Hemopexin. *Antioxid Redox Signal* **2009**, *12* (2), 305–320. https://doi.org/10.1089/ars.2009.2787.

(21) Mauk, M. R.; Rosell, F. I.; Lelj-Garolla, B.; Moore, G. R.; Mauk, A. G. Metal Ion Binding to Human Hemopexin. *Biochemistry* **2005**, *44* (6), 1864–1871. https://doi.org/10.1021/bi0481747.

(22) Smith, A.; Rish, K. R.; Lovelace, R.; Hackney, J. F.; Helston, R. M. Role for Copper in the Cellular and Regulatory Effects of Heme-Hemopexin. *BioMetals* **2009**, *22* (3), 421–437. https://doi.org/10.1007/s10534-008-9178-z.

(23) MUTCH, N. J.; WATERS, E. K.; MORRISSEY, J. H. Immobilized Transition Metal Ions Stimulate Contact Activation and Drive Factor XII-Mediated Coagulation. *Journal of Thrombosis and Haemostasis* **2012**, *10* (10), 2108–2115. https://doi.org/https://doi.org/10.1111/j.1538-7836.2012.04890.x.

(24) Magrì, A.; Grasso, G.; Corti, F.; Finetti, F.; Greco, V.; Santoro, A. M.; Sciuto, S.; la Mendola, D.; Morbidelli, L.; Rizzarelli, E. Peptides Derived from the Histidine-Proline Rich Glycoprotein Bind Copper Ions and Exhibit Anti-Angiogenic Properties. *Dalton Transactions* **2018**, *47* (28), 9492–9503. https://doi.org/10.1039/c8dt01560k.

(25) La Mendola, D.; Magrì, A.; Santoro, A. M.; Nicoletti, V. G.; Rizzarelli, E. Copper(II) Interaction with Peptide Fragments of Histidine-Proline-Rich Glycoprotein: Speciation, Stability and Binding Details. *J Inorg Biochem* **2012**, *111*, 59–69. https://doi.org/10.1016/j.jinorgbio.2012.02.027.

(26) Jahnen-Dechent, W.; Heiss, A.; Schäfer, C.; Ketteler, M.; Towler, D. A. Fetuin-A Regulation of Calcified Matrix Metabolism. *Circ Res* **2011**, *108* (12), 1494–1509. https://doi.org/10.1161/CIRCRESAHA.110.234260.

(27) Bourebaba, L.; Marycz, K. Pathophysiological Implication of Fetuin-A Glycoprotein in the Development of Metabolic Disorders: A Concise Review. *J Clin Med* **2019**, *8* (12), 2033. https://doi.org/10.3390/jcm8122033.

(28) Nan, R.; Gor, J.; Lengyel, I.; Perkins, S. J. Uncontrolled Zinc- and Copper-Induced Oligomerisation of the Human Complement Regulator Factor H and Its Possible

Implications for Function and Disease. *J Mol Biol* **2008**, *384* (5), 1341–1352. https://doi.org/https://doi.org/10.1016/j.jmb.2008.10.030.

(29) Sarma, J. V.; Ward, P. A. The Complement System. *Cell Tissue Res* **2011**, *343* (1), 227–235. https://doi.org/10.1007/s00441-010-1034-0.

(30) Djoko, K. Y.; Ong, C. Y.; Walker, M. J.; McEwan, A. G. The Role of Copper and Zinc Toxicity in Innate Immune Defense against Bacterial Pathogens. *J Biol Chem* **2015**, *290* (31), 18954–18961. https://doi.org/10.1074/jbc.R115.647099.

(31) Church, W. R.; Jernigan, R. L.; Toole, J.; Hewick, R. M.; Knopf, J.; Knutson, G. J.; Nesheim, M. E.; Mann, K. G.; Fass, D. N. Coagulation Factors V and VIII and Ceruloplasmin Constitute a Family of Structurally Related Proteins. *Proceedings of the National Academy of Sciences* **1984**, *81* (22), 6934 LP – 6937. https://doi.org/10.1073/pnas.81.22.6934.

(32) Mann, K. G.; Lawler, C. M.; Vehar, G. A.; Church, W. R. Coagulation Factor V Contains Copper Ion. *Journal of Biological Chemistry* **1984**, *259* (21), 12949–12951. https://doi.org/10.1016/S0021-9258(18)90637-X.

(33) Kirsipuu, T.; Zadorožnaja, A.; Smirnova, J.; Friedemann, M.; Plitz, T.; Tõugu, V.; Palumaa, P. Copper(II)-Binding Equilibria in Human Blood. *Sci Rep* **2020**, *10* (1), 5686. https://doi.org/10.1038/s41598-020-62560-4.

(34) Ramasamy, I. Recent Advances in Physiological Lipoprotein Metabolism. *Clinical Chemistry and Laboratory Medicine (CCLM)* **2014**, *52* (12), 1695–1727. https://doi.org/doi:10.1515/cclm-2013-0358.

(35) Mazi, T. A.; Shibata, N. M.; Medici, V. Lipid and Energy Metabolism in Wilson Disease. *Liver Res* **2020**, *4* (1), 5–14. https://doi.org/10.1016/j.livres.2020.02.002.

(36) Huster, D.; Purnat, T. D.; Burkhead, J. L.; Ralle, M.; Fiehn, O.; Stuckert, F.; Olson, N. E.; Teupser, D.; Lutsenko, S. High Copper Selectively Alters Lipid Metabolism and Cell Cycle Machinery in the Mouse Model of Wilson Disease. *Journal of Biological Chemistry* **2007**, *282* (11), 8343–8355. https://doi.org/10.1074/jbc.M607496200.

(37) Gangadharan, B.; Bapat, M.; Rossa, J.; Antrobus, R.; Chittenden, D.; Kampa, B.; Barnes, E.; Klenerman, P.; Dwek, R. A.; Zitzmann, N. Discovery of Novel Biomarker Candidates for Liver Fibrosis in Hepatitis C Patients: A Preliminary Study. *PLoS One* **2012**, *7* (6), e39603–e39603. https://doi.org/10.1371/journal.pone.0039603.

(38) Lei, K. Y. Alterations in Plasma Lipid, Lipoprotein and Apolipoprotein Concentrations in Copper-Deficient Rats. *Journal of Nutrition* **1983**, *113* (11), 2178–2183. https://doi.org/10.1093/jn/113.11.2178.

(39) Batthyány, C.; Santos, C. X. C.; Botti, H.; Cerveñansky, C.; Radi, R.; Augusto, O.; Rubbo, H. Direct Evidence for Apo B-100-Mediated Copper Reduction: Studies with Purified Apo B-100 and Detection of Tryptophanyl Radicals. *Arch Biochem Biophys* **2000**, *384* (2), 335–340. https://doi.org/https://doi.org/10.1006/abbi.2000.2102.

(40) Topham, R. W.; Frieden, E. Identification and Purification of a Non-Ceruloplasmin Ferroxidase of Human Serum. *Journal of Biological Chemistry* **1970**, *245* (24), 6698–6705. https://doi.org/10.1016/s0021-9258(18)62590-6.

(41) Garner, A.; Tosi, L.; Steinbuch, M. FERROXIDASE II. THE ESSENTIAL ROLE OF COPPER IN ENZYMATIC ACTIVITY. **1981**, *98*, 66–71.

(42) Ciccone, L.; Tonali, N.; Shepard, W.; Nencetti, S.; Orlandini, E. Physiological Metals Can Induce Conformational Changes in Transthyretin Structure: Neuroprotection or Misfolding Induction? *Crystals (Basel)* **2021**, *11* (4). https://doi.org/10.3390/cryst11040354.

(43) Costa, R.; Ferreira-da-Silva, F.; Saraiva, M. J.; Cardoso, I. Transthyretin Protects against A-Beta Peptide Toxicity by Proteolytic Cleavage of the Peptide: A Mechanism Sensitive to the Kunitz Protease Inhibitor. *PLoS One* **2008**, *3* (8). https://doi.org/10.1371/journal.pone.0002899.

(44) Gouvea, I. E.; Kondo, M. Y.; Assis, D. M.; Alves, F. M.; Liz, M. A.; Juliano, M. A.; Juliano, L. Studies on the Peptidase Activity of Transthyretin (TTR). *Biochimie* **2013**, *95* (2), 215–223. https://doi.org/10.1016/j.biochi.2012.09.014.

(45) Costa, R.; Gonçalves, A.; Saraiva, M. J.; Cardoso, I. Transthyretin Binding to A-Beta Peptide - Impact on A-Beta Fibrillogenesis and Toxicity. *FEBS Lett* **2008**, *582* (6), 936–942. https://doi.org/10.1016/j.febslet.2008.02.034.

(46) Shih, A. W. Y.; McFarlane, A.; Verhovsek, M. Haptoglobin Testing in Hemolysis: Measurement and Interpretation. *Am J Hematol* **2014**, *89* (4), 443–447. https://doi.org/https://doi.org/10.1002/ajh.23623.

(47) Phillips, J.; Henderson, A. C. Hemolytic Anemia: Evaluation and Differential Diagnosis. *Am Fam Physician* **2018**, *98* (6), 354–361.

(48) Zhang, C.; Peng, W.; Jiang, X.; Chen, B.; Zhu, J.; Zang, Y.; Zhang, J.; Zhu, T.; Qin, J. Transgene Expression of Human PON1 Q in Mice Protected the Liver against CCl4-Induced Injury. *J Gene Med* **2008**, *10* (1), 94–100. https://doi.org/https://doi.org/10.1002/jgm.1128.

(49) Lacombe, M.; Jaquinod, M.; Belmudes, L.; Couté, Y.; Ramus, C.; Combes, F.; Burger, T.; Mintz, E.; Barthelon, J.; Leroy, V.; Poujois, A.; Lachaux, A.; Woimant, F.; Brun, V. Comprehensive and Comparative Exploration of the Atp7b−/− Mouse Plasma Proteome†. *Metallomics* **2020**, *12* (2), 249–258. https://doi.org/10.1039/c9mt00225a.

(50) Gaberc-Porekar, V.; Menart, V. Perspectives of Immobilized-Metal Affinity Chromatography. *J Biochem Biophys Methods* **2001**, *49* (1), 335–360. https://doi.org/https://doi.org/10.1016/S0165-022X(01)00207-X.

(51) Lake, D. F.; Faigel, D. O. The Emerging Role of QSOX1 in Cancer. *Antioxid Redox Signal* **2014**, *21* (3), 485–496. https://doi.org/10.1089/ars.2013.5572.

(52) Morel, C.; Adami, P.; Musard, J.-F.; Duval, D.; Radom, J.; Jouvenot, M. Involvement of Sulfhydryl Oxidase QSOX1 in the Protection of Cells against Oxidative Stress-Induced Apoptosis. *Exp Cell Res* **2007**, *313* (19), 3971–3982. https://doi.org/https://doi.org/10.1016/j.yexcr.2007.09.003.

(53) Barca, A.; Ippati, S.; Urso, E.; Vetrugno, C.; Storelli, C.; Maffia, M.; Romano, A.; Verri, T. Carnosine Modulates the Sp1-Slc31a1/Ctr1 Copper-Sensing System and Influences Copper Homeostasis in Murine CNS-Derived Cells. *Am J Physiol Cell Physiol* **2019**, *316* (2), C235–C245. https://doi.org/10.1152/ajpcell.00106.2018.

(54) Arnal, N.; de Alaniz, M. J. T.; Marra, C. A. Carnosine and Neocuproine as Neutralizing Agents for Copper Overload-Induced Damages in Cultured Human Cells. *Chem Biol Interact* **2011**, *192* (3), 257–263. https://doi.org/https://doi.org/10.1016/j.cbi.2011.03.017.

(55) Wolfe, B. M.; Kvach, E.; Eckel, R. H. Treatment of Obesity: Weight Loss and Bariatric Surgery. *Circ Res* **2016**, *118* (11), 1844–1855. https://doi.org/10.1161/CIRCRESAHA.116.307591.

(56) Garibay, D.; Lou, J.; Lee, S. A.; Zaborska, K. E.; Weissman, M. H.; Sloma, E.; Donahue, L.; Miller, A. D.; White, A. C.; Michael, M. D.; Sloop, K. W.; Cummings, B. P. β Cell GLP-1R Signaling Alters α Cell Proglucagon Processing after Vertical Sleeve Gastrectomy

in Mice. *Cell Rep* **2018**, *23* (4), 967–973. https://doi.org/https://doi.org/10.1016/j.celrep.2018.03.120.

(57) Griffith, D. P.; Liff, D. A.; Ziegler, T. R.; Esper, G. J.; Winton, E. F. Acquired Copper Deficiency: A Potentially Serious and Preventable Complication Following Gastric Bypass Surgery. *Obesity* **2009**, *17* (4), 827–831. https://doi.org/https://doi.org/10.1038/oby.2008.614.

(58) Gletsu-Miller, N.; Broderius, M.; Frediani, J. K.; Zhao, V. M.; Griffith, D. P.; Davis Jr, S. S.; Sweeney, J. F.; Lin, E.; Prohaska, J. R.; Ziegler, T. R. Incidence and Prevalence of Copper Deficiency Following Roux-En-y Gastric Bypass Surgery. *Int J Obes (Lond)* **2012**, *36* (3), 328–335. https://doi.org/10.1038/ijo.2011.159.

(59) Kumar, P.; Hamza, N.; Madhok, B.; De Alwis, N.; Sharma, M.; Miras, A. D.; Mahawar, K. K. Copper Deficiency after Gastric Bypass for Morbid Obesity: A Systematic Review. *Obes Surg* **2016**, *26* (6), 1335–1342. https://doi.org/10.1007/s11695-016-2162-8.

(60) Liz, M. A.; Coelho, T.; Bellotti, V.; Fernandez-Arias, M. I.; Mallaina, P.; Obici, L. A Narrative Review of the Role of Transthyretin in Health and Disease. *Neurol Ther* **2020**, *9* (2), 395–402. https://doi.org/10.1007/s40120-020-00217-0.

(61) Mody, N.; Graham, T. E.; Tsuji, Y.; Yang, Q.; Kahn, B. B. Decreased Clearance of Serum Retinol-Binding Protein and Elevated Levels of Transthyretin in Insulin-Resistant Ob/Ob Mice. *American Journal of Physiology-Endocrinology and Metabolism* **2008**, *294* (4), E785–E793. https://doi.org/10.1152/ajpendo.00521.2007.

(62) He, Y.; Qiu, R.; Wu, B.; Gui, W.; Lin, X.; Li, H.; Zheng, F. Transthyretin Contributes to Insulin Resistance and Diminishes Exercise-Induced Insulin Sensitivity in Obese Mice by Inhibiting AMPK Activity in Skeletal Muscle. *American Journal of Physiology-*

Endocrinology and Metabolism **2021**, *320* (4), E808–E821. https://doi.org/10.1152/ajpendo.00495.2020.

(63) Rindler, P. M.; Plafker, S. M.; Szweda, L. I.; Kinter, M. High Dietary Fat Selectively Increases Catalase Expression within Cardiac Mitochondria. *J Biol Chem* **2013**, *288* (3), 1979–1990. https://doi.org/10.1074/jbc.M112.412890.

(64) Nakao, C.; Ookawara, T.; Sato, Y.; Kizaki, T.; Imazeki, N.; Matsubara, O.; Haga, S.; Suzuki, K.; Taniguchi, N.; Ohno, H. Extracellular Superoxide Dismutase in Tissues from Obese (Ob/Ob) Mice. *Free Radic Res* **2000**, *33* (3), 229–241. https://doi.org/10.1080/10715760000301401.

(65) Hilner, E.; Håkanson, U.; Fröberg, L. E.; Karlsson, M.; Kratzer, P.; Lundgren, E.; Samuelson, L.; Mikkelsen, A. Direct Atomic Scale Imaging of III-V Nanowire Surfaces. *Nano Lett* **2008**, *8* (11), 3978–3982. https://doi.org/10.1021/nl802500d.

(66) Kern, P. A.; Di Gregorio, G. B.; Lu, T.; Rassouli, N.; Ranganathan, G. Adiponectin Expression From Human Adipose Tissue. *Diabetes* **2003**, *52* (7), 1779 LP – 1785. https://doi.org/10.2337/diabetes.52.7.1779.

(67) Belalcazar, L. M.; Lang, W.; Haffner, S. M.; Schwenke, D. C.; Kriska, A.; Balasubramanyam, A.; Hoogeveen, R. C.; Pi-Sunyer, F. X.; Tracy, R. P.; Ballantyne, C. M.; Group, the L. A. (Action for H. in D. R. Improving Adiponectin Levels in Individuals With Diabetes and Obesity: Insights From Look AHEAD. *Diabetes Care* **2015**, *38* (8), 1544 LP – 1550. https://doi.org/10.2337/dc14-2775.

(68) Illán-Gómez, F.; Gonzálvez-Ortega, M.; Orea-Soler, I.; Alcaraz-Tafalla, M. S.; Aragón-Alonso, A.; Pascual-Díaz, M.; Pérez-Paredes, M.; Lozano-Almela, M. L. Obesity and Inflammation: Change in Adiponectin, C-Reactive Protein, Tumour Necrosis Factor-

Alpha and Interleukin-6 after Bariatric Surgery. *Obes Surg* **2012**, *22* (6), 950–955. https://doi.org/10.1007/s11695-012-0643-y.

(69) Simpson, F.; Whitehead, J. P. Adiponectin—It's All about the Modifications. *Int J Biochem Cell Biol* **2010**, *42* (6), 785–788. https://doi.org/https://doi.org/10.1016/j.biocel.2009.12.021.

(70) Hada, Y.; Yamauchi, T.; Waki, H.; Tsuchida, A.; Hara, K.; Yago, H.; Miyazaki, O.; Ebinuma, H.; Kadowaki, T. Selective Purification and Characterization of Adiponectin Multimer Species from Human Plasma. *Biochem Biophys Res Commun* **2007**, *356* (2), 487–493. https://doi.org/https://doi.org/10.1016/j.bbrc.2007.03.004.

(71) Kong, A. T.; Leprevost, F. V; Avtonomov, D. M.; Mellacheruvu, D.; Nesvizhskii, A. I. MSFragger: Ultrafast and Comprehensive Peptide Identification in Mass Spectrometry-Based Proteomics. *Nat Methods* **2017**, *14* (5), 513–520. https://doi.org/10.1038/nmeth.4256.

(72) Yu, F.; Teo, G. C.; Kong, A. T.; Haynes, S. E.; Avtonomov, D. M.; Geiszler, D. J.; Nesvizhskii, A. I. Identification of Modified Peptides Using Localization-Aware Open Search. *Nat Commun* **2020**, *11* (1), 4065. https://doi.org/10.1038/s41467-020-17921-y.

(73) Yu, F.; Haynes, S. E.; Nesvizhskii, A. I. IonQuant Enables Accurate and Sensitive Label-Free Quantification With FDR-Controlled Match-Between-Runs. *Molecular & Cellular Proteomics* **2021**, *20*, 100077. https://doi.org/https://doi.org/10.1016/j.mcpro.2021.100077.

Chapter 5

Influence of Glucose on the Stability and Ferroxidase Activity of Ceruloplasmin

This work is in collaboration with Nathaniel Harder and this data will also be presented in his thesis. Project conceptualization and experimental design was conducted by SEJ, NH, and MCH. UV-Vis data and western blot analysis was collected by NH. ELISA and activity assays were conducted by SEJ and NH. Mass spectrometry was conducted and analyzed by SEJ.

5.1 Abstract

Copper regulation is vital for maintaining biological homeostasis. Complex networks of biomolecules dictate the fate of copper acquisition. Ceruloplasmin is a large cuproprotein involved in iron and copper homeostasis. A link between ceruloplasmin bioactivity and blood monosaccharide levels has been established; however, the mechanisms are unknown. In this work, we show an increase in ceruloplasmin fragmentation in the presence of glucose. Activity studies reveal glucose-dependent activity changes in both long- and short-term 37°C incubation. Spectroscopic investigation by UV-Vis indicated a decrease in intensity of the LMCT (λ_{max} 610 nm) and 610/280 nm ratio corresponding to a loss of ceruloplasmin's type 1 copper center. Lastly, we sought to determine the location of the fragmentation site that produces a fragment of ~18 kDa through mass spectrometry-based techniques, resulting in the identification of the tryptic peptide sequence N-ALYLQYTDETFR-C.

5.2 Introduction

5.2.1 Copper Regulation

Biology has evolved to take advantage of copper's unique properties to perform complex reactions in an aqueous environment and thus are essential in many physiological processes. Through a complex network of biochemical pathways, copper is tightly regulated to ensure proper biological homeostasis. Copper is acquired through the diet, reduced from Cu^{2+} to Cu^{+}, and transported across the apical membrane of the intestine via CTR1 – a copper importer.[1] After absorption, copper chaperones (ATOX1 and COMMD1) bind, and transports copper to ATP7B where it is incorporated into various metalloproteins during maturation in the *trans*-Golgi network. The export of copper occurs primarily through two means: the first is the loading and excretion of ceruloplasmin – a copper transporter with ferroxidase activity or through export via ATP7A/7B.[2]

Interference with any level of copper regulation leads to the onset of various disease states. Examples of genetic diseases producing copper dysregulation are Wilson and Menkes disease. Wilson disease involves gene mutations of ATP7B resulting in the accumulation of copper in various tissues, such as the liver.[3,4] If left untreated, increased copper levels can ultimately lead to organ failure.[5] Conversely, mutations in ATP7A as found in Menkes disease result in the accumulation of copper in the intestine and an inability to mobilize copper to organs producing a copper deficient-like status.[6,7]

In addition to genetic predispositions to copper imbalances, extrinsic factors (nutrition and environmental) have been implicated in copper dysregulation.[8,9] For example, under a high-fat diet, intracellular copper has been observed to delocalize into various organelles producing a pseudo copper-deficient state while increases in intracellular copper have been linked to a decrease

in AMPK activation increasing the likelihood of insulin resistance.[10] Moreover, a recent study aimed to assess nutritional sugar intake and metal metabolism showed a correlation between glucose intake, and copper.[11]

5.2.2 Ceruloplasmin

Ceruloplasmin is a ~120 kDa glycoprotein synthesized in the liver and involved in a range of biological processes including iron metabolism, acute phase response, and copper metabolism.[12,13] Ceruloplasmin contains six copper domains with three type 1 copper centers and a tri-nuclear copper cluster responsible for its catalytic activity and overall stability of the protein.[14–16] It is hypothesized that iron binds near domains 4 and 6 in the vicinity of the type 1 copper centers. Ceruloplasmin's main role is to reduce ferrous iron to ferric iron through an electron transfer from the reduction of O_2 to H_2O.[17] Mutations of ceruloplasmin have direct influences on iron metabolism and are correlated to a plethora of deleterious physiological outcomes such as diabetes and neurological disorders resulting from aberrant iron accumulation in tissues.[18,19]

In addition to genetic predispositions to decrease ceruloplasmin levels and activity, nutritional intake has been shown to influence ceruloplasmin. Work by Harder *et al.* showed that over two weeks, human subjects given daily dietary sugar supplements (glucose, fructose, and high fructose) had lower serum copper and lower ceruloplasmin ferroxidase activity than the control group despite ceruloplasmin concentration being constant.[11]

In this work, we investigate the link between glucose and ceruloplasmin through a combination of biochemical assays, spectroscopy, and mass spectrometry. Specifically, we probe the changes in ceruloplasmin stability and ferroxidase activity through long and short-term

exposure to glucose. We propose that glucose directly interacts with ceruloplasmin and promotes increased degradation and decreased ferroxidase capacity leading to the observed decoupling of ceruloplasmin concentration and activity previously observed.

5.3 Results and Discussion

5.3.1 Glucose-Induced Fragmentation of Ceruloplasmin

Previous studies have illustrated that incubation of ceruloplasmin with monosaccharides, such as glucose and fructose led to increased degradation of ceruloplasmin.[20] This observation, in addition to ceruloplasmin's activity being decoupled from its concentration in high sugar diets, suggests a link between sugar and ceruloplasmin function. To this end, we sought to explore this link using a combination of immunochemical, mass spectrometry, and spectroscopic approaches.

1D gel electrophoresis of ceruloplasmin with and without glucose reveals distinct changes with respect to both time and presence of glucose. At day 0, minimal fragmentation is observed for both glucose and control samples (Figure 5.1A). The initial ceruloplasmin fragmentation is believed to have occurred during the manufacturing process as they are present immediately upon reconstitution (data not shown). After 10 days at 37°C the intensity of fragment bands increases for both glucose and control. Ceruloplasmin incubated with glucose led to a higher level of fragmentation compared to the control. Specifically, bands at ~70, 50, and 18 kDa are higher in abundance at day 10 with glucose. Taken together, these data agree with previously published work investigating ceruloplasmin glycation.

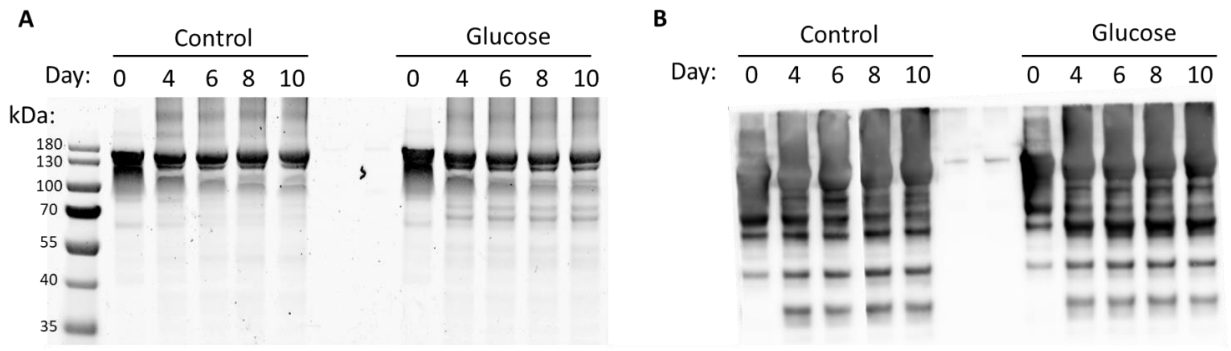

Figure 5.1. Ceruloplasmin fragment visualization. A) Imperial stain of ceruloplasmin and ceruloplasmin fragments separated via SDS-PAGE. B) Western blot of ceruloplasmin separated via SDS-PAGE for the determination of antibody recognition.

5.3.2 Antibody Recognition of Ceruloplasmin Fragments

We next sought to assess if the non-enzymatically generated fragments from ceruloplasmin could be detected by antibody recognition. Western blot analysis revealed a similar band profile as total protein staining (Figure 5.1B). Most significant is the increase in intensity of the 50 kDa band after 10 days of incubation with glucose. Antibody recognition of ceruloplasmin fragments suggested antibody-based methods for profiling ceruloplasmin may lead to superfluous ceruloplasmin assessment and overestimation of bioactive ceruloplasmin. To investigate if the independence of ceruloplasmin activity from concentration is due to antibody recognition of fragments rather than holo-ceruloplasmin we performed an ELISA on each sample. ELISA-based assays provide a high level of quantitative power and robustness and are routinely used in the clinic to determine ceruloplasmin concentration. Ceruloplasmin concentration decreased with respect to time in both the presence and absence of glucose. A decrease from 302.17 ± 16.5 mg/mL to 171.88 ± 8.6 mg/mL between day 0 and 10 occurred for non-glucose incubated ceruloplasmin while a

decrease from 345.70 ± 25.0 mg/mL to 149.72 ± 3.7 mg/mL for ceruloplasmin with glucose (Figure 5.2). The difference between glucose-treated and non-glucose-treated ceruloplasmin concentration is minor for both day 0 and day 10. These data indicate that antibody recognition of ceruloplasmin is not significantly altered by the presence of glucose but antibody based quantitation is influenced by general degradation.

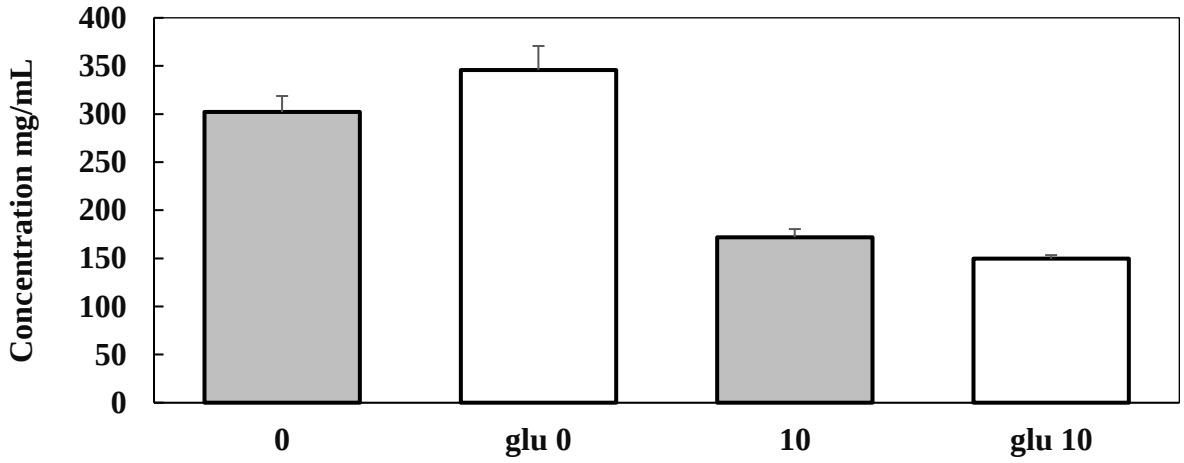

Figure 5.2. Ceruloplasmin concentration determined by ELISA. Grey bars: day 0 and 10 of ceruloplasmin with no glucose addition. White bars: day 0 and 10 of ceruloplasmin with 100 mM glucose addition. Error bars represent standard error of the mean (SEM).

5.3.3 Profiling the Influence of Glucose on Ceruloplasmin Activity

Having established the influence of glucose on ceruloplasmin degradation and antibody recognition we next investigated the level of activity with respect to the presence of glucose and

time. A common method to monitor ceruloplasmin activity is the use of the chemical probes such as *p*-phenylenediamine or *o*-dianisidine chloride.[21,22] These assays involve the oxidation of a substrate by ceruloplasmin which can be measured colorimetrically. The rate of oxidation is then correlated back to ceruloplasmin's ferroxidase efficiency. Interestingly, at day 0 ceruloplasmin activity is elevated in the presence of glucose; however, after 10 days activity levels are similar between the two conditions (Figure 5.3). While the increase in activity at day 0 for ceruloplasmin with 100 mM glucose is unknown, we speculate that this is due to glucose acting as a cryopreservant as sugars have been linked to increasing protein stability during drying and storage.[23] Increased ceruloplasmin activity in the presence of glucose after freeze-thaw may be a result in direct glucose interaction of ceruloplasmin allowing for the preservation of the native structure.

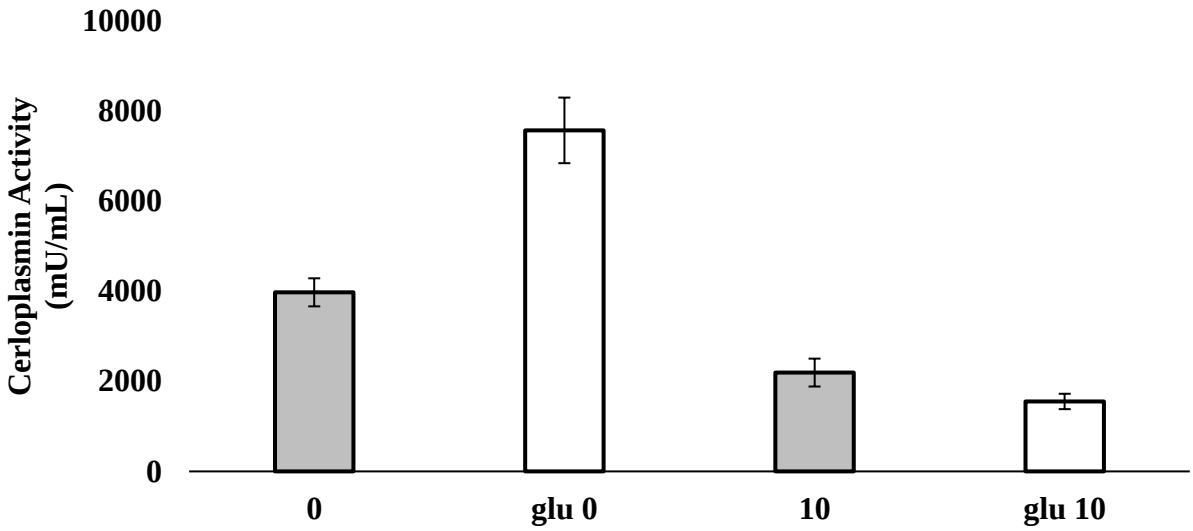

Figure 5.3. Long-term incubation of ceruloplasmin with glucose alters activity. Activity determined colorimetrically**.** Activity of ceruloplasmin after incubation with 100 mM glucose for 0 and 10 days expressed in mU/mL. Error bars represent SEM.

Direct binding of glucose to ceruloplasmin may also impact its activity through changes in the coordination environment of the copper centers. Biologically relevant concentrations of glucose range between less than 5 mM in fasting in non-diabetics to as high as 15 mM after feeding.[24] Previous experiments were conducted at a glucose concentration far exceeding (100 mM) the highest physiological level of glucose and at a timescale longer than normally required for glucose clearance. Therefore, we incubated ceruloplasmin for 30 min with increasing concentrations of glucose that mimic fasting (1 mM and 5 mM), pre-perianal (10 mM and 15 mM), and extreme levels (100 mM). Moreover, the freeze-thaw cycle was eliminated to eliminate confounding factors.

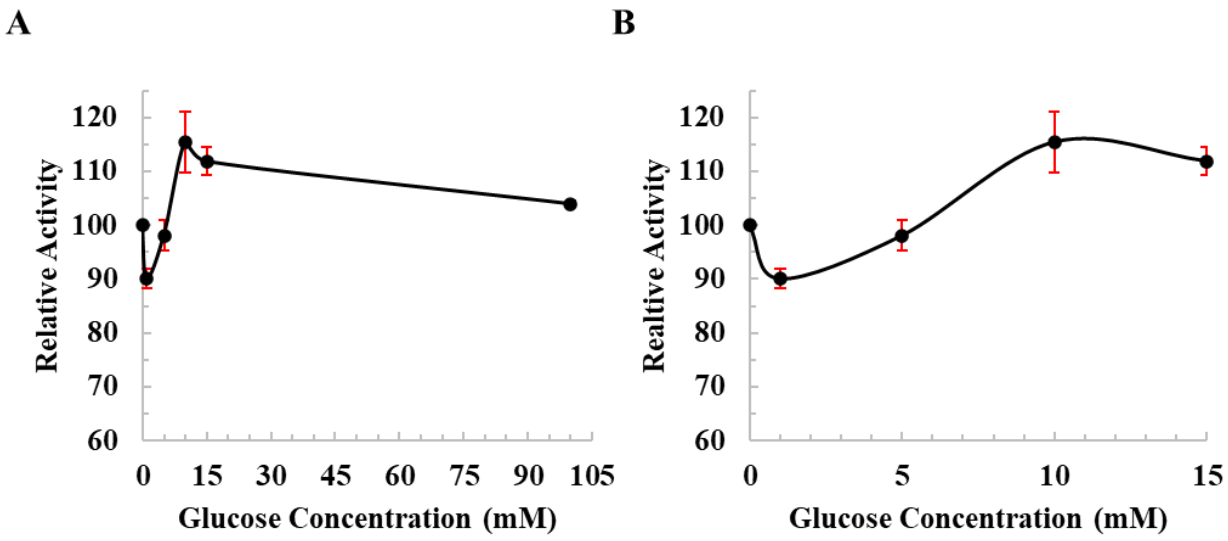

Figure 5.4. Ceruloplasmin's relative activity after 30 min incubation with physiologically relevant concentrations of glucose. A) Relative activity of ceruloplasmin with 0, 1, 5-, 10-, 15-, and 100 mM glucose. B) Relative activity of ceruloplasmin with 0, 1-, 5-, 10-, and 15 mM glucose. Error bars represent SEM.

Normalizing activity to no glucose added, 1 mM and 5 mM show a 10% and 5% decrease, respectively (Figure 5.4). Glucose concentrations of 10 mM and 15 mM increases ceruloplasmin's activity by 15% and 10%, respectively. 100 mM increases the activity of ceruloplasmin by approximately 4%, however, the magnitude is substantially less than when undergoing a single freeze-thaw. Nevertheless, the addition of glucose at fasting levels decreases ceruloplasmin activity ability while glucose concentrations resembling post-prandial levels increases the activity. Differences in activity after a short incubation time support the hypothesis that glucose is directly interacting with ceruloplasmin and altering its ability to oxidize its substrate.

5.3.4 Spectroscopic Investigation of Glucose Binding to Ceruloplasmin

Shifts in the coordination environment of ceruloplasmin catalytic center(s) by direct binding of glucose can be monitored spectroscopically. The type 1 copper center of ceruloplasmin, responsible for electron transfer, can be assessed by monitoring the characteristic blue color absorbance (600-650 nm) from LMCT.[25] Leveraging this property we analyzed the UV-Vis spectrum of ceruloplasmin incubated with and without glucose for 0 and 10 days. While there was not a shift from the maximum absorbance at 610 nm (data not shown), there was a noticeable decrease in the intensity of the LMCT band with respect to time and addition of glucose. Taking the ratio of 610 nm to 280 nm provides an estimation of ceruloplasmin purity.[26] After incubation for 10 days with and without glucose the 610/280 nm decreases in both conditions (Figure 5.5A). The percent change between the two conditions highlights the influence glucose has on ceruloplasmin stability over 10 days with the 610/280 nm being 31.18 % of the magnitude at day 0 with glucose compared to 53.54% without (Figure 5.5B).

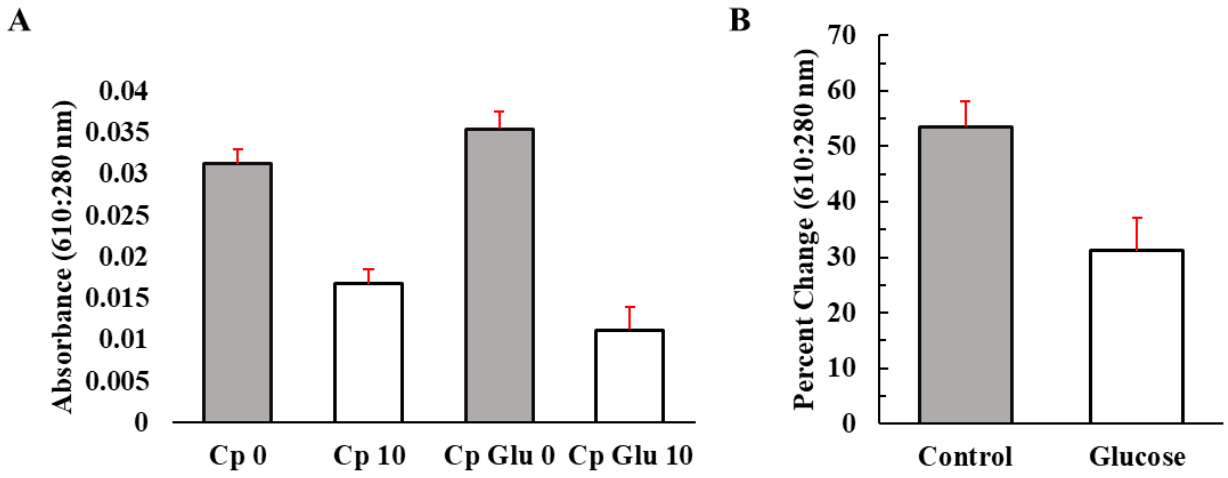

Figure 5.5. Monitoring the type 1 center of ceruloplasmin by UV-Vis spectroscopy. 610/280 nm of ceruloplasmin incubated with and without glucose for 0 and 10 days at 37°C. A) 610/280 nm. B) Relative percentage of 610/280 nm magnitude of day 10 compared to day 0.

Loss of signal at 610 nm as opposed to a shift in λ_{max} indicates complete loss of the type 1 copper center. While control samples exhibit a decrease in 610/280 nm the decrease was not to the same extent as in the presence of glucose. Differences between the two conditions could be explained by the facilitated fragmentation of ceruloplasmin by glucose in regions necessary for copper coordination. Work conducted by Islam *et al.* hypothesized that fragmentation was due to ceruloplasmin undergoing glycation, which is the non-enzymatic addition of sugar moieties to amino acid residues.[20] In addition to internally bound copper, ceruloplasmin also contains several labile copper binding sites with ongoing research pointing to surface-exposed residues as the location of binding.[27] Addition of EDTA in the presence of glucose leads to a reduction of fragmentation, pointing to a role of liberated catalytic metal in generating ceruloplasmin fragments. Under this hypothesis, the addition of glucose and direct binding by ceruloplasmin

liberates labile copper which proceeds to generate hydroxide radicals that cleave the peptide backbone.

5.3.5 Elucidating Fragmentation Sites of Ceruloplasmin

In both our work and that of Islam *et al.*, a fragment of approximately 18 kDa is produced in higher quantities in the presence of glucose. The site of fragmentation was unable to be elucidated. To substantiate our hypothesis that ceruloplasmin undergoes site-specific fragmentation induced by direct glucose binding and liberation of catalytic copper, we applied a combination of in-gel digestion and mass spectrometry. In-gel digestion of the ~18 kDa ceruloplasmin fragment and subsequent desalting followed by MALDI-TOF/TOF generated ions (Figure 5.6A). Fragmentation by post-source decay (PSD) produced minimal ion fragmentation except for the ion at 1520.35 m/z (Figure 5.6B). Searching the spectra against Uniprot *homo sapiens* database with MACOT we identified the peptide sequence (N-ALYLQYTDETFR-C) corresponding to residues 70-81 of ceruloplasmin. The ability to determine the exact fragmentation site that produces the ~18 kDa fragment is hindered by the lack of peptide recovery from the in-gel digest. Extrapolating the segment of ceruloplasmin including the identified peptide we hypothesize that the fragment likely contains the N-terminus and fragments in a region between residues Val156 and Ile164, which correspond to a molecular weight between ~18-19 kDa for non-glycosylated ceruloplasmin. However, considering ceruloplasmin is known to be glycosylated at Asn138 with either the glycans A2G2SE and FA2G2S2 or with the structures A3G3S3 and A3FG3S3, it is likely that the fragmentation site is located prior to residue 156.[28]

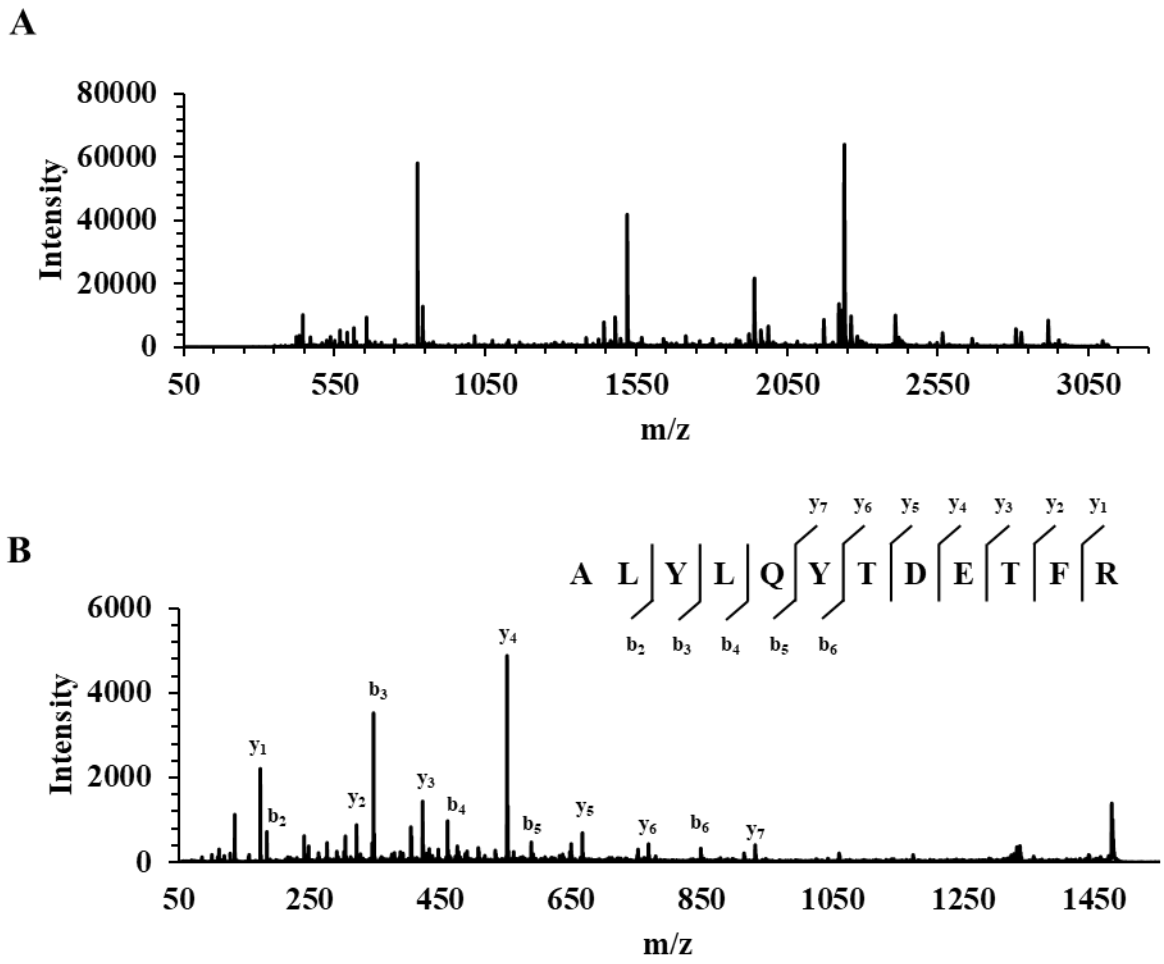

Figure 5.6. MALDI-TOF of trypsin peptides derived from in-gel digestion of 18 kDa fragment of ceruloplasmin. A) MS spectrum of trypsin digest of ~18 kDa ceruloplasmin fragment. B) MS/MS spectrum from the fragmentation of 1520.35 m/z ion. MASCOT search of spectrum results in the identification of the peptide ALYLQYTDETFR.

5.4 Conclusions and Outlook

Elucidating the link between dietary sugar intake and metal micronutrient intake is vital for improving human health outcomes. Previous literature and work in the Heffern lab have

illustrated a decoupling of ceruloplasmin concentration and ferroxidase activity in individuals given an increased sugar diet.[11] Through these studies we show that the presence of glucose leads to an increased rate of ceruloplasmin's degradation. Western blot analysis of ceruloplasmin and ceruloplasmin fragments reveal ambiguous antibody recognition. However, a decrease in the concentration of ceruloplasmin is detected by ELISA-based methods after 10-day incubation at 37°C. This implies care must be taken when assessing ceruloplasmin concentration with antibody-based methods to ensure only intact ceruloplasmin is detected, and the decoupling of concentration and activity occurs through a different mechanism. While the drastic differences in activity between day 0 ceruloplasmin samples are likely due to protein stabilization by glucose during freezing, short incubation times with physiologically relevant concentrations of glucose also modulate ferroxidase activity.

Activity differences observed may be a result of direct glucose binding by ceruloplasmin that alters the catalytic center(s); however, no shifts in the type-1 copper center maximum are observed suggesting minimal copper center perturbation. These results do not definitively omit the possibility of direct glucose interaction altering ceruloplasmin's ternary structure and additional experiments that probe protein structure, such as circular dichroism, should be performed. One possible mechanism for increased ceruloplasmin fragmentation is due to the liberation of labile catalytic copper by glucose leading to the generation of hydroxide radicals that proceed to cleave the protein backbone. Moreover, cleavage may be directed more frequently to sites of glycation, which occurs readily under increased glucose. Our attempts to substantiate this hypothesis using a combination of in-gel digestion of the ~18 kDa ceruloplasmin revealed the tryptic peptide ALYLQYTDETFR. This peptide corresponds to residues 70-81 in ceruloplasmin, indicating the site of cleavage could be before residue 156, depending on glycosylation status. Follow-up studies

should include optimization of the in-gel digestion procedure to increase tryptic peptide recovery and sequence coverage of the fragment.

5.5 Methods

5.5.1 Ceruloplasmin Incubation with Glucose

Lyophilized ceruloplasmin (239799-1MG, Millipore Sigma) was dissolved in 500 mL of nanopure water. Resuspended ceruloplasmin was dialyzed (Slide-A-Lyzer™ Dialysis Cassettes 20K MWCO 0.5 mL, ThermoFisher Scientific) 500 mL PBS for 18 h at room temperature. After initial dialysis, PBS was replaced with an additional 500 mL of PBS and dialyzed again for 2 h at room temperature. The resulting ceruloplasmin solution was diluted to 1 mL in PBS and split into two 500 mL aliquots. To the control samples 170 mL of nanopure water was added. To the glucose-treated sample 103 mL of nanopure water and 67 mL of 1 M glucose dissolved in nanopure water was added. An aliquot of the control and glucose sample were immediately frozen at -80°C whereas and an equal volume aliquot was incubated at 37°C for either 4, 8, or 10 days then frozen at -80°C.

5.5.2 1D Gel Electrophoresis and Western Blot

To each sample, LDS sample buffer (B0007, ThermoFisher Scientific) was added to reach a final dilution factor of 4x. Protein fragments were separated on a Bis-Tris 4-12% gel (NW04125BOX, ThermoFisher Scientific) at 120 V for 1 h. Protein bands were visualized by a Coomassie-based Imperial stain followed by de-staining with ultrapure water. Ceruloplasmin assessment by western blot was conducted as follows: SDS-page was performed as described

above then transferred onto a low fluorescent PVDF membrane (1704274, Bio-Rad) using a Trans-Blot Turbo Transfer System (Bio-Rad). After transfer membranes were blocked in 5% BSA in TBST (9997S, Cell Signaling Technology) for 1 h at room temperature and placed in anti-Ceruloplasmin (1:1000 sc-365205, SCBT) primary antibody and incubated at 4˚C overnight. Membranes were washed 3 times for 5 minutes before the addition of anti-mouse Alexafluor 555 (1:2000 A28180 ThermoFisher Scientific) secondary antibody in 5% milk powder in TBST for 1 h. Images were taken by a Chemidoc MP (BioRad).

5.5.3 Ceruloplasmin ELISA

Ceruloplasmin samples were diluted 1:10,000 in dilution buffer and ELISA was carried out according to the manufacturer's instructions (EC4201-1, Assaypro).

5.5.4 Ceruloplasmin Activity Assay

Ceruloplasmin activity (EIACPLC, ThermoFisher Scientific) was assessed by the colorimetric assay of the ferroxidase activity of the protein. The sample was diluted 1:20 and data were normalized to the control sample at day 0. Assays were read on the Spectramax i3x plate reader (Molecular devices) and processed on Excel (Microsoft).

5.5.5 In-gel Digestion of Ceruloplasmin

Bands corresponding to ceruloplasmin and ceruloplasmin fragments were excised, diced into small 1 mm pieces, and placed in nano pure water. Samples were spun and supernatant was removed and replaced with 25 mM ammonium bicarbonate (AMBIC). The pieces were vortexed for 10 seconds and the AMBIC was removed. This was done for a total of three times. After the third wash, 50% ACN in 25 mM AMBIC was added to cover the gel pieces. Samples were then vortexed for 10 seconds and replaced with fresh 50% ACN in AMBIC. This was done four times

and on the fourth time, the samples were placed on the shaker for 10 min. To the dried pieces, 10 mm DTT in 25 mM AMBIC was added (~100 μL) and incubated at 56 °C for 1 h. After reduction by DTT, the samples were removed and allowed to cool to room temperature. The 10 mM DTT was replaced with 55 mM iodoacetamide (IAA) in 25 mM AMBIC and placed in the dark for 30 min. After alkylation, the IAA solution was removed, and the gel pieces were washed with 25 mM AMBIC and then dried via 50% ACN in 25 mM AMBIC following the sample drying procedure as described previously. To the dried reduced/alkylated gel pieces 75 μL of a 25 ng/μL trypsin solution was added and allowed to swell on ice for 10 min before incubating overnight at 37°C. Once digested the trypsin solution was removed and peptides were eluted with 5% formic acid followed by 50% ACN in 5% formic acid. The peptides were then dried to ~50-75 μL before being desalted and further concentrated by a C18 Zip-Tip. The desalted peptides were further dried to about 10-15 μL and spotted on a MALDI plate with a 1:1 CHCA matrix.

5.5.6 MALDI- TOF/TOF

Mass spectra was collected using a Bruker UltraFlextreme MALDI-TOF/TOF operated in reflection mode. Spectra were summed from randomized locations on the dried droplet and until an acceptable intensity was reached. MS/MS spectra were collected using the LIFT mode and spectra were summed from randomized locations on the dried droplet.

5.5.7 Peptide Identification

Raw spectra were imported into FlexAnalysis and peaks were identified using the “find peaks” function to produce a peak list file containing the identified ion peaks. Files were uploaded onto the MASCOT online MS/MS database search tool. Peak lists were searched against the Uniprot *Homo sapien* database with trypsin enzymatic cleavage and a maximum of four missed

cleavages. Cysteine carboxyamidomethylation set as a fix modification. Variable modifications were set to N-terminus carboxyamidomethylation and acetylation in addition to methionine oxidation. Peptide and fragment tolerance was set to 1.2 kDa and 0.6 kDa, respectively.

5.6 References

(1) Kiela, P. R.; Ghishan, F. K. Physiology of Intestinal Absorption and Secretion. *Best Pract Res Clin Gastroenterol* **2016**, *30* (2), 145–159.

(2) Gupta, A.; Lutsenko, S. Human Copper Transporters: Mechanism, Role in Human Diseases and Therapeutic Potential. *Future Med Chem* **2009**, *1* (6), 1125–1142.

(3) Członkowska, A.; Litwin, T.; Dusek, P.; Ferenci, P.; Lutsenko, S.; Medici, V.; Rybakowski, J. K.; Weiss, K. H.; Schilsky, M. L. Wilson Disease. *Nature Reviews Disease Primers*. Nature Publishing Group December 1, 2018.

(4) Bandmann, O.; Weiss, K. H.; Kaler, S. G. Wilson's Disease and Other Neurological Copper Disorders. *Lancet Neurol* **2015**, *14* (1), 103–113.

(5) Gerosa, C.; Fanni, D.; Congiu, T.; Piras, M.; Cau, F.; Moi, M.; Faa, G. Liver Pathology in Wilson's Disease: From Copper Overload to Cirrhosis. *J Inorg Biochem* **2019**, *193*, 106–111.

(6) Kreuder, J.; Otten, A.; Fuder, H.; Tümer, Z.; Tønnesen, T.; Horn, N.; Dralle, D. Clinical and Biochemical Consequences of Copper-Histidine Therapy in Menkes Disease. *Eur J Pediatr* **1993**, *152* (10), 828–832.

(7) Tümer, Z.; Møller, L. B. Menkes Disease. *European Journal of Human Genetics* **2010**, *18* (5), 511–518.

(8) Ge, E. J.; Bush, A. I.; Casini, A.; Cobine, P. A.; Cross, J. R.; DeNicola, G. M.; Dou, Q. P.; Franz, K. J.; Gohil, V. M.; Gupta, S.; Kaler, S. G.; Lutsenko, S.; Mittal, V.; Petris, M. J.; Polishchuk, R.; Ralle, M.; Schilsky, M. L.; Tonks, N. K.; Vahdat, L. T.; van Aelst, L.; Xi, D.; Yuan, P.; Brady, D. C.; Chang, C. J. Connecting Copper and Cancer: From Transition Metal Signalling to Metalloplasia. *Nat Rev Cancer* **2021**.

(9) Zheng, Y.; Li, X. K.; Wang, Y.; Cai, L. The Role of Zinc, Copper and Iron in the Pathogenesis of Diabetes and Diabetic Complications: Therapeutic Effects by Chelators. *Hemoglobin* **2008**, *32* (1–2), 135–145.

(10) Harder, N. H. O.; Lee, H. P.; Flood, V. J.; San Juan, J. A.; Gillette, S. K.; Heffern, M. C. Fatty Acid Uptake in Liver Hepatocytes Induces Relocalization and Sequestration of Intracellular Copper. *Front Mol Biosci* **2022**, *9* (April), 1–13.

(11) Harder, N. H. O.; Hieronimus, B.; Stanhope, K. L.; Shibata, N. M.; Lee, V.; Nunez, M. v.; Keim, N. L.; Bremer, A.; Havel, P. J.; Heffern, M. C.; Medici, V. Effects of Dietary Glucose and Fructose on Copper, Iron, and Zinc Metabolism Parameters in Humans. *Nutrients* **2020**, *12* (9), 1–14.

(12) Giclas, P. C.; Manthei, U.; Strunk, R. C. *The Acute Phase Response of C3, C5, Ceruloplasmin, and C-Reactive Protein Induced by Turpentine Pleurisy in the Rabbit*.

(13) Orzheshkovskyi, V. v; Trishchynska, M. A. *Ceruloplasmin: Its Role in the Physiological and Pathological Processes*; 2019.

(14) Vashchenko, G.; MacGillivray, R. T. A. Multi-Copper Oxidases and Human Iron Metabolism. *Nutrients*. MDPI AG June 27, 2013, pp 2289–2313.

(15) Lindley, P. F.; Card, G.; Zaitseva, I.; Zaitsev, V.; Reinhammar, B.; Selin-Lindgren, E.; Yoshida, K.; Lindley, P. F.; Card, G.; Zaitseva, I.; Zaitsev, V.; Reinhammar, B.; Selin-Lindgren, E.; Yoshida, K. *An X-Ray Structural Study of Human Ceruloplasmin in Relation to Ferroxidase Activity*; 1997; Vol. 2.

(16) Bento, I.; Peixoto, C.; Zaitsev, V. N.; Lindley, P. F. Ceruloplasmin Revisited: Structural and Functional Roles of Various Metal Cation-Binding Sites. *Acta Crystallogr D Biol Crystallogr* **2007**, *63* (2), 240–248.

(17) Hellman, N. E.; Gitlin, J. D. Ceruloplasmin Metabolism and Function. *Annual Review of Nutrition*. 2002, pp 439–458.

(18) Xu, X.; Pin, S.; Gathinji, M.; Fuchs, R.; Harris, Z. L. Aceruloplasminemia: An Inherited Neurodegenerative Disease with Impairment of Iron Homeostasis. *Annals of the New York Academy of Sciences*. New York Academy of Sciences 2004, pp 299–305.

(19) Judith A. Simcox, D. A. M. Iron and Diabetes Risk. *Cell Metab* **2013**, *17* (3), 329–341.

(20) Nazrul Islam, K.; Takahashi, M.; Higashiyama, S.; Myint, T.; Uozumi, N.; Kayanoki, Y.; Kaneto, H.; Kosaka, H.; Taniguchi, N. *Fragmentation of Ceruloplasmin Following Non-Enzymatic Glycation Reaction 1*; 1995; Vol. 118.

(21) Sunderman Jr., F. W.; Nomoto, S. Measurement of Human Serum Ceruloplasmin by Its P-Phenylenediamine Oxidase Activity. *Clin Chem* **1970**, *16* (11), 903–910.

(22) Schosinsky, K. H.; Lehmann, H. P.; Beeler, M. F. Measurement of Ceruloplasmin from Its Oxidase Activity in Serum by Use of O-Dianisidine Dihydrochloride. *Clin Chem* **1974**, *20* (12), 1556–1563.

(23) Mensink, M. A.; Frijlink, H. W.; van der Voort Maarschalk, K.; Hinrichs, W. L. J. How Sugars Protect Proteins in the Solid State and during Drying (Review): Mechanisms of Stabilization in Relation to Stress Conditions. *European Journal of Pharmaceutics and Biopharmaceutics*. Elsevier B.V. May 1, 2017, pp 288–295.

(24) Baura, G. Artificial Pancreas. In *Medical Device Technologies*; Elsevier, 2021; pp 503–537.

(25) Artyukhov, V. G.; Basharina, O. v.; Bragin, M. v.; Sukhanov, D. Y.; Vashanov, G. A. Spectral and Functional Properties of Ceruloplasmin under UV Irradiation. *Biophysics (Russian Federation)* **2012**, *57* (3), 295–299.

(26) Sedlák, E.; Žoldák, G.; Wittung-Stafshede, P. Role of Copper in Thermal Stability of Human Ceruloplasmin. *Biophys J* **2008**, *94* (4), 1384–1391.

(27) Samygina, V. R.; Sokolov, A. v.; Bourenkov, G.; Schneider, T. R.; Anashkin, V. A.; Kozlov, S. O.; Kolmakov, N. N.; Vasilyev, V. B. Rat Ceruloplasmin: A New Labile Copper Binding Site and Zinc/Copper Mosaic. *Metallomics* **2017**, *9* (12), 1828–1838.

(28) Clerc, F.; Reiding, K. R.; Jansen, B. C.; Kammeijer, G. S. M.; Bondt, A.; Wuhrer, M. Human Plasma Protein N-Glycosylation. *Glycoconj J* **2016**, *33* (3), 309–343.